Dissertation

submitted to the

Combined Faculty of Natural Sciences and Mathematics

of Heidelberg University, Germany

for the degree of

Doctor of Natural Sciences

Put forward by

Matteo Pais

born in: Cagliari, Italy

Oral examination: 19 October 2020

Magneto-hydrodynamical simulations with cosmic ray acceleration at supernova remnants

Referees:

Prof. Dr. Christoph Pfrommer
Prof. Dr. Ralf Klessen

Zusammenfassung

Stoßwellen von Supernovaüberresten werden als die besten Orte für die Produktion von galaktischer kosmischer Strahlung betrachtet. Aus der Wechselwirkung von dort produzierter kosmischer Strahlung mit Photonenfeldern und mit dem interstellaren Medium entsteht ein Multiwellenlängenspektrum vom Radio bis zur Gammastrahlung. Insbesondere die TeV Gammastrahlung könnte aus beiden, hadronischen und leptonischen, Wechselwirkungen hervorgehen. Neue Ergebnisse aus kinetischen Simulationen schlagen vor, dass die Beschleunigung von Ionen der kosmischen Strahlungen stark vom relativen Winkel zwischen der Stoßrichtung und dem lokalen Magnetfeld abhängt. Dies bedeutet, dass die zugrundeliegende Topologie des interstellaren Magentfelds, in das sich die Supernovaüberrest ausbreitet, die Morphologie der Strahlungsemission bestimmt.

Durch das Verwenden von dreidimensionalen, magnetohydrodynamischen Simulationen mit dem AREPO code, studiere ich die Effekte der winkelabhängigen Beschleunigung an anhand der Emissionsmorphologie von hellen Supernovaüberresten. Wir wenden die Ergebnisse der idealisierten Tests auf wohl bekannte, helle Supernovaüberreste unter der Annahme eines hadronisches Modells an, um verschiedene Emissionsmorphologien zu reproduzieren. Anhand der TeV Morphologie sagen wir die Zusammensetzung des interstellaren Mediums und die Kohärenzlänge des interstellaren Magnetfelds voraus. Darüberhinaus untersuchen wir den Einfluss von verschiedenen interstellaren Umgebungen, unter anderem für den Fall eines klumpigen Mediums bei Kernkollapssupernovaüberresten. Wir zeigen, dass das hadronische Modell eine gute Übereinstimmung sowohl mit den beobachteten Morphologien als auch mit den Spektren aufweist.

Summary

Supernova remnants shocks are considered the best sites for the production of Galactic cosmic rays. The interactions of cosmic rays produced at supernova shocks with photon fields and the interstellar medium generate a multi-wavelength spectrum from radio to gamma rays. In particular, TeV gamma-ray emission may originate from both hadronic and leptonic interactions. Recent results from kinetic simulations suggest that the acceleration of cosmic ray ions strongly depends on the relative angle between the shock normal and the local magnetic field orientation. This means that the underlying topology of the interstellar magnetic field in which the supernova remnant expands determines the emission morphology.

Using 3D magneto-hydrodynamical simulation with the code AREPO, we study the effect of the obliquity dependent shock acceleration on the emission morphology of bright supernova remnants. We apply the results of idealized cases to well-known bright supernova remnants assuming a hadronic model to reproduce different emission morphologies. From the TeV gamma-ray morphology we predict the local composition of the interstellar medium and the coherence scale of the interstellar magnetic field. Furthermore we study the impact of different interstellar

environments, such as the case of a clumpy medium for core-collapse supernova remnants. We show that the hadronic model provides a good match for both the observed morphologies and the spectra.

Contents

1. Cosmic Rays

Abstract

In this chapter the physics of cosmic rays is discussed with a focus on both on the theoretical and observational aspects. In Sect. 1.1 the theory on the origin of galactic cosmic rays is exposed. The theory of the transport of cosmic rays and its implications are discussed in Sect. 1.2. I introduce the fluid description of cosmic rays in Sect. 1.3. Non-thermal emission processes originating from the interaction of cosmic rays with matter, magnetic and photon fields are discussed in Sect. 1.4 with a particular focus on their hadronic and leptonic origin. Finally, a consequence of plasma interactions and catastrophic losses of cosmic rays are discussed in Sect. 1.5.

1.1. Origin of cosmic rays

1.1.1. Observations - Galactic population

Cosmic rays (CRs) are charged particles with an the energy density in the Galaxy of ~ 1 eV cm^{-3}. Early observation conducted by the Austrian physicist Victor Hess via atmospheric balloons in 1912 (Hess, 1912) confirmed the existence of a type radiation of great penetrating power entering in the atmosphere and originating from outside the Earth.

Most of CRs are hydrogen nuclei (protons) with a relevant fraction ($\sim 10\%$) of helium nuclei and a negligible presence of heavy elements ($\sim 1\%$). The chemical composition of CRs provides important information about their origin and their transport through the Galactic magnetic field.

The CRs spectrum spans for several decades in energy and intensity of flux. Charged particles experience gyration around the magnetic field lines with a radius, called Larmor radius or gyroradius, proportional to the particle momentum perpendicular to the magnetic field:

$$r_{\rm L} = \frac{p_\perp c}{ZeB} = \frac{2}{Z}\left(\frac{E}{10\ \text{GeV}}\right)\left(\frac{B}{\mu\text{G}}\right)^{-1}\ \text{AU} \tag{1.1}$$

CRs with energies $\lesssim 30$ GeV are modulated by the magnetized solar wind. Because their Larmor radius is smaller than the characteristic dimension of the magnetic field in the interplanetary medium, CRs are scattered by the magnetic field irregularities and eventually swept out of the Solar System reducing their observed flux

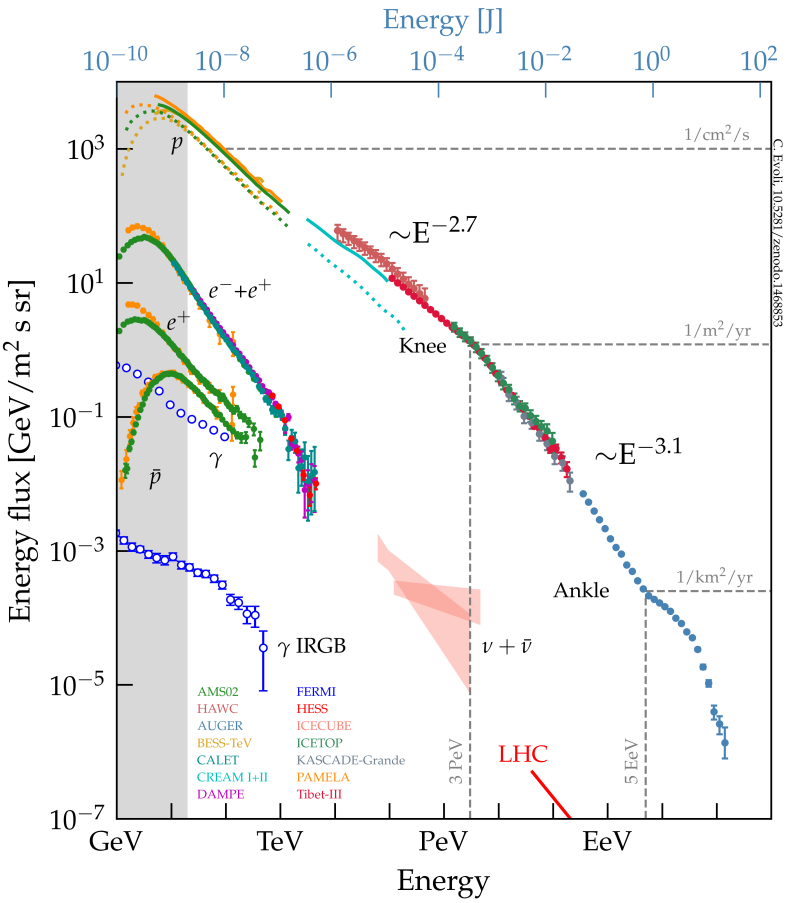

Figure 1.1.: All-particle spectrum of CRs at the Earth measured by different experiments in the course of years (Evoli, 2018). The observed slope transitions are highlighted: the knee is located at 3PeV and the ankle at 5EeV.

on Earth (Parker, 1965). Above 30 GeV the CR spectrum of all nuclear components is well described by a power law spanning up to 10^{11} GeV in energy (Fig. 1.1). The spectrum exhibits a steepening around $E_k = 3$ PeV known as *the knee* passing from a slope of -2.7 to -3.1. There is evidence that the chemical composition of CRs depends on the energy and remarkably changes across the knee region with a dominance of heavy nuclei at very high energies. A possible explanation is the superposition of cutoffs from different chemical species (Hörandel, 2004).

A second, less pronounced, *knee* possibly associated with the steepening of the Galactic Fe component is present at 10^{17} eV (Candia et al., 2002). At energies around 5×10^{18} eV the spectrum exhibits a ankle-like structure and its logarithmic slope flattens again to around -2.75 (Fisk & Gloeckler, 2012). Some authors suggest as this feature may be a sign of the transition from Galactic to extragalactic CRs (Blasi, 2014). In fact, assuming a standard galactic magnetic field strength of about 10μG, these particles can not gyrate in the galactic disk because their Larmor radius is larger than the thickness of the galactic disk (500 pc).

At energies around 10^{20} eV CR protons are able to interact with the cosmic microwave background radiation (CMB) via producing both neutral and positive pions and lose energy on scales of about $\simeq$ 10 Mpc. This corresponds to the

suppression of the observed spectrum at these energies and is named GZK-cutoff (Greisen, 1966; Zatsepin & Kuzmin, 1966).

1.1.2. SNR paradigm

The presence of a knee and the simultaneous change in chemical composition at those energies suggests that the bulk of CRs with energies $\lesssim 10^{15}$ eV originates from the Milky Way. The main accelerator candidates for CRs are galactic supernova remnants (SNRs) as first proposed by Baade & Zwicky (1934) and Ginzburg & Syrovatsky (1961). Our observational evidence is corroborated by several independent phenomena such as the detection of gamma rays associated with the production of neutral pions in SNRs close to molecular clouds (Ackermann, 2013; Sano et al., 2015; Fukui et al., 2017) and the bright X-ray filaments detected in many young SNRs that prove an amplification of the magnetic field in the shock region (Vink, 2012).

The Hillas criterion provides an estimate of the maximum energy $E_{\max}$ achievable in an accelerator and is derived by a confinement argument. Given the accelerator size L, the upstream magnetic field strength B_0 and the charge q it reads

$$E_{\max} = qB_0L \tag{1.2}$$

For typical SNR parameters $L = 1$ pc and $B_0 = 10\mu$G an energy of $E_{\max} = 1$ PeV is reachable in such objects.

The process of diffusive shock acceleration (DSA) provides a way to accelerate charged particles at supernova shocks (Krymskii (1977); Axford et al. (1977); Blandford & Ostriker (1978); Bell (1978a)). In order to match the CR flux observed in the Galaxy an efficiency of ~ 10 per cent is required (Hillas, 2005). The theory naturally predicts an energy spectrum of the accelerated particles that is proportional to a power law $E^{-\alpha}$ whose spectral index α depends only on the shock compression ratio $\mathcal{R}$ experienced by the particles and reads:

$$\alpha = \frac{\mathcal{R}+2}{\mathcal{R}-1} \tag{1.3}$$

which tends to 2 for strong shocks ($\mathcal{R} = 4$). It needs to be pointed out that a dynamical backreaction of the charged accelerated particles is likely to occur modifying the shock structure and affecting the slope of the CR spectrum (Malkov & Drury (2001); Caprioli (2012) for a review). This non linear theory is also likely to predict the generation of the magnetic field amplification by CR-driven instabilities (Bell (2004); Amato & Blasi (2006); Caprioli et al. (2010) for a semi-analytic solution of the problem).

The CR flux observed at Earth ($\propto E^{-2.75}$) is steeper than the injected spectrum in the test particle approximation ($\propto E^{-2}$). CRs accelerated at SNR shocks reach our planet after experiencing a propagation with energy dependent diffusion in the Galaxy. Because the CR flux at Earth has to be proportional to the injection spectrum and the spectrum scales as $1/D(E) \propto E^{-\delta}$, where $D(E)$ is the energy-dependent diffusion coefficient, this implies that that the observed slope needs a diffusion coefficient that scales as $D(E) \propto E^{0.7}$.

The combination of acceleration of charged particles via DSA at SN shocks and the diffusive propagation of CRs in the Galaxy are the basis of the so-called *supernova remnant paradigm* which represents one of the best studied models to explain the bulk of CRs we detect at Earth.

1.2. Theory - Transport of Cosmic Rays

The acceleration and transport of CRs is essential to understand several high energy astrophysical problems. CRs generally propagate in a collisionless, magnetized and tenuous background plasma consisting of protons and electrons. The CR energy density is approximately in equipartition with the thermal and turbulent density of the background medium and the magnetic field.

Measurements of the ratio of boron to carbon fluxes and the associated grammage traversed by CRs allow to estimate the residency time of CRs within the galaxy to about 2×10^7 yrs (Kulsrud, 2005; Blasi, 2013). This time scale exceeds the ballistic propagation time scale of CRs by at least three orders of magnitude. The CRs arising from plasma processes arriving at the Earth have a remarkably high level of isotropy with anisotropies of the order of 10^{-4} (Kulsrud, 2005). This isotropy is a consequence of the interaction of the fast scattering of CR particles by the magneto-hydrodynamic (MHD) turbulence. It is concluded that the propagation of CR is dominated by interactions with the magnetic fields.

For a stationary one-dimensional shock, in which the normal to the shock is parallel with respect to the orientation of the magnetic field, the transport of particles moving in a fluid with bulk velocity $v \ll c$ is described by a Fokker-Planck type equation that includes diffusion and advection, namely the *transport equation* in the absence of CR streaming (Skilling, 1975; Schlickeiser, 2002) that reads

$$\frac{\partial f}{\partial t} + v\frac{\partial f}{\partial x} = \underbrace{-\frac{1}{p^2}\frac{\partial}{\partial p}[p^2 A_1(x,p) f]}_{\text{Fermi I acc.}} + \underbrace{\frac{1}{p^2}\frac{\partial}{\partial p}\left[p^2 A_2(x,p)\frac{\partial}{\partial p} f\right]}_{\text{Fermi II acc.}} + \underbrace{\frac{\partial}{\partial x}\left[\kappa\frac{\partial f}{\partial x}\right]}_{\text{spatial diff.}} + \underbrace{\frac{1}{3}\frac{\mathrm{d}v}{\mathrm{d}x} p\frac{\partial f}{\partial p}}_{\text{adiab. changes}} + Q \tag{1.4}$$

where $f = f(x,p,t)$ is the CR distribution function normalized such that the number density is $n_{\mathrm{cr}} = \int 4\pi p^2 f \mathrm{d}p$, the third term on the right-hand side represents the spatial diffusion, $\kappa(x,p)$ is the diffusion coefficient, the fourth term on the right-hand side represents the adiabatic changes of CRs, $Q(x,p)$ is the injection rate. The terms $A_1(x,p)$ and $A_2(x,p)$ are related to the acceleration of CRs via respectively the first (Fermi, 1954) and second (Fermi, 1949) order Fermi processes. Both processes are based on the idea of CRs colliding against moving magnetic fields with a certain pitch angle (i.e. the angle between the direction of motion of the particle and the magnetic field vector):

- **First order Fermi acceleration**. It occurs when the charged particle is trapped between two approaching clouds on the same magnetic field, resulting in an extremely efficient acceleration. An ideal environment is represented by shocks. We can consider a particle crossing the shock from the

upstream (pre-shock regime) to the *downstream* (post-shock regime) with energy E. If the particle scatters on the downstream magnetic irregularities and returns to the shock and can cross is surface again with a different pitch angle. Assuming that the velocity of the particles is isotropized by scatterings both upstream and downstream the mean value of the energy change per upstream-downstream-upstream cycle is $\propto v/c$, which is first order in velocity (Bell, 1978a). The advantage is that there are no configurations that lead to energy losses and the energy gain is independent of the scattering process.

- **Second order Fermi acceleration**. It describes stochastic acceleration ($\langle E^2 \rangle \neq 0$) in which an injected particle with energy E scatters on the magnetic irregularities of a cloud and experiences a net gain of energy transferred from the cloud to the particle. At each interaction the particle experiences a gain or loss in energy depending whether the particle-cloud collision occurred head-on or tail-on. Assuming the isotropization of the pitch angle the net energy gain is a second order quantity in velocity and reads $\langle \Delta E/E \rangle \propto v^2/c^2$. This process is thus less efficient than the previously discussed one.

Along with energy gaining processes CRs experience also a loss of energy by several mechanisms. Some of the most important ones are the following:

- **Synchrotron losses**. Particles accelerated by magnetic fields radiate energy. In particular, for a relativistic particle with a given Lorentz factor γ the energy loss by gyration in a magnetic field is given by:

$$\frac{\mathrm{d}E}{\mathrm{d}t} = -\frac{4}{3}\sigma_T c \beta^2 \gamma^2 \varepsilon_B \tag{1.5}$$

  where $\varepsilon_B = B^2/8\pi$ is the magnetic field energy density, $\beta = v/c$, $\gamma = (1 - \beta^2)^{-1/2}$ is the Lorentz factor, $\sigma_T = 8\pi r_0^2/3$ is the Thomson cross section and $r_0 = e^2/(m_\mathrm{e} c^2)$ is the classical electron radius;

- **Inverse Compton losses**. Relativistic charged particles can scatter with a photon field. If the particle energy is greater than the energy of the photon, a part of the particle energy is transferred to the incident photon resulting in a loss of energy for the particle. The total power emitted by Compton scattering off of a single electron reads

$$\frac{\mathrm{d}E}{\mathrm{d}t} = -\frac{4}{3}\sigma_T c \beta^2 \gamma^2 \varepsilon_\mathrm{ph} \tag{1.6}$$

  where ε_ph is the photon energy density;

- **Coulomb and ionization losses**. Dominant for low energy CR nuclei and relevant for electrons the particles experience both energy losses via the loss of electron in ionization processes and via Coulomb interaction in an ionized medium.

- **Hadronic interactions**. Dominant for α high energy nuclei when a kinematic energy threshold of 0.78 GeV is reached the collision processes can open a channel production for light mesons such charged and neutral pions that consequently decay into high-energy photons, muons and neutrinos;
- **Spallation**. The interaction of primary CR nuclei (protons and alpha particles) with the ISM is responsible of the production of light (Li, Be, B) and sub-iron elements (Sc, Ti, V, Cr, and Mn) which are over-abundant in CRs with respect to the solar system abundances.

1.2.1. Diffusive Shock Acceleration

The equations of motion for an ideal fluid (with no viscosity, thermal conductivity and electric resistance) admit the presence of discontinuous flows. Astrophysical shock waves are at the basis of highly energetic phenomena.

Once a shock forms it moves through the fluid supersonically and the material behind the shock is hotter, denser and has a higher pressure. Given the reference frame of the shock, an incoming supersonic material with velocity v_1, density ρ_1 and pressure P_1 crossing the shock becomes subsonic with velocity v_2, density ρ_2 and pressure P_2, where the subscripts 1 and 2 denote the upstream (pre-shock) and downstream (post-shock) regimes, respectively.

In the approximation of an indefinitely thin shock surface is possible to write conservation relation for mass, momentum, and pressure flux across the discontinuity. These conditions are named Rankine-Hugoniot equations or jump conditions and read:

$$\rho_1 v_1 = \rho_2 v_2 \tag{1.7}$$

$$P_1 + \rho_1 v_1^2 = P_2 + \rho_2^2 \tag{1.8}$$

$$(\varepsilon_1 + P_1) + \rho_1 \frac{v_1^2}{2} = (\varepsilon_2 + P_2) + \rho_2 \frac{v_2^2}{2} \tag{1.9}$$

where ρ_i is the density, P_i is the pressure and ε_i is the internal energy density or region i (pre- and post-shock). These conservation laws admit both trivial solutions (i.e. $\rho_i = \text{const.}$, $P_i = \text{const.}$, $\varepsilon_i = \text{const.}$) and the following discontinuous solutions:

$$\mathcal{R} = \frac{\rho_2}{\rho_1} = \frac{u_1}{u_2} = \frac{\gamma + 1}{(\gamma - 1) + 2/\mathcal{M}_1^2} \tag{1.10}$$

$$\frac{P_2}{P_1} = \frac{2\gamma \mathcal{M}_1^2}{\gamma + 1} - \frac{\gamma - 1}{\gamma + 1} \tag{1.11}$$

$$\frac{T_2}{T_1} = \frac{[2\gamma - \gamma(\gamma - 1)/\mathcal{M}_1^2][(\gamma - 1) + 2/\mathcal{M}_1^2]}{(\gamma + 1)^2} \mathcal{M}_1^2 \tag{1.12}$$

where $\mathcal{M}_1 = v_1/c_1$ is the upstream Mach number, which denotes the shock strength. From Eq. (1.10) we notice that in the limit of strong shocks ($\mathcal{M}_1 \gg 1$) for a thermal fluid with adiabatic index $\gamma = 5/3$ it is limited by $\mathcal{R} = 4$ while a relativistic

fluid ($\gamma = 4/3$) allows $\mathcal{R} = 7$, meaning that the shock is more compressed. From Eq. (1.12) we also notice that a shock is efficient in transforming the kinetic energy of the upstream particles to downstream internal energy.

In the case of magnetized shocks additional jump conditions involving the components of the magnetic field are present. For a magnetic field with components $\boldsymbol{B} = (B_x, B_y, 0)$, a velocity flow with components $\boldsymbol{v} = (v_x, v_y, 0)$ and a shock normal $\boldsymbol{n} = (1, 0, 0)$ the magnetic field experiences continuity of the normal magnetic field component and the Maxwell stress tensor component which expresses the continuity of the normal-momentum flux and of the transverse-momentum flux. These conditions read (Schlickeiser, 2002):

$$B_{x,1} = B_{x,2} \tag{1.13}$$

$$P_1 + \rho_1 v_{x,1}^2 + \frac{B_{y,1}^2}{8\pi} = P_2 + \rho_2 v_{x,2}^2 + \frac{B_{y,2}^2}{8\pi} \tag{1.14}$$

$$\rho_1 v_{x,1} v_{y,1} - \frac{1}{4\pi} B_{x,1} B_{y,1} = \rho_2 v_{x,2} v_{y,2} - \frac{1}{4\pi} B_{x,2} B_{y,2} \tag{1.15}$$

The shocks involving magnetic fields can be classified as:

- **Parallel or quasi-parallel shocks**. Shocks where the vector normal to the shock surface is parallel or quasi-parallel to the direction of the local magnetic field. The angle between the shock normal and the magnetic field is $0° \leq \theta < 45°$;

- **Perpendicular or quasi perpendicular shocks**. Shocks where the shock normal is oriented perpendicularly or quasi-perpendicularly to the direction of the local magnetic field vector with angles $45° < \theta \leq 90°$.

In the microscopic picture, collisionless shocks, namely shocks mediated by electromagnetic forces between charged particles, form because of the excitation of electromagnetic instabilities present in the flow. An exhaustive review of collisionless shocks and the associated microphysics can be found in Marcowith et al. (2016).

In diffusive shock acceleration (DSA) particles gain energy by scattering off of magnetic disturbances present in the upstream and downstream media. The difference of velocity propagation of the scattering centers induces a systematic energy gain at each shock crossing.

However the injection of new particles participating at the acceleration process is still a problematic aspect of particle acceleration at shocks. Before the onset of numerical plasma-kinetic simulations, the properties of injection were related to the microphysics of the particles moving in the plasma behind the shock via models of thermal leakage (Malkov, 1998). The introduction of particle-in-cell (PIC) simulations helped to cast light on the formation of collisionless shocks with promising results (Spitkovsky, 2008a,b; Caprioli & Spitkovsky, 2014a).

Using the same procedure described in Blandford & Ostriker (1978), for a stationary parallel shock a simple treatment of DSA can be carried out using a simplified version of Eq. (1.4) that reads

$$v\frac{\partial f}{\partial x} = \frac{\partial}{\partial x}\left[\kappa\frac{\partial f}{\partial x}\right] + \frac{1}{3}\frac{\partial f}{\partial x}p\frac{\partial f}{\partial p} + Q(x,p) \tag{1.16}$$

The shock is supposed to be indefinitely thin and located at $x = 0$. The injection term Q can be approximated supposing that the particles in the Maxwellian tail are injected immediately downstream of the shock if their momentum is larger than a critical value $p_{\rm inj}$ (Blasi et al., 2005):

$$p_{\rm inj} = \xi_{\rm inj} p_{\rm th,2} = \xi_{\rm inj}\sqrt{2m_p k_B T_2}\ , \tag{1.17}$$

where $\xi_{\rm inj}$ is the injection efficiency, k_B is the Boltzmann constant, $m_{\rm p}$ is the proton mass and T_2 the downstream temperature. This value in momentum corresponds to a Larmor radius large enough to allow the particles to cross the shock and return upstream. This leads to the following expression for the injection term Q:

$$Q(p,x) = \frac{\eta n_1 v_1}{4\pi p_{\rm inj}^2}\delta(p - p_{\rm inj})\delta(x) = q_0(p, p_{\rm inj})\delta(x)\ , \tag{1.18}$$

where n_1 is the number density upstream and $\eta = \eta(\xi)$ represents the fraction of the particle flux across the shock surface participating to the acceleration process. A more recent formulation of the theory of ion injection at non-relativistic collisionless shocks based on kinetic hybrid simulation is given by Caprioli et al. (2015).

The integration of the transport equation across the shock surface between 0^+ and 0^- leads to the continuity equation:

$$\left[\kappa\frac{\partial f}{\partial x}\right]_2 - \left[\kappa\frac{\partial f}{\partial x}\right]_1 + \frac{1}{3}(v_2 - v_1)p\frac{\partial f_0}{\partial p} + q_0(p) = 0 \tag{1.19}$$

with $f_0(p)$ representing the distribution function of the CR at the shock. The scattering downstream leads to a homogeneous distribution of particles, thus $[\partial f/\partial x]_2 = 0$, while in the upstream $[\partial v/\partial x]_1 = 0$. The last condition translates in

$$\left[\kappa\frac{\partial f}{\partial x}\right]_1 = v_1 f_0\ . \tag{1.20}$$

This leads to the equation

$$v_1 f_0 = \frac{1}{3}(v_2 - v_1)p\frac{\partial f_0}{\partial p} + \frac{\zeta n_1 v_1}{4\pi p_{\rm inj}^2}\delta(p - p_{\rm inj}) \tag{1.21}$$

The solution of this equation takes the form of a power-law in momenta with a lower cutoff:

$$f_0 = A\left(\frac{p}{p_{\rm inj}}\right)^{-\alpha}\Theta(p - p_{\rm inj}) \tag{1.22}$$

where α is the spectral index and A is a normalization constant. Substituting the latter into Eq. (1.21) and equating similar terms, we find a relation that links the spectral index α to the compression ratio $\mathcal{R}$ and the expression for the normalization:

$$f_0 = \frac{3\mathcal{R}}{\mathcal{R}-1}\frac{\eta n_1}{4\pi p_{\rm inj}^3}\left(\frac{p}{p_{\rm inj}}\right)^{-\frac{3\mathcal{R}}{\mathcal{R}-1}}\Theta(p-p_{\rm inj}) \tag{1.23}$$

where $\alpha = 3\mathcal{R}/(\mathcal{R}-1)$. We notice that for strong shocks $\mathcal{R}=4$ so $\alpha=4$. The advantage of this models is its independence on the diffusion coefficient and the complicated underlying physics. On the other hand this power law extends up to infinite energy and does not predict a cutoff which emerges from the diffusion coefficient. Furthermore the presence of CR pressure modifies the shock itself and the predicted spectral index. Recent studies show how the spectral slope increases with the increase of the injection efficiency up to $\alpha = 2.6$ (Caprioli, 2011).

1.2.2. The microscopic picture - Pitch angle scattering

Because CRs are composed of charged particles, in the presence of a magnetic field B_0 they gyrate along magnetic field lines with characteristic gyration frequency $\Omega = qB_0/(\gamma mc)$. For a pitch angle of $\mu = \cos\theta$ between the magnetic field direction and the particle velocity the equation of motion is

$$v_x(t) = v_\perp\cos(\Omega t+\phi)\,, \qquad v_y(t) = -v_\perp\sin(\Omega t+\phi)\,, \qquad v_z(t) = v_\parallel = \mu v\,, \tag{1.24}$$

where $v_\parallel = \mu v$, $v_\perp = v\sqrt{1-\mu^2}$ and v is the absolute value of the particle velocity.

However, CRs also scatter on magnetic fluctuations. Second-order Fermi acceleration models a random walk of particles and the role of the scattering centers is played by the moving magnetized clouds. In DSA the role of magnetized clouds is played by plasma waves, namely Alfvén waves, which move with Alfvén velocity $v_{\rm A} = B/\sqrt{4\pi\rho_i} = 2B_{\mu\rm G}n_{i,\rm cm^{-3}}$ km s^{-1}, where $n_i = \rho_i\mu_{\rm w}m_{\rm p}$ with $\mu_{\rm w}$ is the mean molecular weight.

A wave packet consisting of a superposition of Alfvén waves that are polarized along the $x-$axis and with amplitude $\delta\boldsymbol{B}$ superposed on the background magnetic field B_0 exerts a Lorentz force on the CR's motion. The individual Fourier modes of the perturbations have the wave form:

$$\delta\boldsymbol{B} = \delta B\hat{\boldsymbol{x}}\sin(k_\parallel z-\omega t)\,, \tag{1.25}$$

with $z = v_\parallel t = v\mu t$. The motion along z is modified according to the Lorentz force:

$$\begin{aligned}(\boldsymbol{v}\times\delta\boldsymbol{B})_z &= -ev_y\delta B_x\hat{\boldsymbol{z}} = -v_\perp\delta B_0\hat{\boldsymbol{z}}\sin(\Omega t+\phi)\sin(kz-\omega t)\\ &= -\frac{1}{2}v_\perp\delta B_0\{\cos[(\Omega-k_\parallel v\mu+\omega)t+\phi]-\cos[(\Omega+k_\parallel v\mu-\omega)t+\phi]\}\,.\end{aligned} \tag{1.26}$$

In the case of $\Omega + kv\mu - \omega \simeq 0$ the second cosine averages to 0 while the first term disappears only if the resonant conditions $\Omega - kv\mu + \omega = 0$ is met. The

associated change in momentum along z is

$$\Delta p_z = \frac{e}{c}(\boldsymbol{v} \times \delta\boldsymbol{B})_z \Delta t = p_\perp \frac{\delta B}{B_0} \delta\left(k_\parallel \mu v - \Omega - \omega\right) \tag{1.27}$$

where $\Delta t = \Omega^{-1}$ and $p_\perp = \gamma m v_\perp$. The Dirac δ function expresses the resonance condition for a right moving CR particle. Because $p_z = p\mu$ then $\Delta p_z = p\Delta\mu = -p \sin\theta \delta\theta$ which translates in a condition for the pitch angle,

$$\delta\theta \propto -\frac{\delta B}{B_0} \ , \tag{1.28}$$

which increases or decreases according to the relative phase of the interaction.

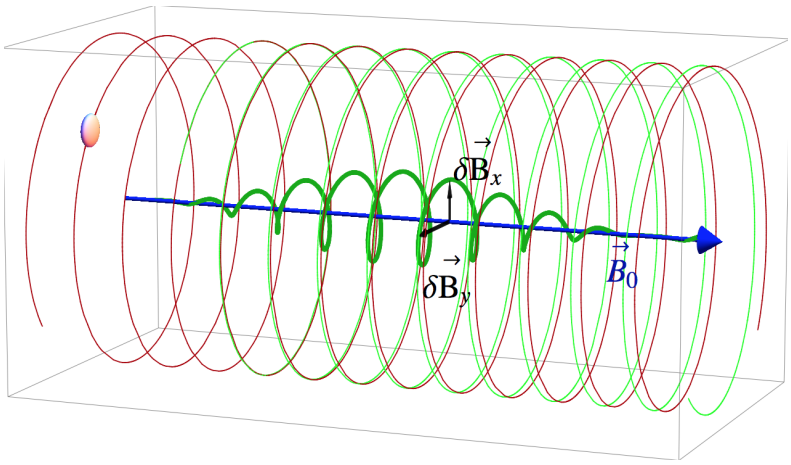

Figure 1.2.: Motion of a particle in a magnetic field. The red spiral represents the motion of he particle in a homogeneous magnetic field B_0 while the green spiral represents the motion of the same particle in a perturbed magnetic field with perturbations perpendicular to the direction of the motion (Morlino, 2017).

The resulting averaged scattering rate for the pitch angle over a period is then

$$\nu = \left\langle \frac{\Delta\theta \Delta\theta}{\Delta t} \right\rangle \sim \Omega \left\langle \left(\frac{\delta B}{B_0}\right)^2 \right\rangle \ , \tag{1.29}$$

which has the form of a pitch-angle diffusion of CRs in the wave frame. Introducing the wave energy density $\mathcal{E}(k)$ at the wave number k such that $(\delta B)^2/8\pi \sim k\mathcal{E}(k)$, Eq. (1.29) becomes

$$\nu \sim \Omega \frac{k\mathcal{E}(k)}{B_0^2/8\pi} = \Omega \mathcal{F}(k) \ , \tag{1.30}$$

where $\mathcal{F}(k)$ is the gyrofactor. The scale of magnetic fluctuations is of extreme importance in this process. Small fluctuations (below the gyroradius of the particle) are averaged out, which results in a null net force on the particle motion. On the other hand, fluctuations on large scale adiabatically change the equations of motion of an orbit. If the scale of the magnetic fluctuations is of the same order of the gyroradius of the particle the effect is maximized. This leads to two resonance conditions:

- **Landau resonance** for the condition $\omega - k_\parallel v_\parallel = 0$
- **Gyroresonances** for the condition $\omega - k_\parallel v_\parallel = \mathcal{N}\Omega$ with $\mathcal{N} \in \mathbb{N}$.

The Alfvén wave has a velocity of $\pm v_\mathrm{A} = \omega/k$ where the positive sign stands for co-propagating waves, and the negative sign stands for counter-propagating waves. If the particle velocity is $v \sim c$ a Landau resonance translates in the condition $k_\parallel/k = v_\mathrm{A}/v_\parallel \ll 1$.

The condition in the case of gyroresonances similarly reads $\pm k_\parallel v_\mathrm{A} - k_\parallel v_\parallel = \mathcal{N}\Omega$ which means that (Thomas & Pfrommer, 2019)

$$k_\parallel = \frac{\Omega}{\mu v \mp v_\mathrm{A}} \sim \frac{1}{\mu r_g} \,, \tag{1.31}$$

for a right-hand polarized wave with $\mathcal{N} = 1$ and $\Omega = v/r_g$, meaning that the fluctuations are dynamically important when the wavelength associated to the Alfvén waves is of the same order of magnitude of the gyroradius of the particles. The time required for a particle to change its direction (i.e. $\delta\theta \sim 1$) and isotropise the CR distribution can be calculated using Eq. (1.29) and roughly corresponds to $\tau \sim 1/\nu$.

For an escape time of CRs of the order of $t_\mathrm{esc} = 3 \times 10^7$ yrs, as measured by Boron to Carbon ratio, and an estimate of the Galactic halo scale of $H \sim 3$ kpc the galactic diffusion coefficient is estimated to be $\kappa \sim H^2/t_\mathrm{esc} \sim (1-3)\times 10^{28}$ cm^2 s^{-1}. If the diffusion coefficient for CRs is estimated as $1/3v^2\tau$ where τ is the scattering time then at the resonant wave number this corresponds to magnetic fluctuations of the order of $\delta B/B_0 \sim 10^{-4}$. This means that a small amplitude of Alfvén waves can account for the level of diffusion needed to confine the CRs in the Galaxy (see also Sect. 1.2.4)

The perturbative nature of this treatment is valid until the condition $\delta B/B_0 \ll 1$ holds. Magnetic field amplification led by a net current of CRs may lead to instabilities (i.e. when $\delta B/B \gg 1$) in the plasma (Bell, 2004).

1.2.3. Maximum energy

In order to estimate the maximum energy achievable by a particle we need to calculate how much time it spends in the acceleration process. If CRs are accelerated at SNR shocks, the acceleration time t_acc has to be less than the age of the remnant t_age. The repeated shock crossing of the particle in the acceleration process of DSA illustrates the process through which a particle gains energy in each cycle via a pitch-angle scattering by Alfvén waves (Skilling, 1975). The scattering process confines the particles to the region around the shock allowing a first-order Fermi acceleration process (Bell, 1978a). A particle after scattering with magnetic inhomogeneities in the upstream with energy E_1 crosses the shock with pitch angle $\mu_1 = \cos\theta_1$. In the reference frame of the downstream it has an energy of:

$$E_2 = \gamma E_1(1 + \beta\mu_1) \tag{1.32}$$

where $\beta = u_2 - u_1$ and $\gamma = (1-\beta^2)^{-1/2}$. If the particle returns from the downstream and crosses the shock again with a pitch angle $\mu_2 = \cos\theta_2$ then in the upstream reference frame its energy is:

$$E_1' = \gamma E_2(1-\beta\mu_2) = \gamma^2 E_1(1+\beta\mu_1)(1-\beta\mu_2) \simeq \gamma^2 E_1[1+\beta(\mu_1-\mu_2)] \quad (1.33)$$

We notice that after a cycle $E_1' > E_1$. If we assume isotropization of the particle distribution by scattering both upstream and downstream we can substitute the average values of the pitch angles, namely $\langle\mu_1\rangle = 2/3$ and $\langle\mu_2\rangle = -2/3$, such that the average fractional energy change per cycle is then

$$\langle E_1'\rangle \simeq \gamma^2 E_1 \left(1+\frac{4}{3}\beta\right) \quad (1.34)$$

For a non-relativistic shock with $\gamma = 1$ the average fractional energy change per cycle is then

$$\left\langle \frac{E_1' - E_1}{E_1} \right\rangle = \frac{4}{3}\beta \quad (1.35)$$

After k cycles the net energy gain $(E_1')^k/E_1$ diverges geometrically. Assuming isotropy the flux of particles crossing a surface Σ is given by $\Phi_2 = nv_2$ and isotropically half of them will return upstream with an average velocity of $c/2$. The flux coming upstream is $\Phi_r = nc/4$. The ratio between the downstream flux and the return flux gives the escape probability of CRs from the acceleration process

$$\mathcal{P}_{\rm esc} = \frac{\Phi_2}{\Phi_r} = \frac{4v_2}{c} = \frac{v_1}{c} \quad (1.36)$$

which means that the number of original particles n after a shock crossing will be $1-\mathcal{P}_{\rm esc}$. After k cycles the CR population will be reduced by a factor $(1-\mathcal{P}_{\rm esc})^k$.

The total number of particles crossing the shock from the downstream to the upstream for a surface Σ and a time $\tau_{\rm diff,1}$, namely $nc/4\Sigma\tau_{\rm diff,1}$, must be equal to the number of particles crossing the same surface and within a diffusion length upstream $L_1 = \kappa_1/v_1$:

$$\frac{nc}{4}\Sigma\tau_{\rm diff,1} = n\Sigma\frac{\kappa_1}{v_1} \qquad \Longrightarrow \qquad \tau_{\rm diff,1} = \frac{4\kappa_1}{cv_1} \quad (1.37)$$

A similar estimate is valid downstream so that the total amount of time the particles spend to diffuse in a cycle is simply $\tau_{\rm diff} = \tau_{\rm diff,1} + \tau_{\rm diff,2}$. This helps to estimate the acceleration time as

$$\tau_{\rm acc} \simeq \frac{\tau_{\rm diff}}{\Delta E/E} = \frac{3}{v_1 - v_2}\left[\frac{\kappa_1}{v_1} + \frac{\kappa_2}{v_2}\right] \quad (1.38)$$

which is qualitatively similar to the more general expression calculated by Lagage & Cesarsky (1983). The acceleration time is dominated by diffusion in the region with less scattering (i.e. the larger diffusion coefficient). The first criterion we need to impose is that the acceleration time is equal or smaller than the age of the

remnant $\tau_{\rm SNR} \sim r_s/v_s$ where r_s and v_s are the shock radius and the shock velocity, respectively. Recalling the pitch-angle scattering of CRs on magnetic irregularities, the diffusion coefficient takes the form

$$\kappa = \frac{1}{3}\frac{r_{\rm L}c}{\mathcal{F}(k)} \ . \tag{1.39}$$

Imposing the condition of maximum momentum $p_{\rm max}$, imposing $\tau_{\rm SNR} = \tau_{\rm acc}$ the gyrofactor $\mathcal{F}(k)$ calculated at the maximum energy $p_{\rm max} = 1/k_{\rm min} \sim 1$PeV is

$$\mathcal{F}(k_{\rm min}) \simeq \frac{r_{\rm L}}{r_s}\frac{c}{v_s} \ . \tag{1.40}$$

Since $c/v_s \sim 100$ for reference parameters of SNRs ($v_s \sim 3000$ km s^{-1}, $r(p_{\rm max}) \sim 0.1$ pc from Eq. (1.1) and $r_s = 2$ pc) then $\mathcal{F}(k_{\rm min}) \gg 1$ which means that to achieve such energies the random component of the magnetic field at the resonant scale must be much larger than the background field ($\delta B/B \gg 1$). This demonstrates that a significant magnetic field amplification is needed to reach PeV energies implying a non linear regime at the shock.

1.2.4. Self confinement of Cosmic Rays

The source of Alfvén waves responsible for the scattering of CRs are another important aspect of this treatment. Cascade of large MHD turbulence in the ISM is a natural source responsible for the magnetic fluctuations δB. However there is a separation of scales of several orders of magnitude between the driving scale for MHD turbulence from (SNR) shocks interacting with density inhomogeneities and the gyroresonant scale of GeV CRs. As the scale decreases below the driving scale of the turbulence, the effect of the Galactic magnetic field is expected to dramatically increase the anisotropy of the turbulence (i.e. $k_\perp/k_\parallel \gg 1$).

The interstellar Alfvén wave cascade alone in an anisotropic regime is not the only source of cosmic ray scattering. Detailed kinetic calculations involving the Vlasov equation for CRs show that if the CR distribution is sufficiently anisotropic they will destabilize the Alfvén present in the ISM. If the source of this anisotropy is due to a bulk drift velocity $v_{\rm D} > v_{\rm A}$ then the waves are unstable (Kulsrud, 2005).

A candidate to drive the turbulence is represented by the gyroresonant instability (Kulsrud & Pearce, 1969) which transfers energy from the CRs to the waves. The instability and the particle-wave interaction, as well as the procedure of how waves are damped, form the basis of the *self-confinement picture* of CRs and of how CRs interact in a collisionless way with the thermal background. Another condition required for the self-confinement is that $v_{\rm D}$ is not too large.

To calculate the growth rate of the waves a perturbative approach to the Vlasov equation is applied. In case of low CR density the real part of the dispersion relation is negligible and the analysis of the imaginary part gives the necessary information for the growth (or damping) rate (Zweibel, 2017):

$$\Gamma_{\rm cr} = \frac{\pi^2}{2}\frac{q^2 v_{\rm A}^2}{c^2}\int v(1-\mu^2)\delta\left(\omega - kv\mu \pm \Omega\right)\left[\frac{\partial f}{\partial p} + \left(\frac{kv}{\omega} - \mu\right)\frac{1}{p}\frac{\partial f}{\partial \mu}\right] p^2 {\rm d}p{\rm d}\mu \tag{1.41}$$

The Dirac's δ function encapsulate the resonant conditions for gyroresonances (i.e. $\omega - kv\mu \simeq -kv\mu = \mathcal{N}\Omega$, with $\omega \equiv k_{\parallel} v_{\rm A}$). The formula shows that only CRs above a minimum momentum $p_{\rm min} = m\gamma\Omega/k$ can resonate with the wave. Furthermore only waves with an anisotropy propagating in the same direction as the CRs can grow. For positive waves this translates in imposing $\partial f/\partial\mu > 0$. If the distribution is isotropic then $\mu = p/p_{\parallel} = 1$ and $\Gamma_{\rm cr} \equiv 0$. Assuming a power law distribution for CRs ($f \propto p^{-\alpha}$) the growth rate for linearly polarized waves propagating parallel to the background magnetic field reads (Kulsrud & Cesarsky, 1971):

$$\Gamma_{\rm cr} = \frac{\pi}{4}\frac{\alpha - 1}{\alpha}\Omega_0 \frac{n_{\rm cr}(p > p_{\rm min})}{n_i}\left(\frac{v_{\rm D}}{v_{\rm A}} - 1\right) \ , \tag{1.42}$$

where n_i is the ion number density of the ambient medium and $\Omega_0 = \gamma\Omega$ is the non-relativistic gyrofrequency. For CRs of few GeV, $(\frac{v_{\rm D}}{v_{\rm A}} - 1) \sim 1$ and standard ISM densities the growth time is $\sim$ 300 yrs, long compared to the wave periods ($\sim$yrs) but short in comparison to galactic scales. This suggests that CRs adjust quicky to these local conditions (Zweibel, 2013). From Eq. (1.42) is also evident that for particles drifting with bulk velocity $v_{\rm D} \simeq v_{\rm A}$ there is no wave growth and for $v_{\rm D} < v_{\rm A}$ wave damping applies (Wiener et al., 2013).

In the presence of strong shocks responsible for CR acceleration, the CR flux $\propto n_{\rm cr} v_{\rm D}$ is several orders of magnitude larger corresponding to a fast wave growth. Because $n_{\rm cr}(p > p_{\rm min}) \propto p_{\rm min}^{1-\alpha}$ the growth rate $\Gamma_{\rm cr}$ is expected to decrease with increasing particle energy. This means that CR above a certain energy are not expected to generate enough waves to confine themselves.

Another instability arising from the DSA picture is connected to a strong CR current which results in a non-resonant streaming instability that amplifies the fluctuations on scales smaller than the CR particle gyroradius. Using a perturbative approach in the MHD limit the dispersion relation for this instability reads (Bell, 2004):

$$\omega^2 - k^2 v_{\rm A}^2 = \pm\frac{\xi}{2}\frac{k}{r_g} = \frac{kB_0 j_{\parallel,{\rm cr}}}{\rho c} \tag{1.43}$$

where the different signs refers to growing or decaying modes, $j_{\parallel,{\rm cr}}$ is the CR current density and ξ is a parameter connected to the maximum CR momentum $p_{\rm max}$ and the fraction of CR energy density. These parameters are themselves connected to the net CR current component parallel to the shock direction. The maximum growth rate associated with this instability is given by (Schure et al., 2012):

$$\Gamma_{\rm NR,max} = \frac{1}{2}\sqrt{\frac{4\pi}{\rho}\frac{j_{\parallel,{\rm cr}}}{c}} \tag{1.44}$$

Numerical and analytical works demonstrated how this instability grows much faster than its resonant counterpart (Bell, 2005; Bykov et al., 2012). The combined processes of fast amplification at small scales ($k^{-1} < r_g$) and long wave-length fluctuations would allow an effective confinement and acceleration of high-energy particles.

1.2.5. Wave damping

The energy transfer from CRs to turbulent waves is affected by damping processes that impede the growth of the waves. A typical damping mechanism working for fully ionized gases is *non-linear Landau damping* (NL) occurring when two superimposing CR-generated Alfvèn waves form a beat wave and thermal ions are in Landau resonance with it (Lee & Völk, 1973). The corresponding damping rate for a plasma with ion velocity v_i is (Kulsrud, 2005):

$$\Gamma_{\rm NL} = \sqrt{\frac{\pi}{8}} \simeq 0.3 \frac{\Omega}{\mu} \frac{v_i}{c} \mathcal{E}(k) \tag{1.45}$$

where the resonance condition $k = \Omega/\mu c$ is applied.

Another type of wave damping is represented by the *turbulent damping*. In this context waves are damped by shearing caused by the small scale perpendicular magnetic field structure from the MHD turbulente cascade. The minimum damping rate associated with the turbulent damping is (Zweibel, 2013):

$$\Gamma_{\rm turb} = \frac{k v_{\rm A}}{\sqrt{kL}} \tag{1.46}$$

where L is the driving scale of the turbulence.

When both damping processes are acting CR above 100 GeV appear not to be self-confined by intrinsic turbulence anywhere in the ISM but confined by externally driven turbulence. Since the bulk of the CR energy is below this threshold the overall energy flow contained in CRs should obey the self-confinement picture. However the determination of this threshold depends on the details of the ISM and the nature of the interstellar turbulence.

1.2.6. Non linear diffusive shock acceleration

The previous sections exposed the generalities of the DSA process and its ability to derive some of the fundamental results that explain the CR spectrum. At the same time many non-linear processes concur in this picture limiting the applicability of a first-order test particle theory:

- **CR pressure**. The shocks accelerating CRs are subject to the dynamical reaction of the accelerated particles. To explain the level of CRs observed at Earth the average acceleration efficiency (i.e. the quantity of explosion energy channeled into CRs) must be of the order of $\sim 10\%$ (Gabici & Aharonian, 2016). This non-negligible fraction of accelerated particles exerts an effective pressure $P_{\rm cr}$ on the plasma affecting the shock dynamics and thus the acceleration process, resulting in a higher compression factor felt by the plasma at the shock and creating a precursor (Blasi, 2013).

- **Instabilities at the shock**. In order to reduce the acceleration time of the particles, the magnetic field needs to be substantially amplified at the shock

with a process that is likely driven by the accelerated particles themselves. The diffusion coefficient describing the motion of the particles is therefore determined by the distribution function of the same accelerated particles in a specific region (Bell, 2004). The magnetic field amplification may be also proven by the presence of numerous bright X-ray rims and filaments in young SNRs (Uchiyama et al., 2007; Vink, 2012).

A full treatment of all these effects combined requires semi-analytic approaches or the use of PIC simulations (Caprioli (2012) for a review).

1.2.7. Cosmic Ray injection and PIC simulations

The treatment of the injection of charged particles to the acceleration process is a crucial problem in understanding the CR physics. A method to investigate how efficiently the particles participate in the process for a given set of shock conditions and the growth of instabilities in the acceleration process is the use of particle-in-cell (PIC) simulations of collision-less shocks.

In these simulations, the astrophysical plasma and the interplay between particles and fields is calculated from first principles. The charged particles are moved by the Lorentz force and the currents deposited by the particles on the computational grid are subsequently used to compute the electromagnetic fields via Maxwell equations.

In order to consistently quantify the injection the fraction of particles injected into DSA is regulated by the quasi-periodic reformation of the shock barrier and by gyro-scale phenomena (Caprioli et al., 2018).

The problem of resolving ion and electron scales at the same time is a computationally expensive problem. For this reason hybrid-PIC simulations are generally used: these treat the ions as particles and the electrons as a massless fluid where the physics is not resolved at the grid size.

Hybrid simulations have recently been used to investigate the role of shock obliquity relative to the magnetic field in the acceleration of particles. In particular Caprioli & Spitkovsky (2014b) tested consistently the validity of the efficient acceleration at quasi-parallel shocks in contrast to other scenarios where efficient perpendicular acceleration of CR is thought to be efficient (Jokipii, 1987). In this scenario the particles can cross the shock several times during Larmor gyration while moving along the magnetic field. The particles are accelerated by drifts associated to the electric fields that the particles experience because of the different plasma velocity upstream and downstream. However the particles spend considerably less time in the shock region because they are advected at the plasma speed with the magnetic field line that they are trapped on (Blasi, 2013). This shortcoming can be solved introducing a random walk of the magnetic field lines, however implying pre-existing turbulence (Giacalone, 2005).

1.3. Fluid description of Cosmic Rays

In the self-confinement picture and because of the continuous pitch angle scattering of CRs, a fluid description of the problem is possible. In this picture the pitch angle scattering that CRs experience translates into an effective pressure $P_{\rm cr}$ affecting the thermal gas. Given a CR distribution in momenta expressed by $f(p)$ we define the following quantities as moments of the CR distribution:

$$n_{\rm cr} = 4\pi \int_0^\infty f(p) p^2 {\rm d}p \ , \tag{1.47}$$

$$P_{\rm cr} = \frac{1}{3} 4\pi mc^2 \int_0^\infty f(p) \beta p^3 {\rm d}p \ , \tag{1.48}$$

$$\varepsilon_{\rm cr} = 4\pi \int_0^\infty p^2 E_p(p) f(p) {\rm d}p \ , \tag{1.49}$$

where $n_{\rm cr}$ is the CR number density, $P_{\rm cr}$ is the CR pressure, $\varepsilon_{\rm cr}$ is the CR energy density and $E_p(p)$ is the CR kinetic energy

$$E_p(p) = (\sqrt{1+p^2} - 1) mc^2 \ . \tag{1.50}$$

Pressure and energy density are related via

$$P_{\rm cr} = (\gamma_{\rm cr} - 1) \varepsilon_{\rm cr} \ , \tag{1.51}$$

where $\gamma_{\rm cr} = 4/3$ is the CR adiabatic index. The transport equation Eq. (1.4) can be re-written in terms of the CR energy density (Pfrommer et al., 2017a):

$$\frac{\partial \varepsilon_{\rm cr}}{\partial t} + \boldsymbol{\nabla} \cdot [\varepsilon_{\rm cr} (\boldsymbol{v} + \boldsymbol{v}_{\rm st}) - \mathcal{D} \boldsymbol{b} (\boldsymbol{b} \cdot \boldsymbol{\nabla} \varepsilon_{\rm cr})] = (\boldsymbol{v} + \boldsymbol{v}_{\rm st}) \cdot \boldsymbol{\nabla} P_{\rm cr} + \Gamma_{\rm cr} + \Lambda_{\rm cr} + Q_{\rm cr} \tag{1.52}$$

where $\boldsymbol{b} = \boldsymbol{B}/\sqrt{\boldsymbol{B}^2}$, $Q_{\rm cr}$ is the CR source term (containing both gains and losses $\Lambda_{\rm cr}$) and $\Gamma_{\rm cr}$ is the CR acceleration term. A term represented the streaming velocity $\boldsymbol{v}_{\rm st}$ of CRs is added in the equation. Because only CRs with that stream down their gradient are propagating it results that in the limit $v_{\rm D} \to v_{\rm A}$ the streaming velocity can be written as

$$\boldsymbol{v}_{\rm st} = -{\rm sgn}(\boldsymbol{b} \cdot \boldsymbol{\nabla} P_{\rm cr}) \boldsymbol{v}_{\rm A} \tag{1.53}$$

The average spatial diffusion coefficient κ is defined as:

$$\kappa(x) = \frac{\int_0^\infty {\rm d}p 4\pi p^2 T(p) \kappa(p) \boldsymbol{b} \cdot \boldsymbol{\nabla} f}{\int_0^\infty {\rm d}p 4\pi p^2 T(p) \boldsymbol{b} \cdot \boldsymbol{\nabla} f} \ , \tag{1.54}$$

while

$$Q_{\rm cr} = 4\pi \int_0^\infty Q(x,p) p^2 E_p(p) {\rm d}p \ , \tag{1.55}$$

and

$$\Gamma_{\rm acc} = -4\pi mc^2 \int_0^\infty \beta p^2 \Gamma_{\rm p} \frac{\partial f}{\partial p} {\rm d}p \ . \tag{1.56}$$

Finally, the equilibrium condition for Alfvén waves requires that $\Gamma_{\rm growth} = \Gamma_{\rm damp}$. In this condition it can be demonstrated that the volumetric heating rate associated with the CRs is (Wentzel, 1971; Wiener et al., 2013)

$$\mathcal{H} = -\boldsymbol{v}_{\rm A} \cdot \boldsymbol{\nabla} P_{\rm cr} \tag{1.57}$$

This heat loss indicates that the CRs loose a net amount of energy for a positive gradient and this energy is transferred to the Alfvén waves as required in the self-confining picture.

1.4. Non-thermal emission of Cosmic Rays

As seen in the previous sections, CRs accelerated at supernova shocks suffer of different loss processes that affect their energy budget during their propagation in the Galaxy. The different loss mechanism that cause the emergence of an electromagnetic spectrum from radio to γ-rays. In the following paragraphs losses from the hadronic and leptonic populations of CR particles are introduced. We only consider synchrotron, inverse Compton (IC) and pion-decay related losses, while losses originated from non-thermal bremsstrahlung are not discussed because of the lack of conclusive evidence at SNRs. The processes described hereafter are based on Rybicki & Lightman (1986) and Schlickeiser (2002).

1.4.1. Synchrotron radiation

According to electrodynamics, a relativistic charged particle with momentum $\gamma m \boldsymbol{v}$ in a magnetic field $\boldsymbol{B}$ of strength B that is uniform on scales much larger than the gyroradius of the particle is subject to a Lorentz force (Rybicki & Lightman, 1986)

$$\frac{\mathrm{d}\gamma m \boldsymbol{v}}{\mathrm{d}t} = \gamma m \frac{\mathrm{d}\boldsymbol{v}_\perp}{\mathrm{d}t} = \frac{q}{c} \boldsymbol{v} \times \boldsymbol{B} \ , \tag{1.58}$$

where the last passage is justified by the fact that the Lorentz force does no work and affects only the direction of the motion, so $|v| = \text{const.}$ and $\mathrm{d}\boldsymbol{v}_\parallel/\mathrm{d}t = 0$. This particle gyrates with gyrofrequency of $\Omega = eB/\gamma m v$ and the centripetal acceleration associated to the perpendicular component of the velocity with respect to the magnetic field direction is $\dot{\boldsymbol{v}}_\perp = \gamma \Omega \boldsymbol{v}_\perp$. According to the Larmor formula an accelerated electron emits a power of

$$P_w = \frac{2e^2 \dot{\boldsymbol{v}}'^2}{3c^3} = \frac{2q^4}{3c^3} \gamma^2 \frac{B^2}{m^2 c^2} v_\perp^2 \ , \tag{1.59}$$

where $\dot{\boldsymbol{v}}' = \gamma^2 \dot{\boldsymbol{v}}$ is the acceleration of the particle in its instantaneous rest frame. Introducing the Thompson cross section $\sigma_{\rm T} = 8\pi e^4/(3m^2c^4)$ and the magnetic field energy density ε_B, Eq. (1.59) becomes

$$P_w = \frac{2}{c} \sigma_{\rm T} \gamma^2 \varepsilon_B v_\perp^2 = 2c\sigma_{\rm T} \beta^2 \gamma^2 \varepsilon_B \sin^2 \phi \ , \tag{1.60}$$

where ϕ is the pitch angle between the magnetic field and the momentum of the particle.

The angular distribution of the emitted power is worthy of discussion. Because of the beaming effects the emitted radiation will appear with respect to an external observer to be concentrated. The pitch angle between the line of sight of the observer and the direction of the motion of the emitting particle is proportional to $1/\gamma$. From the arrival times of the radiation from two different points at the observer the width of the pulse is derived with a critical frequency $\nu_{\rm crit}$ corresponding to the cutoff of the continuous spectrum. It reads

$$\nu_{\rm crit}(E) = \frac{3}{4\pi}\gamma^3 \Omega \sin\phi = \frac{3eB}{4\pi m_e c}\left(\frac{E}{m_e c^2}\right)^2 \sin\phi \ , \tag{1.61}$$

where $\gamma = E/(m_e c^2)$ is used to make the dependency of the critical frequency on the energy of the electron explicit. For typical SNR parameters and accounting for magnetic field amplification at the shock, the corresponding critical photon energy for a very high energy electron is:

$$E_{\gamma,\rm crit} = h\nu_{\rm crit} \simeq 0.6 \text{ keV} \left(\frac{B_\perp}{100\ \mu\text{G}}\right)\left(\frac{E_e}{10 \text{ TeV}}\right)^2 \ . \tag{1.62}$$

Because the emitting power spectrum is proportional to the Fourier transform of the square of the electric field $\boldsymbol{\mathcal{E}}(\nu)$, the emitted power of the synchrotron radiation per solid angle as a function of the frequency reads

$$P_w(\nu, E) = \frac{\sqrt{3}e^3 B \sin\alpha}{m_e c^2} F\left(\frac{\nu}{\nu_{\rm crit}}\right) \tag{1.63}$$

with

$$F(x) = x\int_x^\infty K_{5/3}(x')\mathrm{d}x' \ , \tag{1.64}$$

where $K_{5/3}(x')$ is the modified Bessel function of the second kind. Assuming a power-law distribution of the relativistic particles such that $n(E)\mathrm{d}E = CE^{-\alpha_e}\mathrm{d}E$ the emitted power of the synchrotron radiation for an interval of energies $[E_1, E_2]$ is

$$\begin{aligned} P_w(\nu) = \int_{E_1}^{E_2} P(E,\nu)n(E)\mathrm{d}E = \frac{\sqrt{3}e^3 B\sin\alpha}{m_e c^2}\left(\frac{3e}{4\pi m_e^3 c^5}\right)^{\alpha_\nu} C(B\sin\phi)^{\alpha_\nu+1}\nu^{-\alpha_\nu} \\ \times \int_{E_1}^{E_2} \mathrm{d}E E^{\alpha_\nu - 1} F\left(\frac{\nu}{\nu_{\rm crit}(E)}\right) \end{aligned} \tag{1.65}$$

where $\alpha_\nu = (\alpha_e - 1)/2$. If the energy range is sufficiently wide the extreme of integration can be takes as $E_1 = 0$ and $E_2 = \infty$ the previous equation reduces to a simple power law (Rybicki & Lightman, 1986)

$$P_w(\nu) \propto \nu^{-\alpha_\nu} B_\perp^{\alpha_\nu+1} \ , \tag{1.66}$$

where $B_\perp$ is the projection of the magnetic field on the plane of the sky.

1.4.2. Inverse Compton Scattering

The inverse Compton (IC) scattering originates when a photon with an energy less than the energy of an electron is scattered inelastically by a highly energetic electron gaining energy in the process and redirecting its direction of motion along the electron. In astrophysical environments, these electrons can originate from an interstellar radiation field as well as the CMB. A photon of energy $E_1 = h\nu$ in the rest frame of the electron is scattered off and gains an energy $E_1 = h\nu_1$ equal to (Rybicki & Lightman, 1986)

$$E_1 = \frac{E}{1 + E/(m_e c^2)(1 - \cos\theta)} \ , \tag{1.67}$$

where θ is the angle between the incident and the scattered direction. So far the scattering is described by the classical Thomson cross section σ_T

$$\frac{\mathrm{d}\sigma_\mathrm{T}}{\mathrm{d}\Omega_s} = \frac{3\sigma_\mathrm{T}}{16\pi}\left(1 + \cos^2\theta\right) \ . \tag{1.68}$$

As long as the energy of the photon is below the rest energy of the electron the non-relativistic approximation applies. Above this threshold relativistic corrections due to the photon recoil modify the cross section of the process and the Klein-Nishina (KN) formula applies (Klein & Nishina, 1929). In this case electrodynamical calculation give the following cross section per solid angle

$$\frac{\mathrm{d}\sigma_\mathrm{KN}}{\mathrm{d}\Omega_s} = \frac{3\sigma_\mathrm{T}}{16\pi}\left(\frac{E_1}{E}\right)^2\left(\frac{E}{E_1} + \frac{E_1}{E} - \sin^2\theta\right) \tag{1.69}$$

In the non-relativistic limit Eq. (1.69) reduces to Eq. (1.68). Integrating Eq. (1.69) over the solid angle it yields the following expression at high energies $E \gg h\nu$ for the scattering cross section:

$$\sigma_\mathrm{KN} = \frac{3}{8}\sigma_\mathrm{T}\frac{1}{x}\left[\frac{1}{2} + \ln(2x)\right] \ , \tag{1.70}$$

where $x = h\nu/(m_e c^2)$. The formula indicates how the relativistic effects heavily suppress the energy gain of photon on the electrons at very high energies. Considering the electron rest frame with respect to the observer's rest frame, the energy of the incoming photon E' with an incident angle θ and the energy of the outcoming photon E_1' with angle θ_1' are

$$E' = E\gamma(1 - \beta\cos\theta) \ , \qquad \text{and} \qquad E_1' = \frac{E_1}{\gamma(1 + \beta\cos\theta_1')} \ . \tag{1.71}$$

In the Thomson limit $E_1' = E'$ and the scattering happens typically for $\theta = \pi/2$ so that the previous equation yields $E_1 = \gamma^2 E$. Integrating the spectral emissivity over the incident photon energy distribution gives the total emitted power by IC scattering

$$P_{w,\mathrm{IC}} = \frac{4}{3}\sigma_\mathrm{T} c\beta^2\gamma^2 u_\mathrm{ph} \ , \tag{1.72}$$

where $u_{\rm ph}$ is the total photon energy density. Following the derivation of Blumenthal & Gould (1970) the total emitting power is given by

$$\frac{\mathrm{d}N(E,\gamma)}{\mathrm{d}t\mathrm{d}E_1} = \frac{3}{4}\sigma_{\rm T}\frac{c}{\gamma^2 E} f\left(\frac{E_1}{4E\gamma^2}\right) n(E)\mathrm{d}E \tag{1.73}$$

with $n(E)$ the number density of photons and $f(x) = 2x\ln x + x + 1 - 2x^2$. The function $f(x)$ has a minimum for $x = 1$, which corresponds to the maximum energy that can be produced in the scattering process. Equivalently if the electron spectrum has a cutoff $E_{\rm max}$, the IC spectrum will cut off at a corresponding frequency $h\nu_{\rm max} = 4\gamma^2\langle E\rangle$, where $\langle E\rangle$ is the average energy of the incident photon field. In case the photon field is the CMB the photon spectrum $\mathrm{d}n_\gamma(E_\gamma)/\mathrm{d}V$ is a black body at a temperature of $T = 2.34$ K:

$$\frac{\mathrm{d}n_\gamma(E)}{\mathrm{d}V} = \frac{8\pi}{h^3c^3}\frac{E^2}{\exp(E/k_{\rm B}T) - 1}\ . \tag{1.74}$$

The average energy from a CMB photon is then $\langle E\rangle = 7.7\times10^{-4}$eV. If the incident radiation is x times the CMB energy and the cutoff energy of the electrons is 10 TeV, then the cutoff energy for the IC spectrum is

$$E_{\rm IC,max} = 1.2\ \mathrm{TeV}\left(\frac{x}{1}\right)\left(\frac{E_e}{10\ \mathrm{TeV}}\right)^2\ . \tag{1.75}$$

Assuming a power law distribution for the energy of the electrons, namely $n(\gamma) = C\gamma^{-\alpha_e}$, and integrating over all the photon energies from 0 to ∞ the total power emitted by the IC scattering per unit volume is (Rybicki & Lightman, 1986)

$$\begin{aligned} P_{w,\rm IC}(E_1) &= \frac{3\sigma_{\rm T}cC}{8}\frac{2^{\alpha_e+3}(\alpha_e^2+4\alpha_e+11)}{(\alpha_e+3)^2(\alpha_e+1)(\alpha_e+5)}E_1^{-\alpha_\nu}\int_0^\infty E^{\alpha_\nu}n(E)\mathrm{d}E \\ &= \frac{3\pi\sigma_{\rm T}cC}{(hc)^3}\frac{2^{\alpha_e+3}(\alpha_e^2+4\alpha_e+11)}{(\alpha_e+3)^2(\alpha_e+1)(\alpha_e+5)}\Gamma(\alpha_\nu+3)\zeta(\alpha_\nu+3)E_1^{-\alpha_\nu}(kT)^{\alpha_\nu+3}\ , \end{aligned} \tag{1.76}$$

where the last passage is valid for a black body distribution of photons. $\Gamma(x)$ represents the Euler Γ function and $\zeta(x)$ the Riemann ζ function. From the formula, it is evident that below the cutoff the spectrum will follow the same slope of the synchrotron spectrum $\nu^{-\alpha_\nu}$.

1.4.3. Hadronic interactions

Inelastic collisions of CR nuclei with atoms and molecules of the ISM are another important set of reactions. In these proton−proton, α−nuclei − proton, proton − α−nuclei collisions a considerable amount of light mesons are produced. In particular the kinematic production of charged and neutral pions and their subsequent decay in other particles are regarded as the most important source of secondary cosmic electrons, positrons and neutrinos. Of particular interest is the decay of neutral

pions (π^0) with mass equal to 135 MeV/c^2 after a mean lifetime of $\sim 8.4 \times 10^{-17}$ s (Tanabashi, 2018) in two high-energy gamma-rays. The ensemble of these decays is summarized as follows:

$$\begin{aligned} &\pi^{\pm} \rightarrow \mu^{\pm} + \nu_{\mu}/\bar{\nu}_{\mu} \rightarrow e^{\pm} + \nu_e/\bar{\nu}_e + \nu_{\mu} + \bar{\nu}_{\mu} \ , \\ &\pi^0 \rightarrow \gamma\gamma \ . \end{aligned} \tag{1.77}$$

In relativistic kinematics the collision of two massive particles a and b with 4-momenta $p_a^i c = (E_a, \boldsymbol{p}_a c)$ and $p_b^i c = (E_b, \boldsymbol{p}_b c)$ respectively may lead to the creation of new particles

$$a + b \longrightarrow c + d + e + f + \ldots \tag{1.78}$$

To open the production channel of these particles the requirement of a minimum energy in the center-of-momentum of the system (CMS, denoted by the superscript $'$) equal to the rest mass of the outgoing particles needs to be satisfied. This requires that $\boldsymbol{p}_a' + \boldsymbol{p}_b' = \boldsymbol{0}$. For the relativistic invariance of the 4-momentum ($p^i p_i \equiv p'^i p'_i$) the total energy E' in the CMS reads (Schlickeiser, 2002)

$$E'^2 = (E_a' + E_b')^2 = c^2 (p_a^i + p_b^i)(p_{i,a} + p_{i,b}) = m_a^2 c^4 + m_b^2 c^4 + 2E_a E_b - 2p_a p_b c^2 \cos(\theta) \ . \tag{1.79}$$

In a pion production process the collision of two protons is responsible for the creation of a pion according to the process $p + p \rightarrow p + p + \pi$. Following Eq. (1.79)

$$2\gamma' m_{\mathrm{p}} c^2 = 2 m_{\mathrm{p}} c^2 + m_{\pi} c^2 \ , \qquad \gamma' = 1 + \frac{m_{\pi}}{2 m_{\mathrm{p}}} = 1.072 \ . \tag{1.80}$$

Applying a Lorentz transformation such that one of the incoming protons is at rest the threshold energy for the pion production can be calculated and is equal to $\gamma_{\mathrm{thr}} = \gamma'^2 (1 + \beta_{\mathrm{p}}'^2) = 2\gamma'^2 - 1 = 2[1 + m_{\pi}/(2m_{\mathrm{p}})]^2 - 1 = 1.22 \ \mathrm{GeV}/(m_p c^2)$ meaning that the minimum kinetic energy requested for a proton is ~ 280 MeV (Mannheim & Schlickeiser, 1994).

Assuming an isotropic decay of the particle in their rest frame the energy spectrum of the decay products per unit time and unit volume integrated over the whole solid angle is (Mannheim & Schlickeiser, 1994)

$$q_{\gamma}(E_{\gamma}, \boldsymbol{r}) = 2 \int_{E_{\gamma} + \frac{m_{\pi}^2 c^4}{4E_{\gamma}}}^{\infty} \mathrm{d}E_{\pi} \frac{q_{\pi}(E_{\pi}, \boldsymbol{r})}{\sqrt{E_{\pi}^2 - m_{\pi}^2 c^4}} \tag{1.81}$$

where $q_{\pi}(E_{\pi}, \boldsymbol{x})$ denotes the source function of pions.

To obtain the source function of the neutral pions the pion power of a single relativistic proton with energy $E_{\mathrm{p}} = \gamma m_{\mathrm{p}} c^2$ reads

$$P(E_{\mathrm{p}}, E_{\pi}) = c E_{\pi} n_{\mathrm{H}} \cdot \xi_{\pi}(E_{\mathrm{p}}) \sigma_{\mathrm{pp}}^{\pi} \delta[E_{\pi} - \langle E_{\pi} \rangle] \Theta(E_{\mathrm{p}} - E_{\mathrm{thr}}) \tag{1.82}$$

where n_{H} denotes the target hydrogen number density, $\xi_{\pi}(E_{\mathrm{p}})$ is the multiplicity of pions and $E_{\mathrm{thr}} = 1.22$ GeV the threshold energy. $\langle E_{\pi} \rangle$ is the average energy of a single produced pion. If the Dermer's model is adopted the multiplicity of pions remains constant ($\xi_{\pi} = 2$) in contrast to the previously adopted

Fireball model (Pfrommer & Enßlin, 2004) based on Fermi's original idea of pion production (Fermi, 1950). The energy dependence of the mean proton energy is $\langle E_\pi \rangle \simeq K_\mathrm{p} T_\mathrm{p}/\xi \simeq T_\mathrm{p}/4$.

For a differential distribution of CR protons $f_\mathrm{p}(E_\mathrm{p})$ the source function of pions reads

$$q_{\pi^\pm}(E_\pi) = \frac{2}{3} q_\pi(E_\pi) = \frac{2}{3} \int_{-\infty}^{+\infty} \mathrm{d}E_\mathrm{p} f_\mathrm{p}(E_\mathrm{p}) P(E_\mathrm{p}, E_\pi) \ . \tag{1.83}$$

For a generic power-law distribution of CR protons with slope α_p, namely $f_\mathrm{p}(E_\mathrm{p}) = C_p \left(E_\mathrm{p}/\mathrm{GeV}\right)^{-\alpha_\mathrm{p}}$, the resulting pion source function reads:

$$q_{\pi^\pm}(E_\pi) = 2 q_{\pi^0}(E_\pi) = \frac{4}{3} \sigma_\mathrm{pp} c n_\mathrm{N} \xi^{2-\alpha_\gamma} \left(\frac{2E_\pi}{\mathrm{GeV}}\right)^{-\alpha_\mathrm{p}} \tag{1.84}$$

The resulting analytical formula for the total gamma-ray source function is given by (Pfrommer & Enßlin, 2004):

$$q_\gamma \simeq \sigma_\mathrm{pp} c n_\mathrm{N} 2^{2-\alpha_\gamma} C_p \frac{4}{3\alpha_\gamma} \left(\frac{m_\pi}{m_\mathrm{p}}\right)^{-\alpha_\gamma} \left[\left(\frac{2E_\gamma}{m_\pi c^2}\right)^{\delta_\gamma} + \left(\frac{2E_\gamma}{m_\pi c^2}\right)^{-\delta_\gamma}\right] \tag{1.85}$$

where $\delta_\gamma = 0.14\alpha_\gamma^{-1.6} + 0.44$ and $\sigma_\mathrm{pp} = 32$ mbarn$[0.96 + \exp(4.4 - 2.4\alpha_\gamma)]$. If the proton spectrum has a cutoff $E_\mathrm{p,max}$, because $\langle E_\pi \rangle \simeq T_\mathrm{p}/4 \simeq E_\mathrm{p}/4$ and because each neutral pion decay produces two photons the resulting cutoff in the gamma-ray spectrum from pion decay is:

$$E_\mathrm{\gamma,max} = \frac{E_\mathrm{p,max}}{8} = 12.5 \ \mathrm{TeV} \left(\frac{E_\mathrm{p,max}}{100 \ \mathrm{TeV}}\right) \ . \tag{1.86}$$

1.5. Cosmic Ray cooling

A net amount of energy is lost by CRs in the emitting processes described in the previous paragraphs. Electrons scattering in the Coulomb field of CR particles propagating in a plasma cause CRs to lose their energy. This effect combined to momentum transfer via quantised plasma oscillations constitute the Coulomb losses of CRs. Additionally catastrophic energy losses from the production of pions affect the CR energy budget. While the first ones affect the low-momentum part of the energy spectrum the hadronic losses are more effective at high energies.

Following Gould (1972) kinetic energy losses for a non-relativistic proton via Coulomb interaction in the plasma are expressed by

$$-\left(\frac{\mathrm{d}E_\mathrm{p}(p)}{\mathrm{d}t}\right)_\mathrm{Coulomb} = \frac{4\pi e^4 n_\mathrm{e}}{m_\mathrm{e} \beta c} \left[\ln\left(\frac{2m_\mathrm{e} c^2 \beta p}{\hbar \omega_\mathrm{pl}}\right) - \frac{\beta^2}{2}\right] \tag{1.87}$$

where $\omega_\mathrm{pl} = \sqrt{4\pi e^2 n_\mathrm{e}/m_\mathrm{e}}$ is the plasma frequency. The associated timescale to this process is $\tau_\mathrm{Coulomb} = \varepsilon_\mathrm{cr}/\dot{\varepsilon}_\mathrm{cr,Coulomb}$. The energy losses caused by hadronic interactions are (Pfrommer et al., 2017a)

$$-\left(\frac{\mathrm{d}E_\mathrm{p}(p)}{\mathrm{d}t}\right)_\mathrm{hadronic} = n_\mathrm{N} \sigma_\mathrm{pp} K_\mathrm{p} m_\mathrm{p} c^3 (\gamma - 1) \Theta(p - p_\mathrm{thr}) \tag{1.88}$$

where $p_{\rm thr} = 0.78$ GeV$/(m_{\rm p}c^2)$ is the dimensionless momentum associated to the kinematic threshold for the pion production, $\sigma_{\rm pp} \simeq 44$ mbarn is the pion cross section, $K_{\rm p} \simeq 1/2$ is a factor associated to the inelasticity of the hadronic reactions, $n_{\rm N} = n_{\rm e}/(1-X_{\rm He}/2) \simeq 1.14 n_{\rm e}$ is the nucleon target density assuming an primordial element composition of $X_{\rm He} = 0.24$. The associated hadronic loss timescale is $\tau_{\rm hadronic} = \varepsilon_{\rm cr}/\dot{\varepsilon}_{\rm cr,hadronic}$.

In a condition of equilibrium where the energy losses are balanced with a continuous energy injection, the equilibrium loss rates for Coulomb losses reads (Enßlin et al., 2007):

$$\Lambda_{\rm Coulomb} = \int_0^\infty f_{\rm p}^{(1)} \left(\frac{{\rm d}E_{\rm p}}{{\rm d}t}\right)_{\rm Coulomb} {\rm d}p = -2.78 \times 10^{-16} \left(\frac{n}{\rm cm^{-3}}\right) \ {\rm erg\ s^{-1}\ cm^{-3}}\ , \tag{1.89}$$

while for hadronic losses reads:

$$\Lambda_{\rm hadronic} = \int_0^\infty f_{\rm p}^{(1)} \left(\frac{{\rm d}E_{\rm p}}{{\rm d}t}\right)_{\rm hadr} {\rm d}p = -7.44 \times 10^{-16} \left(\frac{n}{\rm cm^{-3}}\right) \ {\rm erg\ s^{-1}\ cm^{-3}}\ , \tag{1.90}$$

where $f^{(1)}$ represents the 1D power law distribution of CRs. The total loss rate for the system is given by $\Lambda_{\rm cr} = \Lambda_{\rm hadronic} + \Lambda_{\rm Coulomb} = -\lambda_{\rm cr} n_e \varepsilon_{\rm cr}$, where $\lambda_{\rm cr} = \lambda_{\rm hadronic} + \lambda_{\rm Coulomb} \simeq 10^{-15} {\rm cm^3\ s^{-1}}$. The CR energy evolves following the solution (Pfrommer et al., 2017a)

$$E_{\rm cr}(t) = E_{\rm cr}(0) e^{-\lambda_{\rm cr} n_e t}\ . \tag{1.91}$$

The associated timescales, assuming an electron number density of $n_{\rm e} = 1\ {\rm cm^{-3}}$, are

$$\begin{aligned} \tau_{\rm Coulomb} &= \frac{1}{n_e \lambda_{\rm Coulomb}} = 1.14 \times 10^8\ {\rm yr} \left(\frac{n_e}{1\ {\rm cm^{-3}}}\right)^{-1}\ , \\ \tau_{\rm hadronic} &= \frac{1}{n_e \lambda_{\rm hadronic}} = 4.26 \times 10^7\ {\rm yr} \left(\frac{n_e}{1\ {\rm cm^{-3}}}\right)^{-1}\ . \end{aligned} \tag{1.92}$$

A portion of the energy lost through these processes is assumed to heat the surrounding gas. A fraction of 1/6 of the dissipated luminosity produced via hadronic interactions goes in secondary electrons/positrons. The most energetic electron lose their energy via synchrotron and IC scattering while the mildly-energetic ones are able to thermalize their energy via other Coulomb collisions. The thermal energy gain by these processes is summarized in the following expression:

$$\Delta E_{\rm th} = E_{\rm cr}(1 - e^{-\lambda_{\rm th} n_{\rm e} t}) \tag{1.93}$$

with $\lambda_{\rm th} = 4 \times 10^{-16}\ {\rm cm^3\ s^{-1}}$. From Eq. (1.92) is evident how these timescales exceed by many orders of magnitude the timescale for efficient acceleration of CRs in SNR, making this effect negligible.

2. Supernova remnants

In this chapter the main characteristics of supernova remnants (SNR) are presented. In Sect. 2.1 a general discussion of the theory of SNR progenitors is presented. In Sect. 2.2 the general properties of SNR are exposed with a particular focus on the mathematical formulation of the self-similar solutions describing its evolution. Finally, in Sect. 2.3 a short description of the MHD code AREPO used in this thesis is presented.

2.1. Supernova explosions

A supernova originates from a powerful stellar explosion. This transient event is the result of the last evolutionary stages of a massive star or the thermonuclear explosion of a white dwarf pushed over the Chandrasekhar limit.

Multiple supernovae events can have a strong influence on local galactic regions, the entire parent Galaxy, and the intergalactic medium (Reynolds, 2017).

The outcome of this explosion, a supernova remnant (SNR) expands in the surrounding circumstellar and interstellar medium depositing a considerable amount of mechanical momentum and energy. The collective effect of supernova events in the Galaxy have a strong influence driving outflows and sourcing one of the major feedback mechanisms in galaxy formation. Furthermore SNe play an essential role in the synthesis of many elements apart from the lightest (H, He and traces of Be, B and Li, produced in the Big Bang).

Supernova events are quite rare and generally occur at a rate of ~ 2 per century per galaxy. Historical records suggest that SN events have been observed for centuries (Alsabti & Murdin, 2017). Historical evidence has been provided by the discovery of actively expanding SNRs related to the SN explosions. Famous examples of SNRs associated to historical SN events are SN1006, SN 1054 (Crab nebula), SN 1181, Tycho's SN 1572 and Kepler's SN 1604.

The first classification of SN explosion, based on spectroscopic observations, was introduced by Minkowski (1941). Of the fourteen events observed nine presented strong similarities and the lack of hydrogen (Type I) while the remaining five had different spectral features and were hydrogen-rich (Type II). Sub-classes of Type I and Type II, nominally (Ia, Ib, Ic, IIa, IIb etc...) are summarized in Fig. 2.1.

The progenitor of the SN determines the energy budget and the peculiarities of the event as well as the local properties of the ISM in which the explosion happens. A chemical analysis helps to define a taxonomy for different type of SN events and associated to each specific physical characteristics. Currently a classification scheme for SNe is present and includes many types and subtypes, some of which

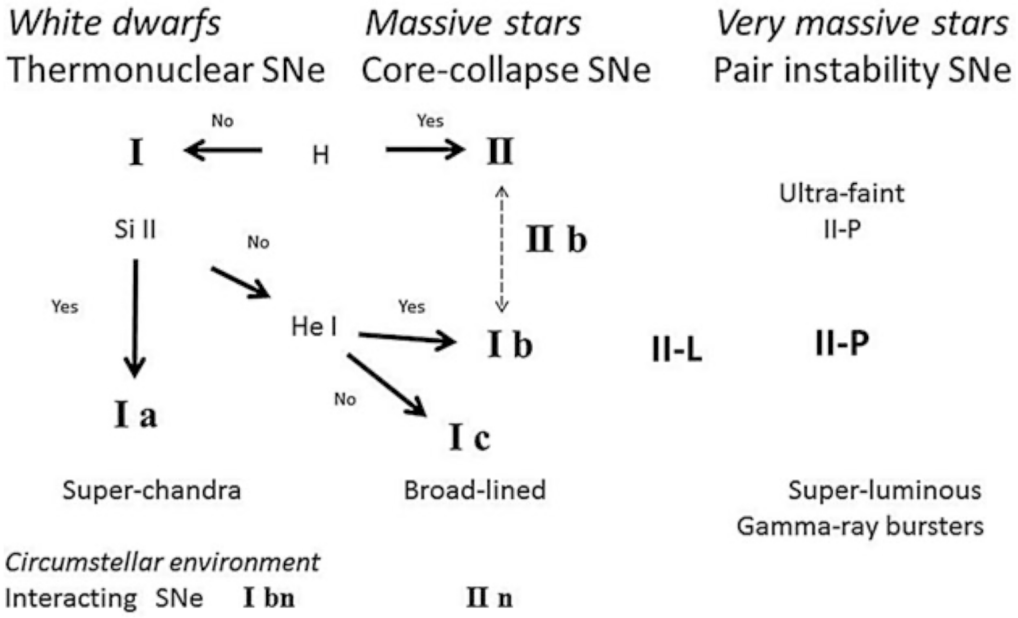

Figure 2.1.: Taxonomy of the various SN classifications and their interrelationships (Alsabti & Murdin, 2017).

not universally recognized.

An SN explosion releases about 10^{51} erg of kinetic energy. In Type Ia SN the energy of the explosion is determined by the energy released in the nuclear burning (Woosley et al., 2007). A single core-collapse SN event deposits in the ISM an energy in form of neutrinos of the order of $\sim 10^{53}$ erg and a kinetic energy of $\sim 10^{51}$ erg, resulting from the release of the gravitational binding energy of the core of the original star (Alsabti & Murdin, 2017). These events happen at the end of the evolved stage of a star under particular conditions and there is no visible sign in the outer layers of the progenitor that the explosion is imminent. Thus the totality of these events is unannounced.

The main characteristics of Type I and Type II SNe are exposed in the following paragraphs.

2.1.1. Thermonuclear supernovae

Type Ia SNe are commonly observed and they account for roughly 60 per cent of the spectroscopically confirmed SNe by the large public ESO survey PESSTO.

The explosion mechanism producing Type Ia Supernova is still matter of controversy. Two main models compete: single- and double- degenerate. In a single-degenerate scenario the mass transfer from a main-sequence sub-giant or giant star to a carbon-oxygen white dwarf triggers a thermonuclear explosion reached when the object approaches the Chandrasekhar mass (1.37 $M_{\odot}$) (Mazzali et al., 2007). The accretion is expected to happen via a stellar wind or via Roche-lobe overflow where the material of the companion star lies outside the Loche lobe and becomes gravitationally unbound from its source.

In a double-degenerate scenario both binary stars are carbon-oxygen white dwarfs. Again the accretion of the second white dwarf onto the primary triggers an explosion when the latter reaches a Chandrasekhar mass. Other hypothesis includes the detonation of both dwarfes or their violent merger, as showed by recent hydrodynamical simulations (Pakmor et al., 2012).

Type Ia SN have a fundamental importance as cosmological distance indicators and represent the class of most efficient probes to verify the expansion history of the Universe.

2.1.2. Core collapse supernovae

Originally labeled as Type II SNe by Minkowski (1941), core collapse SNe are characterized by a very massive progenitor. During the evolution of the most massive stars various heavy elements are produced in the core. In such environments the production of oxygen, neon, iron, magnesium and silicon is not rare. The mass required to produce such elements ranges between 8 and 140 solar masses and the ultimate explosion of the star produces a core-collapse supernova.

The core of these SN collapses in a time of the order of seconds into a compact object (i.e., a neutron star or a black hole if the mass exceeds 40 solar masses). An exception is represented by pair-instability SNe, where collisions between nuclei and gamma rays in the core result in a pair production, which reduces the thermal pressure in the oxygen core, which collapses dramatically, leaving no stellar remnant behind.

A core collapse supernova is powerful enough to release a considerable amount of energy in the galaxy in form of neutrinos, gravitational waves, kinetic energy and radiation stretching for decades in frequencies.

In core collapse SNe most of the collapse energy is released in form of neutrinos which heat and drive the ejection of the star envelope. In case the central compact object is a black hole there is no surface on which the infalling material can bounce thus reducing the energy deposited on the envelope. In the extreme case no outer shock wave is formed and all the material of the star falls in the rapidly degenerating core resulting in the absence of a SNR.

Another possible interesting effect is given by the companion star of the SN. If the companion star survives to the catastrophic explosion, the left compact object can accrete material from the companion star and producing an additional polluting source of radiation (i.e. X-rays).

From a spectroscopic point of view, this type of SNe is dominated by broad and strong lines of hydrogen (in particular Balmer Hα). However the subclasses Ib, Ic, and IIb are hydrogen-poor and probably they are associated with more massive progenitors or even Wolf-Rayet stars (Crowther, 2007).

2.2. Supernova remnants

The outcome of an SN explosion is the formation of a SNR. During their dynamical evolution the SN ejecta drive a blast wave that starts to interact with the circumstellar material. As the blast wave keeps expanding it will merge at a certain point with the interstellar medium. (Reynolds, 2017). Three main stages can be identified in the evolution of a SNR:

- **Ejecta dominated stage (ED)**. Shortly after the explosion, the stellar ejecta are accelerated by a shock wave reaching a velocity of the order of 10000 km s^{-1}. In this stage the material may be quite anistropic and may expand in an anisotropic circumstellar environment due to the previous presence of stellar winds. Almost immediately the blast wave decelerates and heats the CSM to X-ray emitting temperatures. A contact discontinuity separates the shocked CSM/ISM from the ejecta. The rapid expansion cools the ejecta adiabatically to very low temperatures. This causes that a deceleration of the blast waves results in velocity difference greater than the sound speed in the cold unshocked ejecta thus triggering a *reverse* shock moving inwards which reheats the ejecta. The duration of the ED stage lasts for some hundred years.

- **Adiabatic stage**. The energy radiated away from the SN is a small fraction compared to the kinetic energy. The progressive deceleration of the blast wave during the adiabatic expansion stage can be conveniently described by a constant expansion parameter n such that $r_s \propto t^n$. This stage was studied and mathematically modeled for idealized case independently by Sedov (1959) and Taylor (1950) supposing that the pressure of the medium where the blast wave expands is negligible. For this reason, we refer to this evolutionary stage of the remnant as Sedov-Taylor stage.

- **Radiative stage**. As the blast wave further decelerates the radiative cooling of the shocked material becomes relevant. The hot gas in the SNR interior continues to operate in a so called pressure-driven snowplow phase. At this stage the SNR has interacted with a quite inhomogeneous ISM and thus its shape is quite irregular, followed by a momentum-driven snowplow phase. When the shock speed is of the same order of the local ISM sound speed the shock dissipates and the remnant merges with the ISM.

The past decades saw a surge of both space-based and ground-based instruments to capture different aspects of SNR's spectra. For example, the ground-based instruments VERITAS, MAGIC, and H.E.S.S. helped to study SNRs at gamma-ray energies. These imaging atmospheric Čerenkov telescopes are able to detect Čerenkov light emitted by charged particles in an electromagnetic extensive air shower initiated when a primary photon (gamma-ray) of sufficient energy enters Earth's atmosphere.

Many radiative processes happen in SNRs: the passage of a supersonic shock heats the material producing emission in the X-ray waveband while, at higher

energies, scattering of energetic electrons on photon fields produce inverse Compton emission and collision of high energy protons and nuclei with the ISM material produces neutral pions that eventually decay in high-energy photons. Detailed reviews on how a SNR evolves both in homogeneous and inhomogeneous media are reported in Chevalier (1982), Ostriker & McKee (1988) and Truelove & McKee (1999).

2.2.1. Evolution of a non-radiative supernova remnant

A peculiarity of the Euler equations is the lack of dimensional constant which defines a characteristic scale of the problem. A SNR can be characterized from a mathematical point of view by a sequence of self-similar solutions (Cioffi et al., 1988). More specifically the remnant transits through different stages which are described by self-similar solutions under certain limits.

The introduction of a characteristic scale for a SNR is possible considering three main quantities: the initially ejected mass $M_{\rm ej}$, the explosion energy $E_{\rm SN}$ and the ambient density ρ. The blast wave is characterized by a spatial and a time scale. From a simple dimensional analysis the characteristic scales are:

$$r_{\rm ch} \equiv M_{\rm ej}^{1/3}\rho^{-1/3} = 3.07 \text{ pc} \left(\frac{M}{M_\odot}\right)^{1/3} \left(\frac{n}{1 \text{ cm}^{-3}}\right)^{-1/3} \tag{2.1}$$

$$t_{\rm ch} \equiv E_{\rm SN}^{-1/2} M_{\rm ej}^{5/6} \rho^{-1/3} = 423 \text{ yr} \left(\frac{E}{10^{51} \text{ erg}}\right)^{-1/2} \left(\frac{M}{M_\odot}\right)^{5/6} \left(\frac{n}{1 \text{ cm}^{-3}}\right)^{-1/3} , \tag{2.2}$$

where $n = \rho/\mu_{\rm w} m_{\rm p}$ is the number density assuming a molecular weight of $\mu_{\rm w} = 1.4$. The ratio of these two scales yields the characteristic scale for the velocity,

$$V_{\rm ch} \equiv \frac{R_{\rm ch}}{t_{\rm ch}} \equiv E_{\rm SN}^{1/2} M_{\rm ej}^{-1/2} = 7090 \text{ km s}^{-1} \left(\frac{E}{10^{51} \text{ erg}}\right)^{1/2} \left(\frac{M}{M_\odot}\right)^{-1/2} . \tag{2.3}$$

All the quantities involved in a SNR can be normalized to these scales and indicated as $r^* = r_{\rm s}/r_{\rm ch}$, $t^* = t/t_{\rm ch}$, $v^* = v_{\rm s}/v_{\rm ch}$. The set up of the initial conditions generally requires an assumption on the distribution of the ejecta. A common assumption is to impose that the ejecta are distributed according to a power law in distance, namely $\rho_{\rm ej} \propto r^{-n}$. The simplest case is represented by $n = 0$ and solving the Euler problem yields the corresponding numerical solutions are (Truelove & McKee, 1999)

$$r^* \simeq 2t^*[1 + 1.72(t^*)^{3/2}]^{-2/3} , \qquad v^* \simeq 2[1 + 1.72(t^*)^{3/2}]^{-5/3} . \tag{2.4}$$

A coarse approximation is to consider the ejecta-dominated stage as a free expansion phase with $v_{\rm s} = \text{const.} = v_{\rm ej}$ and $r_{\rm s} = v_{\rm s} t$. The velocity of the ejecta is simply given by the formula

$$v_{\rm ej} = \sqrt{\frac{2E_{\rm SN}}{M_{\rm ej}}} = 10000 \text{ km s}^{-1} \left(\frac{E}{10^{51} \text{ erg}}\right)^{1/2} \left(\frac{M}{M_\odot}\right)^{-1/2} \simeq 0.7 v_{\rm ch} . \tag{2.5}$$

At this stage the blast wave is characterized by a very high Mach number. For a ISM sound speed of

$$c_s = \sqrt{\frac{\gamma k_{\rm B} T}{\mu_w m_{\rm p}}} \simeq 10 {\rm km\ s^{-1}} \left(\frac{T}{10^4\ {\rm K}}\right)^{1/2} , \tag{2.6}$$

the corresponding Mach number in the ED stage is

$$\mathcal{M}_s = \frac{v_{\rm ej}}{c_s} \simeq 1000 \left(\frac{E}{10^{51}\ {\rm erg}}\right)^{1/2} \left(\frac{M}{M_\odot}\right)^{-1/2} \left(\frac{T}{10^4\ {\rm K}}\right)^{-1/2} . \tag{2.7}$$

For a cold ISM this number is even higher suggesting that the shocks produced by a supernova explosion can be treated as *strong* for the majority of the evolutionary history of the object.

The transition from an ejecta dominated phase to an adiabatic expansion (Sedov-Taylor stage) happens when the swept up mass by the blast wave equals the initial ejected mass. Equating these quantities enables to approximately calculate the transition time between these two phases:

$$\frac{4}{3}\pi r^3(t)\rho = \frac{4}{3}\pi (v_{\rm s} t_{\rm st})^3 \rho = M_{\rm ej} , \tag{2.8}$$

$$t_{\rm ST} = 0.44 t_{\rm ch} = 186\ {\rm yr} \left(\frac{E}{10^{51}\ {\rm erg}}\right)^{-1/2} \left(\frac{M}{M_\odot}\right)^{5/6} \left(\frac{n}{1\ {\rm cm^{-3}}}\right)^{-1/3} \tag{2.9}$$

A more precise calculation gives $t_{\rm ST} = 0.495 t_{\rm ch}$. The free expansion radius corresponding to this free expansion time is $r_{\rm ST} = 0.726 r_{\rm ch}$ (~ 2.2 pc) for standard parameters.

These values are generally taken as order of magnitude estimates. For core collapse SNe the material ejected during the pre-supernova stage may dominate the density in the initial phases. The presence of winds, such as in the case of Wolf-Rayet SNe, blows a cavity characterized by a hot dilute gas meaning that the initial stage may last longer because very little resistance is encountered by the powerful shock wave. At the same time this hot phase implies that the shock's Mach number is sensibly lower (Eq (2.7)).

For core-collapse SNR the inhomongeous initial distribution surrounding the explosion may lead to a modified version of the classical self-similar solution. On the contrary, for Type Ia SNe it is not rare to find an almost spherically symmetric blast wave.

The simplest solution for an adiabatically expanding SNR is obtained by assuming a point-like explosion in a homogeneous medium:

$$r_{\rm s}(t) = \left(\frac{E}{\alpha\rho}\right)^{1/5} t^{2/5} , \qquad r^*(t^*) = \alpha^{-1/5} (t^*)^{2/5} , \tag{2.10}$$

$$v_{\rm s}(t) = \frac{2}{5} \left(\frac{E}{\alpha\rho}\right)^{1/5} t^{-3/5} , \tag{2.11}$$

with $\alpha \simeq 0.5$ a dimensionless constant. To describe the full range of non-radiative remnant evolution, the velocity expressed by Eq. (2.11) can be rewritten as:

$$r_{\rm s}^{3/2} {\rm d}r_{\rm s} = \frac{2}{5} \left(\frac{E}{\alpha \rho} \right)^{1/2} {\rm d}t \ . \tag{2.12}$$

Integrating the previous equation a modified solution, valid for $t > t_{\rm ST}$, is obtained in the form of an offset power-law (Truelove & McKee, 1999) and reads

$$r_{\rm s} = \left[r_{\rm ST}^{5/2} + \left(\frac{E}{\alpha \rho} \right)^{1/2} (t - t_{\rm st}) \right]^{2/5} , \qquad r^*(t^*) \simeq (1.42 t^* - 0.254)^{2/5} \ . \tag{2.13}$$

The Sedov-Taylor regime ends when the age of the remnant is comparable to the characteristic cooling time for the ISM gas (which depends on its composition). The pressure of the hot gas behind the shock drives the further expansion of the remnant. The first portion of the shock material cools at a specific critical cooling time when a thin shell forms. The resulting radiative remnant consists of a thin, dense shell of cooled material and a radiative shock. The cooling time can be estimates as Blondin et al. (1998)

$$t_{\rm cool} \simeq \frac{0.69 k_{\rm B} T}{n \Lambda} \ , \tag{2.14}$$

where $\Lambda(T) \simeq 10^{-16} T^{-1}$ erg cm^3 s^{-1} is the temperature-dependent volume cooling function and $T \equiv T_2$ the post-shock temperature. From the Rankine-Hugoniot jump conditions for a strong shock and a thermal gas $\gamma = 5/3$ the downstream temperature reads

$$T_2 = \frac{5}{16} \mathcal{M}_1^2 T_1 = \frac{3}{16} \frac{\mu_w m_{\rm p}}{k_{\rm B}} v_{\rm sh}^2 = 3 \times 10^7 {\rm K} \left(\frac{v_{\rm sh}}{10^3 \ {\rm km \ s^{-1}}} \right)^2 \ . \tag{2.15}$$

Using this relation and setting $t_{\rm age} = t_{\rm cool}$ for the velocity in the Sedov-Taylor regime, the critical time is

$$t_{\rm crit} \simeq 2.9 \times 10^4 \ {\rm yr} \left(\frac{E_{\rm SN}}{10^{51} \ {\rm erg}} \right)^{4/17} \left(\frac{n}{1 \ {\rm cm^{-3}}} \right)^{-9/17} \ . \tag{2.16}$$

For standard parameters of an SNR ($n \sim 1$ cm^{-3}, $E_{\rm SN} = 10^{51}$ erg) the corresponding radius is $r_{\rm s} = 19$ pc, the swept-up mass is $M_{\rm swept} = 10^3 \ M_\odot$, the blastwave velocity is $v_{\rm sh} \simeq 200$ km s^{-1} and the critical temperature is $T_2 = 10^6$ K. In this scenario the shock radius of the remnant evolves as $r \propto t^{2/7}$ (McKee & Ostriker, 1977). However a unified solution consisting of an offset power-law suggests that $r \propto t^{3/10}$ and better represents the behavior (Cioffi et al., 1988).

The SNR merges with the ISM when $\mathcal{M}_1 \simeq 1$ (i.e $v_{\rm sh} \simeq c_s$). Adopting $r \propto t^{3/10}$, the merging time is between few 10^5 yr to 10^6 yrs (Cioffi et al., 1988). For a remnant in an ISM of $n \sim 1$ cm^{-3} the merging happens at 200 kyr after the initial explosion as shown by hydrodynamical simulations of Blondin et al. (1998). The momentum conserving phase ($r \propto t^{1/4}$) in most cases is delayed beyond the merger of the remnant with the ISM(Cioffi et al., 1988).

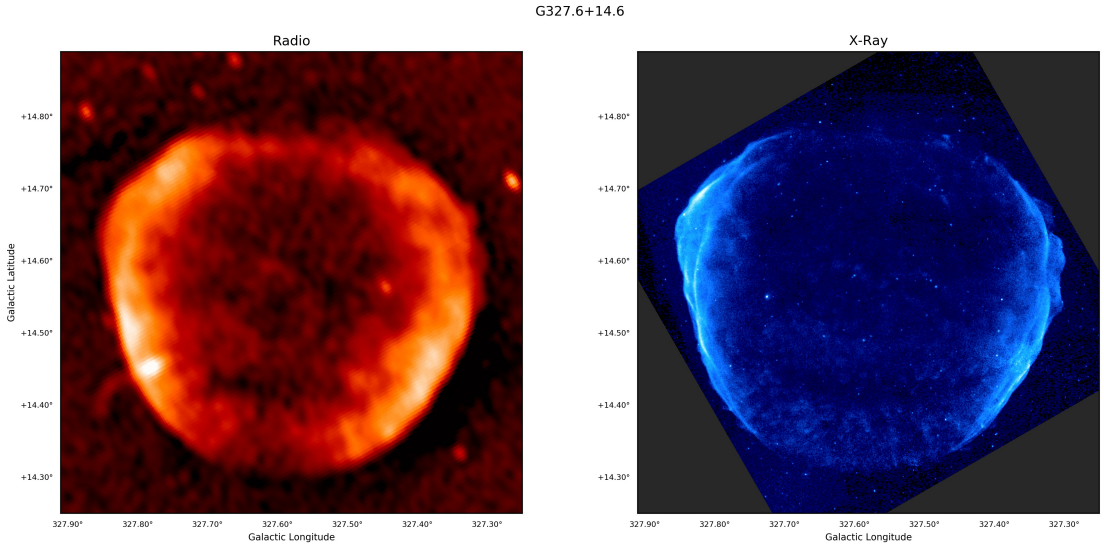

Figure 2.2.: Emission features of the SNR G327.6+14.6 (SN 1006) showing radio emission (left) (Dyer et al., 2009) and bright filamentous X-ray emission (right) (Cassam-Chenaï et al., 2008).

2.2.2. Cosmic Ray population in supernova remnants

There are several proofs of the acceleration of CRs at SNR shocks. The acceleration of electrons at SNR shocks has been confirmed by the observation of synchrotron emission at radio and X-ray energies in several young SNRs. A clear hint is given by the detection of small emitting filaments in the shock region of these objects, suggesting a strong amplification of the magnetic field up to 100μG (a factor 20 of amplification with respect to the galactic magnetic field strength) (Uchiyama et al. (2003); Uchiyama & Aharonian (2008)).

At the present time, there are 294 firmly classified SNRs in our Galaxy, of which 280 are radio sources. The ratio between synchrotron emission and inverse Compton emission can be used to estimate the strength of the magnetic field. Under this assumption Aharonian et al. (2005) calculated the lower limit for the post shock magnetic field for SN1006 to be around 25μG assuming that magnetic fields are volume filling.

The acceleration of protons is harder to detect since they do not radiate as readily as the electrons. Evidence of CR proton acceleration in SNRs emerges more clearly from the interaction of the shock with molecular clouds. Independent surveys confirmed the detection of gamma rays related to the decay of neutral pions in the spectrum of these objects (Giuliani et al. (2011); Abdo et al. (2010b)).

SNR RXJ1713.7-3986 proved for the first time a clear detection of TeV gamma rays from a SNR (Aharonian et al., 2004) followed by the GeV detection in the same remnant by the Fermi-LAT telescope (Abdo et al., 2011).

The TeV gamma-ray emission from these objects proves that there is an effective acceleration of CRs to energies above 10 TeV, however the nature of the emitting particles (protons or electrons) remains controversial. Relatively young SNRs are the dominant population that exhibit TeV energies. Of particular interest are the

shell type SNRs RX J1713 and Vela Jr. whose spectra show remarkable similarities. The spectral shapes and the very low level of thermal X-ray emission emitted by the shock-heated gas that works as a target material for the accelerated nuclei, suggest in principle a leptonic origin (Ellison & Vladimirov, 2008). However core collapse SNRs show a rather complex composition of the ISM. Non uniformity in form of clumps can accommodate the upper limits on the thermal X-ray emission and a hadronic scenario (Zirakashvili & Aharonian, 2010).

Another well-known example is represented by Tycho SNR whose multifrequency spectrum extends from the radio to the high-energy gamma rays. A thin X-ray rim is observed all around the remnant implying efficient amplification of the magnetic field. The morphology of the X-ray emission from the synchrotron radiation of the electrons is consistent with a magnetic field of 300 μG, implying a maximum energy for the protons of around 500 TeV. As argued by Morlino & Caprioli (2012) the spectrum observed at GeV and TeV energies for this remnant and the magnetic field amplification are compatible with a hadronic scenario.

2.3. Numerical modeling of supernova remnants

In this thesis we used the magneto-hydrodynamical code AREPO (Springel, 2010), The code is based on a moving unstructured mesh defined by the Voronoi tessellation of a set of discrete points. The mesh is used to solve the hyperbolic conservation laws of ideal hydrodynamics with a finite-volume approach. The moving points yield a Lagrangian formulation of continuum fluid dynamics that does not suffer of mesh distortion typical of other mesh-based Lagrangian schemes. Another advantage of the code is that it shows second order numerical convergence (Pakmor et al., 2016a) and keeps at the same time a low level of numerical truncation errors.

Ideal MHD in AREPO is computed by solving a system of hyberbolic conservation laws derived from Euler's equations (Pakmor et al., 2011; Pakmor & Springel, 2013). The general form of these conservation laws has the form

$$\frac{\partial \boldsymbol{U}}{\partial t} + \boldsymbol{\nabla} \cdot \boldsymbol{F} = \boldsymbol{0} \tag{2.17}$$

where $\boldsymbol{U}$ and $\boldsymbol{F}(\boldsymbol{U})$ are given by

$$\boldsymbol{U} = \begin{pmatrix} \rho \\ \rho \boldsymbol{v} \\ \rho e \\ \boldsymbol{B} \end{pmatrix} \qquad \boldsymbol{F}(\boldsymbol{U}) = \begin{pmatrix} \rho \boldsymbol{v} \\ \rho \boldsymbol{v}\boldsymbol{v}^{\mathrm{T}} + P\boldsymbol{I} - \boldsymbol{B}\boldsymbol{B}^{\mathrm{T}} \\ \rho e \boldsymbol{v} + \rho \boldsymbol{v} - \boldsymbol{B}(\boldsymbol{v} \cdot \boldsymbol{B}) \\ \boldsymbol{B}\boldsymbol{v}^{\mathrm{T}} - \boldsymbol{v}\boldsymbol{B}^{\mathrm{T}} \end{pmatrix} \tag{2.18}$$

where $P = P_{\mathrm{gas}} + \boldsymbol{B}^2/2$ is the total gas pressure and $e = u + \boldsymbol{B}^2/(2\rho)$ is the total energy per unit mass. The magnetic field is expressed using the Heaviside-Lorentz unit system. The closure relation is given by the equation of state $P = \rho e(\gamma - 1)$.

For clarity no source terms are explicitly shown on the right hand-side. The code accounts for various physics source terms, including radiative cooling, gravity for example. Additionally MHD equations have to satisfy the divergence free constrain

$\boldsymbol{\nabla \cdot B} = \mathbf{0}$. A divergence-free initial magnetic field should maintain this property in its evolution, however the discretization errors preclude this. To avoid the accumulation of errors, a Powell-type scheme is adopted (Powell et al., 1999). The term describing the passive advection of the magnetic fields with the flow is added to the momentum, energy and induction equations prohibiting the growth of the magnetic field divergences.

CRs are added as a second fluid next to the thermal gas and evolved according to the advection-diffusion approximation described in the previous chapter (Pfrommer et al., 2017a). Because CRs with GeV energies dominate the CR pressure, the code AREPO focuses on them because of their maximized dynamical impact. Adiabatic changes $P_{\rm cr}\boldsymbol{\nabla \cdot v}$ are calculated by employing Gauss' divergence theorem in every Voronoi cell and exchanging the corresponding fluxes across the interfaces to the neighboring cells. CR energy sources (i.e. acceleration) are accounted for at resolved shock or via subgrid-scale model of injection at supernova remnants (Schaal & Springel, 2015). The formulation is equivalent to the standard MHD with the addition of a source term $\boldsymbol{S}$:

$$\frac{\partial \boldsymbol{U'}}{\partial t} + \boldsymbol{\nabla \cdot F'} = \boldsymbol{S} \tag{2.19}$$

where $\boldsymbol{U'}$ and $\boldsymbol{F'(U')}$ are given by

$$\begin{aligned}
\boldsymbol{U'} &= \begin{pmatrix} \rho \\ \rho \boldsymbol{v} \\ \varepsilon \\ \varepsilon_{\rm cr} \\ \boldsymbol{B} \end{pmatrix}, \qquad \boldsymbol{F'(U')} = \begin{pmatrix} \rho \boldsymbol{v} \\ \rho \boldsymbol{v}\boldsymbol{v}^{\rm T} + P\boldsymbol{I} - \boldsymbol{B}\boldsymbol{B}^{\rm T} \\ (\varepsilon + p)\boldsymbol{v} - \boldsymbol{B}(\boldsymbol{v}\cdot\boldsymbol{B}) \\ \varepsilon_{\rm cr}\boldsymbol{v} + (\varepsilon_{\rm cr} + P_{\rm cr})\boldsymbol{v}_{\rm st} - \mathcal{D}\boldsymbol{b}(\boldsymbol{b}\cdot\boldsymbol{\nabla}\varepsilon_{\rm cr}) \\ \boldsymbol{B}\boldsymbol{v}^{\rm T} - \boldsymbol{v}\boldsymbol{B}^{\rm T} \end{pmatrix}, \\
\boldsymbol{S} &= \begin{pmatrix} 0 \\ \mathbf{0} \\ P_{\rm cr}\boldsymbol{\nabla\cdot v} - \boldsymbol{v}_{\rm st}\cdot\boldsymbol{\nabla}P_{\rm cr} + \Lambda_{\rm th} + \Gamma_{\rm th} \\ -P_{\rm cr}\boldsymbol{\nabla\cdot v} + \boldsymbol{v}_{\rm st}\cdot\boldsymbol{\nabla}P_{\rm cr} + \Lambda_{\rm th} + \Gamma_{\rm th} \\ \mathbf{0} \end{pmatrix},
\end{aligned} \tag{2.20}$$

where $\Gamma_{\rm cr}$ is the CR source term and $\Lambda_{\rm cr}$ is the CR sink term. The total pressure and the energy density become:

$$P = P_{\rm th} + P_{\rm cr} + \frac{\boldsymbol{B}^2}{2}, \qquad \varepsilon = \varepsilon_{\rm th} + \frac{\rho}{2}\boldsymbol{v}^2 + \frac{\boldsymbol{B}^2}{2}. \tag{2.21}$$

The CR streaming velocity is given by $v_{\rm st} = -v_{\rm A}{\rm sgn}(\boldsymbol{B}\cdot\boldsymbol{\nabla}P_{\rm cr})$ meaning that is always along the magnetic field lines and down the CR gradient. The second closure relation is given by the equation of state for CRs $P_{\rm cr} = \varepsilon_{\rm cr}(\gamma_{\rm cr} - 1)$ with $\gamma_{\rm cr} = 4/3$.

3. The effect of cosmic-ray acceleration on supernova blast wave dynamics

This chapter is an adapted version of the paper *The effect of cosmic-ray acceleration on supernova blast wave dynamics* published on Monthly Notices of Royal Astronomical Society (Pais et al., 2018).

Abstract

Non-relativistic shocks accelerate ions to highly relativistic energies provided that the orientation of the magnetic field is closely aligned with the shock normal (quasi-parallel shock configuration). In contrast, quasi-perpendicular shocks do not efficiently accelerate ions. We model this obliquity-dependent acceleration process in a spherically expanding blast wave setup with the moving-mesh code Arepo for different magnetic field morphologies, ranging from homogeneous to turbulent configurations. A Sedov-Taylor explosion in a homogeneous magnetic field generates an oblate ellipsoidal shock surface due to the slower propagating blast wave in the direction of the magnetic field. This is because of the efficient cosmic ray (CR) production in the quasi-parallel polar cap regions, which softens the equation of state and increases the compressibility of the post-shock gas. We find that the solution remains self-similar because the ellipticity of the propagating blast wave stays constant in time. This enables us to derive an effective ratio of specific heats for a composite of thermal gas and CRs as a function of the maximum acceleration efficiency. We finally discuss the behavior of supernova remnants expanding into a turbulent magnetic field with varying coherence lengths. For a maximum CR acceleration efficiency of about 15 per cent at quasi-parallel shocks (as suggested by kinetic plasma simulations), we find an average efficiency of about 5 per cent, independent of the assumed magnetic coherence length.

3.1. Introduction

Diffusive shock acceleration (DSA) is a universal process that operates at strong, non-relativistic collisionless shocks and enables a small fraction of particles impinging on the shock to gain more energy than the average particle through multiple shock crossings (Axford et al., 1977; Krymskii, 1977; Bell, 1978a; Blandford & Ostriker, 1978). The blast waves of supernova remnants (SNRs) are the most likely

sources of Galactic CRs (Neronov 2017; for extensive reviews, see Reynolds 2008; Marcowith et al. 2016). There are other potential sources that might contribute, including shocks associated with young star forming regions (Yang et al., 2018a), high-energy processes at the Galactic center (HESS Collaboration et al., 2016), or shocks associated with a large-scale Galactic wind that are driven by thermal or CR pressure gradients (Sarkar et al., 2015; Pfrommer et al., 2017b).

CR acceleration modifies the expansion history of a SNR shock due to the additional CR pressure. While the most energetic CRs escape the SNR upstream and propagate into the interstellar medium (ISM), most of the CRs, by energy content and by particle number, are swept downstream and end up in the interior of the SNR (Bell et al., 2013) until they are eventually released to the ISM when the SNR shell breaks into individual pieces as a result of Rayleigh-Taylor instabilities that develop once the shock wave has sufficiently slowed down. A self-similar Sedov-Taylor blast wave solution that accounts for CR pressure was developed by Chevalier (1983) and generalized to include a CR spectrum and the maximum CR energy (Bell, 2015). Those works demonstrate that the CR pressure inevitably dominates the thermal pressure in the SNR interior even if only a small fraction of the shock kinetic energy is converted to CRs. This is because of the smaller ratio of specific heats of CRs ($\gamma_{\rm cr} = 4/3$) in comparison to a thermal fluid ($\gamma_{\rm th} = 5/3$), which cause the thermal pressure to decrease at a faster rate in comparison to CRs upon adiabatic expansion. Simulations of DSA at Sedov-Taylor blast waves confirmed that the increased compressibility of the post-shock plasma due to the produced CRs decreases the shock speed (Castro et al., 2011; Pfrommer et al., 2017a, for one- and three-dimensional simulations, respectively).

However, these approaches missed one important plasma physics aspect of the acceleration process: the orientation of the upstream magnetic field. Hybrid particle-in-cell (PIC) simulations (with kinetic ions and fluid electrons) of non-relativistic, large Mach number shocks demonstrated that DSA of ions operates for quasi-parallel configurations (i.e., when the upstream magnetic field is closely aligned with the shock normal), and becomes ineffective for quasi-perpendicular shocks (Caprioli & Spitkovsky, 2014a). Ions that enter the shock when the discontinuity is the steepest are specularly reflected by the electrostatic shock potential and are injected into DSA (Caprioli et al., 2015). Scattering of protons and electrons is mediated by right-handed circularly polarized Alfvén waves excited by the current of energetic protons via non-resonant hybrid instability (Bell, 2004). After protons gained energy through a few gyrocycles of shock drift acceleration (SDA), they participate in the DSA process. On the contrary, after preheated via SDA, electrons are first accelerated via a hybrid process that involves both SDA and Fermi-like acceleration mediated by Bell waves, before they get injected into DSA (Park et al., 2015).

While quasi-perpendicular shocks are unable to accelerate protons, these configurations can energize thermal electrons at the shock front via SDA. The accelerated electrons are then reflected back upstream where their interaction with the incoming flow generates oblique magnetic waves that are excited via the firehose instability (Guo et al., 2014a,b). The efficiency of electron injection is strongly

modulated with the phase of the shock reformation. Ion reflection off of the shock leads to electrostatic Buneman modes in the shock foot, which provide first-stage electron energisation through the shock-surfing acceleration mechanism (Bohdan et al., 2017).

In this work, we are studying magnetic obliquity-dependent acceleration of protons at a strong, total energy conserving shock that is driven by a point explosion (similar in spirit to the analytic model by Beshley & Petruk, 2012). Hence, our setup models the Sedov-Taylor phase of an expanding SNR and we examine how CR acceleration modifies its propagation depending on the upstream properties of the magnetic field. We emphasize that we do not consider the pressure-driven snowplow phase of SNRs that begins $\sim 2 \times 10^4$ years after the explosion and is characterized by radiative losses of the shocked medium. The snowplough effect adiabatically compresses ambient magnetic fields, which modifies the morphological appearance of the remnant considerably (van Marle et al., 2015).

This chapter is organized as follows. In Section 3.2 we present our methodology, explain how we model magnetic obliquity-dependent CR shock acceleration, and demonstrate the accuracy of our algorithm. In Section 3.3 we present our Sedov-Taylor simulations with CR acceleration: after deriving an analytical model on how the effective ratio of specific heats depends on the CR acceleration efficiency, we show our blast wave simulations with obliquity-dependent CR acceleration at homogeneous and turbulent magnetic field geometries with varying correlation lengths. In Section 3.4 we summarize our main findings and conclude. In Appendix A.1 we assess numerical convergence of our algorithm. In Appendix A.2, we numerically solve the system of equations of a spherically symmetric gas flow to determine a relation between the effective adiabatic index of the gas interior to the blast wave and the self-similarity constant in the Sedov-Taylor solution. In Appendix A.3 we define the ellipsoidal reference frame that we adopt for our oblate explosions and in Appendix A.4 we show our results for obliquity dependent CR acceleration of a Sedov-Taylor explosion into a dipole magnetic field configuration.

3.2. Methodology

Here we present our methodology and explain the numerical algorithms to implement magnetic obliquity dependent CR acceleration. We then validate our implementation with shock tube simulations that exhibit homogeneous magnetic fields. Finally, we lay down our procedure of setting up a turbulent magnetic field that finds application in Sedov-Taylor explosions in Sect. 3.3.

3.2.1. Simulation method

All simulations in this chapter are carried out with the massively parallel code AREPO (Springel, 2010) in which the gas physics is calculated on a moving Voronoi mesh, using an improved second-order hydrodynamic scheme with the least-squares-fit gradient estimates and a Runge-Kutta time integration (Pakmor et al., 2016a).

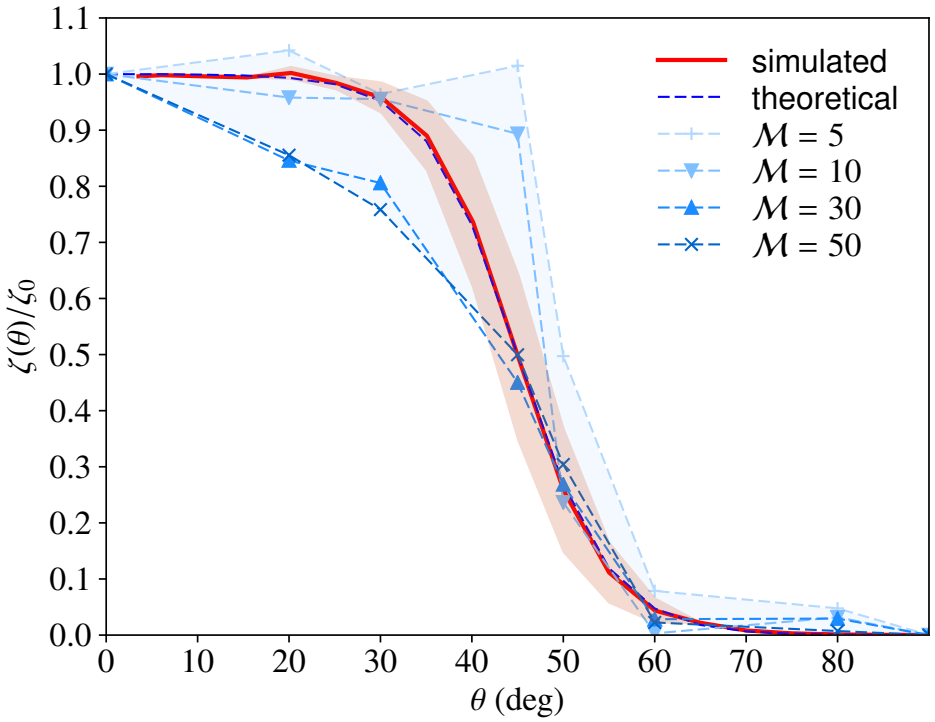

Figure 3.1.: Functional dependence of the CR acceleration efficiency on the magnetic obliquity angle from hybrid PIC simulations of non-relativistic shocks (Caprioli & Spitkovsky, 2014a). The blue points and dashed curves represent the results for different Mach numbers ranging from $\mathcal{M} = 5$ to 50, normalized to the maximum efficiency, respectively. The red curve represents our analytical model (equation 3.7). All hybrid PIC simulations exhibit a sharp drop of the acceleration efficiency at the critical angle for shock acceleration, $\theta_{\rm crit} = 45°$. The coloured red region around our analytical model shows the accuracy of recovering this functional form in our 3D shock tube simulations (see Fig. 3.2).

θ	$\sqrt{\boldsymbol{B}^2}$	$\rho_{\rm l}$	$\rho_{\rm r}$	$P_{\rm l}$	$P_{\rm r}$	$X_{\rm l}^{\rm cr}$	$X_{\rm r}^{\rm cr}$	$r_{\rm c}$	$\mathcal{M}_1$	$\gamma_{\rm eff}$
0°	10^{-6}	1	0.125	51.516	0.1	2	1	4.78	9.56	1.50
45°	10^{-6}	1	0.125	51.516	0.1	2	1	4.28	9.78	1.58
90°	10^{-6}	1	0.125	51.516	0.1	2	1	3.90	10.00	1.66

Table 3.1.: Initial setup for the shock tubes shown in Fig. 3.2. The columns show magnetic obliquity θ, magnetic field strength $\sqrt{\boldsymbol{B}^2}$, initial mass density on the left- and right-hand sides, $\rho_{\rm l}$ and $\rho_{\rm r}$, total pressure on the left- and right-hand sides, $P_{\rm l}$ and $P_{\rm r}$, CR-to-thermal pressure ratio on the left- and right-hand sides, $X_{\rm l}^{\rm cr}$ and $X_{\rm r}^{\rm cr}$. The resulting shock has a compression ratio, $r_{\rm c}$, Mach number $\mathcal{M}_1$, and effective adiabatic index in the post-shock regime $\gamma_{\rm eff}$ (see equation 3.12).

We calculate the fluxes across the moving interface from the reconstructed primitive variables using the HLLD Riemann solver (Miyoshi & Kusano, 2005). We follow the equations of ideal MHD coupled to a second, CR fluid using cell-centred magnetic fields and the Powell et al. (1999) scheme for divergence control (Pakmor et al., 2011; Pakmor & Springel, 2013).

We model the relativistic CR fluid with an adiabatic index $\gamma = 4/3$ and account for diffusive shock acceleration of CRs at resolved shocks in the computational domain, following a novel scheme (Pfrommer et al., 2017a). In our subgrid model for CR acceleration, we assume that diffusive shock acceleration operates efficiently provided there are favorable conditions (e.g., Sect. 3.2.2). This can be realized in the physical scenario, in which the current associated with the forward streaming CRs excites the non-resonant hybrid instability (Bell, 2004). This leads to exponential growth of magnetic fluctuations until the instability saturates at equipartition with the kinetic energy flux. This also implies efficient pitch angle scattering of CRs so that they approach the Bohm limit of diffusion. In such a situation, we can calculate the CR precursor length for the pressure-carrying protons between 1 to 10 GeV,

$$\begin{aligned} L_{\rm prec} &\sim \sqrt{\kappa_{\rm Bohm} t} \\ &\sim 0.001\,{\rm pc} \left(\frac{pc}{10\,{\rm GeV}}\right)^{1/2} \left(\frac{B}{100\,\mu{\rm G}}\right)^{-1/2} \left(\frac{t}{10^3\,{\rm yr}}\right)^{1/2}. \end{aligned} \tag{3.1}$$

The CR precursor length only raises to 0.1 pc for TeV CRs gyrating in μG fields, which is still smaller than the numerical resolution $\Delta x = 0.125$ pc of our simulations and thus unresolved (assuming a typical box size of 25 pc and 200^3 grid cells for SNR simulations). Hence, in the interest of a transparent setup, we only model the dominant advective CR transport and neglect CR diffusion and streaming.

Similarly, we only account for adiabatic CR losses and neglect non-adiabatic CR losses such as Coulomb, hadronic and Alfvén-wave losses. In particular, we neglect the small effect of energy loss from the blast wave due to CRs escaping upstream. This effect softens the Sedov-Taylor solution from $r_s \propto t^{0.4}$ to $r_s \propto t^{0.39}$ (Bell, 2015). That calculation assumed a momentum spectrum of p^{-4}, which provides an upper limit to the energy contribution of escaping high-energy CRs. For observationally inspired softer spectra, the softening of the Sedov-Taylor solution becomes even smaller, thus justifying our neglect.

To localize shocks and their up- and downstream properties during the run time of the simulation, we adopt the method by Schaal & Springel (2015) that is solely based on local cell-based criteria. The method identifies the direction of shock propagation in Voronoi cells that exhibit a converging flow with the negative gradient of the pseudo-temperature that is defined as

$$kT^* = \frac{P}{n} = \frac{\mu m_{\rm p}(P_{\rm th} + P_{\rm cr})}{\rho}, \tag{3.2}$$

where n is the number density, $m_{\rm p}$ is the proton rest mass, and μ is the mean

molecular weight. Hence, the shock normal is given by

$$\hat{\boldsymbol{n}}_{\rm s} = -\frac{\boldsymbol{\nabla} T^*}{|\boldsymbol{\nabla} T^*|}. \tag{3.3}$$

Voronoi cells with shocks are identified with (i) a maximally converging flow along the direction of shock propagation, while (ii) spurious shocks such as tangential discontinuities and contacts are filtered out, and (iii) the method provides a safeguard against labelling numerical noise as physical shocks. In particular, in our study the magnetic field is dynamically irrelevant at the shock, such that the non-MHD jump conditions are valid. Typically, shocks in AREPO are numerically broadened to a width of two to three cells. By extending the stencil of the shock cell into the true pre- and post-shock regime, we determine the Mach number and dissipated energy of the shock. This enables us to inject a pre-determined energy fraction into our CR fluid into those Voronoi cells that exhibit a shock and into the adjacent post-shock cells (see Pfrommer et al., 2017a, for more details).

3.2.2. Obliquity-dependent CR acceleration

We adopt the following relation between the injected CR energy, $\Delta E_{\rm cr}$ and the dissipated energy at the shock, $E_{\rm diss}$,

$$\Delta E_{\rm cr} = \zeta(\mathcal{M}_1, \theta) E_{\rm diss}. \tag{3.4}$$

The injection efficiency $\zeta(\mathcal{M}_1, \theta)$ depends on the shock Mach number, $\mathcal{M}_1 = v_{\rm s}/c_1$ (i.e., the shock speed in units of the pre-shock sound speed, c_1) and the *u*pstream magnetic obliquity, θ, defined as the angle between the normal to the shock front, $\boldsymbol{n}_{\rm s}$, and the direction of the magnetic field, $\hat{\boldsymbol{b}} = \boldsymbol{B}/|\boldsymbol{B}|$:

$$\cos\theta = \hat{\boldsymbol{n}}_{\rm s} \cdot \hat{\boldsymbol{b}}. \tag{3.5}$$

Since the physics does not depend on the actual direction of the unit vectors $\hat{\boldsymbol{n}}_{\rm s}$ and $\hat{\boldsymbol{b}}$ (i.e., whether the vectors point in the same quadrant or not), we re-define the magnetic obliquity via

$$\theta = \arccos(|\cos\theta|) \tag{3.6}$$

In practice, for every shocked cell we collect the magnetic obliquity in the corresponding pre-shock region and communicate it to the shocked cell.

We calibrate $\zeta(\mathcal{M}_1, \theta)$ with hybrid PIC simulations performed by Caprioli & Spitkovsky (2014a). The authors find that DSA of ions is very efficient at quasi-parallel shocks, producing non-thermal ion spectra with the expected universal power-law distribution in momenta equal to p^{-4}. At very oblique shocks, ions can be accelerated via shock drift acceleration, but they only gain a factor of a few in momentum, and their maximum energy does not increase with time. In this chapter, we only consider strong shocks (i.e., $\mathcal{M}_1 \gg 1$) for which the injection efficiency saturates to a maximum value, ζ_0. The saturation happens for shocks with $\mathcal{M} \gtrsim 30$, according to Kang & Ryu (2013).

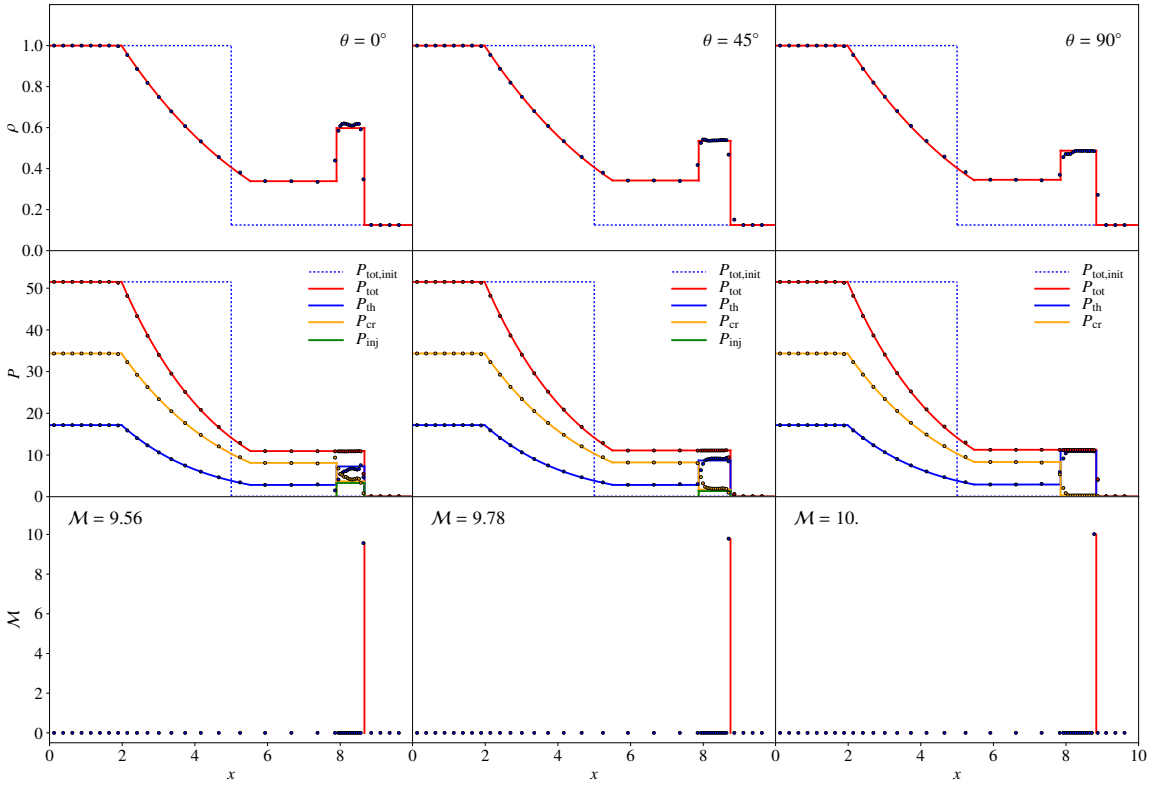

Figure 3.2.: Shock-tube tests for different magnetic field orientations that account for pre-existing and freshly accelerated CRs (solid lines show the analytic solution of Pfrommer et al. (2017a), data points show mean simulation values, each averaged over 250 Voronoi cells). Shown are 3D simulations at time $t = 0.35$. For each simulation we show density ρ, pressure P and Mach number (top to bottom). The left panels show the simulation with a parallel magnetic shock configuration ($\theta = 0$), where the acceleration efficiency ζ is maximized. The middle panels adopt an oblique configuration with $\theta = 45°$. We notice that the post-shock gas is less dense in comparison to the parallel case due to the smaller CR pressure as a result of a lower acceleration efficiency. In the right column, we show a perpendicular magnetic configuration ($\theta = 90°$), for which CR acceleration is completely inefficient. In this case, the shock propagates fastest (i.e., with the largest Mach number $\mathcal{M}$) of all three cases for otherwise identical initial conditions because of the absence of freshly injected CRs in the post-shock gas, which results in the hardest adiabatic index of $\gamma = 5/3$ in the post-shock regime.

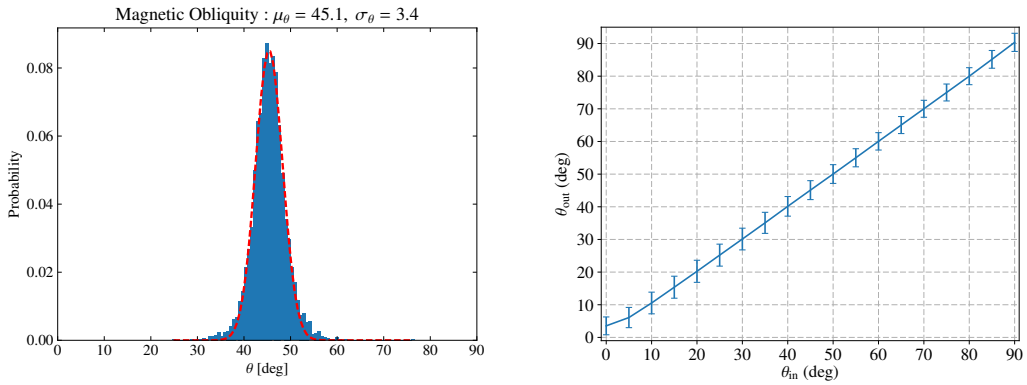

Figure 3.3.: Left: probability distribution function (PDF) of the magnetic obliquity for a shock-tube simulation with initial obliquity of 45°. To increase the statistics, we use obliquity values of all shocked cells for 40 equally-spaced snapshots of that simulation and fit the mean and variance of a Gaussian distribution (red dashed) to the PDF (blue histogram). Right: comparison between the intrinsic ($\theta_{\rm in}$) and recovered magnetic obliquity ($\theta_{\rm out}$) for different shock-tube simulations. We recover the initial obliquity with an accuracy of $\sigma_\theta = 3.4°$ for all simulations except for the case $\theta = 0$ (which is however of little practical relevance due to the very similar shock acceleration efficiencies in this regime).

Hence, we only need to model the scaling of the injection efficiency with magnetic obliquity, which is shown in Fig. 3.1 for different shock strengths. All simulated curves of the injection efficiency (light blue curves in Fig. 3.1) show a similar qualitative behavior: saturation at quasi-parallel shocks, a steep decline at the threshold obliquity of $\theta_{\rm crit} \simeq 45°$, and leveling off at zero for quasi-perpendicular shocks. However, at a given magnetic obliquity, the function $\zeta(\theta, \mathcal{M})$ is not always monotonically rising with Mach number and shows substantial scatter (see Fig. 3 of Caprioli & Spitkovsky, 2014a). Hence, we decided to capture the qualitative behavior of all four curves of the normalized injection efficiency, $\zeta(\theta, \mathcal{M})/\zeta_0$, for different shock strengths with the following functional form:

$$\zeta(\theta) \simeq \frac{\zeta_0}{2}\left[\tanh\left(\frac{\theta_{\rm crit} - \theta}{\delta}\right) + 1\right]. \tag{3.7}$$

We adopted a threshold obliquity of $\theta_{\rm crit} = \pi/4$ and a shape parameter of $\delta = \pi/18$ (red curve in Fig. 3.1). Hybrid PIC simulations by Caprioli & Spitkovsky (2014a) demonstrate that the CR ion acceleration efficiency saturates for large Mach numbers at a value of $\zeta_0 \simeq 0.15$. In our simulations however, we adopt a maximum acceleration efficiency of $\zeta_0 = 0.5$ to amplify the (dynamical) effects of CR acceleration. We checked that reducing the acceleration efficiency to realistic values results in qualitatively similar effects, albeit with a smaller amplitude.

3.2.3. Code validation with shock tubes

To validate our implementation and to test the correctness of our obliquity dependent shock acceleration algorithm, we performed several Riemann shock-tube simulations with different orientations of the magnetic field. A solution to the

shock-tube problem with accelerated CRs is derived analytically in Pfrommer et al. (2017a) for a purely thermal gas and for a composite of thermal gas and pre-existing CRs. In the limit of weak background magnetic fields the solutions proposed in Pfrommer et al. (2017a) are still applicable. We simulate three-dimensional (3D) shock tubes with initially 10^4 cells in a box of dimension $10 \times 1 \times 1$. The initial Voronoi mesh is generated by randomly distributing mesh-generating points in the simulation box and relaxing the mesh via Lloyd's algorithm (1982) to obtain a glass-like configuration. All other initial parameters are laid down in Table 3.1.

In Fig. 3.2, we show three simulations with characteristically different magnetic obliquities, $\theta = 0°, 45°$, and $90°$. Our choice of a larger total pressure on the left-hand side (with the tube initially at rest), implies a rightwards moving shock, which is followed by a contact discontinuity, as well as a leftwards moving rarefaction wave. We show mean simulation values of density, pressure and Mach number, each averaged over 250 Voronoi cells to ensure an identical Poisson error per bin and to demonstrate the change of volume at the shock and over the rarefaction wave as a result of the moving-mesh nature of AREPO.

Changing the orientation of the magnetic field from quasi-parallel ($\theta \gtrsim 0°$) to quasi-perpendicular geometries ($\theta \lesssim 90°$), the acceleration process becomes less and less efficient (as manifested from the fractions of post-shock CR pressure, see second row in Fig. 3.2). In the case of $\theta = 90°$, CR acceleration is absent and the purely thermal case is restored with a compression ratio of $r = 3.9$ (for the adopted initial conditions). In the first column of Fig. 3.2 ($\theta = 0°$), we see an increased compressibility of the post-shock gas over the thermal case due to the abundantly produced CRs, which yields a shock compression ratio of $r = 4.78$. Because of mass conservation, the shock cannot advance as fast in comparison to the purely thermal case and the Mach number is accordingly lower.

Our implementation records the magnetic obliquity in the upstream of the shocked Voronoi cells. In the left panel of Figure 3.3, we present the probability distribution function for θ for the intermediate case $\theta = 45°$. To improve our statistics, we used 40 different snapshots. We find normally distributed obliquity values around the expected value, with a standard deviation of 3.4°. We repeated the experiment for 18 simulations with an input obliquity that differed by 5° from the preceding simulation. The correspondence between injected angles $\theta_{\rm in}$ and simulated angles $\theta_{\rm out}$ of shocked Voronoi cells becomes apparent in the right panel of Figure 3.3, with a 1-sigma accuracy of 3.4°. This accuracy is numerically converged as we show in Appendix A.1. We only observe a small numerical deviation at small obliquities $\theta_{\rm in} < 3°$. However, the resulting acceleration efficiency is not affected due to the constant efficiency at quasi-parallel shocks.

3.2.4. Turbulent magnetic fields

In order to generate turbulent magnetic fields with an average value $\langle \boldsymbol{B} \rangle = \boldsymbol{0}$ but $\langle \sqrt{\boldsymbol{B}^2} \rangle \neq 0$, we adopt a magnetic power spectrum of Kolmogorov type and scale the field strength to an average plasma beta factor of unity. The three components of the magnetic field B_i ($i \in \{1, 2, 3\}$) are treated independently to ensure that the

final distribution of $\boldsymbol{B}(\boldsymbol{x})$ has a random phase. To proceed, we assume Gaussian-distributed field components that follow a one-dimensional power spectrum $P_i(k)$, defined as $P_i(k) \propto k^2|\tilde{B}_i(k)|^2$, of the form

$$|\tilde{B}_i(k)|^2 = \begin{cases} A, & k < k_{\rm inj}, \\ A\left(\dfrac{k}{k_{\rm inj}}\right)^{-11/3}, & k_{\rm inj} \leq k, \end{cases} \tag{3.8}$$

where A is normalization constant, $k = |\boldsymbol{k}|$, and $k_{\rm inj}$ is the injection scale of the field. Modes on larger scales ($k < k_{\rm inj}$) follow a white noise distribution and modes with $k > k_{\rm inj}$ obey a Kolmogorov power spectrum. For each magnetic field component, we set up a complex field such that

$$[\Re(\tilde{B}_i(\boldsymbol{k})), \Im(\tilde{B}_i(\boldsymbol{k}))] = [G_1(X_1, X_2)\sigma_k, G_2(X_1, X_2)\sigma_k], \tag{3.9}$$

where G_i ($i \in \{1, 2\}$) is a distribution of uniform random deviates X_1 and X_2 that returns Gaussian-distributed values. We set the corresponding standard deviation σ_k to $\tilde{B}_i$ for every value of k. We normalize the spectrum to the desired variance of the magnetic field components in real space, σ_B using Parseval's theorem,

$$\sigma_B^2 = \frac{1}{N^2}\sum_k^N |\tilde{B}_i(k)|^2. \tag{3.10}$$

We then subtract the radial field component in k space to fulfill the constraint $\mathrm{div}\boldsymbol{B} = 0$, via

$$\tilde{\boldsymbol{B}}_k \rightarrow \tilde{\boldsymbol{B}}_k - \hat{\boldsymbol{k}}(\hat{\boldsymbol{k}} \cdot \tilde{\boldsymbol{B}}_k). \tag{3.11}$$

Applying an inverse fast Fourier transform to $\tilde{\boldsymbol{B}}_k$ and re-scaling the magnetic field to the desired average magnetic-to-thermal pressure ratio yields a turbulent magnetic field distribution. To ensure pressure equilibrium in the initial conditions, we adopt temperature fluctuations of the form $nk_{\rm B}\delta T = -\delta\boldsymbol{B}^2/(8\pi)$. This setup does not balance the magnetic tension force. The resulting turbulent motions have a small amplitude in comparison to the velocity of the expanding blast wave so that to good approximation, the ambient gas can be considered frozen and does not contribute to the dynamics.

3.3. Sedov-Taylor explosions

In order to understand the non-thermal properties of supernova remnants, we model the explosion as an expanding Sedov-Taylor blast wave in the magnetised interstellar medium. After deriving an analytical solution for the Sedov-Taylor problem in the presence of CR acceleration with an arbitrary shock acceleration efficiency, we study magnetic obliquity dependent CR acceleration in homogeneous and turbulent fields with varying coherence scales and formulate an analytic theory that enables us to obtain the average CR efficiency.

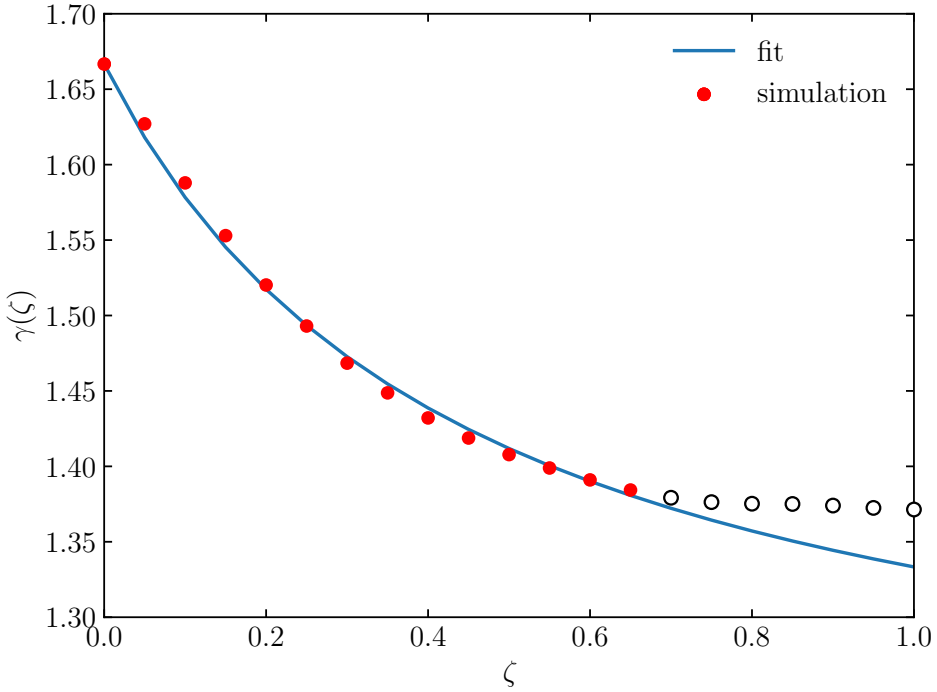

Figure 3.4.: Effective ratio of specific heats γ as a function of CR acceleration efficiency ζ for the Sedov-Taylor blast wave (ignoring the obliquity dependence of CR acceleration). The simulations (dots) and analytical fit (solid, equation 3.15) interconnect the thermal gas case without CR acceleration ($\zeta = 0$) and the opposite extreme of a (hypothetical) 100% efficient acceleration process, which yields a fully relativistic gas in the post-shock region ($\gamma = 4/3$). The simulations do not reproduce the limit $\gamma \to 4/3$ for $\zeta \to 1$ due to residual thermalization.

Parameter	**Value**	**Approximation**
a	1.185	32/27
$b = 20/3 - 9a + 3a^2$	0.214	52/243
$c = 4 - 3a$	0.445	4/9

Table 3.2.: Best-fit parameters of the effective ratio of specific heats as a function of CR acceleration efficiency, $\gamma(\zeta)$, of equation (3.15) for the Sedov-Taylor blast-wave problem. The fit and the simulated points are shown in Fig. 3.4

3.3.1. Analytical solution with CR acceleration

First, we derive analytical exact solutions of the Sedov-Taylor blast-wave problem with CR acceleration without an obliquity dependent efficiency. If a substantial fraction of the dissipated energy is converted into CRs, this alters the effective adiabatic index $\gamma_{\rm eff}$ that is defined as the logarithmic derivative of the total pressure with respect to density at constant entropy s:

$$\gamma_{\rm eff} \equiv \left.\frac{{\rm d}\ln(P_{\rm cr}+P_{\rm th})}{{\rm d}\ln\rho}\right|_s = \frac{\gamma_{\rm cr}P_{\rm cr}+\gamma_{\rm th}P_{\rm th}}{P_{\rm cr}+P_{\rm th}}, \tag{3.12}$$

Subsequently the radius of the explosion is modified as it depends on the compressibility of the post-shock gas in the interior of the blast wave.

In the case of a single polytropic fluid, the shock radius of the blast wave evolves self similarly according to

$$r_{\rm s}(t) = \left(\frac{E_1}{\alpha\rho_1}\right)^{1/5} t^{2/5}, \tag{3.13}$$

where t is the time since explosion and α is a self-similarity parameter that depends on the effective adiabatic index, which itself is a function of CR shock acceleration efficiency ζ. To determine this relation, we run a set of simulations, varying $\zeta \in [0,1]$ in steps of 0.05. In each simulation, we determine the average shock radii at different times and obtain $\alpha(\zeta)$ via equation (3.13).

In Appendix A.2, we numerically solve the self-similar, spherically symmetric conservation equations of mass, momentum and energy to determine the behavior of $\alpha(\gamma)$. We find an analytical fit to the solution of the form

$$\alpha(\gamma) \approx \frac{16}{75}\left[\frac{\pi(3\gamma-1)}{(\gamma-1)(\gamma+1)^2} - \frac{3}{8}\right], \tag{3.14}$$

which has an accuracy of approximately 0.8%. Combining $\alpha(\zeta)$ (obtained with our simulations with CR acceleration and via equation 3.13) and $\alpha(\gamma)$ (equation 3.14), we arrive at an expression of the effective adiabatic index as a function shock acceleration efficiency, $\gamma(\zeta)$, as shown in Fig. 3.4. In particular, an efficiency of $\zeta = 0.5$ corresponds to an effective ratio of specific heats of $\gamma \simeq 1.408$. As seen in Fig. 3.4, the simulations do not reproduce the limit $\gamma \to 4/3$ for $\zeta \to 1$ due to residual thermalization. Note that this case is purely academic and likely not realised in Nature. Hence, we fit our simulation values for $\zeta \leq 0.65$ with an equation of the form

$$\gamma(\zeta) = a + \frac{b}{c+\zeta}, \tag{3.15}$$

subject to the boundary condition of $\gamma = 5/3$ for $\zeta = 0$ and $4/3$ for $\zeta = 1$. This allows to express the parameters b and c solely as a function of a. The corresponding parameters satisfying these requirements are shown in Table 3.2. Adopting the rational approximation of these fitting parameters (Table 3.2) we obtain

$$\gamma(\zeta) = \frac{4}{3}\left(\frac{8\zeta+5}{9\zeta+4}\right). \tag{3.16}$$

Combining this result with equation (3.14), we get a comprehensive formula for the self-similarity parameter in equation (3.13) as a function of the acceleration efficiency ζ:

$$\alpha(\zeta) = \frac{2}{25}\left[\frac{72\pi(9\zeta+4)^2(23\zeta+16)}{(5\zeta+8)(59\zeta+32)^2} - 1\right]. \tag{3.17}$$

3.3.2. CR acceleration in a homogeneous field

Our initial Voronoi mesh is generated by randomly distributing mesh-generating points in the unit box and relaxing the mesh via Lloyd's algorithm (1982). The self-similarity of the problem, which is not broken by CR acceleration (Pfrommer et al., 2017a), allows us to use scale free units. We use a box of 200^3 cells to ensure convergence also at early times. Throughout the simulation box, we adopt a uniform density of $\rho_1 = 1$, a negligible pressure of $P_1 = 10^{-4}$, a zero initial velocity, and a thermal adiabatic index of $\gamma = 5/3$. At time $t = 0$, we inject thermal energy of $E_1 = 1$ into the central mesh cell. We follow ideal MHD without self-gravity and adopt a maximum acceleration efficiency of $\zeta_0 = 0.5$ to amplify the (dynamical) effects of CR acceleration.

First, we adopt a homogeneous magnetic field in the box that is oriented along the x axis and a plasma beta of $\beta = 1$. In Fig. 3.5 we show maps of different quantities in the equatorial plane at $t = 0.1$, namely the mass density ρ (with the shock normal as measured in situ in the simulations and shown in white), the specific CR energy $u_{\rm cr}$, the magnetic field strength $\sqrt{\boldsymbol{B}^2}$ (with the magnetic orientations at the shock colour coded by upstream magnetic obliquity), and the CR-to-thermal pressure ratio $X_{\rm cr} = P_{\rm cr}/P_{\rm th}$.

The unit vectors of the shock normal in the top left panel of Fig. 3.5 show a deviation from spherical symmetry with a smaller shock radius and an enhanced density in the direction parallel and anti-parallel to the magnetic field. This is the immediate consequence of obliquity-dependent shock acceleration with copious CR production at quasi-parallel shocks, which is accompanied by an increased compressibility due to the softer equation of state of the composite fluid of CRs and thermal gas. This is manifested in the quadrupolar morphology of $u_{\rm cr}$ with the axis of symmetry aligned with the magnetic field orientation (top right of Fig. 3.5). The morphology of $u_{\rm cr}$ is echoed by $X_{\rm cr}$ (bottom right of Fig. 3.5). Adiabatic expansion of a composite of CRs and thermal gas eventually yields a dominating CR pressure in the interior of the explosion for quasi-parallel shock geometries, at $|\theta| \lesssim \pi/4$.

An oblique shock only amplifies the perpendicular field component and leaves the parallel component invariant. This re-orients the oblique magnetic field towards the shock surface and increases the field strength at quasi-perpendicular shocks (bottom left of Fig. 3.5). Our strongly magnetised background plasma with $\beta = 1$ becomes very weakly magnetised at the shock since the adiabatic increase of magnetic pressure falls orders of magnitudes short in comparison to the shock-dissipated thermal pressure at our strong Sedov-Taylor shock. Hence, the magnetic

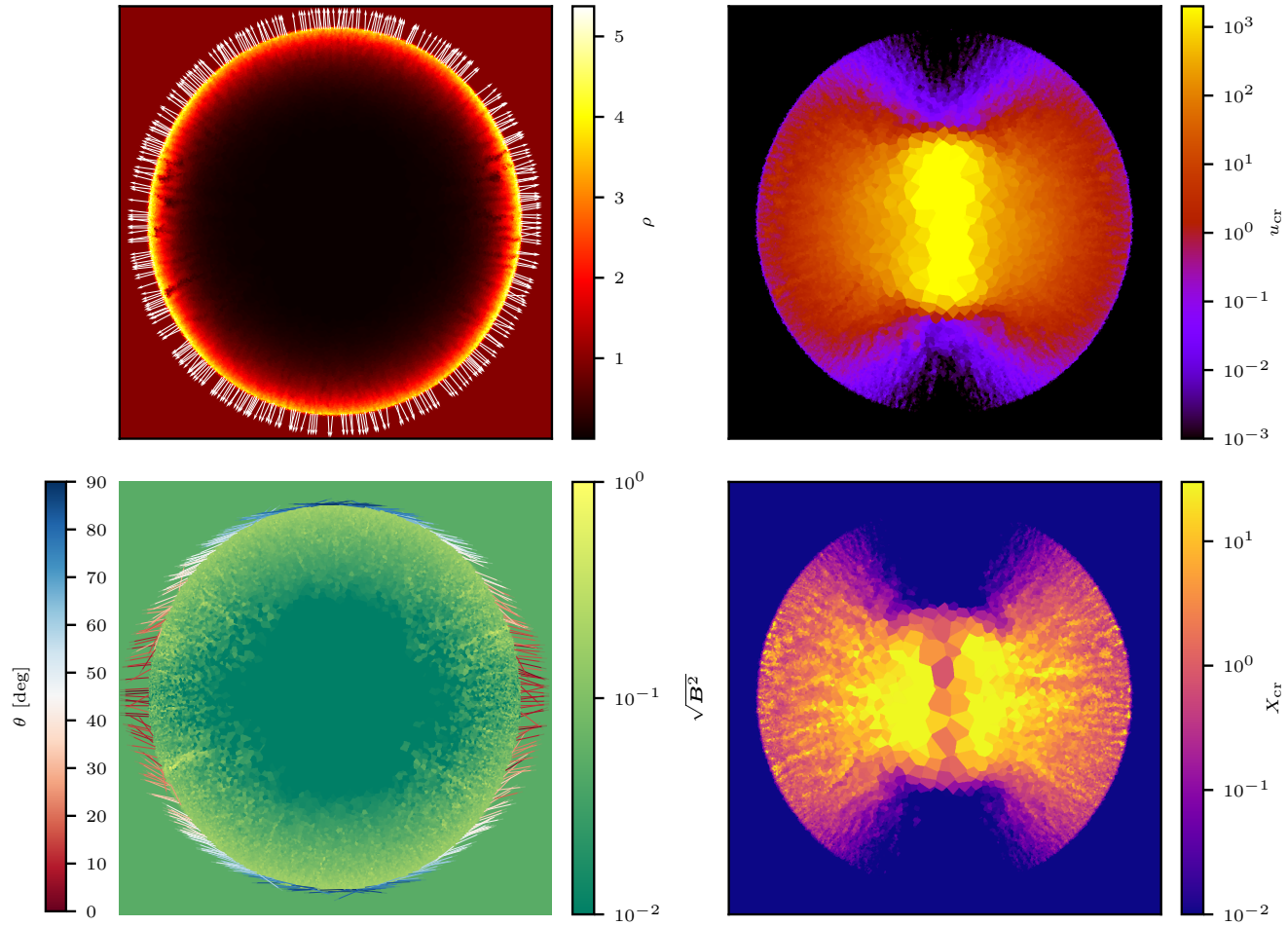

Figure 3.5.: Sedov-Taylor blast wave with obliquity dependent CR acceleration expanding into a homogeneous magnetic field at $t = 0.1$. Initially, the field is aligned with the horizontal direction. We show a 2D cross section of the density ρ (top left) overplotted with normal vectors of the shock (as determined by our shock-finding algorithm); the specific CR energy $u_{\rm cr}$ (top right); the magnetic field strength $\sqrt{\boldsymbol{B}^2}$ (bottom left) overplotted with the outwards directed orientations of the magnetic field at the shocked cells (colour coded by magnetic obliquity θ) and the CR-to-thermal pressure ratio $X_{\rm cr}$ (bottom right). We can see that the specific CR energy exhibits a quadrupolar anisotropy, with the maximum in the direction of the magnetic field (quasi-parallel shock configuration). The increased density in this quasi-parallel direction (due to the higher compressibility of the CR-enriched post-shock plasma) implies a slower shock expansion velocity and hence a slightly oblate shock surface with the two long axis aligned perpendicular to the ambient field direction. Note that the shock compression only amplifies the perpendicular magnetic field component, which re-aligns field vectors for oblique shocks.

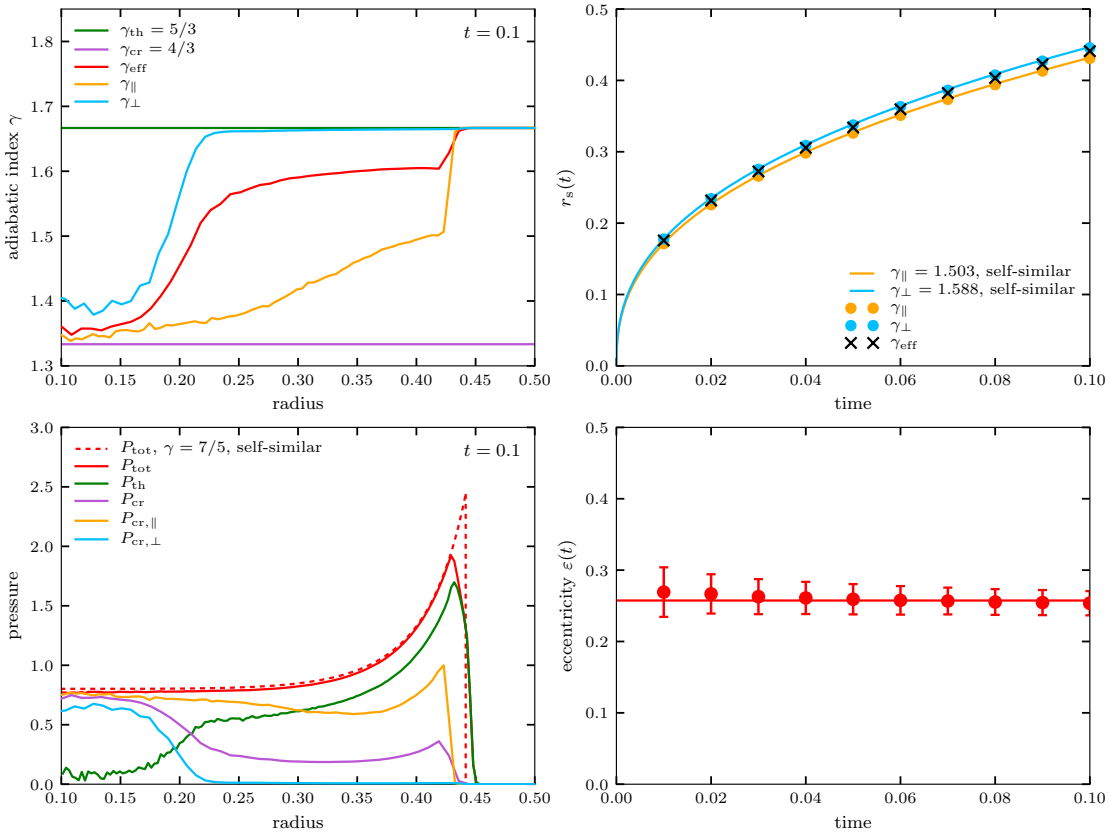

Figure 3.6.: Radial profiles of characteristic quantities of the Sedov-Taylor explosion with obliquity dependent CR acceleration. The top left panel shows the radial profile of the effective adiabatic index. The adiabatic index in the direction perpendicular to the magnetic field (light blue) raises quickly to values comparable with the thermal adiabatic index 5/3 (green) whereas the adiabatic index in the direction parallel to $\boldsymbol{B}$ (yellow) deviates only at larger radii from the relativistic value of 4/3 (violet). The red line represents the effective adiabatic index averaged over all directions. The bottom left panel shows the corresponding radial profiles of the CR pressure in the different directions. The thermal pressure dominates at larger radii while the CR pressure drops significantly outside the center. The top right panel represents the time evolution of the shock radius in the direction of the magnetic field (yellow) and perpendicular to it (light blue). Effective CR acceleration for quasi-parallel shock configurations yields an increased compressibility and hence a slower propagating shock. This is quantified in the time evolution of the shock eccentricity in the bottom right panel. The constant eccentricity of the oblate shock (within the uncertainties) demonstrates self-similar evolution of the blast wave also in this case.

field merely impacts the dynamics of the blast wave through the magnetic obliquity-dependent shock acceleration of CRs and not through its pressure.

This analysis is quantified in Fig. 3.6, where we show radial profiles of different volume-weighted quantities, such as the effective ratio of heat capacities $\gamma_{\rm eff}$, the pressure, and the time evolution of the shock radius and eccentricity of the oblate blast wave. The effective ratio of heat capacities $\gamma_{\rm eff}$ is computed from volume-averaged partial pressures of the CR and thermal gas components via equation 3.12. The top and bottom left panels of Fig. 3.6 show the radial variation of the effective adiabatic index $\gamma_{\parallel,\perp}$ and the partial pressures $P_{\parallel,\perp}$ for two regions: parallel and perpendicular. $\gamma_{\parallel}$ and $P_{\rm cr,\parallel}$ are computed from cells that belong to the hourglass-shaped region inside the blast wave that was overrun by a quasi-parallel shock. Here, we define this quasi-parallel shocked region as a narrow double cone oriented along the original magnetic field with an opening angle of 20°. Similarly, we define the region overrun by quasi-perpendicular shocks as the complement of a wide double cone that is bounded by an equatorial band with latitude 20°. The copious CR production at a quasi-parallel shock with the subsequent adiabatic expansion softens the adiabatic index to values close to that of a fully relativistic gas of 4/3. Since the region overrun by a quasi-perpendicular shock is characterized by a ratio of heat capacities close to a purely thermal gas, the effective adiabatic index $\gamma_{\rm eff}$ (shown in red) as well as the spherically averaged CR pressure (shown in purple) levels off at values in between.

The top-right panel of Fig. 3.6 shows the time evolution of the simulated shock radius (filled circles) and the self-similar analytic solution (continuous lines). In line with the previous discussion, the shock radius in the direction perpendicular to the ambient magnetic field moves faster than the shock in the (anti-)parallel direction owing to the increased compressibility of the latter due to efficient CR acceleration. The continuous lines are obtained by fitting the shock radius evolution (equation 3.13) in double-logarithmic space for $\alpha(\gamma)$. Inverting equation 3.14 yields the corresponding effective adiabatic factor shown in the figure. In between those two curves, we show the solution for the effective adiabatic index (crosses).

The increased compressibility of CR-enriched quasi-parallel shocks implies an oblate shock surface that is characterised by an eccentricity, defined as

$$\varepsilon(t) = \sqrt{1 - \left[\frac{r_{\parallel}(t)}{r_{\perp}(t)}\right]^2}. \tag{3.18}$$

Due to the volumetric distribution of CRs with respect to the thermal gas, the influence of CR production affects the entire explosion. This renders it impossible to separate the cases of purely thermal and maximally efficient CR acceleration for the perpendicular and parallel shock radii, respectively. This means that a direct measurement of the eccentricity assuming a pure thermal $\zeta = 0$ in the perpendicular direction and a CR-modulated $\zeta = \zeta_0$ in the parallel direction yields an incorrect result. Instead, an average efficiency $\langle\zeta\rangle$ is required to determine the average radius of the explosion, representing an intermediate case between the parallel and perpendicular shock radius. In the lower right panel of Fig. 3.6,

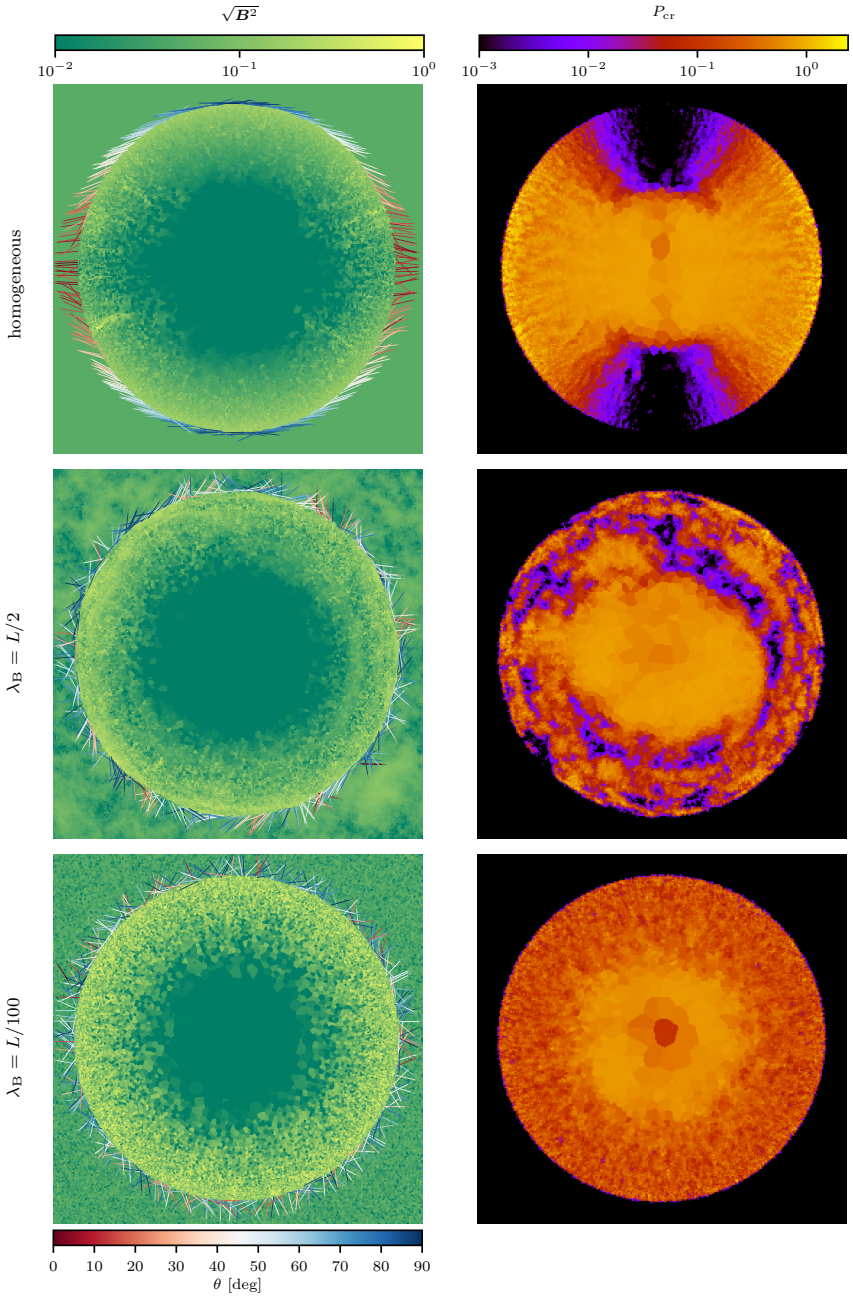

Figure 3.7.: Cross-sections through the centre of 3D simulations of Sedov-Taylor explosions with obliquity-dependent CR acceleration. We show a simulation with a homogeneous, horizontally oriented magnetic field (first row), a turbulent magnetic field with a large correlation length of $\lambda_B = L/2$ (second row) and with a very small correlation length, $\lambda_B = L/100$, in comparison to the radius of the blast wave (third row). We depict magnetic field strength (left column) and CR pressure (right column). In the homogeneous field case we notice a quadrupolar CR distribution that is maximized for quasi-parallel shocks (visualized with red arrows in the left-hand panels) while the magnetic field is only adiabatically amplified at quasi-perpendicular shocks (blue arrows). In the second row we observe a patchy CR distribution with maxima at regions that were over-run with quasi-parallel shocks. The CR distribution in the case of small-scale turbulence (last row) is completely isotropic and the compression of the magnetic field is uniformly distributed across the shock.

we show the eccentricity of the oblate shock surface along with the uncertainty intervals assuming Gaussian statistics,

$$\Delta\varepsilon = \left(\frac{1-\varepsilon^2}{\varepsilon}\right)\sqrt{\left(\frac{\sigma_\parallel}{r_\parallel}\right)^2 + \left(\frac{\sigma_\perp}{r_\perp}\right)^2} \tag{3.19}$$

where $\sigma_\parallel$ and $\sigma_\perp$ are the standard deviations of the shock radius in the direction of the magnetic field and perpendicular to it, respectively. We obtain the theoretical estimate for the eccentricity from our measured self-similar solutions for the parallel and perpendicular shock radii of the top-right panel in Fig. 3.6. There are two strategies to measure the eccentricity: first, determining the distance to the cells of the shock surface inside narrow cones or bands of equal latitude that are centered on the explosion and oriented along the magnetic field direction; second: measuring the momenta of inertia of the entire oblate shock surface, diagonalising the resulting tensor, determining the resulting eigenvalues and extracting the length of the three semi-axes. We decided in favor of the first method because it generates less numerical fluctuations.

We find a constant eccentricity of $\varepsilon = 0.25 \pm 0.02$ during the adiabatic expansion. Note that ε depends on the average efficiency $\langle\zeta\rangle$ and is expected to be smaller for realistic maximum acceleration efficiencies of order 0.15. The constant eccentricity with time demonstrates that the Sedov-Taylor explosion remains self similar also in the presence of obliquity-dependent CR acceleration. In Appendix A.1 we show that the measured eccentricity in our simulations is numerically converged for 100^3 grid cells.

3.3.3. CR acceleration in a turbulent field

After studying magnetic obliquity-dependent CR acceleration at a Sedov-Taylor blast wave that propagates in a homogeneous magnetic field, we now turn to turbulent magnetic fields with different magnetic correlation lengths $\lambda_B = 2\pi/k_{\rm inj}$. As initial conditions for the magnetic field, we adopt a Gaussian random field with a Kolmogorov power spectrum on scales smaller than the coherence length and a white-noise power spectrum on larger scales, as described in Sect. 3.2.4. The larger λ_B in comparison to the shock radius, the fewer statistically independent regions of correlated magnetic fields there are inside the blast wave. Hence we introduce the magnetic coherence length in units of the shock radius, $\Lambda_B = \lambda_B/r_{\rm s}(t)$ as a new parameter. Blast waves with the same Λ_B are statistically self similar.

We perform several simulations with different correlation lengths ranging from $\lambda_B = L$ to $\lambda_B = L/200$ for 200^3-cell runs. In Fig. 3.7 we show different realizations of the CR pressure for varying the correlation lengths of the magnetic field and compare the results to our previous simulation with a homogeneous field. Correlated magnetic patches imply a similarly patchy CR distribution: regions that are overrun by quasi-parallel shocks are CR enriched whereas regions that have experienced quasi-perpendicular shocks result in voids without CRs. As the scaled correlation length Λ_B becomes smaller, the magnetic obliquity also changes on

smaller scales and the number of CR islands becomes more frequent to the point that they merge into a single (noisy) CR distribution. This case is similar to uniform CR acceleration (which is independent of magnetic obliquity), but exhibits a lower overall CR acceleration efficiency.

3.3.4. Average CR acceleration efficiency and field realignment

In order to understand the blast wave-averaged CR acceleration efficiency, we consider the two limiting cases of a homogeneous field and a fully turbulent field with a coherence scale of the initial grid resolution ($\lambda_B = \Delta L$) analytically. In the small-scale turbulent case, we consider a fixed shock normal pointing along $\hat{\boldsymbol{z}}$ without loss of generality. The magnetic field vector can then assume any direction on the upper half-sphere because CR acceleration does not depend on the sign of the magnetic field and is symmetric with respect to $\theta = 0$. Hence, the probability distribution of the magnetic obliquity is given by $f(\theta) = \sin\theta$ with $\theta \in [0, \pi/2]$.

Integrating the efficiency over this probability distribution results in the average efficiency according to

$$\langle\zeta\rangle = \int_0^{\pi/2} \zeta(\theta) \sin\theta \, \mathrm{d}\theta = \begin{cases} \zeta_0 \left(1 - \frac{1}{\sqrt{2}}\right), & \text{for } \zeta = \zeta_{\mathrm{toy}}, \\ 0.302\,\zeta_0, & \text{with Equ. (3.7).} \end{cases} \tag{3.20}$$

Here, we introduced a toy example for the obliquity dependent acceleration that is represented by a discontinuous jump of the efficiency at θ_{crit} from ζ_0 to zero:

$$\zeta_{\mathrm{toy}}(\theta) = \zeta_0 \Theta(\theta_{\mathrm{crit}} - \theta), \tag{3.21}$$

where $\Theta(x)$ is the Heaviside function, representing the limiting case of $\delta \to \infty$ in equation (3.7). This gives us a lower limit for the efficiency.

In the case of a homogeneous field, we fix the magnetic field vector in space and point it into the z direction without loss of generality. Again, the shock normal can assume any direction on the upper half-sphere so that we obtain the same probability distribution function as in the small-scale turbulent case, $f(\theta) = \sin\theta$. The average CR shock acceleration efficiency is thus also given by equation (3.20).

We find that eccentricity plays an important role in shaping the probability distribution of the obliquity. To take this into account we define an ellipsoidal reference frame via

$$x = \left(h + \frac{a}{\sqrt{1 - \varepsilon^2 \cos^2\varphi}}\right) \sin\varphi \cos\lambda, \tag{3.22}$$

$$y = \left(h + \frac{a}{\sqrt{1 - \varepsilon^2 \cos^2\varphi}}\right) \sin\varphi \sin\lambda, \tag{3.23}$$

$$z = \left[h + \frac{(1 - \varepsilon^2)a}{\sqrt{1 - \varepsilon^2 \cos^2\varphi}}\right] \cos\varphi, \tag{3.24}$$

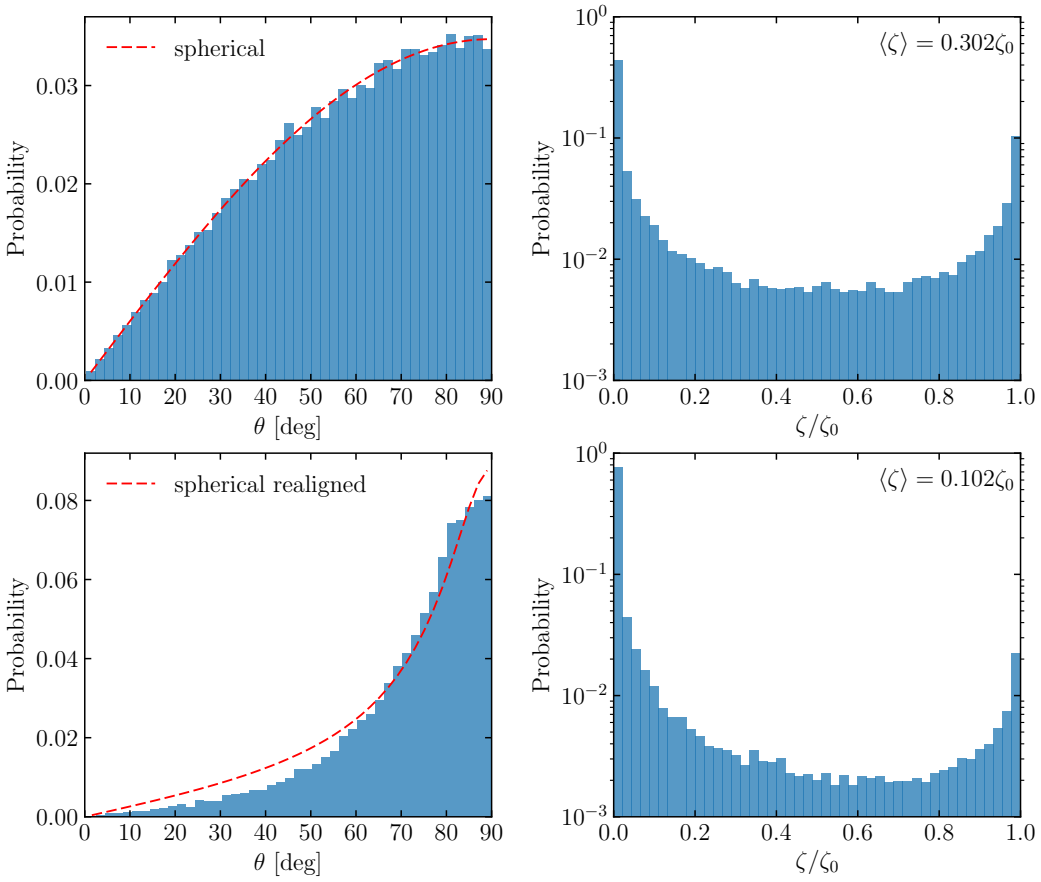

Figure 3.8.: Probability distribution functions (PDFs) of the magnetic obliquity (left) and CR acceleration efficiency ζ (right) in the case of a homogeneous magnetic field in the upstream regime (top panels) and after accounting for magnetic re-orientation in the immediate downstream regime (bottom panels). Here, we adopt an artificially small value for the maximum CR acceleration efficiency of $\zeta_0 = 0.02$, which implies an almost spherical shock due to the negligible CR backreaction in this case. The obliquity distribution follows the theoretical expectation of $f(\theta) = \sin(\theta)$. Accounting for magnetic re-orientation at oblique shocks skews this distribution towards quasi-perpendicular geometries (bottom left), which can be analytically described by equation (3.31) for $\varepsilon = 0$ (dashed line). Note that ζ follows a bimodal distribution as a result of the flatness of the efficiency function (equation 3.7) at quasi-perpendicular and -parallel shocks with a sharp transition in between.

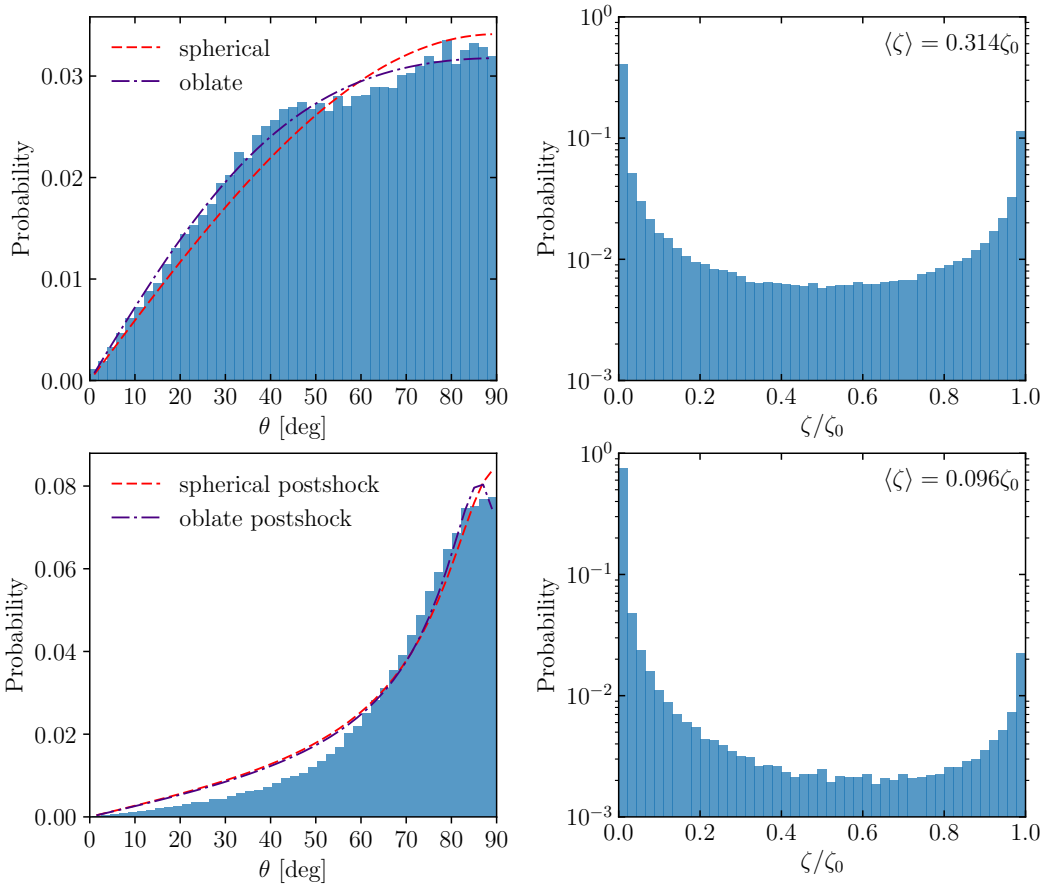

Figure 3.9.: PDF of the magnetic obliquity (left) and CR acceleration efficiency ζ (right) in the case of a homogeneous magnetic field in the upstream regime (top panels) and after accounting for magnetic re-orientation (bottom panels) with a maximum efficiency of $\zeta_0 = 0.5$. The obliquity distribution in the top left panel follows our theoretical prediction $f(\theta, \varepsilon)$ (purple, equation 3.26) of an oblate expanding shock. For comparison, we also show the spherical PDF (red dashed, see Fig. 3.8). Accounting for magnetic re-orientation at oblique shocks skews this distribution towards quasi-perpendicular geometries (bottom left), which can be analytically described by equation (3.31).

where λ and φ are the longitude and pseudo-latitude from the ellipsoid, respectively, h is the height above the surface of the ellipsoid, a the semi-major axis, and ε the eccentricity.

As shown in Appendix A.3, for a homogeneous magnetic field that points into the positive z direction (short axis of the oblate ellipsoid) the angle φ is by construction equal to the definition of the magnetic obliquity θ. Using the fact that $\varphi \equiv \theta$, the Jacobian of this coordinate transformation on the oblate surface ($h = 0$) is given by

$$S(\theta, \varepsilon) = \sin\theta \frac{1-\varepsilon^2}{(1-\varepsilon^2\cos^2\theta)^2}. \tag{3.25}$$

Hence, the normalized distribution function for the obliquity θ reads

$$f(\theta, \varepsilon) = S(\theta, \varepsilon)\left[\int_0^{\pi/2} S(\theta, \varepsilon)\mathrm{d}\theta\right]^{-1}, \tag{3.26}$$

which reduces to $\sin\theta$ for $\varepsilon = 0$.

For our simulations with $\zeta_0 = 0.5$, we obtain an eccentricity of $\tilde{\varepsilon} = 0.25$, and hence an average efficiency of

$$\langle\zeta(\tilde{\varepsilon})\rangle = \int_0^{\pi/2} \zeta(\theta) f(\theta, \tilde{\varepsilon})\mathrm{d}\theta = 0.316\zeta_0. \tag{3.27}$$

The error $\Delta\zeta$ on this quantity derives from the uncertainty on the eccentricity:

$$\Delta\tilde{\zeta} = \left.\frac{\partial\langle\zeta(\varepsilon)\rangle}{\partial\varepsilon}\right|_{\tilde{\varepsilon}} \Delta\tilde{\varepsilon} = \left[\int_0^{\pi} \zeta(\theta)\left.\frac{\partial f(\theta,\varepsilon)}{\partial\varepsilon}\right|_{\tilde{\varepsilon}}\mathrm{d}\theta\right]\Delta\tilde{\varepsilon} = 0.002\zeta_0, \tag{3.28}$$

such that the efficiency for this oblate reads

$$\tilde{\zeta} = (0.316 \pm 0.002)\zeta_0. \tag{3.29}$$

Because we propagate the upstream value of the magnetic obliquity to the shock surface, the resulting obliquity distribution at the shock is expected to follow $f(\theta) = \sin(\theta)$ in the case of a sphere and equation (3.26) for ellipsoids.

In the next step, we assess the distribution of downstream magnetic obliquity as a result of realignment of the tangential component of the magnetic field due to the shock. We can estimate the obliquity after magnetic realignment with the aid of the Rankine-Hugoniot jump conditions:

$$\cos\theta_2(r_\mathrm{c}) = \frac{\cos\theta_1}{\sqrt{\cos^2\theta_1 + r_\mathrm{c}^{-2}\sin^2\theta_1}} \tag{3.30}$$

where r_c is the compression ratio at the shock. We can then insert this formula into equation (3.25) to obtain the expected distribution of realigned angles for oblates:

$$f[\theta(r_\mathrm{c}), \varepsilon] = S[\theta(r_\mathrm{c}), \varepsilon]\left[\int_0^{\pi/2} S[\theta(r_\mathrm{c}), \varepsilon]\mathrm{d}\theta\right]^{-1} \tag{3.31}$$

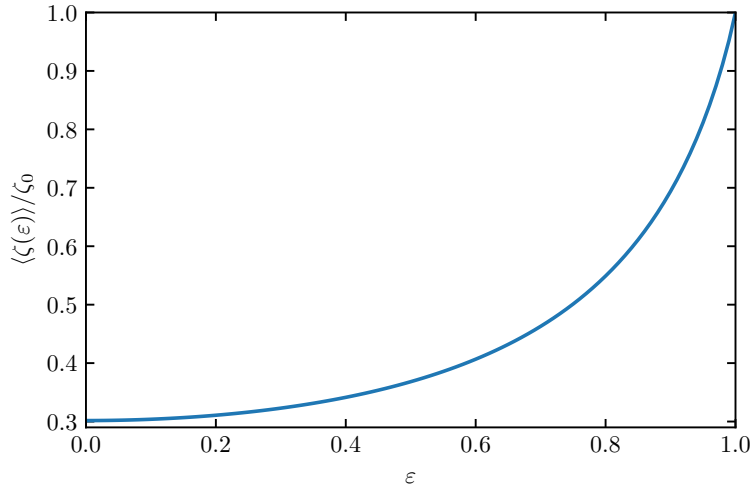

Figure 3.10.: Average acceleration efficiency as a function of the eccentricity ε of the oblate according to the distribution shown in equation (3.25) and equation (3.27) in a homogeneous magnetic field configuration. For $\varepsilon = 0$ the original value of equation (3.20) is restored while for an eccentricity of unity the oblate degenerates into a circle, yielding everywhere a maximum efficiency.

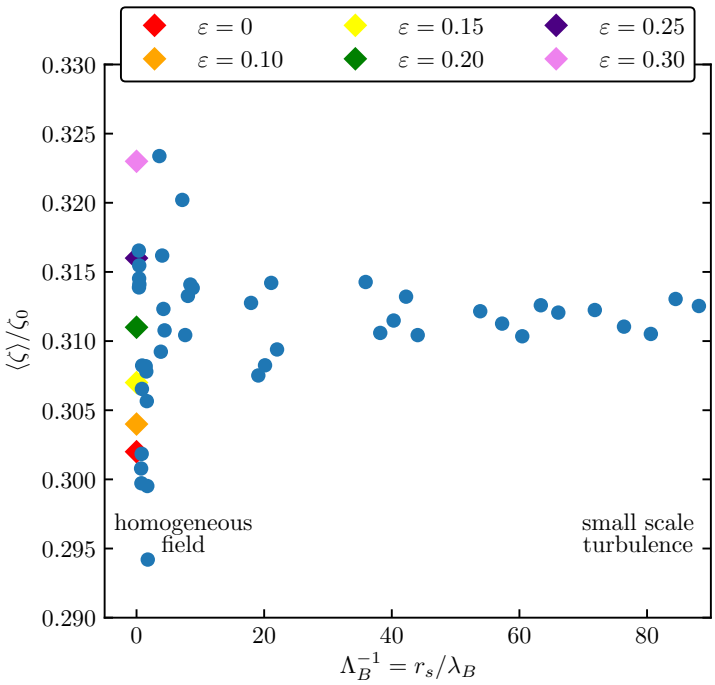

Figure 3.11.: Average CR acceleration efficiency for a turbulent magnetic field with different correlation lengths $\Lambda_B = \lambda_B/r_s(t)$. The case $\Lambda_B^{-1} = 0$ corresponds to a homogeneous magnetic field and $\Lambda_B^{-1} = 85$ relates to the small-scale turbulent case with a coherence scale equal to the initial grid resolution of our simulation. The coloured diamonds at $\Lambda_B^{-1} = 0$ show the homogeneous field case for different average CR acceleration efficiencies corresponding to different eccentricities. The simulation points scatter around the value $\langle\zeta\rangle = (0.311 \pm 0.005)\zeta_0$.

which reduces to $\sin[\theta(r_c)]$ for $\varepsilon = 0$. We find good agreement of these theoretical distributions and our simulations in Figs. 3.8 and 3.9 for a maximum efficiency of $\zeta_0 = 0.02$ and of $\zeta_0 = 0.5$, respectively. Note that the low CR acceleration efficiency in Fig. 3.8 allows to neglect the geometrical anisotropy of the shock surface that results from copious CR production in the direction of the magnetic field. In all cases, we find a bimodal distribution of ζ as a result of the flat efficiencies at quasi-perpendicular and -parallel shocks with a sharp transition in between. We also find a good agreement of the realigned obliquity distributions, which are skewed towards quasi-perpendicular geometries.

The effect of an oblate geometry becomes evident in Fig. 3.9 (upper left panel), which shows an improved fit of the elliptical distribution in comparison to the spherical sinusoidal distribution. However, the resulting shape of the efficiency distribution is only little affected. Thus, its average value is only slightly increased over the spherical case as can be inferred from Figs. 3.8 and 3.9. The full evolution of $\langle\zeta\rangle$ as a function of ε is shown in Fig. 3.10. The academic case of $\varepsilon = 1$ represents an unphysical limit where the oblate degenerates into a circle. This orients the shock surface in such a way so that it is always parallel to the direction of the magnetic field and yields the maximum possible acceleration efficiency.

In Fig. 3.11 we summarize results for different simulations with varying correlation lengths of $\lambda_B^{-1} = [2, 4, 10, 20, 50, 100, 150, 200]$ each at times $t = [5, 6, 7, 8, 9, 10]\times$ 0.01 in simulation units. The expanding shock front starts to embrace more and more coherent magnetic patches whose number scales as $N \propto \Lambda_B^{-3}$. For comparison, we also show the theoretically expected eccentricities for the homogeneous field case with coloured diamonds. There is no trend in the evolution of the average acceleration efficiency as a function of Λ_B^{-1}. Instead, the simulation values scatter between an eccentricity of $\varepsilon = 0.10$ (orange diamond) and $\varepsilon = 0.3$ (violet diamond), yielding a value of $\langle\zeta\rangle = (0.311 \pm 0.05)\zeta_0$. For $\lambda_B \gg \Delta L$, CR-rich patches give rise to corrugations of the shock surface causing local small deviations from spherical symmetry. If the correlation length becomes comparable to the initial grid resolution then the blast wave becomes spherical, albeit with a slightly higher efficiency.

3.4. Conclusions

In this chapter we perform MHD simulations of the evolution of supernova remnants in the Sedov-Taylor phase. For the first time, we model magnetic obliquity dependent CR acceleration and study i) its dynamical effects on the overall evolution of the blast wave and ii) how different magnetic geometries affect the resulting CR distribution. To this end, we use results from hybrid PIC simulations (with kinetic ions and fluid electrons) of non-relativistic, large Mach number shocks. Those demonstrate that only quasi-parallel magnetic shock configurations can accelerate ions while quasi-perpendicular shocks are ineffective.

Using idealized shock tube experiments, we show that our algorithm is able to recover the input direction of the magnetic field with a Gaussian scatter of

around 3°. When we change the magnetic orientation from quasi-perpendicular to quasi-parallel configurations, the efficiency of CR acceleration and the associated post-shock compressibility increase. This leads to density jumps that exceed the theoretical limit $\rho_2/\rho_1 = 4$ (valid for a thermal gas), slows down the shock and decreases the Mach number.

We derive analytical exact solutions of the Sedov-Taylor blast-wave problem with CR acceleration (neglecting obliquity dependent effects). We numerically solve the self-similar, spherically symmetric conservation equations of mass, momentum and energy to determine the behavior of the shock radius. This enables us to derive analytical fitting functions for the effective ratio of specific heats for a composite of thermal gas and CRs as a function of the maximum acceleration efficiency.

Our simulations of the Sedov-Taylor blast wave problem with obliquity dependent CR acceleration in a homogeneous magnetic field geometry show the emergence of an oblate ellipsoidal shock surface. Its short axis is aligned with the ambient magnetic field orientation due to the efficient CR acceleration at quasi-parallel shocks. The ellipsoidal shock surface has an eccentricity of $\varepsilon = 0.25 \pm 0.02$ for a maximum CR acceleration efficiency of $\zeta_0 = 0.5$ (which decreases for more realistic maximum efficiencies). The shock eccentricity does not change with time, demonstrating that the Sedov-Taylor explosion also remains self similar in the presence of obliquity-dependent CR acceleration. Because an oblique shock only amplifies the perpendicular field component, this re-orients an oblique magnetic field towards the shock surface. We find that this re-orientation effect has no practical influence on the average CR acceleration efficiency because the acceleration efficiency exhibits two flat plateaus at quasi-parallel and -perpendicular shocks and a fast transition in between.

Sedov-Taylor explosions in a turbulent magnetic field yield a patchy CR distribution with tangential, filamentary overdensities delineating regions that were over-run by quasi-parallel shocks and filamentary patches devoid of CRs, which were swept by quasi-perpendicular shocks. The CR distribution becomes completely isotropic if the magnetic turbulence exhibits a very small coherence scale in comparison to the shock radius. We derive the averaged CR acceleration efficiency to ≈ 0.3 of the maximum CR acceleration efficiency for our adopted CR efficiency function, independent of coherence scale.

In particular, the peculiar morphology of the CR pressure distribution that result from obliquity-dependent CR acceleration in a turbulent magnetic field could be the origin of the observed tangential filamentary morphology of some shell-type middle-aged supernova remnants at TeV gamma rays. We will study this effects in a separate publication. We finally note that the fluctuating TeV gamma-ray morphology would be a direct consequence of the obliquity dependent acceleration in this picture and does not require large upstream CR fluctuations or strong gradients in the ambient density; thereby opening the possibility of realistically modelling supernova remnants at gamma rays in the future.

4. The coherence scale of the ISM magnetic field via TeV γ-ray observations of SNRs

This chapter is an adapted version of the paper *Constraining the coherence scale of the interstellar magnetic field using TeV gamma-ray observations of supernova remnants* published on Monthly Notices of Royal Astronomical Society (Pais et al., 2020).

Abstract

Galactic cosmic rays (CRs) are believed to be accelerated at supernova remnant (SNR) shocks. In the hadronic scenario the TeV gamma-ray emission from SNRs originates from decaying pions that are produced in collisions of the interstellar gas and CRs. Using CR-magnetohydrodynamic simulations, we show that magnetic obliquity dependent shock acceleration is able to reproduce the observed TeV gamma-ray morphology of SNRs such as Vela Jr. and SN1006 solely by varying the magnetic morphology. This implies that gamma-ray bright regions result from quasi-parallel shocks (i.e., when the shock propagates at a narrow angle to the upstream magnetic field), which are known to efficiently accelerate CR protons, and that gamma-ray dark regions point to quasi-perpendicular shock configurations. Comparison of the simulated gamma-ray morphology to observations allows us to constrain the magnetic coherence scale λ_B around Vela Jr. and SN1006 to $\lambda_B \simeq 13^{+13}_{-4.3}$ pc and $\lambda_B > 200^{+50}_{-40}$ pc, respectively, where the ambient magnetic field of SN1006 is consistent with being largely homogeneous. We find consistent pure hadronic and mixed hadronic-leptonic models that both reproduce the multi-frequency spectra from the radio to TeV gamma rays and match the observed gamma-ray morphology. Finally, to capture the propagation of a SNR shock in a clumpy interstellar medium, we study the interaction of a shock with a dense cloud with numerical simulations and analytics. We construct an analytical gamma-ray model for a core collapse SNR propagating through a structured interstellar medium, and show that the gamma-ray luminosity is only biased by 30% for realistic parameters.

4.1. Introduction

SNR shocks energize Galactic CRs via diffusive shock acceleration. This converts about $5 - 10\%$ of the kinetic energy into a non-thermal, power-law momentum distribution of CRs (Bell, 1978a; Blandford & Ostriker, 1978). The most direct observational evidence for this is the GeV and TeV gamma-ray emission from SNRs. There are two competing models: in the leptonic model, CR electrons Compton upscatter (interstellar) radiation fields whereas in the hadronic model inelastic collisions between the interstellar medium (ISM) and CRs produce neutral pions that decay into gamma rays (Hinton & Hofmann, 2009; Zirakashvili & Aharonian, 2010). The latter process produces a kinematic spectral feature below GeV energies, as recently observed by the Fermi gamma-ray telescope (Ackermann, 2013). However, the steep high-energy spectral slope raises questions whether this represents an unambiguous proof of CR hadron acceleration at this SNR (Cardillo et al., 2016).

The hadronic model requires efficient CR hadrons acceleration, which must be accompanied by substantial magnetic field amplification via the hybrid non-resonant instability (Bell, 2004). This finding received strong observational support with the detection of thin X-ray synchrotron filaments at several SNR shocks. Those filaments exhibit fast (year-scale) variability and likely result from cooling of freshly accelerated electrons in magnetic fields of $\approx 1\,\mathrm{mG}$ (Uchiyama et al., 2007). Spatial correlations between gamma-ray brightness and gas column density are another consequence of the hadronic model and are expected for core-collapse supernovae, which explode inside molecular clouds due to the fast evolution of their massive progenitor stars. Combining synchrotron and inverse Compton emission in the leptonic model yields volume-filling magnetic field strengths of $\approx 10\,\mu\mathrm{G}$ (Gabici & Aharonian, 2016), which are compatible with mG-field strengths inferred from X-ray synchrotron filaments only when assuming a clumpy medium. It has also been argued that a rising gamma-ray energy spectrum with increasing photon energy provides evidence for leptonic models. However, such a spectrum can also be obtained in the hadronic model when considering a clumpy ISM because of proton propagation effects that substantially harden the proton spectrum inside dense clumps in comparison to the acceleration spectrum in the diffuse ISM (Gabici & Aharonian (2014); Celli et al. (2019)). The absence of thermal X-rays from the remnant provides additional support for this scenario because the shock will considerably slow down while penetrating into dense clumps and thus cannot heat them up to X-ray emitting temperatures (Inoue et al., 2012).

Alternatively, leptonic scenarios have been proposed to explain the gamma-ray emission from young SNRs in an ISM model with homogeneous density (e.g., Pohl, 1996) in order to overcome the lack of thermal X-ray emission. This results in a low upper limit on the ISM density. Leptonic models evoke inverse Compton (IC) scattering of CR electrons with a photon field that is provided by the ubiquitous cosmic microwave background in combination with (dust-processed) stellar light. For example, Xing et al. (2016) uses leptonic models to explain the emission from

the South-Western limb of SN1006 while this explanation is extended to the entire remnant (Petruk et al., 2011; Araya & Frutos, 2012). The leptonic scenario naturally explains the correlation between X-ray synchrotron and IC gamma-ray emitting regions such as in Vela Jr. (Aharonian et al., 2007) and matches the observed broadband spectrum. On the other hand, this model implies low magnetic field strengths, which are in contradiction to the narrow filamentary structures detected in X-rays. Hence, we need to understand the detailed spatial structure of SNRs across different wave lengths to unambiguously identify emission and particle acceleration processes.

The high angular resolution ($< 0.1°$) of imaging air Čerenkov telescopes H.E.S.S., VERITAS, and MAGIC enables detailed morphological gamma-ray studies of SNRs and to separate or exclude contributions by compact sources such as pulsars. In particular, TeV gamma-ray observations have delivered a rich morphology of shell-type SNRs, ranging from the bi-lobed emission of SN1006 (H.E.S.S. Collaboration, 2010) to the filamentous, patchy appearances of Vela Jr. (H.E.S.S. Collaboration, 2018b) and RX-J1713 (H.E.S.S. Collaboration, 2018a), to the young, type Ia SNR Tycho G120.1+01.4 (Archambault et al., 2017). In principle, the patchy gamma-ray morphology could result from density inhomogeneities (Berezhko & Völk, 2008; Atoyan et al., 2000) of the ambient ISM. It yet remains to be seen whether the fluctuation amplitude necessary for the observed gamma-ray patchiness does not introduce a corrugated shock surface (Ji et al., 2016) that is inconsistent with the observed spherical blast wave.

Here, we propose a different model in which the acceleration process imprints a rich gamma-ray morphology due to the global magnetic morphology (Pais et al., 2018). Hybrid particle-in-cell simulations of non-relativistic, strong shocks show that diffusive shock acceleration of hadrons efficiently operates for quasi-parallel configurations (i.e., when the shock propagates along the upstream magnetic field or moves at a narrow angle to it) and converts around 15% of the available energy to CRs (Caprioli & Spitkovsky, 2014a). In contrast, a shock that propagates perpendicular to the magnetic field (or at a large angle to it, i.e., a quasi-perpendicular configuration) is an inefficient accelerator without strong pre-existing turbulence at the CR gyroscale (Giacalone et al., 1992) because charged particles are bound to gyrate around the flux-frozen magnetic field. As the magnetized plasma sweeps past the shock, so are the gyrating particles, which cannot return back upstream.

We aim to explain the apparently disparate TeV morphologies of SNR 1006 and Vela Jr. within a single physical model assuming a hadronic model linking gamma-ray morphology and local orientation of the magnetic field. To this end, we run a suite of simulations modeling a point explosion that encounters a range in magnetic field morphologies, from a homogeneous field to a mixture of homogeneous and turbulent fields to fully turbulent fields with varying coherence lengths in Section 4.2. We rescale our simulation parameters within observational limits to reproduce the observed gamma-ray spectra and flux (Section 4.3). Comparing simulated to observed morphologies in Section 4.4 allows to constrain the magnetic coherence length that the unperturbed ISM had before it encountered the SNR blast wave. Assuming statistical homogeneity, we thus constrain the magnetic coherence scale

in the immediate vicinity of the SNR. We explore how the gamma-ray signal is modified by launching the SNR into stellar wind profiles instead of a homogeneous ISM environment in Section 4.6 and conclude in Section 4.7. In Sec. 4.5, we study the interaction of a shock with a dense cloud with numerical simuations and analytics and construct an analytical model for the gamma-ray luminosity from a core collapse SNR that interacts with a structured ISM with a large population of dense, cold clouds.

4.2. Simulation setup

4.2.1. Rationale

We aim to produce realistically looking TeV gamma-ray maps with the least amount of necessary physical complexity but including all the required processes for drawing transparent and robust conclusions from our three-dimensional MHD simulations. To this end we follow the following rationale:

- The general numerical setup consists of simulating the Sedov-Taylor phase of SNRs by injecting energy at the initial time into our simulation domain that is filled with magnetized plasma with different correlation lengths. We identify the shock during the run-time of the simulations, inject CR energy at the shock with an efficiency that is in agreement with the results of ab initio particle-in-cell plasma simulations, and advect the CR energy density with the thermal plasma.

- In order to explain the TeV gamma-ray morphology for two famous shell-type SNR, SN1006 and Vela Jr., we have to realistically model the external medium that the remnant shocks are propagating into. Because the thermonuclear supernova SN1006 (of type Ia) is located at a Galactic height of 0.4 kpc, the shock propagates into low-density medium and encounters mostly homogeneous magnetic field that was potentially stretched due to a galactic outflow or the Parker instability.

- In contrast, the Vela Jr. SNR is thought to be associated with a core-collapse supernova explosion (Wang & Chevalier, 2002), which results from the collapse of a massive star. Hence, in the post-processing, we account for the free expansion phase preceeding the Sedov-Taylor phase and rescale the final radii accordingly. The Vela Jr. SNR encounters a highly structured, multi-phase ISM that is typical of star forming regions. This is modelled with a population of dense gaseous clumps embedded in a nearly homogeneous background medium, which simultaneously explains the absence of thermal X-ray emission and hard TeV gamma-ray spectra in the hadronic model (Celli et al., 2019). Finally, we additionally simulate the expansion of the SNR into two different stellar wind profiles that bracket the uncertainty in the progenitor model and study its impact on the TeV gamma-ray morphology.

4.2.2. Simulation setup

We perform our simulations with the second-order accurate, adaptive moving-mesh code AREPO (Springel, 2010; Pakmor et al., 2016a), using standard parameters for mesh regularization. Magnetic fields are treated with ideal magnetohydrodynamics (Pakmor & Springel, 2013), using the Powell scheme for divergence control (Powell et al., 1999). CRs are modelled as a relativistic fluid with adiabatic index 4/3 in a two-fluid approximation (Pfrommer et al., 2017a).

We localize and characterize shocks during the simulation (Schaal & Springel, 2015) to inject CRs into the downstream (Pfrommer et al., 2017a) with an efficiency that depends on the upstream magnetic obliquity (Pais et al., 2018). We adopt a maximum acceleration efficiency for CRs at quasi-parallel shocks of 15% that approaches zero for quasi-perpendicular shocks (Caprioli & Spitkovsky, 2014a). We only model the dominant advective CR transport and neglect CR diffusion and streaming. This is justified since diffusively shock accelerated CRs experience efficient Bohm diffusion with a coefficient $\kappa_{\rm Bohm}$ at the shock (Stage et al., 2006), which implies a CR precursor ($L_{\rm prec}$) that is smaller than our grid cells, $L_{\rm prec} \sim \sqrt{\kappa_{\rm Bohm} t} \sim 0.1\ {\rm pc} \times (pc/10\,{\rm TeV})^{1/2}\,(B/100\,\mu{\rm G})^{-1/2}\,(t/10^3\,{\rm yr})^{1/2}$. We neglect slow non-adiabatic CR cooling processes in comparison to the fast Sedov expansion.

Each simulation follows a point explosion that results from depositing $E_{\rm SN} = 10^{51}$ erg in a homogeneous periodic box (Pfrommer et al., 2017a). This leads to an energy-driven, spherically-symmetric strong shock expanding in a low-pressure ISM with mean molecular weight $\mu = 1.4$. Our initial conditions are constructed by first generating a Voronoi mesh with randomly distributed mesh-generating points in our three-dimensional simulation box with 200^3 cells that we then relax via Lloyd's algorithm (Lloyd, 1982) to obtain a glass-like configuration.

To simulate a realistic star forming environment for Vela Jr. we inserted 7×10^3 uniformly distributed small, dense clumps with a number density of $n_{\rm c} = 10^3\ {\rm cm}^{-3}$ and a diameter of 0.1 pc (McKee & Ostriker, 1977). More details about the clumps can be found in Sec. 4.5.

Our turbulent magnetic fields exhibit magnetic power spectra of Kolmogorov type with different coherence lengths. The three magnetic field components are treated independently so that the resulting field has a random phase. To fulfill the constraint $\boldsymbol{\nabla} \cdot \boldsymbol{B} = 0$ we project out the radial field component in Fourier space. We assume a low ISM pressure of 0.44 eV cm^{-3} and scale the field strength to an average plasma beta factor of unity. To ensure pressure equilibrium in the initial conditions, we adopt temperature fluctuations of the form $nk_{\rm B}\delta T = -\delta \boldsymbol{B}^2/(8\pi)$ (for details, see Pais et al. 2018).

In our physical set-up, there are two different processes driving turbulence. The process of diffusive shock acceleration excites non-linear (turbulent) Bell modes on scales below the CRs' gyroradii (Bell, 2004). Because we adopt the obliquity-dependent CR acceleration efficiency from self-consistent plasma simulations (Caprioli & Spitkovsky, 2014a) in our sub-grid model, we implicitly account for the full kinetic physics.

On the contrary, the magnetic turbulence that we explicitly model in our simu-

lations reflects the supernovae-driven ISM turbulence with varying injection scales from 4 to 200 pc. The magnetic fluctuations cascade down to levels of $\delta B/B \approx 10^{-3}$ at resonant length scales of TeV CRs so that they do not interfere with the large-scale field topology at the shock. To derive this result, we assumed Alfvénic turbulence for parallelly propagating Alfvén waves according to theory of magneto-hydrodynamical turbulence Goldreich & Sridhar (1995) in a mean magnetic field of $10\,\mu$G. Hence, the small fluctuation amplitude and the enormous scale separation of injection-to-gyroscale of $\approx 10^5$ justifies our separate treatment of these two processes.

4.2.3. Observational modeling

In order to connect our simulations to gamma-ray observations, we need to take into account all observational constraints on ISM properties. For practical reasons, here we derive approximate scaling laws of the gamma-ray flux in the Sedov-Taylor regime and adopt the simplified assumption of a CR spectrum with index $\alpha_\mathrm{p} = 2$, which yields an equal contribution to the total CR energy for each decade in CR momentum. These scaling relations enable us to find parameter combinations of the SNR and surrounding ISM, which match observed gamma-ray fluxes in the hadronic model. We will vary those parameter combinations in a detailed multi-frequency analysis in Section 4.3 study how they vary if the SNR shock propagates in a stellar wind profile in Section 4.6.

SN1006

SN1006 represents a good case study of a SNR with a unique gamma-ray morphology. Moreover, its exactly known age allows to tightly constrain other environmental ISM parameters. Low-resolution HI measurements of the density around SN1006 suggest a diffuse density of $n = 0.3$ cm^{-3} and an interaction of the SNR with a dense cloud of $n = 0.5$ cm^{-3} (Dubner et al., 2002). Studies based on X-ray spectroscopy estimate the density of the North-Western rim of the SNR to be $n = (0.15 - 0.25)$ cm^{-3} (Long et al., 2003) which is consistent with hydrodynamic simulations of an explosion energy of 10^{51} erg in a homogeneous medium (Wang & Chevalier, 2001). More recent papers suggest an even lower ambient density for the North-Western rim of $n = 0.085$ cm^{-3}, which is estimated based on X-ray proper motion measurements (Katsuda et al., 2009), down to a density of $n = 0.05$ cm^{-3} for the South-Eastern rim, which is based on X-ray observations in combination with a shock-plasma model (Acero et al., 2007). Such low densities, however, would require an uncomfortably high explosion energy in order to explain the gamma-ray emission of SN1006 in the hadronic model. Assuming a CR proton acceleration efficiency of 10% yields $E_\mathrm{SN} = 3 \times 10^{51}$ erg (H.E.S.S. Collaboration, 2010).

Integrating the differential gamma-ray flux (equation (1) of Gabici & Aharonian, 2016) yields an estimate of the TeV gamma-ray flux, $\mathcal{F}_\gamma$, of a SNR in the hadronic model:

$$\mathcal{F}_\gamma \simeq \int_{1\ \mathrm{TeV}}^{100\ \mathrm{TeV}} F_\gamma \mathrm{d}E_\gamma = \int_{1\ \mathrm{TeV}}^{100\ \mathrm{TeV}} \frac{4W_\mathrm{p}\ E_\gamma^{-2}\mathrm{d}E_\gamma}{\ln(E_\mathrm{max}/E_\mathrm{min})\tau_{\pi^0} 4\pi D^2} \tag{4.1}$$

where $\tau_{\pi^0} \simeq 1.6 \times 10^9 \left(n/0.1\ \mathrm{cm}^{-3}\right)^{-1}$ yr is the energy loss time due to neutral pion production, n is the ISM number density assuming cosmic abundances ($\mu = 1.4$), D is the distance to the SNR, W_p is the total proton energy and E_γ is the gamma-ray energy. Here, we assume that the CR spectrum extends from $E_\mathrm{min} = 1$ GeV to $E_\mathrm{max} = 4$ PeV, which corresponds to the energy of the knee. The factor of 4 accounts for the compression of the density at the shock. The integration yields

$$\mathcal{F}_\gamma \simeq 2.7 \times 10^{-12} \left(\frac{W_\mathrm{p}}{10^{50}\,\mathrm{erg}}\right) \left(\frac{n}{0.1\,\mathrm{cm}^{-3}}\right) \left(\frac{D}{1\,\mathrm{kpc}}\right)^{-2} \frac{\mathrm{ph}}{\mathrm{cm}^2\ \mathrm{s}}. \tag{4.2}$$

The self-similar solution for a strong shock in the Sedov-Taylor regime (Sedov, 1959) states that the shock radius r_ST evolves as

$$r_\mathrm{ST}(t) = \left(\frac{E_\mathrm{SN}}{\alpha\rho}\right)^{1/5} t_\mathrm{age}^{2/5}, \tag{4.3}$$

where ρ is the ISM mass density, t_age is the age of the remnant and α a dimensionless factor depending on the adiabatic index of the fluid. For a mixture of thermal gas and freshly accelerated CRs with a maximum efficiency of 15% we find $\alpha = 0.52$ (Pais et al., 2018). The resulting shock radius for typical ISM parameters is

$$r_\mathrm{ST} = 7.82\ \mathrm{pc} \left(\frac{E_\mathrm{SN}}{10^{51}\ \mathrm{erg}}\right)^{1/5} \left(\frac{n}{0.1\ \mathrm{cm}^{-3}}\right)^{-1/5} \left(\frac{t_\mathrm{age}}{1000\ \mathrm{yr}}\right)^{2/5}. \tag{4.4}$$

The shock radius can be expressed by the angle it subtends on the sky (assuming the small-angle approximation)

$$r_\mathrm{ST} = D \sin\left(\frac{\theta}{2}\right) \simeq 8.7\ \mathrm{pc} \left(\frac{D}{1\ \mathrm{kpc}}\right) \left(\frac{\theta}{\mathrm{deg}}\right). \tag{4.5}$$

Combining Eq. (4.4) with Eq. (4.5) we derive the following formula for the density of SN1006:

$$n = 0.1\ \mathrm{cm}^{-3} \left(\frac{t_\mathrm{age}}{1\ \mathrm{kyr}}\right)^2 \left(\frac{D}{1.79\ \mathrm{kpc}}\right)^{-5} \left(\frac{\theta}{0.5\ \mathrm{deg}}\right)^{-5}. \tag{4.6}$$

Substituting Eq. (5.3) for n in Eq. (4.2) and solving for W_p yields

$$\begin{aligned} W_\mathrm{p} = 4.5 \times 10^{49}\ \mathrm{erg} &\left(\frac{t_\mathrm{age}}{1\ \mathrm{kyr}}\right)^{-2} \left(\frac{\mathcal{F}_\gamma}{3.9 \times 10^{-13}\ \mathrm{ph\ cm^{-2}s^{-1}}}\right) \\ &\times \left(\frac{D}{1.79\ \mathrm{kpc}}\right)^{7} \left(\frac{\theta}{0.5\ \mathrm{deg}}\right)^{5}. \end{aligned} \tag{4.7}$$

Here, we use the observed gamma-ray flux of SN1006, $\mathcal{F}_\gamma(>1\ \mathrm{TeV}) \approx 3.9 \times 10^{-13}$ ph cm^{-2}s^{-1}, the angle it subtends over the sky, $\theta \approx 0.5$, and the canonical energy of a SNR, $E_\mathrm{SN} = 10^{51}$ erg. Estimates for the distance range from 1.45 kpc, calculated using the SNR peak brightness, to 2.2 kpc, based on the comparison of the optical proper motion with the shock velocity derived from optical thermal line broadening (Winkler et al., 2003). More recently, Katsuda (2017) derived a distance of 1.57±0.07 kpc combining the shock speed with the proper motion of the North-Western filament. We chose to adopt an intermediate distance of 1.79 kpc for our model.

Vela Junior

The unknown age of Vela Junior increases the uncertainty for the parameter estimates of Vela Junior in comparison to SN1006. Estimates on the age vary from a very young remnant of $\sim$ 700 yrs (Aschenbach et al., 1999) to an older object of more than 4000 yrs (Katsuda et al., 2008). Distance estimates are also uncertain. The SNR can be a nearby object at $D = 0.2$ kpc, as inferred from studies of the decay of ^{44}Ti nuclei (Iyudin et al., 1998), or a more distant one at $D = 0.75$ kpc, as inferred from the slow expansion of X-ray filaments (Katsuda et al., 2008).

Regarding the density estimates, the lack of thermal X-ray emission places a very low limit at $n = 0.03$ cm^{-3} while assuming a homogeneous environmental density (Slane et al., 2001). However the interaction with dense clumps lowers the resulting thermal X-ray emission and allows a higher average density. A conventional approach in the hadronic model is to use a density of the order of $n \sim 1$ cm^{-3} (Aharonian et al., 2006), while hydrodynamic models suggest values of less than 0.4 cm^{-3} (Allen et al., 2015). More recently HI and CO measurements even suggest an extremely high average ISM density of the order of $n \sim 100$ cm^{-3} (Fukui et al., 2017).

Adopting the observed flux above 1 TeV for Vela Jr. of 2.3×10^{-11}ph cm^{-2} s^{-1} (H.E.S.S. Collaboration, 2018b), we obtain for W_p (using Eqs. (4.2) and (4.7), respectively):

$$\begin{aligned} W_\mathrm{p} &= 4.5 \times 10^{49}\ \mathrm{erg} \left(\frac{n}{0.5\ \mathrm{cm}^{-3}}\right)^{-1} \left(\frac{D}{500\ \mathrm{pc}}\right)^{2} \\ &= 4.5 \times 10^{49}\ \mathrm{erg} \left(\frac{t_\mathrm{age}}{2.9\ \mathrm{kyr}}\right)^{-2} \left(\frac{D}{500\ \mathrm{pc}}\right)^{7} \left(\frac{\theta}{2\ \mathrm{deg}}\right)^{5}. \end{aligned} \tag{4.8}$$

For an explosion energy of 10^{51} erg, the efficiency adopted by Fukui et al. (2017) only amounts to $\sim 0.1\%$ (i.e. $W_\mathrm{p} = 10^{48}$ erg) at $D = 750$ pc. Although this low efficiency is compensated by an extremely high ISM density, in order to maintain a fixed angular size in the sky at 750 pc, from Eq. (4.8) we notice that the age of the remnant would exceed 100 kyr, far beyond the observational estimates, even for the extreme case discussed in Telezhinsky (2009). The choice for the distance is determined by the constraints on the age. An SNR age in the range $(680 - 5100)$ yr corresponds to distance ranging between 0.3 kpc and 0.6 kpc and a density ranging from 0.2 cm^{-3} to 0.66 cm^{-3}. Following the recent estimates on the distance reported in Allen et al. (2015) we decided to place the remnant at $D = 0.5$ kpc, which would correspond to an age of 2900 yrs, assuming that the expansion is solely in the Sedov-Taylor stage and in a uniform medium.

However, a more accurate modeling of the evolution of a core collapse SNR includes an initial phase in which the SNR is freely expanding with constant velocity in a wind-blown environment driven only by the initial kinetic energy and the ejected mass M_ej. Consequently the resulting radius is larger than the value obtained via Eq. (4.4). Following Truelove & McKee (1999), the expanding shock radius that combines the radii in the free expansion (r_free) and Sedov-Taylor phases

reads:

$$\begin{aligned} r_s(t) &= [(r^*_{\rm ST})^{5/2} + r^{5/2}_{\rm free}]^{2/5} \\ &= \left[\left(\frac{E_{\rm SN}}{\alpha\rho}\right)^{1/2}(t_{\rm age} - t_{\rm ST}) + \left(\frac{3M_{\rm ej}}{4\pi\rho}\right)^{5/6}\right]^{2/5}, \end{aligned} \tag{4.9}$$

where $r^*_{\rm ST}$ is the modified Sedov radius starting at the end of the free expansion phase, and

$$t_{\rm ST} = \frac{1}{2}\left(\frac{9}{2\pi^2}\right)^{1/6} M_{\rm ej}^{5/6} E_{\rm SN}^{-1/2} \rho^{-1/3} \tag{4.10}$$

is the transition time between the free expansion and the Sedov-Taylor regime corresponding to the moment when the mass swept up by the explosion equals the ejected mass (Truelove & McKee, 1999). Combining Eqs. (4.5) and (4.9) and solving for $t_{\rm age}$ we find a more precise estimate for the age of Vela Jr.

In order to reliably model the circum-stellar medium of Vela Jr., we include a population of dense gaseous clumps (Maxted et al., 2018) with a typical size of 0.1 pc and a number density of $\sim 10^3 {\rm cm}^{-3}$ (Inoue et al., 2012). The detection of these molecular clouds is linked to the rotational CO lines often observed in these systems (Fukui, 2013). However, it is questionable whether future telescopes will have enough resolution to resolve the emission from a single clump. To include the effect of the clumpy ISM, we redefine Eq. (4.2) as:

$$\begin{aligned} \mathcal{F}_\gamma &\simeq 2.7 \times 10^{-12}(1+\chi) \\ &\times \left(\frac{W_{\rm p}}{10^{50}\,{\rm erg}}\right)\left(\frac{n}{0.1\,{\rm cm}^{-3}}\right)\left(\frac{D}{1\,{\rm kpc}}\right)^{-2} \frac{\rm ph}{{\rm cm}^2\ {\rm s}}, \end{aligned} \tag{4.11}$$

where χ is the ratio between the swept-up mass of the clumps within the SNR volume $V_{\rm SNR}$ and the diffuse ISM mass swept up by the shock. It reads:

$$\begin{aligned} \chi &= \bar{\eta}\frac{M_{\rm c}^{\rm swept}}{M_{\rm ISM}^{\rm swept}} = \bar{\eta}\frac{\langle\rho_{\rm c}\rangle V_{\rm SNR}}{\rho_{\rm ISM} V_{\rm SNR}} \\ &= 0.2\left(\frac{\bar{\eta}(t)}{30\%}\right)\left(\frac{\langle\rho_{\rm c}\rangle}{1.6\times10^{-2}\ M_\odot{\rm pc}^{-3}}\right)\left(\frac{n}{0.42\ {\rm cm}^{-3}}\right)^{-1}, \end{aligned} \tag{4.12}$$

where $\bar{\eta}(t) = 30\%$ is the average percentage of clumped mass penetrated and accelerated by the shock and $\langle\rho_{\rm c}\rangle$ is the average density of dense gas contained in the clumps. More details about the behavior of $\bar{\eta}(t)$ can be found in Sec. 4.5. Inserting Eq. (4.12) into Eq. (4.11) and solving for the ISM density n, we find:

$$\begin{aligned} n = 0.42\ {\rm cm}^{-3}\Bigg[&1.2\left(\frac{\mathcal{F}_\gamma}{2.3\times10^{-11}\ {\rm ph\ cm^{-2}\ s^{-1}}}\right) \\ &\times\left(\frac{W_{\rm p}}{4.5\times10^{49}\ {\rm erg}}\right)^{-1}\left(\frac{D}{0.5\ {\rm kpc}}\right)^2 \\ &- 0.2\left(\frac{\bar{\eta}(t)}{30\%}\right)\left(\frac{\langle\rho_{\rm c}\rangle}{1.6\times10^{-2}\ M_\odot{\rm pc}^{-3}}\right)\Bigg]. \end{aligned} \tag{4.13}$$

In our setup for Vela Jr. we set $\langle \rho_c \rangle = 1.6 \times 10^{-2}\ M_\odot \mathrm{pc}^{-3}$ and we assume a distance of $D = 0.5$ kpc so that the dense-cloud mass in within the supernova remnant volume is similar to the value assumed by Celli et al. (2019) for the cloud mass in RX-J1713,

$$M_c^{\mathrm{swept}} = \frac{4}{3}\pi r_s^3 \langle \rho_c \rangle = 45 M_\odot \left(\frac{D}{0.5\ \mathrm{kpc}}\right)^3 \left(\frac{\theta}{2\ \mathrm{deg}}\right)^3 \times \left(\frac{\langle \rho_c \rangle}{1.6 \times 10^{-2}\ M_\odot \mathrm{pc}^{-3}}\right) \tag{4.14}$$

where we expressed r_s by Eq. (4.5).

Thus, the corresponding diffuse inter-clump density for the ISM is lowered to $n = 0.42\ \mathrm{cm}^{-3}$ (see Eq. (4.13)) and the corresponding age as a function of the ejected mass is

$$t_{\mathrm{age}} = 2.68\ \mathrm{kyr} + 0.12\ \mathrm{kyr} \left(\frac{M_{\mathrm{ej}}}{M_\odot}\right)^{5/6}. \tag{4.15}$$

If we assume an ejected mass of 3 $M_\odot$, the resulting age for Vela Jr. is 3000 yrs, slightly higher than that inferred from considering a Sedov-Taylor phase only in a non-clumpy medium. We adopt this more accurate estimate in our analysis re-scale the distances of our Sedov-Taylor simulations according to Eq. (4.9). We defer a detailed simulation of this combined free expansion and Sedov-Taylor phases to future work, since the dominating CR pressure inside the remnant should also cause the Rayleigh-Taylor instabilities at the contact discontinuity of shocked ISM and shocked ejecta to develop differently.

4.3. Multi-frequency spectral modelling

In order to improve the order of magnitude limits as presented in Sect. 4.2.3, we derive multi-wavelength spectra from radio to TeV gamma-rays. This enables us to carefully investigate the nature of the gamma-ray emission from both SNRs. The data are then compared to a one-zone model in which the integrated particle populations (electrons and protons, denoted by subscripts $i = \{\mathrm{e}, \mathrm{p}\}$) are described by a power law with exponential cutoff of the form:

$$f^{1\mathrm{D}}(p_i) = \frac{\mathrm{d}^2 N_i}{\mathrm{d}p_i \mathrm{d}V} \propto p_i^{-\alpha_i} \exp\left[-\left(\frac{p_i}{p_{i,\mathrm{cut}}}\right)^{\beta_i}\right] \tag{4.16}$$

where $f^{1\mathrm{D}}(p_i) = 4\pi\, p_i^2 f^{3\mathrm{D}}(p_i)$, α_i is the spectral index, $p_{i,\mathrm{cut}}$ is the cutoff momentum and β_i describes the sharpness of the cutoff; with values reported in Table 5.1.

Radio synchrotron and inverse Compton emission (including the Klein-Nishina cross section) are calculated following Blumenthal & Gould (1970). The hadronic gamma-ray emission is calculated from parametrisations of the cross-section of neutral pion production at low and high proton energies, respectively (Yang et al., 2018b; Kelner et al., 2006). Because our simulations only follow CR protons, we

Table 4.1.: Comparison of simulation and observational parameters

SNR	**SN1006**			**Vela Jr.**		
Parameter	Simulation	Observation	Reference	Simulation	Observation	Reference
diameter θ_s [deg]	0.5	0.5	7	2	2	7
spectral index $\Gamma_{\rm HE}$	1.95	1.79 ± 0.44	2, 8	1.81	1.85 ± 0.24	14
spectral index $\Gamma_{\rm TeV}$	2.15	2.30 ± 0.15	2, 8	2.11	2.24 ± 0.19	2
$\mathcal{F}_\gamma(>1\text{TeV})$ [10^{-12}ph cm^{-2} s^{-1}]	0.39	0.39 ± 0.08	9	23.4	23.4 ± 5.6	9
n [cm^{-3}]	$0.1^{\mathbf{H}}$, $0.07^{\mathbf{M}}$	$0.05 - 0.3$	1, 5	$0.42^{\mathbf{H}}$, $0.38^{\mathbf{M}}$	$0.03 - 100$	3, 6, 13
M_c [$M_\odot$]	–	–	–	$45^{\mathbf{H,M}}$	–	–
D [pc]	$1790^{\mathbf{H}}$, $1930^{\mathbf{M}}$	$1450 - 2200$	2, 11	$500^{\mathbf{H}}$, $500^{\mathbf{M}}$	$200 - 750$	4, 10
diameter d_s [pc]	$15.6^{\mathbf{H}}$, $16.8^{\mathbf{M}}$	$12.6 - 19.2$	–	$17.3^{\mathbf{H}}$, $17.3^{\mathbf{M}}$	$7 - 26$	–
$t_{\rm age}$ [yrs]	1012	1012	–	$3000^{\mathbf{H}}$, $2860^{\mathbf{M}}$	$680 - 5100$	4, 10, 12
v [km s^{-1}]	$3000^{\mathbf{H}}$, $3200^{\mathbf{M}}$	2100 - 4980	1, 11, 15	$1800^{\mathbf{H}}$, $2000^{\mathbf{M}}$	> 1000	3
B [μG]	$200^{\mathbf{H}}$, $80^{\mathbf{M}}$	–	–	$40^{\mathbf{H}}$, $10^{\mathbf{M}}$	–	–
$E_{\rm p,cut}$[TeV]	200	–	–	100	–	–
$E_{\rm e,cut}$[TeV]	$1.7^{\mathbf{H}}$, $3^{\mathbf{M}}$	–	–	$0.25^{\mathbf{H}}$, $0.4^{\mathbf{M}}$	–	–
$\beta_{\rm p}$	2	–	–	2	–	–
$\beta_{\rm e}$	0.7	–	–	0.4	–	–

Notes: n denotes the diffuse ISM number density, $M_{\rm c}$ is the target clump mass hit by the remnant, D is the distance to the SNR, $\theta_{\rm s}$ and $d_{\rm s}$ are the angular and proper extent of the blast wave, v denotes the shock velocity, $t_{\rm age}$ is the SNR age, B the magnetic field and $\mathcal{F}_\gamma$ is the gamma-ray flux. The last four lines represent the parameters used for the spectral models described in Sec. 4.3. The superscripts **H** and **M** denote the parameters of the pure hadronic and mixed hadronic/leptonic models, respectively.

References: (1) Acero et al. (2007) ; (2) Acero et al. (2015); (3) Allen et al. (2015); (4) Aschenbach et al. (1999); (5) Dubner et al. (2002); (6) Fukui et al. (2017); (7) Green (2014); (8) H.E.S.S. Collaboration (2010); (9) H.E.S.S. Collaboration (2018b); (10) Katsuda et al. (2008); (11) Katsuda (2017); (12) Ming et al. (2019); (13) Slane et al. (2001); (14) Tanaka et al. (2011); (15) Winkler et al. (2003).

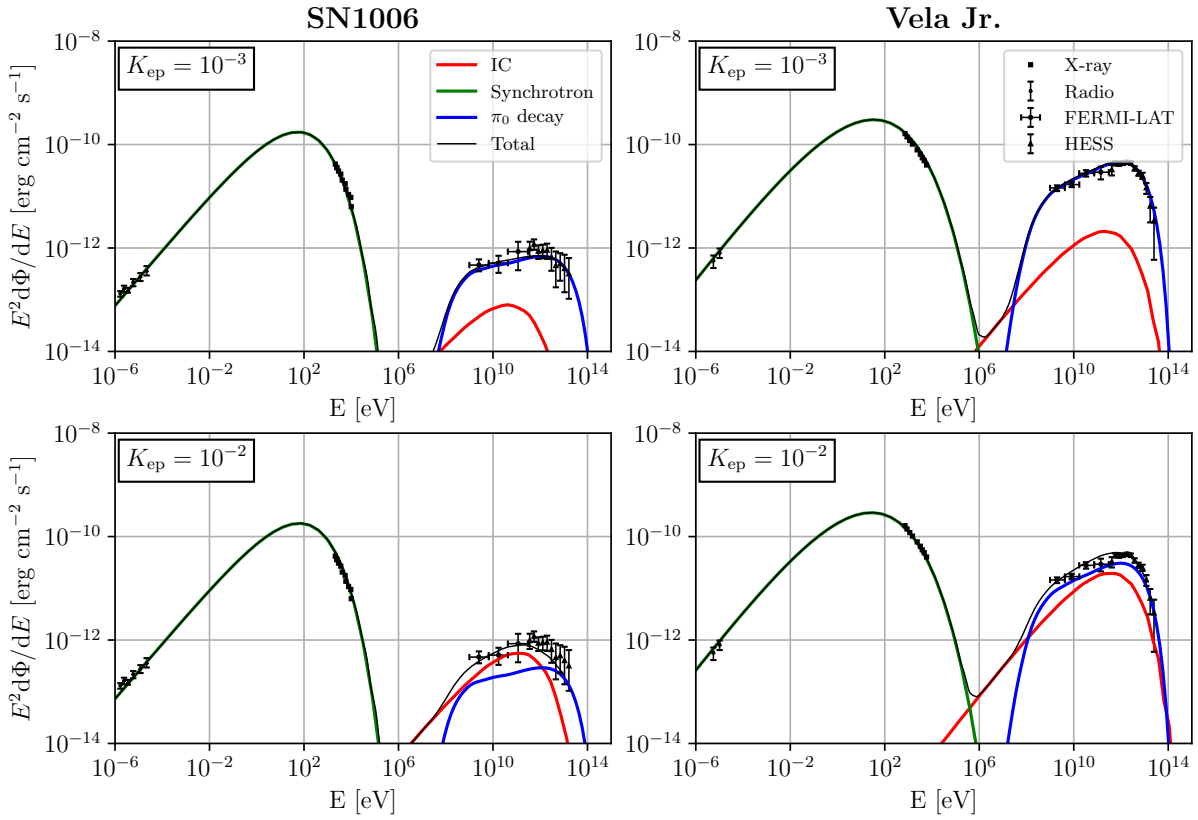

Figure 4.1.: Multi-frequency spectra of SN1006 (left-hand panels) and Vela Jr. (right-hand panels). The top panels show a hadronic scenario for both remnants assuming an electron-to-proton ratio of $K_{ep} = 10^{-3}$. The bottom panels show a mixed hadronic-leptonic scenario with $K_{ep} = 10^{-2}$. For SN1006, we use data in the radio (Reynolds, 1996), X-rays (Bamba et al., 2008), from FERMI (Abdo et al., 2010a) and H.E.S.S. (H.E.S.S. Collaboration, 2010) (sum of the two regions). For Vela Jr., we adopt data in the radio (Duncan & Green, 2000), X-rays (Aharonian et al., 2007), from FERMI (Tanaka et al., 2011) and H.E.S.S. (H.E.S.S. Collaboration, 2018b). We account for the following processes: synchrotron radiation from primary electrons (green lines), IC scattering on the CMB for SN1006 and additionally on starlight for Vela Jr. (red lines) and hadronic interactions (blue lines).

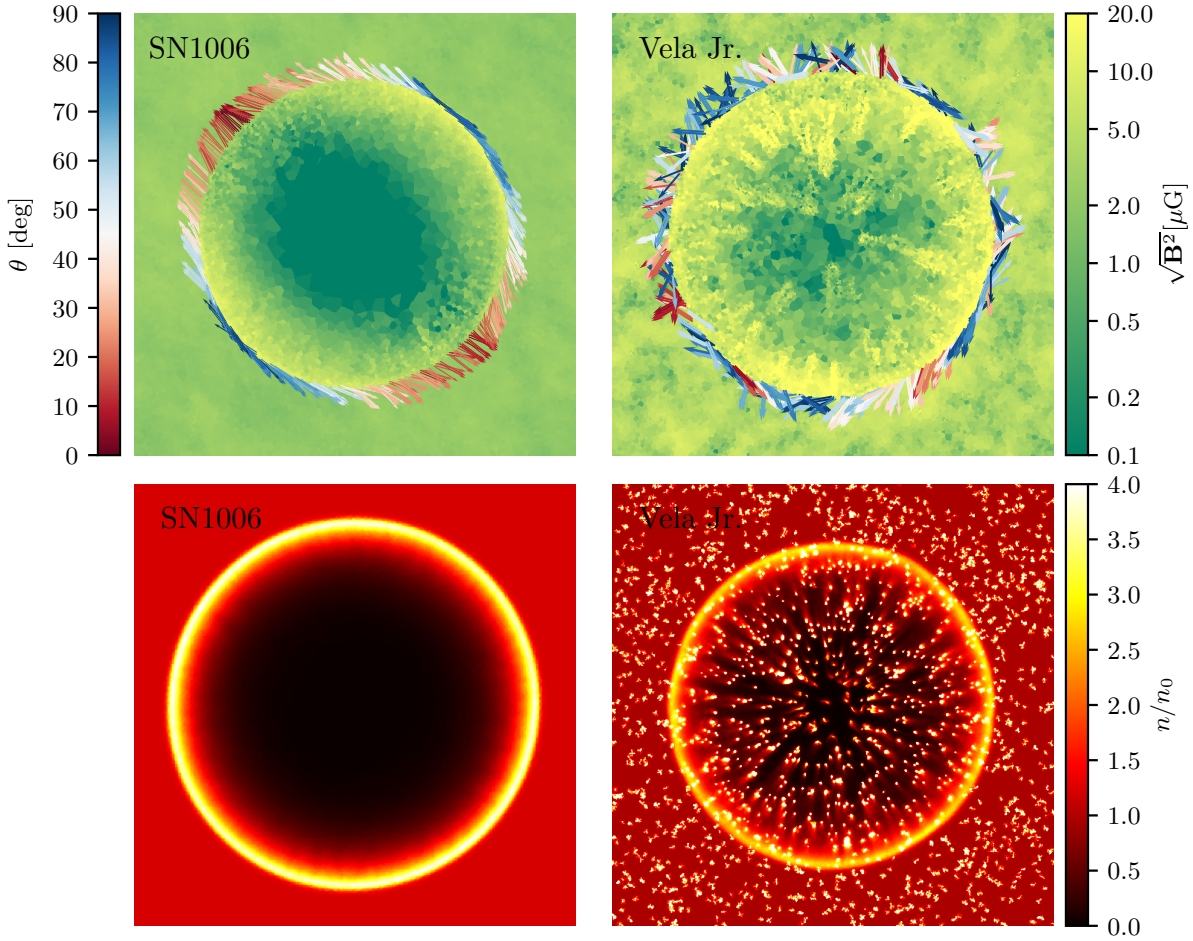

Figure 4.2.: Two-dimensional cross-sections of our SNR simulations. Top row: slices of the magnetic field strengths of SN1006 and Vela Jr.Ḃottom row: 2D slices of the number density n normalized to the background density n_0. The outwards pointing arrows in the top panels show the orientation of the magnetic field at the shock, color-coded by the magnetic obliquity (red/blue for quasi-parallel/-perpendicular shocks). Both simulation models adopt a constant-density ISM and differ only in the assumed magnetic morphology: SN1006 has a homogeneous magnetic field pointing to the top-left augmented with a mildly turbulent field while Vela Jr. adopts a fully turbulent magnetic field with correlation length $\lambda_B = L/2 = 13$ pc.

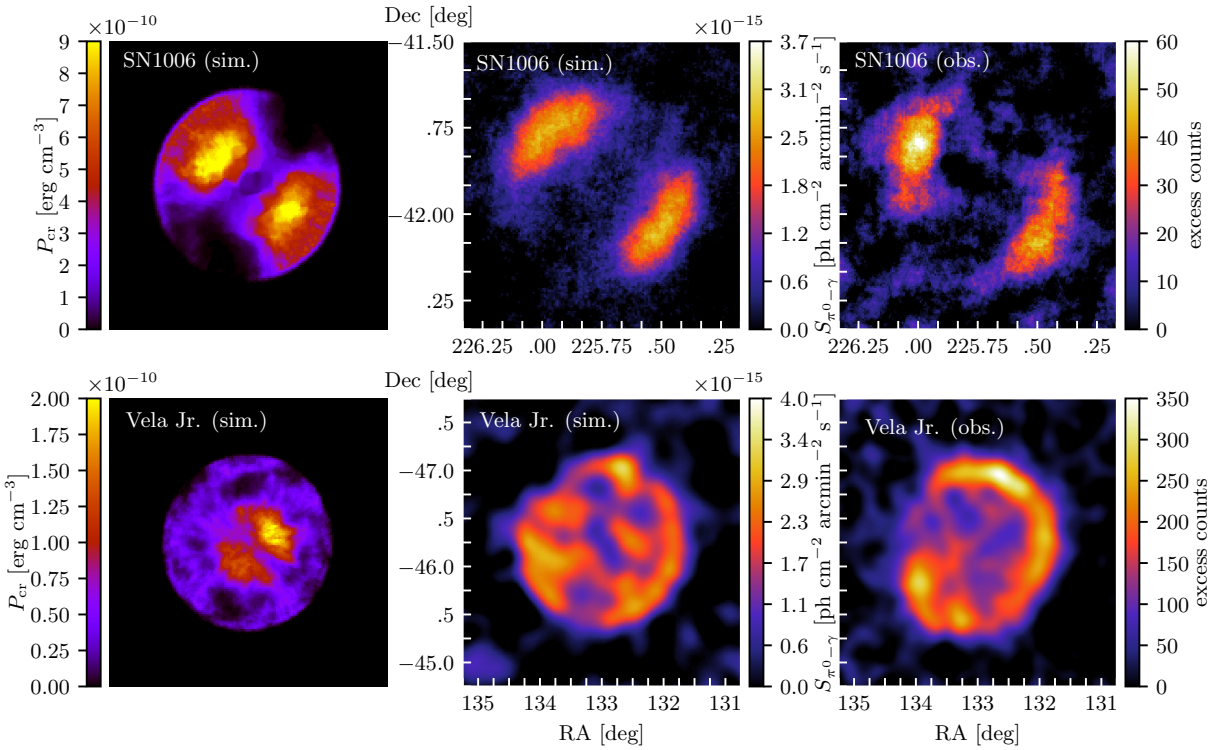

Figure 4.3.: Two-dimensional projected gamma-ray maps of our SNR simulations. Top row, featuring SN1006: CR pressure (left), simulated pion-decay gamma-ray surface brightness resulting from hadronic CR interactions convolved to the observational resolution (middle) and acceptance-corrected excess map for SN1006 with a Gaussian PSF of width $R_{68} = 0.064°$, corresponding to $\sigma = R_{68}/1.515 = 0.042°$ (H.E.S.S. Collaboration, 2010). Bottom row, featuring the same quantities for Vela Jr. with an acceptance-corrected excess map that was convolved with a Gaussian PSF of width $\sigma = 0.08°$ (H.E.S.S. Collaboration, 2018b). We add Gaussian noise at the observed level and power spectrum and convolve both simulated gamma-ray maps to the observational angular resolution.

assume an electron-to-proton ratio $K_{\rm ep}$ at 10 GeV for the normalization of the electron population. For our hadronic model we set $K_{\rm ep} = 10^{-3}$. Since there are parameter degeneracies, we also show a mixed hadronic/leptonic model for the gamma-ray emission with $K_{\rm ep} = 10^{-2}$.

Results for the pure hadronic and the mixed hadronic-leptonic models are shown in Fig. 4.1 for both SNRs. The model parameters are reported in the lower section of Tab. 5.1. Note that the magnetic field entering here is the radio synchrotron emission-weighted magnetic field, which is situated in the post-shock region, interior to the SNR shell. In the case of SN1006, because of its position above the galactic plane, we assume an inverse-Compton (IC) scattering mainly on CMB photons. The location of Vela Jr. in a star forming region suggests that a combination of IC scattering on starlight with an energy density of $5u_{\rm CMB}$ and CMB photons is more appropriate. In particular, we assume that the starlight is reprocessed by warm dust with a temperature of 100 K, which is typical for conditions in star forming regions (Morlino & Caprioli, 2012). Note that we adopt hard CR proton spectral indices of $\alpha_{\rm p} < 2$ in all models, which naturally emerge as a result of streaming CRs inside dense clumps of a clumpy ISM (Celli et al., 2019).

4.4. Morphological gamma-ray modelling

Our simulation models for the two SNRs are described by the energy-conserving Sedov-Taylor solution (Ostriker & McKee, 1988). The solution also remains self similar for obliquity-dependent CR acceleration (Pais et al., 2018). We assume a power-law CR momentum distribution for calculating the pion-decay gamma-ray emissivity (Pfrommer & Enßlin, 2004; Pfrommer et al., 2008). After line-of-sight integrating the gamma-ray emissivity and adding Gaussian noise (so that the synthetic map matches the observational noise properties in amplitude and scale, see Pais & Pfrommer in prep.), we convolve the maps with the observational point-spread function.

First, we perform exploratory simulations with parameter choices guided by the self-similar scaling of the Sedov-Taylor solution. We find parameter combinations that approximately reproduce all observational characteristics (with box size $L = 20$ pc for SN1006 and $L = 26$ pc for Vela Jr.). Fixing angular size, explosion energy, and employing the self-similar solution, we then re-scale the solution by varying the ambient density within observational bounds to match the observed gamma-ray fluxes. In case of the core collapse supernova remnant Vela Jr. we must take into account the free expansion phase, while assuming an ejected mass of 3 $M_\odot$. Thus, we evolve the simulation of the Sedov explosion so that the combination of free expansion and Sedov phase matches its angular size at a given distance following Eq. (4.9), and we re-scale the shock radius accordingly to account for the free expansion phase. The final set of parameters is reported in Table 5.1.

To model SN1006 we assume a dominant homogeneous magnetic field that points to the top-left as supported by studies of radio polarization signatures (Reynoso et al., 2013). We superpose a turbulent magnetic field with a correlation length

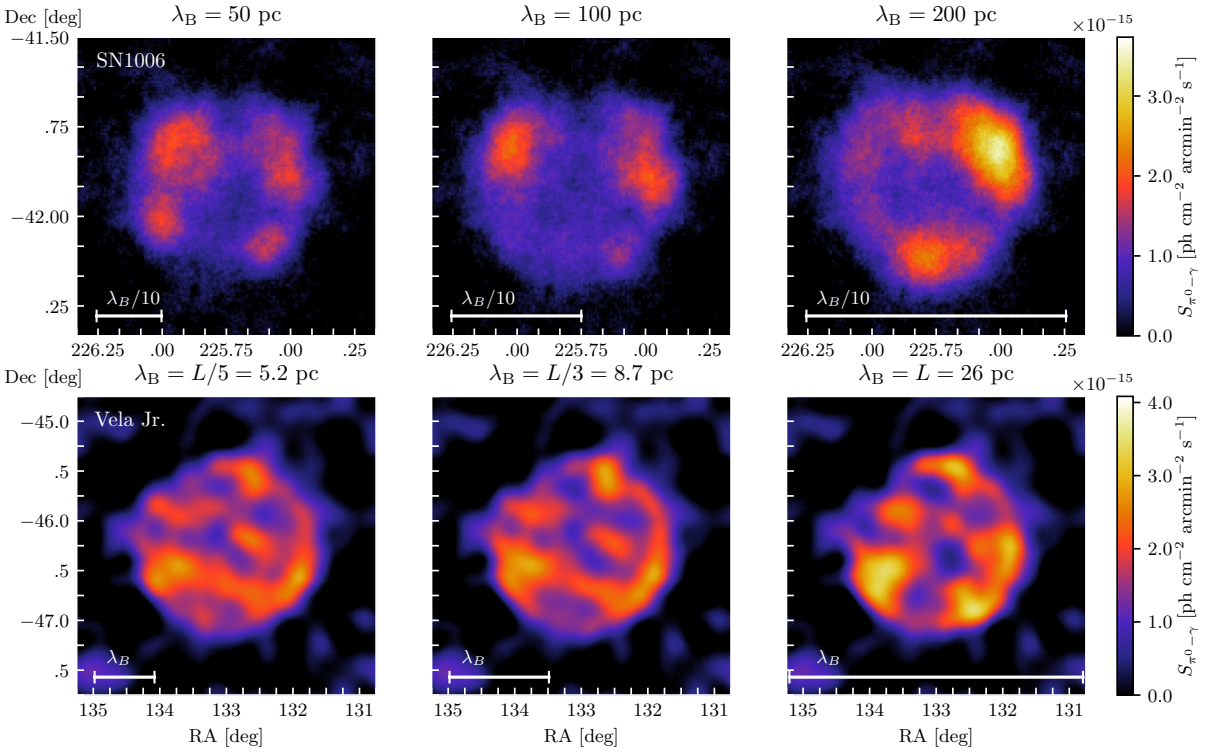

Figure 4.4.: Synthetic gamma-ray maps of SN1006 (first row) and Vela Jr. (second row) for a purely turbulent magnetic field with different coherence lengths (see panels). The sequence towards larger correlation lengths starts to approach more homogeneous magnetic field geometries with the characteristic bi-lobed shell morphology (top right for SN1006) whereas smaller coherence lengths approach the isotropic limit (lower left for Vela Jr.). Clearly, the observed gamma-ray map of Vela Jr. falls in between the cases $\lambda_B = 8.7$ and 26 pc (bottom left and middle panels), justifying our choice of $\lambda_B = 13$ pc.

$\lambda_B = L = 20$ pc ($\approx 0.74^\circ$ at $D = 1.53$ kpc) that contains 1/9 of the energy density of the homogeneous field. For Vela Jr. we perform a range of fully turbulent simulations with magnetic coherence lengths $\lambda_B = L/f$ ($f \in \{1, 2, 3, 4, 5\}$). We find that our simulation model with $\lambda_B = L/2 = 13$ pc ($\approx 2.3^\circ$ at 0.5 kpc) statistically matches the gamma-ray maps best.

We present different physical properties of our simulation models for SN1006 and Vela Jr. in Fig. 4.2 and 4.3. While both simulation models adopt a constant background density, their magnetic structure differs (Fig. 4.2). This results in a significantly different CR pressure distribution owing to the obliquity-dependent shock acceleration (left column of Fig. 4.3).

The hadronically induced gamma-ray maps echo this difference as they depend on the CR pressure distribution multiplied with the target gas density, which peaks at the shock surface (middle column of Fig. 4.3). The bi-lobed gamma-ray morphology of SN1006 is a direct consequence of quasi-parallel shock configuration at the polar caps. This contrasts with the patchy filamentary, limb-brightened gamma-ray morphology of our model for Vela Jr., which results from the small-scale coherent magnetic patches with a quasi-parallel shock geometry.

A direct comparison with observational images is shown in the right column of Fig. 4.3. In the case of SN1006, we convolve the simulated map with a Gaussian of width $\sigma = 0.042^\circ$ (equal to $\sigma = R_{68}/1.515$ where $R_{68} = 0.064^\circ$), in the case of Vela Jr. we use $\sigma = 0.08^\circ$ (the observational point spread function, PSF). The obliquity-dependent shock acceleration model is able to accurately match the TeV gamma-ray morphologies of SN1006 and Vela Jr. solely by changing the magnetic coherence scale (with a homogeneous field representing the limit of an infinite coherence scale). Clearly, in the case of Vela Jr. this match is on a statistical basis as the phases of turbulent fields are random. We emphasize that all our simulations assumed a constant-density ISM that the SNR has expanded into. Note that we also obtain filamentary gamma-ray morphologies due to obliquity dependent shock acceleration in SNRs that are expanding into a stellar wind environment (see Sec. 4.6).

The success of our models enables us to estimate λ_B of the ISM surrounding SN1006 and Vela Jr. by comparing the observed gamma-ray maps to simulations with different values of λ_B. While the morphology of SN1006 is best matched by a homogeneous ambient field (possibly with the addition of a small-amplitude turbulent field), we need to perform an analysis similar to Vela Jr. in order to formally place a lower limit on the magnetic coherence length. To this end, we perform three different simulations that have a purely turbulent field with coherence scales of $\lambda_B = 50$, 100 and 200 pc. Figure 4.4 shows gamma-ray maps of three different magnetic coherence scales for both SNRs, respectively. For SN1006, the number of gamma-ray patches decreases with increasing coherence scale (left to right) to the point where there are two patches visible ($\lambda_B = 200$ pc). Since the alignment of these two patches is not symmetric with respect to the centre, we conclude that the true coherence scale must be larger and in fact is consistent with a nearly homogeneous field across the SNR. For Vela Jr., the sequence of gamma-ray maps with decreasing coherence scale leads to smaller-scale gamma-ray

patches that asymptotically approach an isotropic distribution. We find that the correlation length of Vela Jr. ranges in between the box size L and $L/3$, suggesting $\lambda_B \approx L/2 = 13^{+13}_{-4.3}$ pc, allowing for uncertainties in distance and λ_B.

4.5. An analytical model for the gamma-ray luminosity in a clumped medium

Here, we study the interaction of a shock with a dense cloud with numerical simuations and analytics and construct an analytical model for the gamma-ray luminosity from a core collapse SNR. We assume that the shock propagates through a highly structured ISM with a large population of dense clouds, which plays an important role for the resulting multi-frequency emission (Wang & Chevalier, 2002).

4.5.1. Numerical setup

To capture the clumpy structure of the ISM in these regions we generated 7×10^3 dense gaseous clumps with a radius of $R_c = 0.05$ pc each and uniformly distributed in a box of size $L = 25$ pc, subset of the simulation box of size $L = 26$ pc. We used a margin of 0.5 pc for each side of the cube to avoid any incidental misplacement of the clumps. We deposit a total mass of dense clumps of $M_c^{tot} = 255\ M_\odot$ within the selected box so that each clump has a mass of $M_c = 0.036\ M_\odot$ and the volume-averaged H_2 density is $\langle \rho_c \rangle = 1.6 \times 10^{-2}\ M_\odot \mathrm{pc}^{-3}$. Following a setup similar to Celli et al. (2019), we assume spherical clumps with a number density $n_c = 1.4 \times 10^3$ cm^{-3} and a molecular weight $\mu = 2$ (associated to the clumps) so that the density contrast with respect to the background is $\delta = n_c/n_0 \sim 3 \times 10^3$. Note that we neglect radiative cooling in these simulations, which is negligible over the propagation time of the SNR shocks considered while it is crucial for understanding the (thermo-)dynamics of the system on longer time scales (McCourt et al., 2018; Gronke & Oh, 2018; Sparre et al., 2019).

We use the code AREPO, which employs an unstructured mesh that is defined as the Voronoi tessellation of a set of mesh-generating points. If they move with the local fluid speed, the scheme inherits the advantages of Lagrangian fluid methods that keep the mass per cell approximately fixed. AREPO allows for super-Lagrangian resolution capabilities by inserting new mesh points. Hence, in order to accurately describe the dynamics of the dense clouds, each small clump is resolved with 10^3 cells that are uniformly distributed within a spherical volume. To ensure a smooth transition between the larger cell size in the low-density diffuse ISM and the well-resolved clumps, we initially place a buffer shell of thickness 0.01 pc with the density of the diffuse ISM and the high resolution of the clump cells. Despite the high post-shock vorticity caused by the impact of shock front on the clumps, the volume fraction occupied by the dense bullets is small enough to maintain the shock front practically self similar throughout its evolution in the medium.

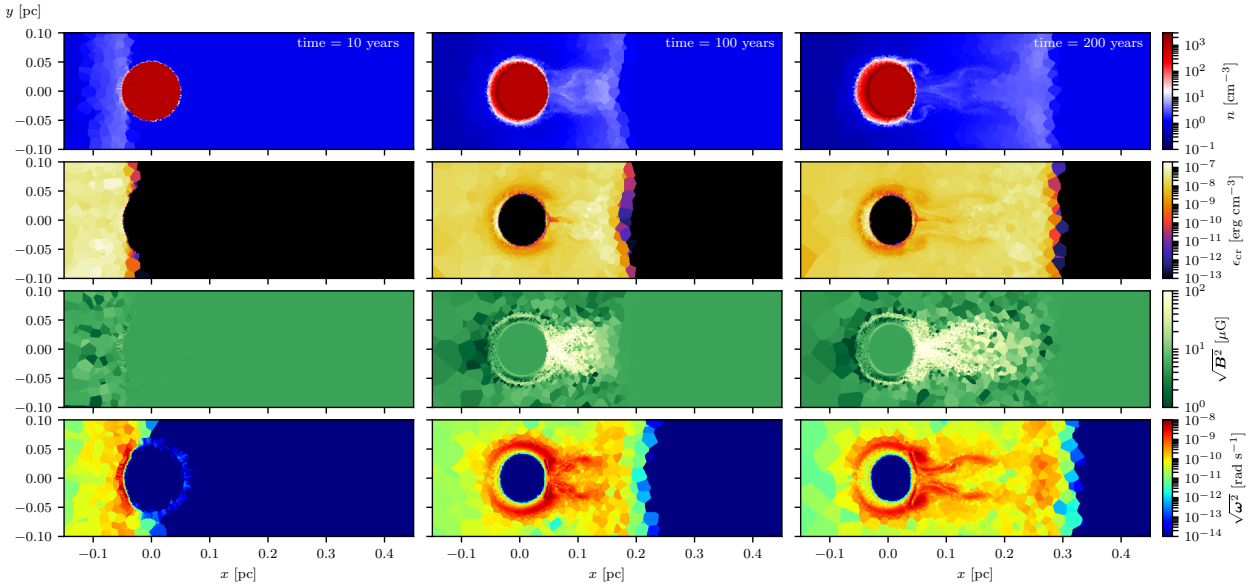

Figure 4.5.: Snapshots of the shock-cloud interaction at $t = 10, 100$ and 200 yrs after the collision for a density contrast of $\delta = 10^3$. For each time we show slices of the gas density (top row), CR energy density (second row), magnetic field strength (third row) and magnitude of the vorticity (fourth row).

4.5.2. Interaction of a shock with a dense clump

Because of momentum conservation, the SNR shock penetrates much slower in the dense clump in comparison to the shock velocity in the dilute medium outside the clump and thus, only a fraction of dense gas inside these objects is accelerated at a given time. To investigate the mass fraction η that is processed by the shock, we conduct simulations with clumps of different density ($n_c = \{10^2, 10^3, 10^4\}$ cm^{-3}). To accurately describe the dynamics, we resolve the cloud with 1.5×10^5 particles within a radius of 0.05 pc. We place the cloud in a shock-tube of length 2 pc and density of $n_0 = 1$ cm^{-3}. The shock is set to propagate in the x direction with initial density and pressure jumps so that the initial shock velocity is $v_s = 5000$ km s^{-1}. Different snapshots of the shock-cloud interaction for a density contrast of $\delta = 10^3$ are reported in Fig. 4.5.

When the supernova blast wave impacts a dense structure at some constant (oblique) angle, it experiences the same "shock deflection" and amount of entropy injection along the shock front because only the parallel velocity component is reduced by the compression ratio while the perpendicular component is conserved. If the blast wave encounters a dense, curved structure, the incoming velocity experiences a different amount of deflection along the shock surface (perpendicular to the shock normal), which injects vorticity according to Crocco's theorem (1937). This vorticity is injected at the length scale of the clump and cascades to smaller scales with increasing distance from the shock. The shock in the dilute phase closes in after passing the clump and eventually straightens up as it closes the dip at the location of the clump after about 100 years (see Fig. 4.5). While the shock front propagates seemingly undisturbed at larger distances from the clump, it has dramatically slowed down inside the clump as a result of momentum conservation.

The relic of such a complex history of the shock evolution is a highly turbulent tail in the downstream of the clump, which is able to drive a small-scale turbulent dynamo that amplifies the magnetic field there. This behavior is consistent with the lower resolution simulation of the entire SNR presented in top right panel of Fig. 4.2, where a system of uniformly distributed clumps leave several magnetized finger-like structures after the collision with the blast wave.

The interaction of a shock with a spherical object has been previously studied by Pfrommer & Jones (2011) for a low-density bubble, the results of which can also be applied to the case of a dense clump by exchanging the rarefaction wave with a reverse shock characteristics that propagates in the opposite direction of the original shock. Solving the Riemann problem in this case, we can relate the initial shock speed $v_{\rm s0}$ in the dilute phase to the shock speed $v_{\rm sc}$ propagating inside the clump. The dilute and the clump phases have the same initial pressure P_0 while the sound speeds of the dense and dilute media are related by $c_{\rm c} = \sqrt{\gamma P_0/\rho_{\rm c}} = c_0/\sqrt{\delta}$. The equation for a left reverse shock condition (Toro, 2009) reads:

$$v_* = v_{\rm L} + (P_{\rm L} - P_*)\sqrt{\frac{2}{\gamma_{\rm L}+1}\left[\rho_{\rm L}\left(P_* + \frac{\gamma_{\rm L}-1}{\gamma_{\rm L}+1}P_{\rm L}\right)\right]^{-1/2}} \tag{4.17}$$

where the subscript "$*$" denotes the state behind the reverse shock while the subscript L represents the state ahead of the reverse shock. Introducing the Mach number ratio $\mu = \mathcal{M}_{\rm c}/\mathcal{M}_0 = \sqrt{\delta}\, v_{\rm sc}/v_{\rm s0}$, assuming $\gamma_0 = \gamma_{\rm c} = 5/3$, and combining the various jump conditions (see eq. (B1) in Appendix B of Pfrommer & Jones 2011 with subscript L = 3) we find an equation for μ as a function of the Mach number $\mathcal{M}_0$ in the dilute phase and the density contrast δ:

$$\begin{aligned} 1 =& \sqrt{\delta}\mu - \mu\mathcal{M}_0^2\left(\sqrt{\delta} - \mu\right) \\ &+ \mu\left(\mu^2 - 1\right)\mathcal{M}_0^2\sqrt{\frac{\delta\left(\mathcal{M}_0^2+3\right)}{\left(4\mu^2+1\right)\mathcal{M}_0^2 - 1}}, \end{aligned} \tag{4.18}$$

which has a numerical solution for μ given $\mathcal{M}_0$ and δ. In the regime of strong shocks (i.e., $\mathcal{M}_0 \gg 1$) Eq. (4.18) is reduced to the simpler form:

$$\mu = (1-\mu^2)\sqrt{\frac{\delta}{4\mu^2+1}} + \sqrt{\delta} \tag{4.19}$$

For $\delta \gg 1$ Eq. (4.19) can be easily solved and has the positive root $\mu = \sqrt{6}$. In order to account for multi-dimensional effects of order unity, we introduce a factor $f_{\rm d}$ that we calibrate on our three-dimensional (3D) simulations and write the solutions as $\mu = f_{\rm d}\sqrt{6}$. Because $\mu = \sqrt{\delta}\, v_{\rm sc}/v_{\rm s0}$ we conclude that $v_{\rm sc} \propto \delta^{-1/2} v_{\rm s0}$. We confirm the applicability of this scaling behavior in 3D simulations by fitting the appropriate power law to the shock tube simulation of the three different density contrasts (see Fig. 4.6). The theoretically expected scaling matches the simulations within the variance of the shock velocity, however the pre-factor found in our 3D simulations is closer to 1.2 rather than 2, which means that $f_{\rm d} \simeq 1/2$. A comparison between

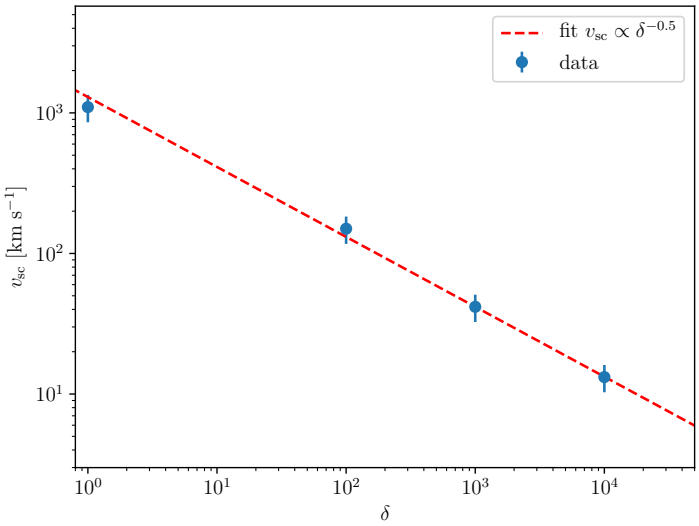

Figure 4.6.: Simulated shock velocity v_{sc} inside a dense clump as a function of the density contrast for the cases $\delta = [10^2, 10^3, 10^4]$. The point for $\delta = 1$ represents the shock velocity in the dilute phase. Within the uncertainty, the simulation points follow the $\delta^{-1/2}$ scaling behaviour derived in Eq. (4.19).

1D runs and 3D runs for density contrasts of 10^2, 10^3 and 10^4 is shown in Fig. 4.7. In the following formulas to construct the analytical model for the gamma-ray luminosity we will apply the 3D pre-factor rather than the 1D prediction.

4.5.3. Constructing the analytical model

To calculate the mass fraction of the clump that is processed by the shock, we proceed as follows. We follow the shock-wave propagation inside the clump and calculate the amount of shocked gas inside the clump as a function of time. We define the shock-processed clump mass fraction $\eta(t)$ as the ratio between the shocked gas mass of the dense clump and its total mass as a function of time.

A shock propagates in a shock-tube with the velocity $\propto t^{-1/3}$ as predicted by the 1D Sedov problem while a 3D blast wave evolves according to $t^{-3/5}$. In the latter case we integrate the velocity to obtain the shock propagation length inside the clump as a function of time:

$$\begin{aligned} r(t, t_0) &= f_\mathrm{d} \sqrt{\frac{6}{\delta}} \int_{t_0}^{t} v_{s0}(t') \mathrm{d}t' \\ &= f_\mathrm{d} \sqrt{\frac{6}{\delta}} \left(\frac{E_\mathrm{SN}}{\alpha \rho_0} \right)^{1/5} [t^{2/5} - t_0^{2/5}] \end{aligned} \tag{4.20}$$

which is valid for $t_0 < t < t_c(t_0)$, where t_0 is the time of the supernova shock impacting the clump and t_c is the crossing time of the shock inside the clump, which can be obtained from the requirement that the shock propagation length

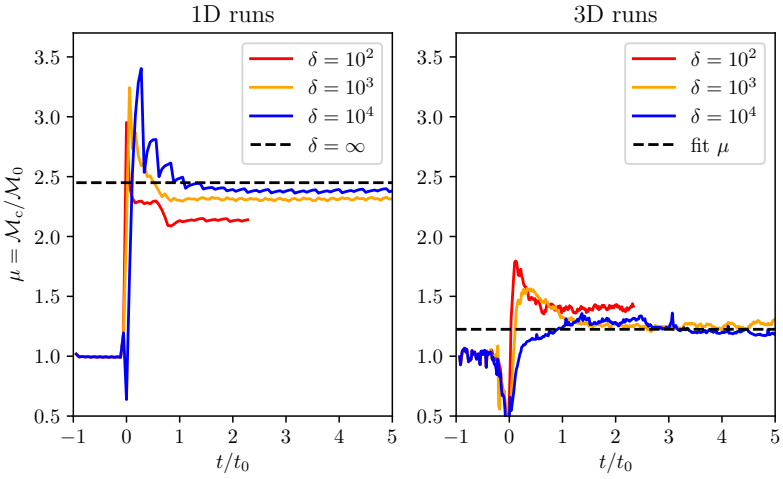

Figure 4.7.: Mach number ratio evolution after the interaction with a dense region for various density contrasts. *Left*: the 1D shocktube runs show a good agreement with the theoretical value reported in Eq. (4.19) (dashed line). *Right*: the 3D runs show a lower pre-factor with respect to the 1D theoretical estimate. The case with $\delta = 10^2$ is interrupted in both case by the finite size of the clumpy region.

has to be smaller than the size of the clump,

$$t_c(t_0) = \left[\frac{2R_c}{f_d\sqrt{6}}\delta^{1/2}\left(\frac{E_{SN}}{\alpha\rho_0}\right)^{-1/5} + t_0^{2/5}\right]^{5/2}. \tag{4.21}$$

This means that for typical values, the shock propagation length in the clump is

$$r(t, t_0) = 0.064 \text{ pc} \left(\frac{\delta}{10^3}\right)^{-1/2}\left(\frac{n}{0.1 \text{ cm}^{-3}}\right)^{-1/5} \tag{4.22}$$

for $t = 1$ kyr and $t_0 = 500$ yr. We can determine the volume of the shocked material inside the clump using Eq. (4.20) as the height of a polar cap as a function of time, while neglecting the curvature of the shock inside the clump. The ratio between the shocked polar cap volume of the clump and its total volume reads

$$\eta(t, t_0) = \frac{V_{cap}}{V_{tot}} = \frac{\pi/3 \times r^2(3R_c - r)}{4\pi/3 \times R_c^3} = \frac{r^2(3R_c - r)}{4R_c^3}, \tag{4.23}$$

where $r = r(t, t_0)$ and we used the fact that the clump density is constant. Eq. (4.23) represents the mass fraction accelerated by the shock as a function of time. For $r(t, t_0) = 2R_c$ we set $\eta(t, t_0) = 0$ to indicate that the clump is either destroyed by MHD instabilities or emptied of CRs.

Assuming that a uniform spatial distribution of clumps is overrun by a self-similar quasi-spherical blast wave, it is clear that the shock interacts at different times with individual clumps. This implies that the innermost clumps close to the explosion site have a higher fraction of shocked mass in comparison to clumps at the periphery. For this reason we have to weight Eq. (4.23) with a distribution of clumps that interact with the shock per unit time. Assuming that the number

of clumps is large so that the continuum limit applies, the number of clumps that start to interact with the SNR shock is given by

$$\begin{aligned}\dot{N}(t) &= \frac{\mathrm{d}N(t)}{\mathrm{d}t} = \frac{\langle\rho_c\rangle}{M_\mathrm{c}}\frac{\mathrm{d}V_s(t)}{\mathrm{d}t} = \frac{4}{3}\pi\frac{\langle\rho_c\rangle}{M_\mathrm{c}}\frac{\mathrm{d}[r_s^3(t)]}{\mathrm{d}t} \\ &= \frac{1.7}{\mathrm{yr}}\left(\frac{t}{1\ \mathrm{kyr}}\right)^{1/5}\left(\frac{\langle\rho_c\rangle}{M_\odot\mathrm{pc}^{-3}}\right)\left(\frac{M_\mathrm{c}}{M_\odot}\right)^{-1}\end{aligned} \tag{4.24}$$

In the last step, we assume the Sedov-Taylor regime for the SNR because the fraction of volume swept-up in the free expansion phase is only about 0.3% of the final volume and it encompasses only less than 20 clumps for our setup. Using Eqs. (4.23) and (4.24) the average efficiency $\eta(t)$ weighted by the number of interacting clumps per unit time for a SNR reads

$$\begin{aligned}\bar{\eta}(t) &= \frac{\int_0^t \dot{N}(t')\eta(t,t')\mathrm{d}t'}{\int_0^t \dot{N}(t')\mathrm{d}t'} \\ &\simeq \left\{\frac{1}{52\tilde{r}^{9/4}(t,\delta,n)} + 7\tilde{r}^{2/3}(t,\delta,n)\right\}^{-1},\end{aligned} \tag{4.25}$$

where

$$\tilde{r}(t,\delta,n) = 0.25\left(\frac{\delta}{10^3}\right)^{-1/2}\left(\frac{n}{0.1\ \mathrm{cm}^{-3}}\right)^{-1/5}\left(\frac{t}{1\ \mathrm{kyr}}\right)^{2/5}. \tag{4.26}$$

Results for different values of δ are plotted in Fig. 4.8. For $\delta = 3\times10^3$ and $t = 2.5$ kyr we find $\eta(t) \simeq 32\%$, which is slightly higher than the value found in the simulation (around 30%). To obtain the gamma-ray luminosity $\mathcal{L}_\gamma = 4\pi D^2\mathcal{F}_\gamma$ due to hadronic CR proton interactions, we separately calculate the contributions from the dilute phase and the clouds and then add them together:

$$\mathcal{L}_\gamma = \int s_{\pi^0\to\gamma}\mathrm{d}V = \mathcal{L}_{\gamma,\mathrm{d}} + \mathcal{L}_{\gamma,\mathrm{c}}, \tag{4.27}$$

where $s_{\pi^0\to\gamma}$ is the neutral pion-decay source function (Pfrommer & Enßlin, 2004). The contribution from the dilute phase is given by

$$\mathcal{L}_{\gamma,\mathrm{d}} = 5.3\times10^{32}\left(\frac{W_\mathrm{p}}{10^{50}\ \mathrm{erg}}\right)\left(\frac{\langle n\rangle}{0.1\ \mathrm{cm}^{-3}}\right)\frac{\mathrm{ph}}{\mathrm{s}}, \tag{4.28}$$

where W_p the total proton energy integrated over the whole SNR volume and $\langle n\rangle$ is the volume averaged number density, which approximately coincides with the number density on the dilute phase due to the negligible volume filling factor of the dense clumps, $f_V = V_\mathrm{c}/V = 2.4\times10^{-4}$ for our parameters. The gamma-ray luminosity associated to the clumped gas is:

$$\begin{aligned}\mathcal{L}_{\gamma,\mathrm{c}} &= \int s_{\pi^0\to\gamma}\mathrm{d}V_\mathrm{c} = \int s_{\pi^0\to\gamma}f_V\mathrm{d}V \\ &= 1.6\times10^{32}\left(\frac{\bar{\eta}(t)}{30\%}\right)\left(\frac{f_V}{10^{-4}}\right)\left(\frac{n_\mathrm{c}}{10^3\ \mathrm{cm}^{-3}}\right)\left(\frac{W_\mathrm{p}}{10^{50}\ \mathrm{erg}}\right)\frac{\mathrm{ph}}{\mathrm{s}}\end{aligned} \tag{4.29}$$

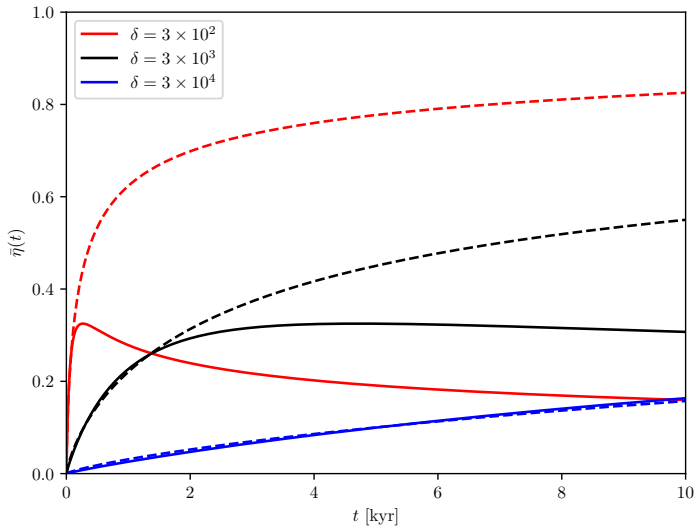

Figure 4.8.: Evolution of $\bar{\eta}(t)$ for different values of $\delta = 3 \times [10^2, 10^3, 10^4]$ for $n = 0.42$ cm^{-3}. The lines represent the theoretical values calculated via Eq. (4.25). Although an increasing number of clumps are hit by the shock the slowdown of the blast wave transfers a decreasing amount of momentum to the clumps leading to an ideal asymptotic value for $\bar{\eta}(t)$. The dashed lines represent the case where the clumps are not destroyed and continue to be active sources of CRs.

where V_c is the volume occupied by the clumps and $\bar{\eta}(t)$ is the average fraction of the shocked clump volume fraction inside the remnant volume. In our setup we set $n_c = 1.4 \times 10^3 \mathrm{cm}^{-3}$. Combining Eqs. (4.28) and (4.29) we get

$$\begin{aligned} \mathcal{L}_\gamma &= \mathcal{L}_{\gamma,\mathrm{s}} + \mathcal{L}_{\gamma,\mathrm{c}} \\ &= 5.3 \times 10^{32}(1+\chi) \left(\frac{W_\mathrm{p}}{10^{50}\ \mathrm{erg}}\right) \left(\frac{n}{0.1\ \mathrm{cm}^{-3}}\right) \frac{\mathrm{ph}}{\mathrm{s}} \end{aligned} \tag{4.30}$$

where

$$\chi = 0.3 \left(\frac{\bar{\eta}(t)}{30\%}\right) \left(\frac{f_V}{10^{-4}}\right) \left(\frac{n_c}{10^3\ \mathrm{cm}^{-3}}\right) \left(\frac{n}{0.1\ \mathrm{cm}^{-3}}\right)^{-1}. \tag{4.31}$$

It is easy to verify that Eq. (4.12) is equivalent to Eq. (4.31) because of the following identity:

$$f_V n_c = \frac{f_V \rho_c}{\mu_\mathrm{H} m_\mathrm{p}} = \frac{\langle \rho_c \rangle}{\mu_\mathrm{H} m_\mathrm{p}} \tag{4.32}$$

In terms of normalized quantities the previous equation becomes:

$$\left(\frac{f_V}{2.4 \times 10^{-4}}\right) \left(\frac{n_c}{1.4 \times 10^3\ \mathrm{cm}^{-3}}\right) = \left(\frac{\langle \rho_c \rangle}{1.6 \times 10^{-2} M_\odot \mathrm{pc}^{-3}}\right). \tag{4.33}$$

4.6. SNR expanding into a stellar wind

Here, we study how different assumptions of the circumstellar medium (CSM) affect the evolution of a SNR and its morphological appearance at gamma-ray

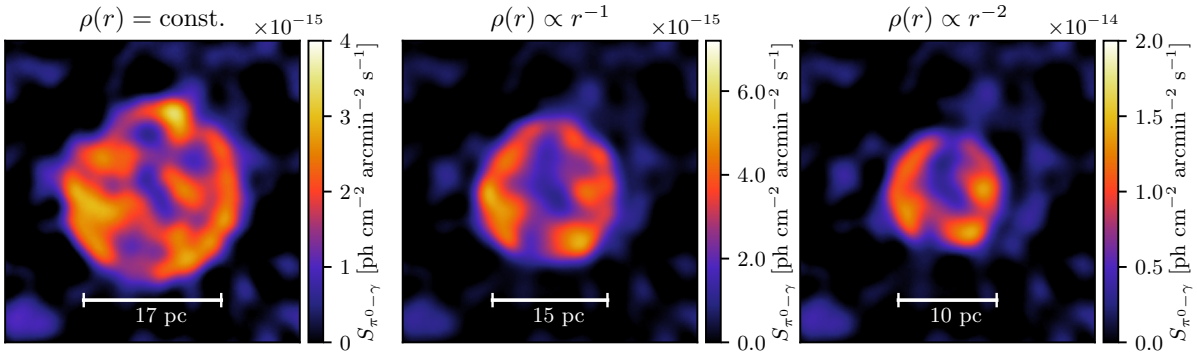

Figure 4.9.: Synthetic γ-ray maps of Vela Jr., which result from simulations of a blast wave expanding into a stellar wind profile. To account for the uncertainties, we adopt different wind density profiles and a purely turbulent magnetic field of coherence scale $\lambda_B = 13$ pc. The panels show SNRs that propagate in a constant density medium (left), in a density profile $\rho \propto r^{-1}$ (middle) and $\rho \propto r^{-2}$ (right) at the same age and same mean density. As expected, the higher central density slows down the expanding shock, modifies the morphology into a more compact emission region, which however maintains the shell-type morphology.

energies. Studies of SNR evolution into stellar-wind-blown environments range from the initial free-expansion phase (Soderberg et al., 2010; Kamble et al., 2014; Fransson et al., 2015) to the self-similar Sedov phase (Landecker et al., 1999).

The Vela Jr. SNR is thought to be associated with a core-collapse supernova explosion (Wang & Chevalier, 2002), which results from the collapse of a massive star of mass $M \geq 8M_\odot$. The particularities of the progenitor are responsible for the evolution of the SNR in a highly modified wind-blown CSM shell, causing a substantially different evolution from the classical sequence of free expansion followed by a Sedov and a radiative stage (Dwarkadas, 2005). As pointed out by Chevalier (1982) and Ostriker & McKee (1988), a SNR that interacts with a CSM density profile $\rho(r) \propto r^{-q}$ has a self-similar analytical solution for the evolution of shock radius and velocity:

$$r_\mathrm{s}(t) = A^{\frac{1}{5-q}} t^{\frac{2}{5-q}}, \tag{4.34}$$

$$v_\mathrm{s}(t) = \frac{2}{5-q} A^{\frac{1}{5-q}} t^{\frac{q-3}{5-q}}, \tag{4.35}$$

where A is a constant depending on the ambient average density, the SN energy and the adiabatic index. Here, $q = 2$ corresponds to the case of constant mass loss from the progenitor star.

We simulate supernova explosions in three different power-law wind profiles with $q \in \{0, 1, 2\}$. To ease comparison we adopt the same average number density for all simulations as reported in Table 5.1. All other initial simulation parameters for the energy and the turbulent magnetic field remain unchanged. We evaluate the SNR simulations at the same age, which emphasizes the effect of a denser central CSM for steeper power-law indices. In order to avoid a non-vanishing magnetic divergence during the generation of the initial density profile, we cap the density in the central cells with a Plummer-type softening length of $r_\mathrm{c} = 0.3$ pc.

The wind speed v_w ranges from values of order $(1000 - 3000)$ km s^{-1} for very young SNRs (Abbott, 1978) to 100 km s^{-1} or less for red-giant stars. Hence, we can neglect v_w in comparison to the shock velocity during the early Sedov phase (Ostriker & McKee, 1988), which means that the approximation of assuming a point explosion in the various density profiles is fully justified and does not affect the final simulation result. This causes the remnant to directly enter the Sedov stage and to bypass the earlier phase of a swept-up wind-blown shell.

In Fig. 4.9 we show simulated gamma-ray maps of Vela Jr. for the three different CSM environments. The primary effect of a stratified wind density profile consists of slowing down the propagating blast wave. This results in a more compact and brighter gamma-ray morphology. Many of the general morphological features of the patchy gamma-ray map previously found for the constant density solution carry over to the stratified density profiles. However, the higher central number density in comparison to the flat profile increases the gamma-ray brightness, with a flux enhancement by a factor of six for the $q = 2$ profile, as expected for the evolution of these profiles at early times (Kirk et al., 1995). Thus, comparing our simulated maps to the observed shell-type morphologies at these ages, this argues for more shallow density profiles $|q| < 1$, with slight preferences for a constant density medium for the SNRs studied here.

4.7. Discussion and Conclusions

We have presented the first global simulations and gamma-ray maps of SNRs in the hadronic model, which account for magnetic obliquity-dependent CR acceleration. We show that the multi-frequency spectrum in the hadronic and mixed hadronic/leptonic models match observational data for our simulation parameters of the ISM, which are motivated by observations.[1] Our synthetic gamma-ray maps match the apparently disparate TeV morphologies and total gamma-ray fluxes of SNR 1006 and Vela Jr. within a single physical model extremely well: SN1006 expands into a homogeneous magnetic field that is reminiscent of conditions for a galactic outflow or a large-scale Parker loop as supported by its Galactic height of $z = 0.6$ kpc (at $D \simeq 1.8$ kpc) above the midplane (Stephenson & Green, 2002). On the contrary, Vela Jr. is embedded in a small-scale turbulent field typical of spiral arms. This suggests that the diversity of shell-type TeV SNRs originates in the obliquity dependence of the acceleration process rather than in density inhomogeneities.

Comparing our simulations of different λ_B to observed TeV maps of shell-type SNRs enables us to estimate λ_B of the unperturbed ISM before it encountered the SNR blast wave. Assuming statistical homogeneity, we constrain λ_B in the vicinity

[1] We note that the purely leptonic scenario can also match the multi-frequency data of our SNRs (SN1006, H.E.S.S. Collaboration 2010; Vela Jr., H.E.S.S. Collaboration 2018b). We will address the interesting question whether three-dimensional MHD simulations with obliquity dependent electron acceleration can produce radio, X-ray and gamma-ray maps in the leptonic model that match observational data in future work.

of SN1006 and Vela Jr. to $> 200^{+50}_{-40}$ pc and $13^{+13}_{-4.3}$ pc, respectively. Simulating the SN explosion that expands into a stratified density profile caused by a stellar wind produces similarly patchy gamma-ray maps and hence does not alter our conclusions that magnetic obliquity-dependent CR acceleration is responsible for this patchy morphology. However, at the same mean density, the blast wave will encounter a denser CSM at small radii, which slows down the propagating blast wave and results in a more compact and brighter gamma-ray map at the same age.

If obliquity-dependent diffusive shock acceleration also applies to electrons, we could produce similar synthetic TeV maps in the leptonic model to constrain the magnetic coherence length. If electron acceleration were independent of magnetic obliquity then this work would provide strong evidence for the hadronic scenario in shell-type SNRs as the necessary element to explain the patchy TeV emission. In any case, we conclude that the inferred coherence scales are robust to specific assumptions of the gamma-ray emission scenario (hadronic vs. leptonic models).

Moreover, here we show that the hadronic model is able to explain shell-type SNR morphologies, which naturally emerge in our simulations due to the peaked density at the shock in combination with the slowly decreasing CR pressure profile (Pais et al., 2018). In the leptonic model, fast electron cooling would have to confine the emission regions close to the shock. However, this would imply strong spectral softening towards the SNR interior, which is not observed in Vela Jr., seriously questioning the leptonic model for this SNR (H.E.S.S. Collaboration, 2018b). Our work opens up the possibility of mapping out the magnetic coherence scale across the Milky Way and other nearby galaxies at the locations of TeV shell-type SNRs, and to study how it varies depending on its vertical height or its location with respect to a spiral arm. Thus, our work represents an exciting new science case for gamma-ray astronomy, in particular for the Cherenkov Telescope Array.

5. Simulating TeV gamma-ray morphologies of shell-type supernova remnants

This chapter is an adapted version of the paper *Simulating TeV gamma-ray morphologies of shell-type supernova remnants* submitted on Monthly Notices of Royal Astronomical Society.

Abstract

Supernova remnant (SNR) shocks provide favourable sites of cosmic ray (CR) proton acceleration if the local magnetic field direction is quasi-parallel to the shock normal. Using the moving-mesh code AREPO we present a suite of SNR simulations with CR acceleration in the Sedov-Taylor phase that combine different magnetic field topologies, density distributions with gradients and large-scale fluctuations, and – for our core-collapse SNRs – a multi-phase interstellar medium with dense clumps with a contrast of 10^4. Assuming the hadronic gamma-ray emission model for the TeV gamma-ray emission, we find that large-amplitude density fluctuations of $\delta\rho/\rho_0 \gtrsim 75$ per cent are required to strongly modulate the gamma-ray emissivity in a straw man's model in which the acceleration efficiency is independent of magnetic obliquity. However, this causes strong corrugations of the shock surface that are ruled out by gamma-ray observations. By contrast, magnetic obliquity-dependent acceleration can easily explain the observed variance in gamma-ray morphologies ranging from SN1006 (with a homogeneous magnetic field) to Vela Junior and RX J1713 (with a turbulent field) in a single model that derives from plasma particle-in-cell simulations. Our best-fit model for SN1006 has a large-scale density gradient of $\nabla n \simeq 0.0034$ cm^{-3} pc^{-1} pointing from south-west to north-east and a magnetic inclination with the plane of the sky of $\lesssim 10°$. Our best-fit model for Vela Junior and RX J1713 adopts a combination of turbulent magnetic field and dense clumps to explain their TeV gamma-ray morphologies and moderate shock corrugations.

5.1. Introduction

Ions are believed to be accelerated to relativistic energies at astrophysical shocks, which gives rise to the observed CR population in the Galaxy (Hillas 2005, Blasi 2013 for a review). In particular, the process of diffusive shock acceleration (Axford

et al., 1977; Krymskii, 1977; Blandford & Ostriker, 1978; Bell, 1978a,b) enables particles to gain energy through multiple shock crossings as they scatter back and forth on magnetic field irregularities. The emerging non-thermal spectrum follows a universal power-law momentum spectrum (Bell, 1978a; Blandford & Ostriker, 1978). Supernova explosions and subsequently formed remnant shocks are considered to be ideal environments for acceleration because of the large spatial extent and lifetime that provides sufficient confinement to reaching high energies (Ghavamian et al., 2013; Neronov, 2017). The most energetic CRs are able to escape upstream the shock and propagate to larger distances in the interstellar medium (ISM) while less energetic CRs are advected downstream and only released at a later time (Bell et al., 2013).

Evidence for efficient acceleration of CR electrons is provided by the observation of elongated but narrow X-ray synchrotron filaments that are aligned with the shock surface such as in Tycho (Hwang et al., 2002; Warren et al., 2005; Cassam-Chenaï et al., 2007), Vela Jr. (Bamba et al., 2005), or SN1006 (Bamba et al., 2003; Katsuda et al., 2010), see also Parizot et al. (2006) for an overview. Modelling the emission requires fast electron synchrotron losses in a strongly amplified magnetic field in the upstream (Morlino et al., 2010, for the case of SN1006), which is likely realised through the non-resonant hybrid instability (Bell, 2004; Caprioli & Spitkovsky, 2014b), providing indirect evidence for efficient proton acceleration. This evidence is further strengthened by multi-wavelength analyses that take into account the SNR evolution, hydrodynamics of the shock (assuming spherical symmetry), magnetic field amplification and the dynamical backreaction of CRs and self-generated magnetic turbulence on the shock (Berezhko et al., 2003; Zirakashvili & Aharonian, 2010; Morlino & Caprioli, 2012). The total density jump as measured from far upstream to the downstream exceeds the canonical limit of four (for an ideal gas with adiabatic index 5/3) due to the increased compressibility of the additional relativistic pressure of CRs (Chevalier, 1983; Castro et al., 2011; Caprioli & Spitkovsky, 2014a; Pfrommer et al., 2017a). This implies a smaller distance between the contact discontinuity (CD) and the forward shock (FS) as observed in Tycho (Warren et al., 2005) as well as in SN1006 (Cassam-Chenaï et al., 2008), where this CD-FS distance shows a distinctive azimuthal variation such that it is shorter in the polar cap regions, which show efficient amplification of the magnetic field due to efficient CR proton acceleration (in part, the CD-FS distance is reduced by the Rayleigh-Taylor instability of the CD).

Of particular interest is the very high energy (VHE) gamma-ray emission from SNRs in the GeV and TeV regimes (Hillas, 2005), which directly probes the CR component without the need to model the magnetic field. Exceptional examples are shell-type SNRs, such as SN1006, Vela Jr. and RX J1713-3948.5 (RX J1713 for short). Gamma-ray emission associated with these objects can be produced in two different models (Gabici & Aharonian, 2016; Marcowith et al., 2016). In the hadronic model π^0 mesons are produced in inelastic CR-gas interactions and decay into pairs of gamma rays (Caprioli, 2011). In the leptonic model the gamma-ray radiation arises from a combination of inverse Compton scattering of the cosmic microwave background (CMB) and starlight photons off of the accelerated CR

electrons and non-thermal bremsstrahlung. Following the CR electron spectrum in three-dimensional MHD simulations of SNRs and modelling the multi-frequency spectrum and emission maps from the radio to gamma-rays suggests that the GeV gamma-ray regime has a significant leptonic contribution while the TeV range is dominated by hadronic gamma rays (Winner et al., 2020).

The leptonic model naturally produces hard gamma-ray spectra while such a spectrum can also be obtained in the hadronic model when considering a clumpy ISM. Magnetic insulation of these dense clumps only allows high-energy CR protons to penetrate into the dense regions, which implies a substantial hardening of the proton spectrum in comparison to the acceleration spectrum in the diffuse ISM (Gabici & Aharonian, 2014; Celli et al., 2019). Combining synchrotron and inverse Compton fluxes in the leptonic model produces volume-filling magnetic field strengths of $\approx (10-35)\,\mu$G (Gabici & Aharonian, 2016; Winner et al., 2020). These are only in agreement with mG-field strengths inferred from X-ray synchrotron filaments when assuming a clumpy medium, arguing for a detailed study of SNR emission maps. By contrast, many previous studies focused on matching the multi-frequency spectra with spherically symmetric models of the SNR evolution and neglecting the diversity of morphological appearances of the observed shell-type SNRs.

In fact, the orientation of the upstream magnetic field plays an important role in the acceleration process. Self consistent hybrid particle-in-cell (PIC) simulations show that a quasi-parallel configuration is much more efficient in accelerating CR protons in comparison to a quasi-perpendicular shock geometry (Caprioli & Spitkovsky, 2014a). These PIC simulations also show that the maximum acceleration efficiency of CR protons is limited to ≈ 15 per cent. The idea that the resulting emission could depend on the direction of the magnetic field in the X-ray band has also been discussed (Rothenflug et al., 2004). In our previous papers (Pais et al., 2018, 2020; Winner et al., 2020), we find that the global topology of the magnetic field is fundamental in reproducing the diversity of observed gamma-ray emission that ranges from a bi-lobed to a patchy morphology. While an approximately homogeneous magnetic field produces a bi-lobed gamma-ray emission, a turbulent field manifests itself in a patchy emission characteristics. In this scenario, gamma-ray bright regions result from quasi-parallel shocks which are known to efficiently accelerate CR protons, and gamma-ray dark regions point to quasi-perpendicular shock configurations. In the case of an extremely small magnetic correlation length the emission approaches an isotropic emission, albeit with a reduced effective acceleration efficiency (Pais et al., 2018).

The interaction of a supernova explosion with a gas cloud has been explored in various works (Chevalier, 1974; Korolev et al., 2015) and more recently with highly-evolved individual explosions (Zhang & Chevalier, 2019). In particular, interstellar turbulence and its effect on CR acceleration (Scalo & Elmegreen, 2004) has been the subject of various studies in the past years (Elmegreen & Scalo 2004 for a review). Simulations of single SNe have been performed in an inhomogeneous ISM (Walch & Naab, 2015) as well as in the presence of a clumpy circumstellar medium (Obergaulinger et al., 2014; Pais et al., 2020). The clumpiness of the medium is

often assumed to be the sole source of irregularity of the emission morphology, especially for strongly asymmetric distributions of heavy elements like Si and Fe in the surroundings of SNRs as confirmed by XMM-Newton measurements (Li et al., 2015).

Following the spirit of this work, we simulate how an inhomogeneous medium affects and regulates the TeV gamma-ray morphology of SNRs in the Sedov-Taylor phase. We perform our simulations with various magnetic field configurations combined with magnetic obliquity-dependent shock acceleration. In order to infer morphological properties of the ambient medium of observed SNRs, we compare the resulting emission maps, radial and azimuthal profiles with three well-known examples of shell-type SNRs such as SN1006, Vela Jr. and RX J1713. For simplicity we use an initial setup of a point explosion that evolves into the Sedov-Taylor solution. The gamma-ray emission from the resulting SNR is then computed using a hadronic model of decaying pions. Our goal is to find a consistent model that simultaneously explains the detailed gamma-ray spectrum as well as the morphological variance of the TeV gamma-ray emission maps.

This chapter is organised as follows. In Section 5.2 we present the methodology used to prepare our initial conditions for the various models with particular focus on the generation of an initial turbulent density and magnetic field. In Section 5.3 we present our suite of SNR simulations with different combinations of magnetic fields (homogeneous and turbulent) and density distributions (homogeneous, with a gradient, turbulent and a combination of a gradient and turbulence), yielding a wide range of different morphologies. For comparison, we also test a straw man's model of an isotropic acceleration scenario (i.e., independent of magnetic obliquity). In Section 5.4 we compare the observed gamma-ray map, radial and azimuthal profiles of SN1006 with our simulations for different degrees of turbulence and inclinations of the field of view and infer properties on the local ISM. In Section 5.5 we compare radial and azimuthal profiles of turbulent SNRs Vela Jr. and RX J1713 to the models with a turbulent magnetic field and a non-obliquity dependent acceleration for various density setups. In Section 5.6, we study the effect of strong density fluctuations on the gamma-ray morphology of a core-collapse SNR in its early Sedov stage. In Section 5.7, we show that we can match the gamma-ray spectra of all three SNRs for our adopted parameters and summarise the main findings and conclude in Section 5.8.

5.2. Methodology

Here we present our methodology and briefly explain the procedure used to implement obliquity dependent CR acceleration, the turbulence in the ISM and in the initial magnetic field. Results of this setup are shown in Section 5.3.

5.2.1. Simulation method

The simulations presented in this chapter are performed with the massively parallel, adaptive moving mesh-code AREPO (Springel, 2010). We use an improved second-order hydrodynamic scheme with the least squares-fit gradient estimate and a Runge-Kutta time integration (Pakmor et al., 2016b). Ideal MHD is used to model the magnetic fields (Pakmor & Springel, 2013) while zero-divergence is enforced through the implementation of a Powell scheme (Powell et al., 1999). CRs are modelled as a relativistic fluid with a constant relativistic adiabatic index of 4/3 in a two-fluid approximation (Pfrommer et al., 2017a).

Shocks are localised and characterised using the method developed by Schaal & Springel (2015), where Voronoi cells that exhibit a maximally converging velocity field along the direction of propagation of the shock are selected, while spurious shocks and numerical noise are filtered out. We inject CR energy into the Voronoi cells in the immediate post-shock regime of shock above a critical Mach number of $\mathcal{M} > 3$ (Pfrommer et al., 2017a).

Following the results of hybrid PIC simulations performed in Caprioli & Spitkovsky (2014a) we assume a maximum CR energy efficiency of 15 per cent for quasi-parallel shocks. On the contrary quasi-perpendicular shocks are found to be extremely inefficient accelerators. The efficiency of the injected CRs is computed using the orientation of the pre-shock upstream magnetic field (Pais et al., 2018).

The presence of a strong current associated with streaming CRs into the upstream region causes an exponential growth of the magnetic fluctuations via the non-resonant hybrid instability (Bell, 2004). These amplified fluctuations saturate at wave amplitudes corresponding to the strength of the mean magnetic field and cause the CR scattering mean free path to decrease to values comparable with the fluctuating gyroradius. This regime approaches the Bohm limit of diffusion. On scales resolved by our simulations, we neglect CR diffusion and streaming. To justify this approach we assume Bohm diffusion and calculate the CR precursor length for SNRs considered in this work and find

$$L_{\rm prec} \sim \sqrt{\kappa_{\rm Bohm} t_{\rm age}} \simeq \\ \simeq 0.3 \text{ pc} \left(\frac{\langle pc \rangle}{10 \text{ TeV}}\right)^{1/2} \left(\frac{B}{10 \mu\text{G}}\right)^{-1/2} \left(\frac{t_{\rm age}}{10^3 \text{yr}}\right)^{1/2}, \tag{5.1}$$

where $\langle pc \rangle$ is the average energy associated with the protons that emit TeV gamma rays through the inelastic proton-proton reaction, B is the root-mean-square of the upstream magnetic field and $t_{\rm age}$ is the age of the remnant. The resulting precursor length is below the size of our numerical resolution $\Delta x = 0.4$ pc, assuming a simulation box size of 40 pc that is filled with 100^3 cells. Energy losses of accelerated CRs escaping upstream from the blast wave do not affect the validity of the self-similar solution of the problem, causing only a negligible softening of the Sedov-Taylor solution (Bell, 2015). On the SNR timescales simulated, the hadronic and Coulomb loss time scales are negligibly small so that we only account for adiabatic CR losses.

5.2.2. Initial conditions

By analogy with Pais et al. (2018), we start with a random Voronoi mesh that is regularised into a glass-like configuration via Lloyd's algorithm (Lloyd, 1982). We inject the equivalent of $E_{\rm SN} = 10^{51}$erg of thermal energy in the central cell of a 100^3-cell periodic box with a side length of $L = 40$ pc. The resulting explosion forms an energy-driven strong shock expanding in an ISM characterised by a low pressure of 0.44 eV cm^{-3}, and a mean molecular weight of $\mu = 1.4$.

Magnetic field setup

To generate a turbulent magnetic field we follow the procedure by Ruszkowski et al. (2017) and Pais et al. (2018). We adopt a Kolmogorov-like power spectrum for the magnetic field and generate the three magnetic vector components independently in Fourier space such that the resulting field exhibits a random phase. We ensure that $\boldsymbol{B}$ is divergence-free by projecting out the radial field component in Fourier space. The degree of turbulence is determined through the fraction f_B of magnetic energy which goes into turbulent modes, yielding

$$B^2_{\rm tot}(\boldsymbol{x}) = B^2_0 + B^2_{\rm turb}(\boldsymbol{x}) = B^2_0 \left[1 - f_B + f_B \delta \boldsymbol{b}^2(\boldsymbol{x})\right], \tag{5.2}$$

where $B_0 = \sqrt{\boldsymbol{B}^2_0}$ represents the strength of the mean field, $\delta\boldsymbol{b} = \delta\boldsymbol{B}/B_0$ is a Gaussian random field, the turbulent energy fraction obeys $0 \leq f_B \leq 1$ and $\boldsymbol{x} = (x, y, z)$ is the spatial vector. We adopt a plasma beta factor of $\beta = 1$ such that the magnetic and thermal pressures are insignificant in comparison to the kinetic energy of the propagating shock front. To maintain hydrostatic equilibrium in the initial conditions, magnetic fluctuations $\delta\boldsymbol{B}(\boldsymbol{x})$ are compensated by adopting temperature fluctuations of the form $nk_B\delta T(\boldsymbol{x}) = -\delta\boldsymbol{B}^2(\boldsymbol{x})/(8\pi)$. The small magnetic field strength implies a small Alfvén speed so that the tension force is only slowly mediated and does not affect the dynamics of our powerful shock wave.

ISM density setup

We model the multiphase structure of the ISM and adopt a combination of (i) a large-scale linear density gradient, (ii) large-scale turbulent density fluctuations that follow a Kolmogorov spectrum, and (iii) a population of small, dense gaseous clumps with a typical overdensity of 10^4 in comparison to the ambient ISM.

The large-scale density gradient $\rho_{\rm grad}$ is determined by the constant density ρ_0 and the slope parameter Δ. Similarly to the magnetic field, we generate turbulent density fluctuations in Fourier space and vary the initial seed, the correlation length and the amplitude of fluctuations $\rho_{\rm turb}(\boldsymbol{x}) = \rho_0\delta\rho(\boldsymbol{x})$. To avoid negative values for the density we adopt a density floor of $10^{-2}\rho_0$. All these elements are combined as follows:

$$\begin{aligned}\rho(\boldsymbol{x}) =& \rho_0 + \rho_{\rm turb}(\boldsymbol{x}) + \rho_{\rm grad}(\boldsymbol{x}) = \rho_0\left[1 + \delta\rho(\boldsymbol{x})\right] \\ &+ \rho_2\left[\left(\frac{x}{L} - \frac{1}{2}\right)\cos\psi + \left(\frac{y}{L} - \frac{1}{2}\right)\sin\psi\right],\end{aligned} \tag{5.3}$$

where L is the side length of our simulation box, ψ represents the angle between the direction of the density gradient and the $x-$axis, $\delta\rho(\boldsymbol{x})$ is the generating functional of the turbulent field, $\rho_2 = \sqrt{2}\Delta\rho_0/(1+\Delta)$ is the amplitude of the gradient such that $\rho = \rho_0(1+\rho_0\delta\rho)$ for $\Delta = 0$ in case of a vanishing gradient. The function $\rho_{\rm grad}(\boldsymbol{x})$ is constructed such that there are no negative values for the density in the simulation box for any $x, y \in [0, L]$ and $\Delta \in [0, \infty)$. To avoid low-density cavities in the surroundings of the central explosion, we shield the region with a constant homogeneous density of $\rho = \rho_0$ extending for a radius of 2 pc.

In order to reliably model the circum-stellar medium of our core-collapse SNRs, we include a population of dense gaseous clumps with a typical size of 0.1 pc and a number density of $\sim 10^3 {\rm cm}^{-3}$ (Inoue et al., 2012). Following the same setup as in Pais et al. (2020) and Celli et al. (2019), we include 7×10^3 uniformly distributed small, dense clumps with a number density of $n_{\rm c} = 10^3$ cm^{-3} and a diameter of 0.1 pc of a total target mass of $M_{\rm c} = 45 M_\odot$ engulfed by the shock.

This flexible setup allows us to study a wide range of different situations and environments by modifying the amplitude of the density fluctuations, their coherence scale and steepness of the gradient as well as their multi-phase nature of thermally unstable dense clumps in the star-forming surroundings of core-collapse SNRs.

5.2.3. Modelling gamma-ray emission and noise

To model the gamma-ray emission in post-processing we assume that the CR population follows a universal power law momentum spectrum. A pion-decay hadronic model is used to calculate the omni-directional gamma-ray emissivity (Pfrommer & Enßlin, 2004; Pfrommer et al., 2008) which depends on the local ISM density, the local CR population, the very-high energy (i.e. > 1 TeV) photon spectral index α_γ, and the energy range.

To compute the emission spectra of our simulations we integrate a particle population described by a power law in momenta with cutoff. The hadronic gamma-ray emission spectrum is calculated from parametrizations of the cross section of neutral pion production at low and high proton energies, respectively (Yang et al., 2018b; Kelner et al., 2006).

In order to match the morphological properties of the observed gamma-ray emission maps we proceed with an analysis of the power spectrum of the noise. We fit the power spectrum with a specific function, convert it into a noise map. This noise map is then superposed on the mock gamma-ray emission map that was convolved with the observational point spread function (PSF). We will detail the method to generate the noise properties in Section 5.4.

5.3. Exploring fluctuations in density and the magnetic field

Using the previously described setup here we present a suite of twelve SNR simulations (each with 100^3 cells) and combine different topologies of the magnetic field

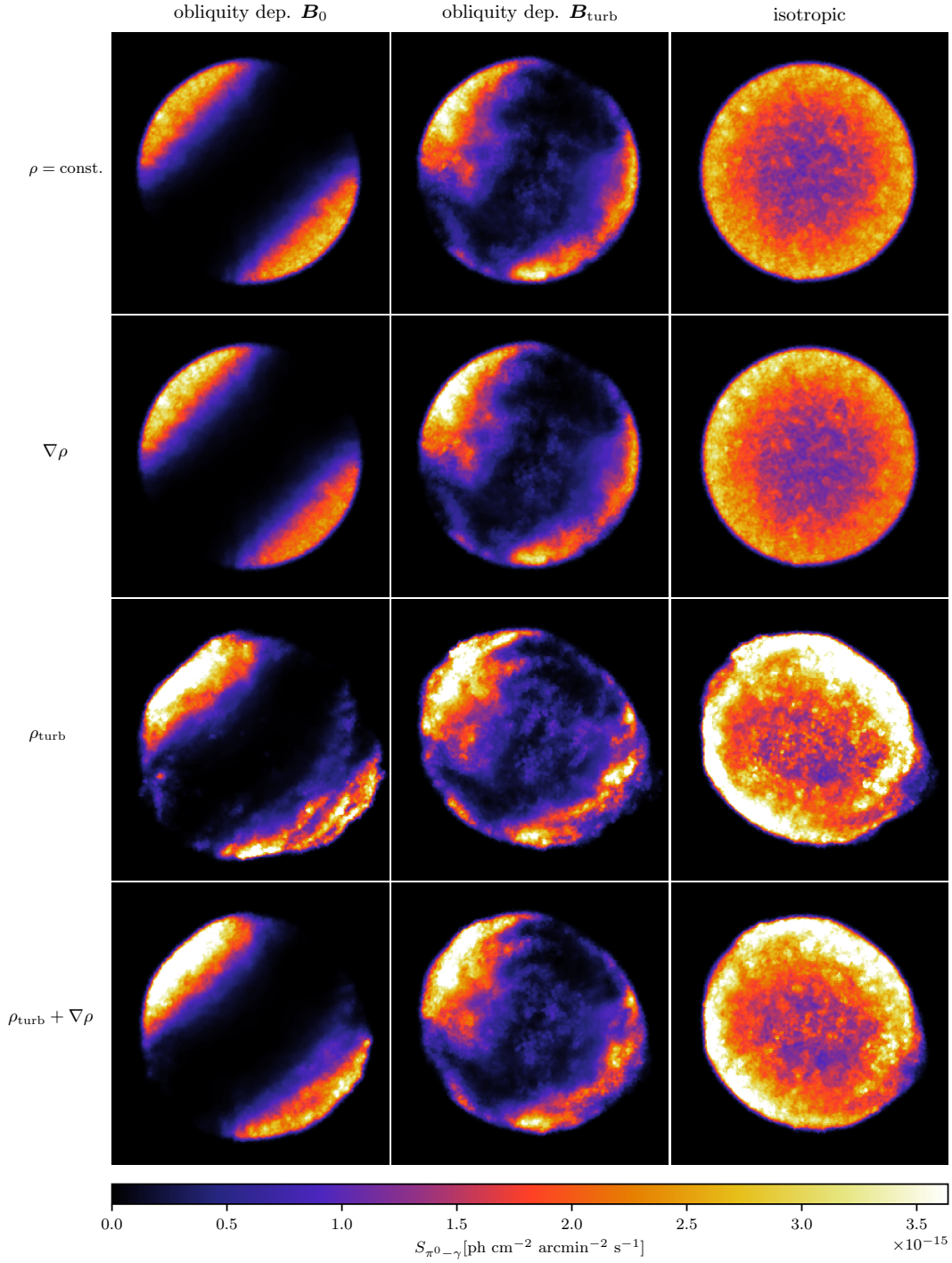

Figure 5.1.: Impact of inhomogeneities density and magnetic field on the gamma-ray maps of SNRs in the Sedov-Taylor phase at $t_{\rm age} = 10^3$yr with side length $L = 40$ pc. The images are ordered according to their different initial conditions: the columns represent different magnetic field configurations and acceleration models, the rows represent different density distributions. The first two columns assume magnetic obliquity dependent CR acceleration at a homogeneous magnetic field (left) and a fully turbulent fluctuations of relative amplitude $f_B = 1$ and coherence length $\lambda_B = 20$ pc (middle) while the third column shows simulations with a turbulent field ($\lambda_\rho = 20$ pc) but with an isotropic CR acceleration model. We adopt a different density distribution in each row: constant density (first row), an increasing gradient pointing from SW to NE (second row), turbulent density fluctuation (third row) and a combination of turbulence and a gradient (fourth row).

and different density distributions. We also compare models of obliquity-dependent CR acceleration to isotropic CR acceleration. The gamma-ray emission maps in the energy range $1 - 80$ TeV with a spectral index of $\alpha = 2.1$ are shown in Fig. 5.1 at a SNR age of $t = 1000$ yrs. The images are not convolved with a PSF and we do not add noise in order to maintain the underlying setup as transparent as possible.

For these theoretical models we chose a simple setup both for the density and the magnetic field. We start by separately considering the components of the density distribution of Eqn. (5.3). For the background density we select a value of $n = 0.1$ cm^{-3}. The density gradient has an inclination of $\psi = 135°$ with respect to the x-axis, i.e., it is pointing from south-west (SW) to north-east (NE) and exhibits a moderate gradient intensity of $\Delta = 1$ to avoid a strong contrast between the upper-left quadrant and the bottom-right one. For the turbulence we chose turbulent fluctuations of $f_\rho = \delta\rho/\rho_0 = 0.5$ and a coherence scale of $\lambda_\rho = L/2$ for our box size $L = 40$ pc. To avoid any correlation between magnetic and density fluctuations in our turbulent simulations, we used two distinct but fixed random seeds, respectively.

5.3.1. Density fluctuations

In the first column of Fig. 5.1 we show the models for a constant magnetic field oriented with an angle of $\theta = 135°$ with respect to the positive x-axis. The effect of the obliquity-dependent shock acceleration in presence of an ordered magnetic field is manifested in the bi-lobed morphology of the gamma-ray emission. The presence of a moderate gradient in the second and fourth row results in NE lobe brighter than the SW lobe as expected in the presence of more ISM material on which the shock impinges so that the freshly accelerated CR protons find more target gas in a hadronic scenario.

5.3.2. Magnetic turbulence

In the central column of Fig. 5.1 we show the effect of a fully turbulent magnetic field ($f_B = 1$) that is superposed on different density distributions. As expected, the obliquity-dependent shock acceleration allows the creation of a patchy distribution of the brightness echoing the distribution of the underlying locally accelerated CR population (Pais et al., 2020). In particular, the combination with a turbulent density distribution (Fig. 5.1, third row, centre) is responsible for a noticeable modulation of the gamma-ray intensity and explains the bright spot in the lower right corner close to the remnant shell, an absent feature in the constant density map (Fig. 5.1, first row, centre).

As expected in an isotropic acceleration scenario (Fig. 5.1, right column) the gamma-ray emissivity shines along the entire SNR shell and is only mildly modulated by local or large-scale variations related to the particular density distribution used in the simulation. Contrarily to the obliquity-dependent case for turbulent fields depicted in the central column, a considerable amount of emission is still present in the centre of the remnant.

For isotropic models the emission in the centre is at least twice as strong as the turbulent case. This is caused by the efficient CR acceleration in the isotropic model so that the emission is projected onto the central parts of the SNR. By contrast, in the obliquity-dependent scenario for the turbulent magnetic case we obtain a patchy structured emission with bright spots in regions with a quasi-parallel shock geometry and dark regions in locally quasi-parallel shocks geometries. On average the acceleration process for medium to large scale turbulence is 70 per cent less efficient with respect to the non obliquity dependent case (Pais et al., 2018). This results in a stronger dispersion of the brightness and a lower average absolute emissivity in the centre. Note that observational noise and the presence of a population of cold-dense clumps in a multi-phase ISM may play an important role and needs to be taken in consideration for the morphological modelling of observed shell-type SNRs.

It is clear that the isotropic acceleration model fails to reproduce both the emission morphologies (lobes and filaments) and the strong azimuthal variation in the emission of SN1006. Despite a significantly varying amplitude of density fluctuations of 50 per cent, the azimuthal variation in the isotropic-acceleration runs does not drop sufficiently to create clearly defined filamentous structures in the shell. High-amplitude turbulence in the ISM on scales comparable to the size of the remnant might be a solution and could potentially mimic a bi-lobed structure. We will come back to this point in Section 5.6 and will show that the almost spherically symmetric blast waves of the SNRs studied here put a strong constraint on the level of large-scale inhomogeneity of the surrounding ISM.

5.4. Morphological modelling of SN 1006

In the following two sections, we use our intuition developed in our parameter study in Fig. 5.1 to find the most promising combination of magnetic and density inhomogeneities in the obliquity-dependent acceleration scenario to mock the observed gamma-ray emission morphology of shell-type SNRs. To this end, we analyse the bi-lobed morphology of Type Ia SN1006 in this section and present our analysis of the two shell-type core-collapse SNRs Vela Jr. and RX J1713 in Section 5.5.

The gamma-ray excess map of SN1006 reported by the H.E.S.S. Collaboration (2010) strongly correlates with the synchrotron X-ray emission map and suggests an emitting region compatible with a thin shell. The peculiar polar cap geometry in the emission is also observed in other wavelengths such synchrotron X-ray emission, indicating an acceleration process compatible with efficient quasi-parallel shock acceleration (Winner et al., 2020). Polarimetric radio observations of the limbs strongly suggests that the ambient field is aligned along the SE−NW direction (Reynoso et al., 2013), as later confirmed by recent theoretical models (Schneiter et al., 2015). Moreover in Pais et al. (2020) is shown that the correlation length of the magnetic field in case of pure turbulence is at least 15 times the angular size of the SNR and consistent with a homogeneous field across the SNR.

All these models used a setup involving a homogeneous ISM. However, if the

Table 5.1.: Comparison of simulation and observational parameters for the presented hadronic morphological models.

	SN1006		**Vela Jr.**		**RX J1713**	
Parameter	**Simulation**	**Observed**	**Simulation**	**Observed**	**Simulation**	**Observed**
diameter θ_s [deg]	0.5	0.5	2	2	1	1
D [kpc]	1.79	$1.45 - 2.2$	0.5	$0.2 - 0.75$	1	$0.5 - 1$
diameter d_s [pc]	15.6	$12.6 - 19.2$	17.4	$7.0 - 26.1$	17.4	$8.7 - 17.4$
t_{age} [kyr]	1	1	2.7	$2.4 - 5.1$	3	$1 - 7.9$
E_{SN} [10^{51} erg]	1	–	1	–	1	–
density n [cm^{-3}]	0.1	$0.05 - 0.3$	0.42	$0.03 - 1$	0.57	$0.02 - 1$
∇n [cm^{-3}pc^{-1}]	0.0034	–	–	–	0.02	–
M_c [$M_\odot$]	–	–	45	–	45	–
$\langle v_s \rangle$ [km s^{-1}]	3000	$2100 - 4980$	2000	$> 1000 - 3000$	1100	$800 - 3900$
$\mathcal{F}_\gamma(> 1\text{TeV})$ [10^{-12}ph cm^{-2} s^{-1}]	0.4	0.39 ± 0.08	24	23.4 ± 5.6	16.3	16.3 ± 0.2
$\alpha_{p,e}$	1.95	1.79 ± 0.44	1.81	1.85 ± 0.24	1.7	1.52 ± 0.31
$E_{p,cut}$[TeV]	200	–	100	–	90	–
$E_{e,cut}$[TeV]	1.7	–	0.25	–	0.25	
β_p	2	–	2	–	2	–
β_e	0.7	–	0.4	–	0.4	–
References	1, 2, 6, 8, 9, 10, 13, 21		2, 3, 4, 8, 10, 14, 16, 17, 19		5, 7, 8, 11, 12, 15, 19, 20	

Notes: n denotes the diffuse ISM number density, ∇n is the large-scale density gradient, M_c is the target clump mass hit by the remnant, D is the distance to the SNR, θ_s and d_s are the angular and proper extent of the blast wave, $\langle v_s \rangle$ denotes the shock velocity, t_{age} is the SNR age and $\mathcal{F}_\gamma$ is the integrated gamma-ray flux above 1 TeV. References: (1) Acero et al. (2007) ; (2) Acero et al. (2015); (3) Allen et al. (2015); (4) Aschenbach et al. (1999); (5) Celli et al. (2019); (6) Dubner et al. (2002); (7) Federici et al. (2015); (8) Green (2014); (9) H.E.S.S. Collaboration (2010); (10) H.E.S.S. Collaboration (2018b); (11) H.E.S.S. Collaboration (2018a); (12) Inoue et al. (2012); (13) Katsuda et al. (2008); (14) Katsuda (2017); (15) Leahy et al. (2020); (16) Ming et al. (2019); (17) Slane et al. (2001); (18) Takahashi et al. (2008) (19) Tanaka et al. (2011); (20) Tsuji & Uchiyama (2016); (21) Winkler et al. (2003).

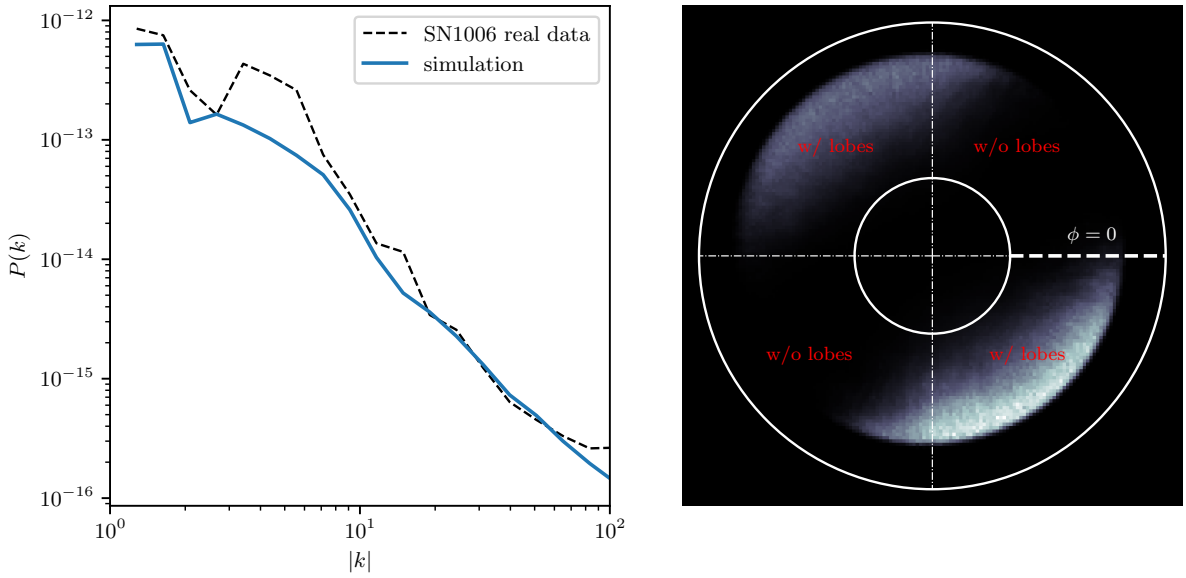

Figure 5.2.: Left: Comparison of the noise power spectra of the observed emission map of SN1006 (H.E.S.S. Collaboration, 2010) with the signal regions masked and of the simulated gamma-ray map of SN1006 with a turbulent density fraction of $\delta\rho/\rho_0 = 0$. This shows that our modelled noise nicely corresponds to the observed noise properties. Right: Sketch of the area used for calculating the azimuthal and the radial profiles of the simulated models. We average the gamma-ray emission in the radial range $2/3 < r/\langle r_s \rangle < 4/3$ to obtain the azimuthal profile while the lobe regions are used to compute the radial profiles for SN1006.

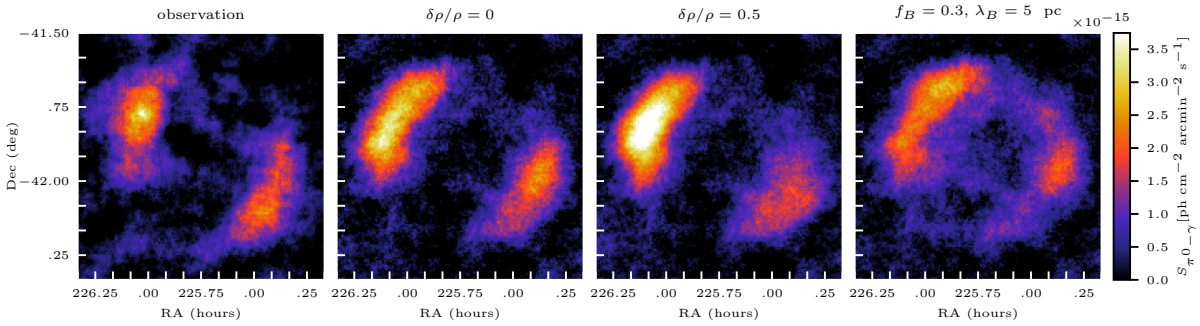

Figure 5.3.: Two-dimensional projected gamma-ray maps for SNR SN1006 and for three simulation models with a fixed density gradient and different amplitudes of turbulent density fluctuations. The second and third panels show the simulated maps for $f_\rho = 5$ pc and $\delta\rho/\rho = 0$ and 0.5, respectively, while the rightmost panel shows the map for $f_B = 0.3$, $\lambda_B = 5$ pc and $\delta\rho/\rho = 0$. The emission in the simulated maps is smoothed with a Gaussian PSF of width $\sigma = 0.045°$. On the top of it, we add Gaussian noise with the power spectrum inferred from HESS data, as shown in Fig. 5.2, at fixed random seed.

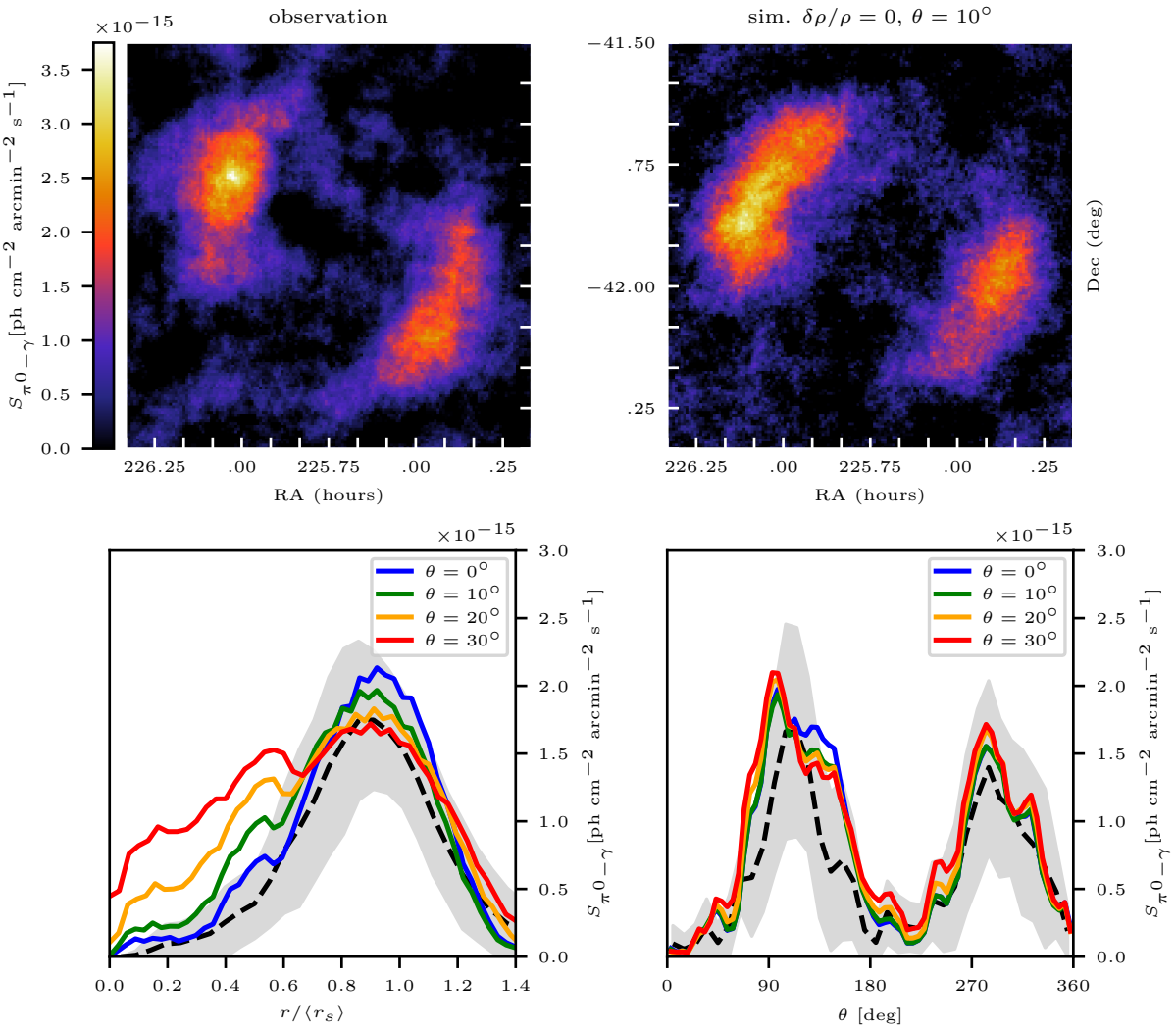

Figure 5.4.: Top left: emission map of SN1006 (H.E.S.S. Collaboration, 2010). Top right: our best match for SN1006 without density fluctuations and a rotation angle $\theta = 10°$. Bottom left: radial profiles of the surface brightness. Profiles of the best match for $\theta = [0°, 10°, 20°, 30°]$ are reported for comparison with the observed one (black dashed line). The grey-filled areas represent the standard deviations of the observed radial profiles, respectively. The more strongly inclined cases ($\theta = 20°$ and $\theta = 30°$) fail to reproduce the declining emission inside and outside the maximum. Bottom right: Comparison of simulated azimuthal profiles of SN1006 and observed data (black dashed line) with standard deviation (grey). While there is broad agreement between the models and observation, the NE cap (at around 90°) is narrower in the HESS observation.

TeV gamma-ray emission is mainly from hadronic sources, the brighter NE lobe suggests the presence of a large scale density gradient pointing from SW to NE. Furthermore, the small-scale brightness variations at the outer shock radius could either be caused by (i) density inhomogeneities in the ISM that would corrugate the shock upon colliding with these inhomogeneous structures or (ii) by obliquity-dependent shock acceleration in combination with small-scale turbulent magnetic field superposed on a homogeneous magnetic field. We will study the impact of both effects on the gamma-ray surface brightness maps in the presence of a large-scale density gradient.

5.4.1. Simulation model

We proceed with a suite of simulations with the same large-scale density gradient but with different setups for the density and magnetic field topology. We conducted a number of exploratory simulations to test the steepness of the gradient in order to faithfully reproduce the different TeV gamma-ray brightness of the two lobes and match the measured fluxes reported in H.E.S.S. Collaboration (2010). For the average value of the density and SNR distance we used the same values reported by the Pais et al. (2020). With reference to Eq. (5.3) we used $\psi = 135°$ for the orientation and $\Delta = 0.9$ for the density slope. In physical units this corresponds to a density gradient of $\nabla n \simeq 0.0034$ cm^{-3} pc^{-1} pointing from SW to NE, which means that in the NE region the average ISM density is $\langle n \rangle \sim 0.12$ cm^{-3} while in the SW rim we find $\langle n \rangle \sim 0.08$ cm^{-3}. Initially, we adopt a homogeneous magnetic field 5 μG throughout the simulation domain.

Our baseline model does not adopt turbulent density and magnetic fluctuations. Our second model assumes turbulent density fluctuations with a amplitude $\delta\rho/\rho \sim 0.5$ and coherence scale $\lambda_\rho = 5$ pc. Finally, our third model has no turbulent density fluctuations, but adopts magnetic turbulence with $f_B \sim 0.3$ and coherence scale $\lambda_B = 5$ pc. We simulated and evolved our SN1006 model for 1010 yrs, constructed the pion-decay gamma-ray surface brightness map resulting from hadronic CR interactions and convolved it to the observational PSF of width $\sigma = R_{68}/1.515 = 0.042°$, with $R_{68} = 0.064°$ (H.E.S.S. Collaboration, 2010). All other parameters used for the simulations are reported in Table 5.1.

5.4.2. Noise modelling

In order to disentangle physical effects that generate small-scale brightness fluctuations from spurious instrumental effects, we need to accurately model the instrumental noise. Here, we explain our procedure of generating such a noise map for our synthetic gamma-ray emission maps. To this end, we calculate the noise power spectrum of the excess map of SN1006 and exclude the emission of the NE and SW lobes. This is done by masking the original excess map from the H.E.S.S. Collaboration (2010) with a sharp cutoff equal to $c_{\rm cut} = |c_{\rm min}|$ where $c_{\rm min} = -20$ is the minimum value of the excess counts. The power spectrum of SN 1006 is obtained via a 2D Fourier transform of the masked data set. The noise power spectrum

presents two features: (i) a large scale Gaussian-like noise as expected from the PSF convolution of the instrument, and (ii) a small scale power law $\propto k^{-2}$ extending to higher modes. We fit the power spectrum with the following function in k-space:

$$P(k) = A \exp\left(-\frac{k^2}{2\sigma_k^2}\right) + Bk^{-2} \tag{5.4}$$

where, σ_k represents the standard deviation in k-space and the variables A and B determine the relative strength of the Gaussian and the power-law tail. The black dashed line in Fig. 5.2 shows the measured noise power spectrum of the SN1006 excess map in comparison to the simulated noise (blue line). We assume that the noise is fully characterised by two-point correlations and obtain a random realisation of the noise via 2D inverse Fourier transform. This noise map is then superposed on the mock gamma-ray emission map that was convolved with the observational point spread function (PSF).

5.4.3. Simulated TeV emission

We show the resulting synthetic maps of SN 1006 in comparison to the original excess map in Fig. 5.3. We report three gradient models with the following assumptions (from left to right): (i) no density fluctuations, (ii) density fluctuations with $\delta\rho/\rho = 0.5$ and no magnetic field fluctuations, and (iii) magnetic field fluctuations with $\delta B/B = 0.3$ and no density inhomogeneities. This enables us to separately analyse the effect of these configurations on the morphology of SN1006.

While our noise modelling is responsible for emission in regions where the acceleration is supposed to be extremely inefficient or absent, the density perturbations are able to corrugate and smooth the boundaries of the lobes, in particular of the SW lobe for the chosen seed. The resulting picture appears with a defined bi-lobed structure and an increasing level of turbulence in the medium causes the emergence of secondary morphological details. We notice that density perturbation of $\delta\rho/\rho = 0.5$ (third picture of Fig. 5.3) affect the morphology of the SW lobe resulting in a fainter surface brightness and a broader shape. This suggests that our preferred model for SN 1006 in the TeV gamma-ray band is given by a model with homogeneous density.

Similarly, we observe the emergence of secondary morphological details from a moderate level of turbulence in the magnetic field (fourth picture of Fig. 5.3) in our obliquity dependent CR acceleration scenario. We compare this model with a coherence scale at $\sim 1/3$ the size of the remnant to our other two models with a homogeneous density and a moderate level of density inhomogeneities. In spite of the low level of magnetic fluctuations ($\delta B/B = 0.3$) the morphology significantly deviates from the observed bi-lobed shell-type morphology of SN1006 and shows significant substructures. In addition, this model is also ruled out by the excess of the emission in the central region of the remnant which contrasts to the clean separation of the two lobes as observed by the H.E.S.S. collaboration. This sets an approximate upper limit for the local turbulence of the magnetic field in a obliquity dependent scenario.

Another degree of freedom is the orientation of the homogeneous magnetic field $\boldsymbol{B}_0$ with respect to the line of sight. To study its influence on the emission map and (radial and azimuthal) profiles, we perform a three-dimensional (3D) rotation of the SNR around the axis perpendicular to the orientation of $\boldsymbol{B}_0$ into the line of sight. We show different inclinations ($\theta = [0°, 10°, 20°, 30°]$) of $\boldsymbol{B}_0$ with respect to the plane of the sky, similarly to Bocchino et al. (2011) for the X-ray emission to constrain the 3D orientation of the magnetic field of SN 1006. Note that this is somewhat degenerate with the assumed 3D orientation of the density gradient that we also assume to lie in the plane of the sky.

An increasing inclination results in a less pronounced peak and a broader distribution of gamma rays as the hadronic emission from the efficiently accelerated CRs at the quasi-parallel shocks changes from being limb-brightened to contributing to a broader solid angle on the sky. The top right panel in Fig. 5.4 shows our best match for SN1006 after the aforementioned rotation of the SNR. Indeed, the lobes appear slightly more diffuse, predominantly in the internal regions.

To quantify the effect of magnetic inclination we compute the radial and azimuthal profiles of our synthetic maps according to the sketch shown on the right-hand side of Fig. 5.2. The radial profiles are computed within the quadrants where quasi-parallel shock acceleration takes place while the azimuthal profiles show an average in the radial range $2/3 < r/\langle r_\mathrm{s} \rangle < 4/3$, where r_s is the average shock radius of the SNR.

The comparison of the post-rotation radial profiles to the observed radial profile of SN 1006 provides an important constraint for the maximum magnetic inclination. These profiles are show in the bottom panels of Fig. 5.4. We include a 1σ standard deviation grey-filled area to the observed SN1006 profiles. While larger inclinations ($\theta > 10°$, orange and red lines) result in emission profiles that are too extended, an inclination of $\theta \leq 10°$ is in better agreement with the observed radial profile. Barring our remark about the orientation of the density gradient, we conclude that the magnetic inclination does not exceed 10° with respect to the plane of the sky.

A minor element of discordance can be also found in the azimuthal profiles (Fig. 5.4, bottom right) for different rotation angles. While the simulated SW lobes coincide with the observed one in relative brightness and extension, the simulated NE lobe is slightly broader in comparison to the observed lobe. This suggests that the critical angle for the magnetic obliquity may be smaller than 45° inferred by recent PIC simulations. Regardless the spatial rotation all the models reproduce the observed modulation of the two lobes within the 1-σ uncertainty.

5.5. Morphological modelling of core collapse SNRs

We now turn to two other well-known SNRs with a clear shell-type morphology: Vela Jr. and RX J1713. Both SNRs are of core-collapse origin which means that the ambient ISM is a star-forming region of multi-phase, turbulent gas. We account for this by simulating the supernova explosion in a multiphase ISM with a large population of small, dense gaseous clumps with a typical overdensity of 10^4

in comparison to the ambient ISM and adopt a purely turbulent magnetic field without a mean field, $\boldsymbol{B}_0 = \mathbf{0}$.

5.5.1. Observational constraints on Vela Jr.

The H.E.S.S. Collaboration (2018b) has observed TeV gamma-ray emission from the SNR Vela Jr. (RX-J0852.0-4622) with a resolved gamma-ray spectrum. Estimates on the SNR age vary from a very young remnant of ~ 700 yrs (Aschenbach et al., 1999) to an older object of more than 5000 yrs (Katsuda et al., 2008). The SNR can be a nearby object at $D = 0.2$ kpc, as inferred from studies of the decay of ^{44}Ti nuclei (Iyudin et al., 1998), or a more distant one at $D = 0.75$ kpc, as inferred from the slow expansion of X-ray filaments (Katsuda et al., 2008). The presence of interstellar molecular clouds suggests that the origin of TeV-gamma rays from these objects is mainly hadronic (Fukui, 2013).

The lack of thermal X-ray emission places a very low limit at $n = 0.03$ cm^{-3} while assuming a homogeneous environmental density (Slane et al., 2001). However, if the ISM is composed of dense clumps that are embedded in a lower-density hot ambient phase, the resulting thermal X-ray emission (of the hot phase) is lower while the presence of the dense clumps implies a higher average density. A conventional approach in the hadronic model is to use a density of the order of $n \sim 1$ cm^{-3} (Aharonian et al., 2006), while hydrodynamic models suggest values of less than 0.4 cm^{-3} (Allen et al., 2015). More recently HI and CO measurements and partial morphological correspondence withe the TeV-gamma ray morphology indirectly suggest an extremely high average ISM density of the order of $n \sim 100$ cm^{-3} (Fukui et al., 2017). However there is no direct observational evidence that the clumped gas is in direct physical contact with the shock-accelerated cosmic rays. In fact the passage of the shock dissipates kinetic energy, heats the ions to particle energies of several keV and is directly responsible of dissociation of CO and H_2 and the ionisation of the neutral part of the clouds on a time-scale of the order of a few years (Celli et al., 2019).

As the shock overruns the magnetised ISM, magnetic fields are draped around the dense clouds, precluding the diffusion of cosmic rays deep into the cloud so that the TeV cosmic rays can only probe a narrow skin of the cloud. The penetration depth of this skin can be estimated by realising that the draped magnetic field reaches strength of order $B \approx \sqrt{8\pi\alpha\rho v^2} \approx 1$mG (Dursi & Pfrommer, 2008; Pfrommer & Jonathan Dursi, 2010) for typical parameters $\alpha = 2$, $n = 0.1$ cm^{-3}, and $v_s = 3000$ km s^{-1}. If the average ISM density were indeed 100 cm^{-3} (Fukui et al., 2017), this should yield draped magnetic field strengths of 32 mG, which should be observable via Zeeman splitting of which there is no evidence which argues against such a high average density. The skin depth of the dense cloud reachable by TeV CRs, assuming Bohm diffusion, varies from a few to several gyro radii:

$$r_g = \frac{p_\perp c}{eB} \approx 10^{-6}\ \mathrm{pc} \left(\frac{pc}{\mathrm{TeV}}\right) \left(\frac{B}{\mathrm{mG}}\right)^{-1} \tag{5.5}$$

which is negligible in comparison of the cloud size (0.1 pc). Even if the magnetic

wrap is not perfect and CRs can penetrate 100 gyro radii inside the cloud, then the fraction of the cloud volume seen by the TeV CRs is $\Delta V \sim 1-(1-10^{-3})^3 \sim 3\times10^{-3}$. Our assumed total dense cloud mass of 45 $M_\odot$ that is physically associated with the SNR is a fraction of 2×10^{-3} of the available gas mass of 2.5×10^4 $M_\odot$ (Fukui et al., 2017) towards the Vela Jr. region, some of which may be projected onto the SNR but is not physically associated to it and only a tiny fraction of the molecular and neutral gas inside the Vela Jr. SNR is seen by cosmic rays due to magnetic draping, suppressing cosmic ray propagation into the cloud before the cold gas gets ionised and dissociated. These considerations justify our assumption of only accounting for CR advection in our simulations.

In addition, not all the mass of the clumps engulfed by the shock has been processed by the shock because of the strong deceleration of the blast wave inside the clumps (see Appendix of Pais et al. 2020). Combining these arguments suggests that only a tiny fraction of the dense (neutral/molecular) phase of the ISM is in physical contact with the shock. For the magnetic field we decided to follow the same prescription used in Pais et al. (2020) setting the coherence scale of the turbulent magnetic field to $\lambda_B = 13$ pc and adopt $f_B = 1$. The entire set of parameters used in the simulation is summarised in Table 5.1.

5.5.2. Observational constraints on RX J1713

RX J1713 represents another bright TeV-emitter with a distinct shell-like emission morphology. This SNR is subject to intense studies thanks to its strong non-thermal X-ray emission and the detection of high-energy and very-high-energy gamma-rays. Wang et al. (1997) suggested that RX J1713 is linked to an AD393 guest star which, according to historical records, appeared in the tail of constellation Scorpius, close to the actual position of the remnant. This would put the age of the remnant close to 1.6 kyr. More recent estimates based on X-ray emission combined with hydro models in homogeneous media suggest an older remnant age of $6.8^{+1.1}_{-2}$kyr (Leahy et al., 2020).

The distance of the object is estimated to be around 1 kpc (Fukui et al., 2003) while Tanaka et al. (2008) suggests a distance interval between 0.5 kpc and 1 kpc. Assuming a free expansion model this translates into an upper limit of the average shock speed of about $\langle v_s \rangle = 6300$ km s^{-1}. Proper motions of bright X-ray filaments instead place the shock velocity between ~ 1000 km s^{-1} and ~ 4000 km s^{-1} (Fukui et al., 2003).

A hadronic origin of the TeV gamma-ray emission in RX J1713 was suggested in several papers (Zirakashvili & Aharonian (2010) ; Gabici & Aharonian (2014)). The distribution of gas in RX J1713 is crucial to establish the origin of the observed gamma-rays. An upper limit for the diffuse density of < 2 cm^{-3} is derived from non thermal X-rays measurements (Takahashi et al., 2008). To explain the lack of thermal X-ray emission Cassam-Chenaï et al. (2004) sets an even lower upper limit for the ambient density of $n \sim 0.02$ cm^{-3}. However, this argumentation can be circumvented by introducing a densely clumped environment.

Studies of non-thermal X-ray emission, TeV gamma-ray emission and their par-

tial spatial correlation with HI ans H2 suggest the presence of numerous dense clumps in the ISM (Fukui et al., 2003; Sano et al., 2015; Rowell et al., 2009). However the same argument used for Vela Jr. applies: the lack of direct evidence of physical contact between the gas distribution and the shock and the subsequent ionisation of HI casts doubts on its physical association with the SNR. The interaction of a blast wave with interstellar clouds and its application to RX J1713 has been studied in Inoue et al. (2012) and applied in Celli et al. (2019) for a shock wave with constant velocity interacting with a target mass of 45 $M_{\odot}$.

Recently, Tsuji & Uchiyama (2016) calculated the evolution of RX J1713 in various scenarios such as the case of an expansion in a wind-blown cavity with a typical density profile $\rho \propto r^{-2}$ and a free expansion dominated by the ejecta ($\rho_{\rm ej} \propto r^{-n}$ with $n = 7$). Here we consider simple Sedov-Taylor expansion models which represent the upper limit for the expansion of a SNR in homogeneous media (Truelove & McKee, 1999).

To reproduce the saturated NW rim of the remnant we applied a homogeneous positive large-scale gradient to the initial conditions pointing from SE to NW with $\Delta = 1.6$, corresponding to a density gradient of $\nabla n = 0.02$ cm^{-3} pc^{-1}. Superposed on this density gradient we insert a population of dense clumps of size 0.1 pc using exactly the same setup as for Vela Jr. For the magnetic field we selected a fully turbulent setup ($f_B = 1$) with a coherence length of $\lambda_B = 13$ pc, not too dissimilar from the size of the remnant (~ 17.4 pc). The entire set of parameters used in the simulation is summarised in Table 5.1.

5.5.3. Simulations

Figure 5.5 shows the comparison between the observed excess brightness maps of Vela Jr. and RX J1713 (left-hand side) and our PSF-convolved synthetic maps derived from turbulent models with density inhomogeneities and dense clumps (right-hand side). To model the noise in the post-processing we applied the same method used for SN1006. In the final step we rotate the surface brightness maps in order to approximately match the low and high emissivity outer shell regions of the observed maps. Our simulation models provide an astonishing agreement with the data.

The presence of high-density molecular clumps provides an important contribution to the global emission morphology. The effect of the clumps on RX J1713 is shown in Fig. 5.6. While we notice that the orientation of the magnetic field is mainly responsible of the patchy morphology of the outer shell the clumps add several bright spots to the map without modifying the expansion history of the SNR due to their negligible volume filling factor. A comparison with the left-hand side figure in the bottom row shows that the strong smoothing applied to the synthetic maps makes it impossible to resolve the emission originating from a single isolated clump and that clusters of bright clumps are similar to large magnetic field patches oriented quasi-parallel to the shock normal, thus enabling efficient CR acceleration.

The effect of obliquity-dependent shock acceleration is better shown in Fig. 5.7, where we compare radial and azimuthal profiles of our simulated gamma-ray maps

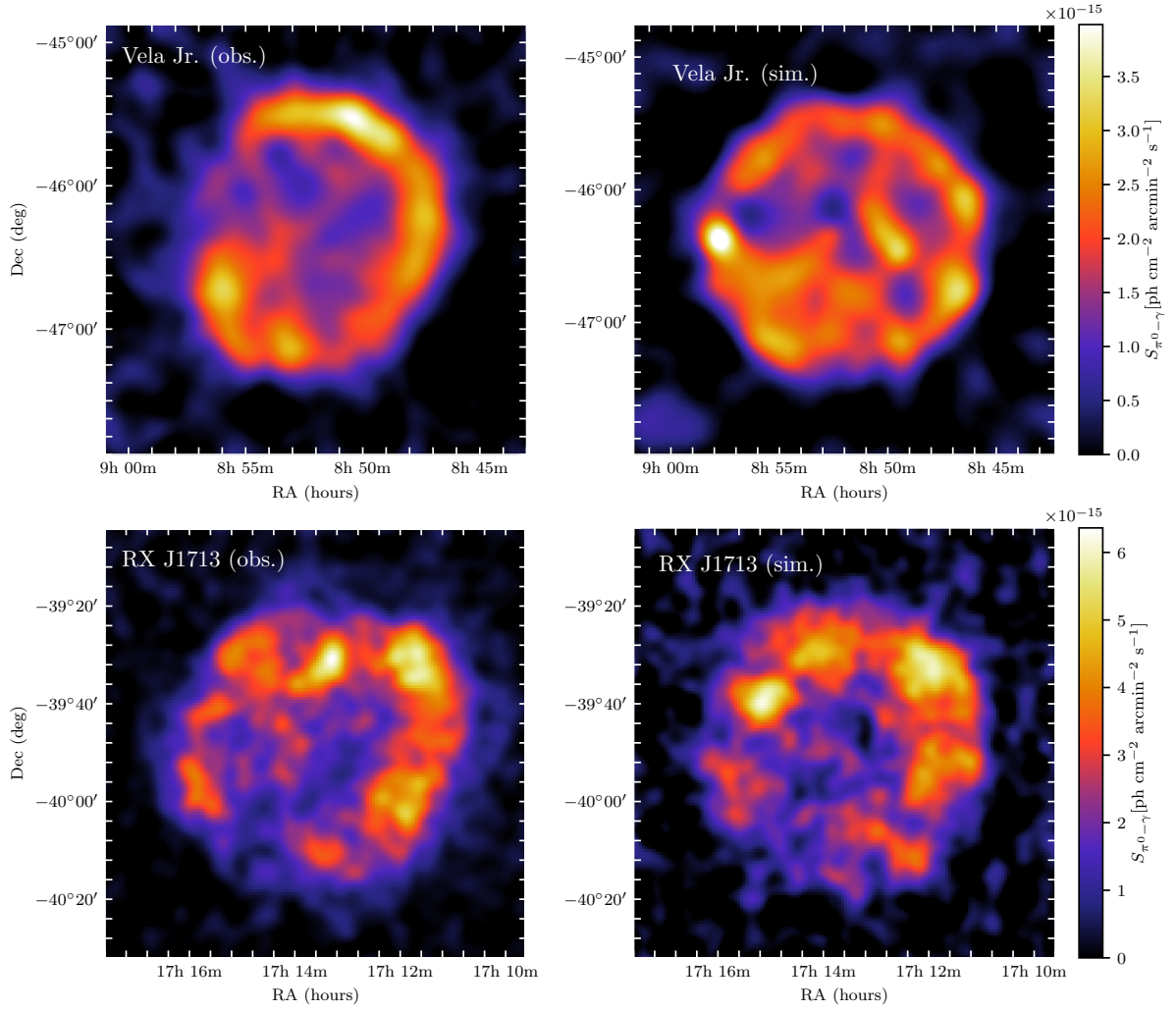

Figure 5.5.: Comparison between observed gamma-ray emission maps (left) of Vela Jr. (H.E.S.S. Collaboration, 2018b) and RX J1713 (H.E.S.S. Collaboration, 2018a) and simulated gamma-ray maps (right) of the SNRs for our model with obliquity-dependent CR acceleration, a turbulent magnetic field with $f_B = 1$ and $\lambda_B = 13$ and additionally a gradient for RX J1713 with $\Delta = 1.6$. In our simulated maps we add Gaussian noise with the observed power spectrum and use the PSFs appropriate to each observation (0.08° and 0.036° for Vela Jr. and RX J1713, respectively). We also rotated mock emission maps of the SNRs to match the azimuthal position of the faintest region in the shell.

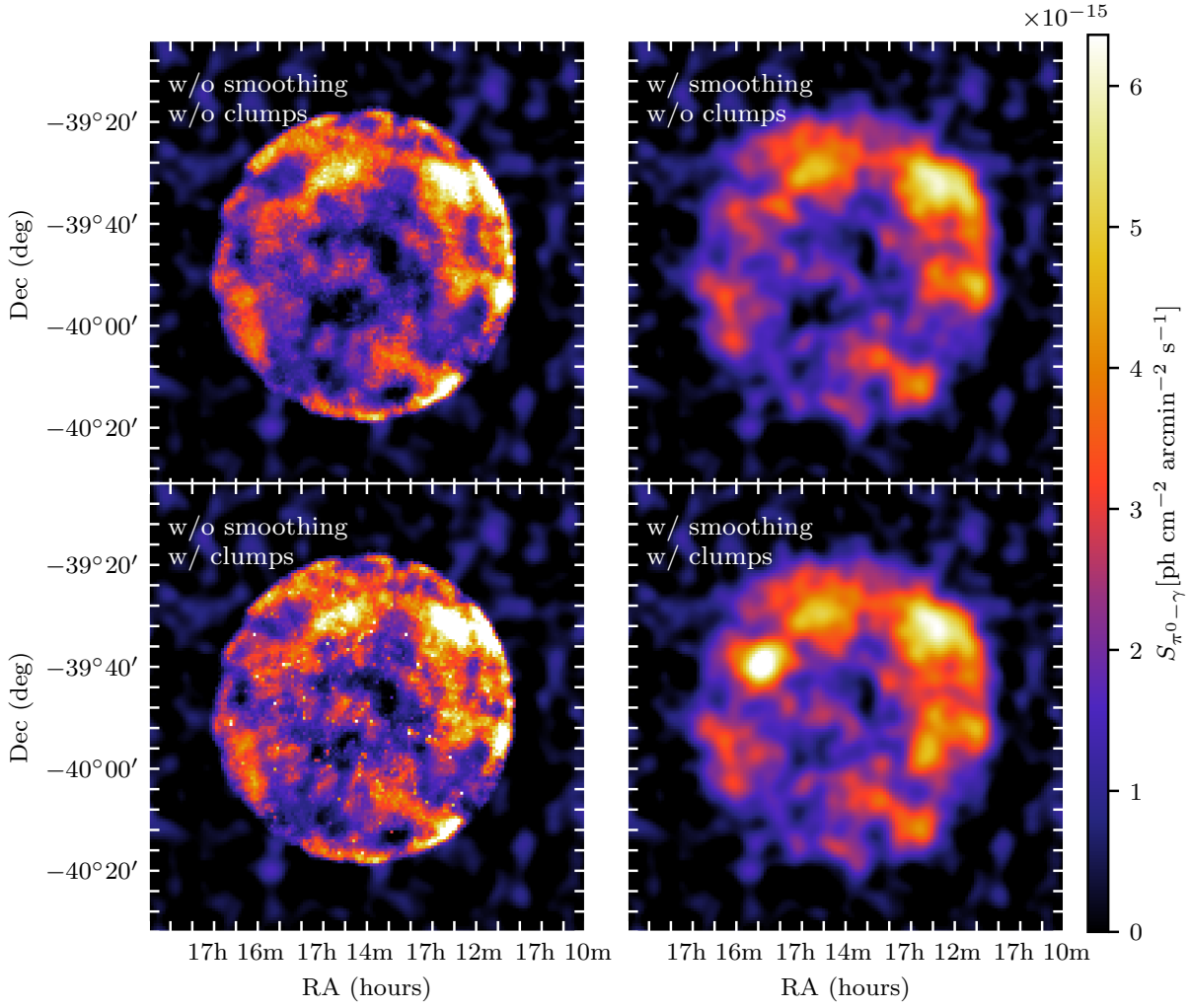

Figure 5.6.: Comparison between the simulated surface brightness maps of RX J1713 without clumps (top row) and with clumps (bottom row). The comparison between the maps without (left) and with PSF smoothing (right) shows the contribution of the clumps in specific portions of the outer shell and in the central region. While most of the gamma-ray substructure is due to obliquity-dependent CR acceleration, individual bright patches in the map can be due to the hadronic emission of dense clumps.

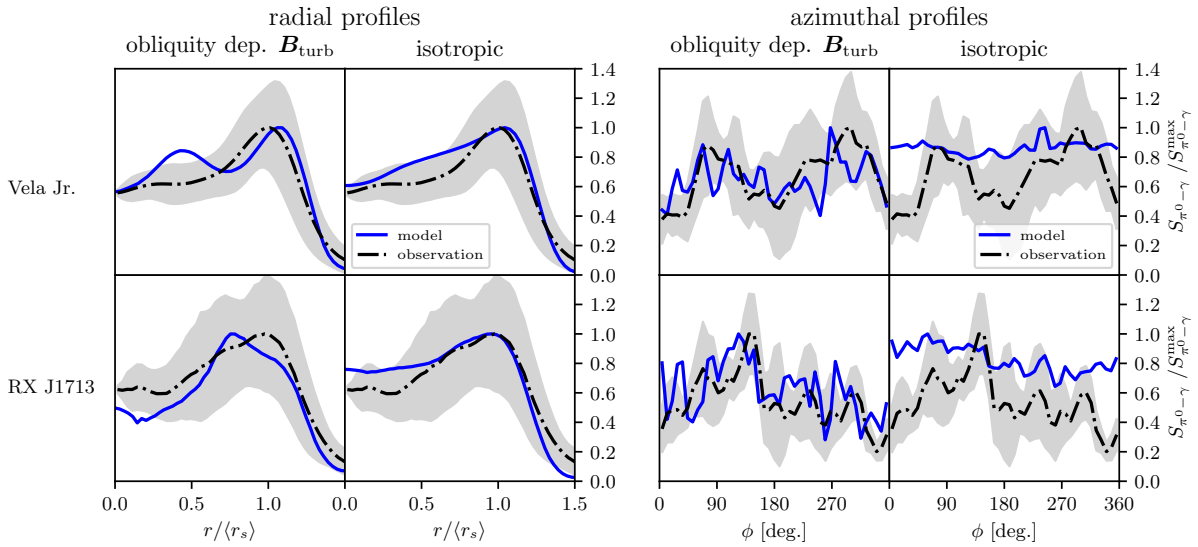

Figure 5.7.: Normalised radial (left-hand side) and angular (right-hand side) profiles of the models (blue lines) shown in Fig. 5.5 compared to SNRs Vela Jr. (dashed dotted lines in the top row, H.E.S.S. Collaboration 2018b) and RX J1713 (dashed dotted lines in the bottom row, H.E.S.S. Collaboration 2018a). The grey-filled area represents the 1σ uncertainty for both SNRs. The column labelled with "obliquity dep. $\boldsymbol{B}_{\rm turb}$" shows our obliquity-dependent acceleration models for a turbulent magnetic field while the label "isotropic" refers to our isotropic acceleration model. While both models reproduce the radial emission profiles well, the isotropic model clearly fails to capture the azimuthal brightness variations seen in the data which is statistically consistent with our obliquity-dependent acceleration model.

to those of the excess maps of Vela Jr. and RX J1713. We consider the two cases of (i) obliquity-dependent shock acceleration in a turbulent magnetic field and (ii) isotropic CR acceleration, both for a constant ambient density and and global density gradient. While the pure isotropic models (without clumps and PSF smoothing) show and enhance level of surface brightness in the central region compared to the obliquity dependent acceleration models (see Fig. 5.1), the inclusion of dense clumps and convolution with the observational PSF fills in the central parts to similar emission levels.

Most notably, the isotropic acceleration models cannot reproduce the observed azimuthal small-scale variations in the surface brightness as shown in the right-hand panels of Fig. 5.7. Interestingly, obliquity-dependent acceleration models are able to modulate the emissivity peaks on a relatively small scale, in a statistically similar fashion. This is a clear prediction of an obliquity-dependent CR acceleration in a turbulently magnetised ISM, in which the morphology of the magnetic field, in tandem with emission from dense clumps, is responsible for the VHE emission morphology observed by imaging air Cerenkov telescope such as H.E.S.S. and enables us to infer the magnetic coherence scale of the ISM surrounding the SNR (Pais et al., 2020). We will address the interesting question whether large-amplitude density perturbations or extreme density gradients alone are able to modulate the surface brightness in a similar way to mimic the VHE observations in Section 5.6.

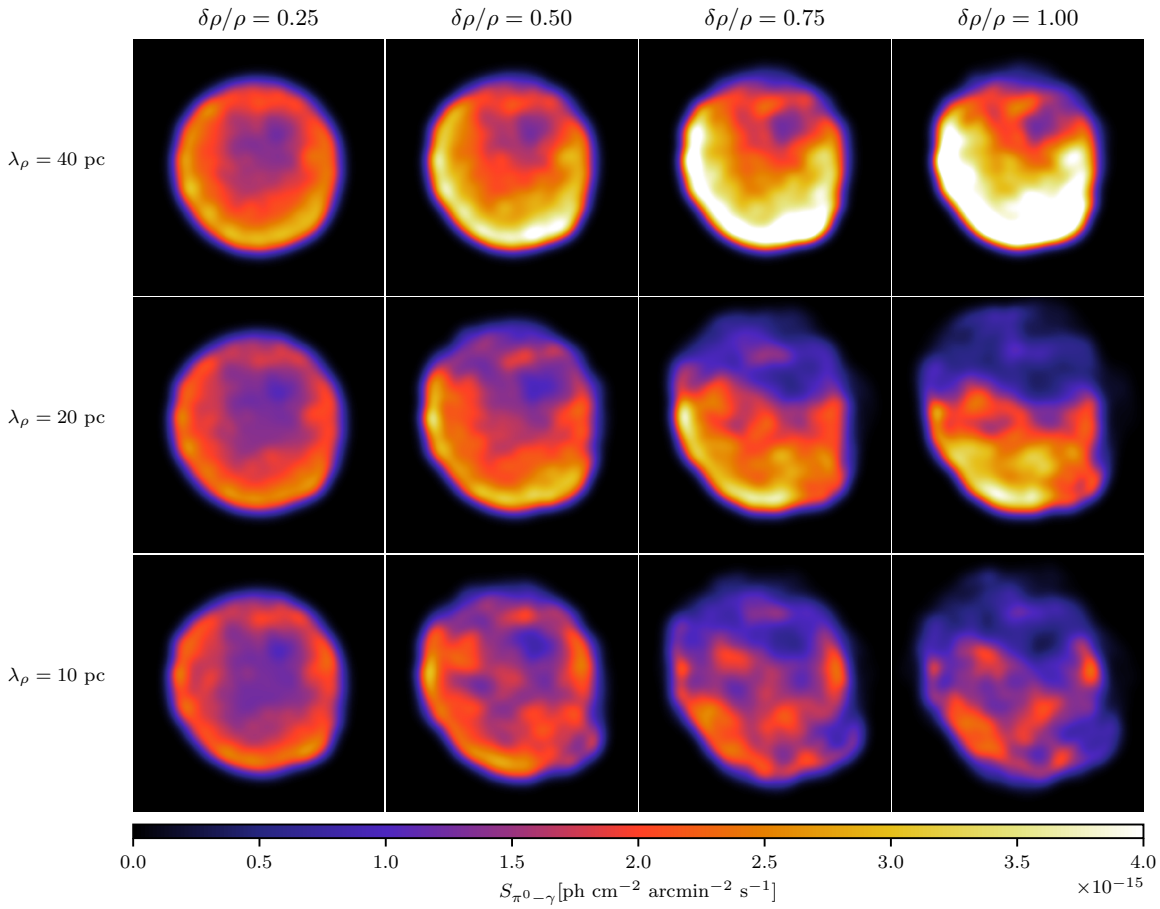

Figure 5.8.: Gamma-ray emissivity from SNRs in the Sedov-Taylor phase with large-amplitude density fluctuations in our isotropic acceleration scenario that does not depend on magnetic obliquity. From left to right the fluctuation strength increases from 0.25 to 1 with respect to the average density in steps of 0.25. From top to bottom the correlation length for the density fluctuations are, in decreasing order: 40 pc (top row), 20 pc (middle row) and 10 pc (bottom row). The maps are taken at $t_{\rm age} = 10^3$ yrs after the explosion and all exhibit the same average number density of 0.1 cm^{-3}. The maps have a side length of $L = 20$ pc and are smoothed with the PSF of RX J1713 with $\sigma = 0.036°$.

5.6. The case of a highly turbulent medium

Here we study the effect of strong density fluctuations on a supernova explosion in its early Sedov stage at $t_{\rm age} = 1$ kyr. We aim at answering two questions: (i) Can high-amplitude turbulence in the ISM on scales comparable to or smaller than the size of the remnant mimic a bi-lobed or patchy VHE gamma-ray emission with strong, small-scale brightness variations observed in the three SNRs studied here and (ii) can localised strong variations of the density be responsible for an extreme corrugation of the shock front and its eventual disruption into smaller clumps, speeding up the end of the Sedov phase, thus anticipating the beginning of the snowplough phase and the eventual merging of the fragments with the ISM? This dynamical effect may feedback on the acceleration mechanism of CRs.

In order to test whether our core-collapse SNRs necessarily require an obliquity-dependent acceleration model, we adopt our isotropic CR acceleration model and

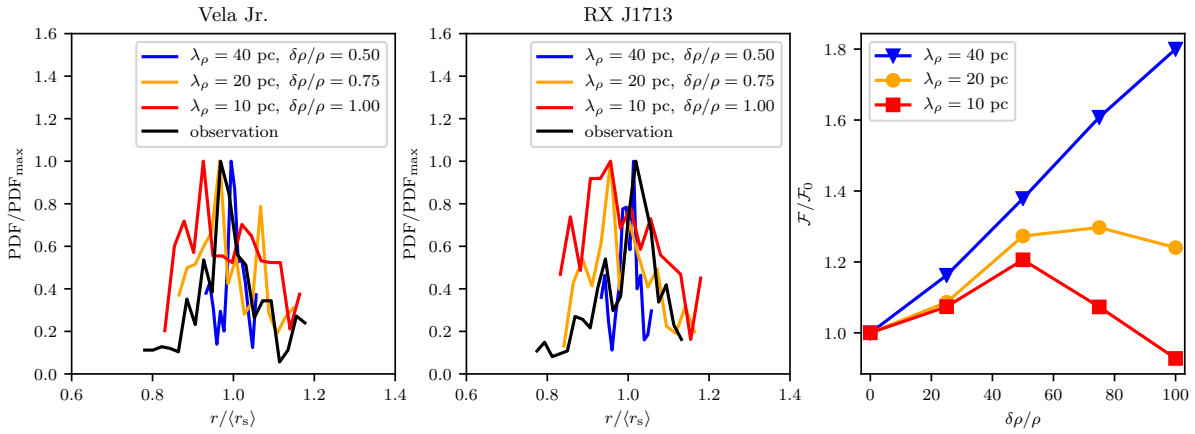

Figure 5.9.: Left and centre: Distribution of the shock radius as measured in the gamma-ray brightness map for three selected models in our isotropic acceleration scenario that does not depend on magnetic obliquity. Increasing fluctuation amplitude and correlation length implies a larger dispersion of the radial distribution and a significant departure from spherical symmetry. For comparison we show the radial distribution of the SNRs Vela Jr.(left) and RX J1713 (centre). Right: Gamma-ray flux of the models pictured in Fig. 5.8 as a function of the amplitude of density fluctuations. The flux is normalised to the flux $\mathcal{F}_0$ of the model without density turbulence. The plot shows an excess emission associated with the coherence length $\lambda_\rho = 40$ pc which grows with increasing degree of turbulence.

systematically vary density fluctuations. To this end, we present a set of 12 simulations with varying amplitude of turbulence from $\delta\rho/\rho = 0.25$ to $\delta\rho/\rho = 1$ at steps of 0.25, and varying coherence scale of the fluctuations at steps of L/n with box size $L = 40$ pc and $n = [1, 2, 4]$. We use the same setup as in our previous models, which is described in Section 5.2, and show results for the exact same random seed in Fig. 5.8. From left to right we present an increasing turbulent amplitude while the coherence scale of turbulence decreases from 40 to 10 pc from top to bottom.

We can clearly see that the shock becomes more corrugated for decreasing coherence scale while increasing the fluctuation amplitude at constant coherence scale has a comparably smaller impact on the azimuthal dependence of the shock propagation speed. We notice that a coherence length of about the size of the remnant or smaller has a strong impact on the corrugation of the outer shell. In particular, the cases of $\lambda_\rho = 10$ pc and $\delta\rho/\rho \geq 0.75$ (two bottom right panels of Fig. 5.8) show a disruption of the shock front at two locations corresponding to extremely under-dense regions. The breaking of the shell corresponds also to a lower global gamma-ray surface brightness, signalling that less material is accelerated and that eventually the shock escapes detection in that region.

Hence the appearance of a bi-lobed structure as in SN1006 would require extreme fine-tuning of the density distribution which clearly rules out this isotropic CR acceleration scenario in this case. Our parameter study presented in Fig. 5.8 shows that in order to obtain significant surface brightness variations as is observed in the core-collapse SNRs RX J1713 and Vela Jr., the level of density fluctuations needs to be significant, with $\delta\rho/\rho \gtrsim 0.75$. However, this implies a heavily corrugated shock surface which appears to be in conflict with the overall spherical appearance

of SNRs RX J1713 and Vela Jr. This observation is separately quantified for both SNRs in Fig. 5.9, where we compute the radial TeV gamma-ray emission profiles by identifying the centroid of the SNRs and determining the radial distributions of excess counts. After excluding the background noise we chose the external emission contour in order to mask the emission for both remnants and identified an average radius $\langle r_s \rangle$ for both remnants.

We compare those observed radial emission profiles to the profiles of our simulation model (assuming isotropic CR acceleration) for $\lambda_\rho = 40$ pc with $\delta\rho/\rho = 0.5$ (blue line), for $\lambda_\rho = 20$ pc with $\delta\rho/\rho = 0.75$ (orange line), and for $\lambda_\rho = 10$ pc with $\delta\rho/\rho = 1$ (red line). While large scale fluctuations with $\lambda_\rho = 40$ pc show a moderate dispersion despite the high level of density fluctuations, the models with $\lambda_\rho \leq 20$ pc are not compatible with the well defined radial dispersion of Vela Jr. and RX J1713. This allows to constrain the level of large-scale density fluctuations to be less than 75 per cent and $\lambda_\rho > 20$ pc. The resulting gamma-ray patchiness is thus not any more strong enough to explain the small-scale gamma-ray brightness variations observed in the SNRs RX J1713 and Vela Jr., which thus rules out this isotropic CR acceleration scenario in these SNRs as well and favours the obliquity-dependent CR acceleration scenario in all shell-type SNRs studied.

The maps with a high level of turbulence and a small coherence scale have a fainter surface brightness. To quantify the lower gamma-ray efficiency of small-scale highly turbulent SNRs, we show the fluxes of our 16 models as a function of the degree of turbulence and of the coherence scale in the right-hand panel of Fig. 5.9. We find a striking increase in flux with increase turbulent amplitude for our model with $\lambda_\rho = 40$ pc. On the contrary for $\lambda_\rho \leq 20$ pc the opposite is true. In order to check whether this is due to a particular random realisation of our turbulent density field or a systematic effect, we simulate the case of $\lambda_\rho = 40$ pc with $\delta\rho/\rho = [0.5, 0.75, 1]$ with three different random realisation of turbulence and show the results in Fig. 5.10. The different monotonic and non-monotonic behaviour of the gamma-ray flux for each random realisation indicates that this behaviour is not systematic and due to random variance.

5.7. Spectra

Recent observations of the ambient density around Vela Jr. and RX J1713 suggest the presence of clumps and thus a hadronic origin of the GeV-TeV gamma-ray emission (Fukui et al., 2003, 2012; Maxted et al., 2012, 2018). On the other hand, the low density of the dilute phase of ISM and X-ray measurements for SN1006 suggest mixed leptonic-hadronic models to explain both the GeV and the TeV flux in a unified picture as shown by recent simulations (Winner et al., 2020): while the GeV gamma-ray regime has a significant leptonic contribution, in this model the TeV range is dominated by hadronic gamma rays (H.E.S.S. Collaboration, 2010).

We can reproduce the observed VHE gamma-ray spectra of all three SNRs for our adopted parameters. To demonstrate this, we compare the observational data

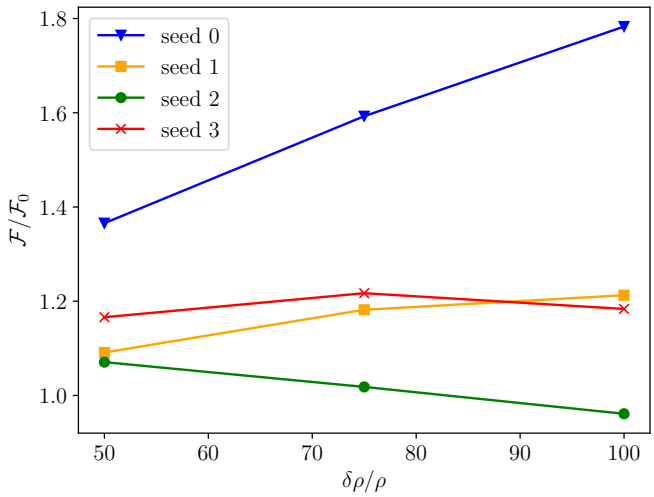

Figure 5.10.: Gamma-ray flux for our turbulent density distribution with $\lambda_\rho = 40$ pc for different random realisations of turbulence as function of the turbulent amplitude. The seed labelled with 0 represents the one used for the realisations in Fig. 5.8. The plot shows no clear trend associated with the turbulent amplitude. Random seed 0 causes a larger gamma-ray intensity because of the specifics of the overdensities which lead to the formation of a bright shell while this effect is not significant for the other tested random seeds.

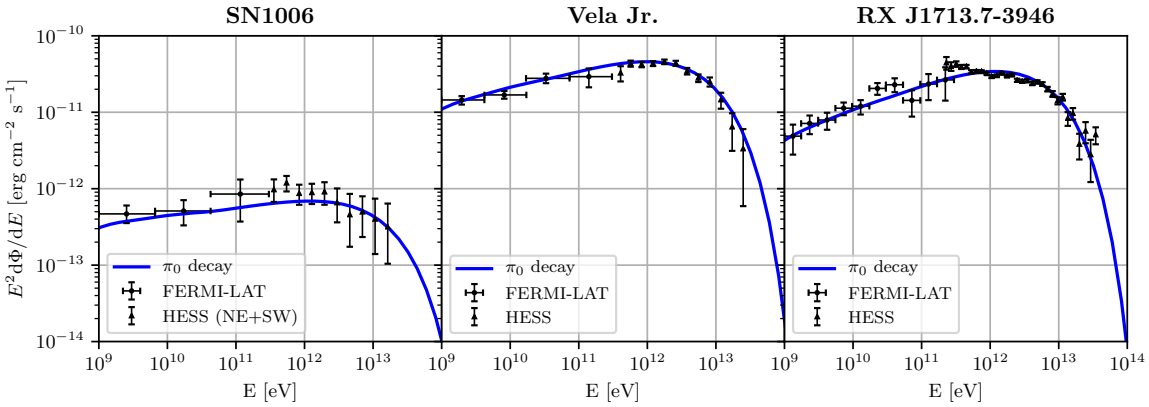

Figure 5.11.: High energy spectra spectra of SN1006 (left), Vela Jr. (centre) and RX J1713 (right). The models assume a hadronic pion-decay emission scenario for the three SNRs. For SN1006, we use data from FERMI (Abdo et al., 2010a) and H.E.S.S. (H.E.S.S. Collaboration, 2010) (sum of the two regions). For Vela Jr., we adopt gamma-ray data from FERMI (Tanaka et al., 2011) and H.E.S.S. (H.E.S.S. Collaboration, 2018b). For RX J1713, the gamma-ray data are taken from FERMI (Abdo et al., 2011) and H.E.S.S. (H.E.S.S. Collaboration, 2018a).

from FERMI and H.E.S.S. to a one-zone model in which the CR proton spectrum is described by a power law with exponential cutoff of the form:

$$f^{1\mathrm{D}}(p) = \frac{\mathrm{d}^2 N}{\mathrm{d}p\mathrm{d}V} \propto p^{-\alpha} \exp\left[-\left(\frac{p}{p_{\mathrm{cut}}}\right)^{\beta}\right] \tag{5.6}$$

where $f^{1\mathrm{D}}(p) = 4\pi\, p^2 f^{3\mathrm{D}}(p)$, α is the spectral index, p_{cut} is the cutoff momentum and β describes the sharpness of the cutoff; with values reported in Table 5.1.

The resulting spectra of our hadronic models are shown in Fig. 5.11 and match the observed spectra. We further notice that in SN1006 the gamma-ray spectrum extends to higher energies, arguing for a larger maximum CR proton energy in comparison to the turbulent cases of Vela Jr. and RX J1713. This difference depends on a range of different factors such the progenitor (SNIa for SN1006 and core-collapse for Vela Jr. and RX J1713), the ISM density, the local magnetic field amplification in the upstream and the time the particles spent in favourable conditions (e.g., quasi-parallel shock geometries) at the shock. However, the limited angular resolution of H.E.S.S. precludes a more in-depth analysis of the acceleration mechanism leaving this task to the next generation of ground-based arrays such the Cherenkov Telescope.

5.8. Conclusions

In this chapter we use MHD simulations with CR physics to explore the effect of density inhomogeneities on the TeV gamma-ray morphology from SNRs during their Sedov-Taylor stage. Our setup allow us to explore several combinations of homogeneous and turbulent magnetic fields and ambient density distributions. We find that a single physical model, namely obliquity-dependent shock acceleration of CRs, is capable of explaining the apparently disparate TeV gamma-ray morphologies of well-known shell-type SNRs. In this hadronic emission scenario, gamma-ray bright regions result from quasi-parallel shocks which are known to efficiently accelerate CR protons, and gamma-ray dark regions point to quasi-perpendicular shock configurations.

The main characteristics of the emission of SN1006 (a type Ia SN) can be explained by a homogeneous magnetic field superposed on a density gradient that explains the different integrated gamma-ray flux of both polar caps. By contrast, the irregular gamma-ray morphologies of the core collapse SNRs Vela Jr. and RX J1713 is owing to a turbulent magnetic field with $\boldsymbol{B}_0 \approx \mathbf{0}$ that is supplemented with a population of multiphase dense molecular clumps that are characteristic for star formation regions (and complemented with a weak density gradient in the case of RX J1713). Adapting a straw man's model of isotropic CR acceleration (that does not depend on magnetic pre-shock orientation) we conclude that this model is not able to reproduce the sharp bi-lobed morphology observed for SN1006 even the presence of moderately strong density fluctuations. Moreover, the simulated azimuthal profiles of this isotropic acceleration model with strong density variations cannot reproduce the observed rapid variations of the gamma-ray emissivity

of Vela Jr. and RX J1713 without significantly corrugating the shock surface, which is then ruled out by the spherical morphologies of these SNRs.

Our main findings are summarised here:

- Moderate density fluctuations can be responsible for a local modulation of the gamma-ray emissivity irrespective of the magnetic morphology both in a constructive and destructive way. We show that density fluctuations on a scale comparable to the size of the remnant and with an amplitude that is stronger than 75 per cent with respect to the mean ISM density causes a corrugated shock front that generates strong local variations in the shock acceleration efficiency and eventually a very asymmetrical appearance of the gamma-ray SNR.

- For SN1006, using the relative brightness of the NE and SW lobes, we constrain the intensity of the density gradient to be no more than 0.0035 $\mathrm{cm}^{-3}/\mathrm{pc}$ and directed from SW to NE. We predict that local density fluctuations with $\lambda_\rho \simeq 4$ pc and $\delta\rho/\rho = 0.5$ are secondary in shaping the morphology of the remnant if compared to a moderate level of turbulence of the local magnetic field with a coherence scale at 1/3 of the size of the remnant. However, we note that the presence of density fluctuations can explain the strong asymmetry of the distribution of Fe and other heavy elements for this remnant.

- The strong noise level surrounding the SN1006 SNR does not allow more precise constraints on the properties of the surrounding ISM. We conclude that for such level of noise a model with negligible density fluctuations better represents the morphology of SN1006. Performing a 3D rotation of the SNR around the axis perpendicular to the orientation of $\boldsymbol{B}_0$ into the line of sight, the emerging radial emission profiles constrain the inclination of the magnetic field to be $\lesssim 10°$. Our azimuthal emission profiles for different magnetic inclinations are rather robust and show an excellent agreement with the observational profile except for the NE lobe, which is somewhat broader in our simulations. While this could signal a different functional form of the obliquity dependence of CR acceleration, this conclusion is unfortunately degenerate with density fluctuations that could also cause a sharper gamma-ray peak.

- Our generated gamma-ray mock maps with obliquity-dependent acceleration are capable of reproducing most of the properties observed for Vela Jr. and RX J1713 such the length of the shell filaments, the internal patchy emission, the large-scale gamma-ray bright rims and moderate (small-scale) corrugations at the shock front. The fainter emission at the centre of the remnants expanding in a turbulent magnetic field is compensated by the addition of molecular clumps and superposing noise to the images. By contrast an isotropic CR acceleration scenario fails to reproduce the azimuthal profiles.

- In addition, by considering an isotropic CR acceleration scenario for Vela Jr. and RX J1713 with a varying level of density fluctuations and coherence

scales, we exclude strong density fluctuations with a coherence scale comparable to the size of the remnant are responsible for the observed emission morphology. This is because sufficiently strong density fluctuations (that would be needed to explain the significant gamma-ray brightness fluctuations) cause a heavily corrugated shock surface which is in direct conflict with the almost spherical shape of SNRs RX J1713 and Vela Jr. The comparison between the radial dispersions of our simulated mock maps and the excess maps of the SNRs RX J1713 and Vela Jr. enables us to limit the density fluctuations to $\delta\rho/\rho_0 \lesssim 75$ per cent of the average ISM density.

For the first time, our models are able to match morphological and spectral properties of all known shell-type TeV gamma-ray SNRs. Remarkable improvements in the angular resolution in future surveys (beyond what is achievable by CTA) are needed to resolve the TeV emission from individual molecular clumps which would yield a deeper insight in the structure of the circumstellar ISM.

6. Conclusions and outlook

In this thesis I explored the effect of the obliquity dependent shock acceleration on the injection and evolution of CRs in SNR shocks via full 3D magneto-hydrodynamical simulations with AREPO. The code follows the evolution of CRs and their advective transport with the magnetized plasma.

Starting from the results of non relativistic hybrid PIC simulations on the acceleration of ions in the approximation of large Mach-number shocks, I modeled obliquity dependent CR acceleration and studied its dynamical effects on the blast wave of a SNR and how the topology of the magnetic field affects the resulting CR distribution. In this picture only quasi-parallel magnetic shock configurations can accelerate ions while quasi-perpendicular shocks are ineffective.

I successfully derived analytic exact solutions of the Sedov-Taylor blast wave problem with CR acceleration for different values of the maximum acceleration efficiency in a scenario with isotropic injection. Furthermore I run simulations with obliquity-dependent CR acceleration in a homogeneous magnetic field geometry showing the emergence of an oblate ellipsoidal shock surface that emerges from efficient acceleration of CRs. I simulated a Sedov-Taylor explosion in a turbulent magnetic field with different coherence scales and showed how this creates a patchy CR distribution with bright filaments corresponding to a parallel alignment between the local magnetic field and the shock and regions devoid of CRs corresponding to local perpendicularity between the local magnetic field and the shock. I derived the averaged CR acceleration efficiency to $\simeq 0.3$ of the maximum CR acceleration efficiency for both homogeneous and turbulent background magnetic fields and independently of the coherence scale.

Accounting for efficient acceleration at quasi-parallel shocks and a maximum efficiency for protons of 15 per cent of the kinetic energy, as suggested by the findings of recent PIC simulations, I applied the previous scale-free results to two well-known cases of bright TeV SNRs with resolved morphology: SN 1006 and Vela Jr. I present the first global simulations and gamma-ray maps of SNRs in the hadronic model accounting for magnetic obliquity-dependent CR acceleration and show that both the hadronic and mixed model can match the observed multi-wavelength spectra. Comparing the simulations for different coherence scale of the magnetic field to the observed TeV gamma-ray maps of these two SNRs, I am able to estimate the coherence scale of the unperturbed ISM before it encounters the SNR blast wave. For SN 1006 this results in a uniform magnetic field whose coherence scale is much larger than the size of the SNR while for Vela Jr. the coherence scale is about the size of the remnant. In particular I demonstrated how obliquity-dependent shock acceleration as a function of the coherence scale of the magnetic field can reproduce in a unified picture for the disparate morphologies of

TeV supernova remnants.

I extended these findings to the case of inhomogeneous configurations of the ISM. In particular I focused on the effect of density inhomogeneities on the TeV gamma-ray morphology from SNRs during their Sedov-Taylor stage. With a flexible setup I put constrains on the ISM properties of three SNRs: the Type Ia SN 1006 and the core-collapse SNRs Vela Jr and RX J1713.

I demonstrated that the relative modulation of the TeV gamma-ray brightness of the two polar caps of SN1006 can be attributed to a large scale gradient in the density assuming a homogeneous profile for the density. By contrast, the irregular gamma-ray morphologies of the core collapse SNRs Vela Jr. and RX J1713 is owing to a turbulent magnetic field that is supplemented with a population of multiphase dense molecular clumps. In particular, I showed how these molecular clumps, which are characteristic of star-forming environments, are fundamental in outlining the morphology of the TeV emission, lower the density of the diffuse phase of the interstellar medium and drive considerable magnetic field amplification in the interaction with the SNR shock wave.

For completeness, adapting a straw man's model of isotropic CR acceleration (that does not depend on magnetic pre-shock orientation) I demonstrate that this model is not able to reproduce the sharp bi-lobed morphology observed for SN1006 even the presence of moderately strong density fluctuations. Moreover, the simulated azimuthal profiles of this isotropic acceleration model with strong density variations cannot reproduce the observed rapid variations of the gamma-ray emissivity of Vela Jr. and RX J1713 without significantly corrugating the shock surface, which is then ruled out by the observed spherical morphologies of these SNRs.

With these models I am able to predict from morphological properties of the TeV gamma-ray emission within a certain level of accuracy the general properties of the interstellar environment surrounding the SNR and match both resolved observations and spectral measurements.

The work presented here can be further expanded and refined. Here I offer some possible prospects to extend this research.

An extension of the present work can be applied for instance to other astrophysical problems such the creation of superbubbles from the merging of various SN explosions. In particular, superbubbles are objects sufficiently spatially and temporally extended to be resolved in galaxy simulations and they carry momentum and radiation to be considered fundamental in feedback models. The superposition of different shock fronts especially leads to the re-acceleration of the propagated CR population possibly increasing the higher average acceleration efficiency with respect to the case of isolated SNRs.

Another front that I am willing to explore is an improvement of what has been carried in Chapter 4. The modeling of clumpy media is rather interesting and complex and accounts for different chemical species as well as for a wide range of densities and scales. The simulations presented in Chapter 4 are sufficient to estimate efficient acceleration of CRs in dense clumps but they are rather simplified and did not include effects such as cooling and diffusion of CRs. My aim is to dramatically improve the resolution and run a highly detailed simulation for a

clumpy medium including all these effects.

Acknowledgments

First of all I'd like to thank my supervisor, Prof. Christoph Pfrommer, for his fundamental guidance through this thesis. His encouragements and enthusiasm have been fundamental to develop self-criticism and overcome some difficult moments. A special mention goes to both Prof. Volker Springel and Prof. Ralf Klessen for their constructive and useful comments in our thesis committee meetings. I acknowledge the support by the European Research Council under ERC-CoG grant CRAGSMAN-646955.

I want to thank my research group, the Cosmology Group at the AIP, for the good moments spent together and the interesting discussions. I'd like to thank Georg Winner, Dr. Philipp Girichidis, Dr. Martin Sparre, Joe Whittingham and Alex Scherrmann for the moments spent in- and outside the office. A special thank goes to Kristian Ehlert and his friendship and support since the beginning of my PhD. I'd like to thank my two office mates and colleagues, Dr. Edoardo Carlesi and Dr. Marcel Pawlowski, for the very relaxed and definitely joyful atmosphere in our office.

Special thanks go to the people of the Milky-Way group I had the luck to meet and interact with: Anna Queiroz, Dalal El Youssoufi, Dr. Marica Valentini, Dr. Guillaume Guiglion and Dr. Cameron Bell. Our weekly informal meetings have been a source of fun and witty discussions about almost every possible topic. I want to thank the friendly people I met during my short staying in Heidelberg: Matteo Mazzarini, Dr. Yulong Zhuang, Michaíl Laktíonov, Cherrie Cruz and Tomi Määttä just to cite some of them.

I also want to thank my friends in Sardinia, for their company, their friendship and interesting discussions.

Last but not least, I warmly thank my parents, *Babbo* and *Mamma*, that have been extremely supportive during these years and endured my fiery temperament. I would like to thank especially my father who despite his health problems has always been interested in my progresses and spurred me on. I dedicate this thesis to the both of you.

A. Appendix

This appendix is an adapted version of the appendices from the paper *The effect of cosmic-ray acceleration on supernova blast wave dynamics* published on Monthly Notices of Royal Astronomical Society (Pais et al., 2018).

A.1. Convergence tests

Here, we perform numerical convergence tests of our shock-tube and the Sedov-Taylor setups with a homogeneous magnetic field (see Sections 3.2 and 3.3, respectively). First, we asses the convergence of the accuracy with which we recover the magnetic obliquity in our simulations. We use several simulation outputs to measure the obliquity distribution, which follows a Gaussian, independent of resolution. Figure A.1 shows the Gaussian standard deviation of the obliquity as a function of grid resolution, featuring 1200, 10^4, 8×10^4 and 64×10^4 cells in our elongated shock tube setup ($10 \times 1 \times 1$). We notice that the standard deviation σ_θ decreases from 1200 to 10^4 cells and levels off for better resolved simulations, indicating convergence for measuring the magnetic obliquity for at least 10^4 cells or equivalently 10^3 cells per individual three-dimensional unit. To assess the numerical convergence of our ellipsoidal Sedov-Taylor problems with obliquity dependent CR acceleration, we perform simulations with $50^3, 100^3$ and 200^3 grid cells. The results are reported in Fig. A.2. The time evolution of the average shock radius (shown in the left panel) already converges for a 50^3 simulation except for the first two points. We derive the radius of our self-similar solution with equation (3.17) using an average efficiency value taken from the 200^3 simulation. Contrarily, the time evolution of the eccentricity of the oblate explosion (shown in the right panel) converges much slower and converges on our theoretical eccentricity at a resolution of 200^3 cells. The self-similar solution of the eccentricity is constructed by fitting a Sedov-Taylor solution of the shock evolution to the data of the 200^3 simulation in the parallel and perpendicular regions (as defined in Sect. 3.3.2).

A.2. Details of the Sedov-Taylor solution

The Sedov-Taylor similarity solution makes two fundamental assumptions: (i) it assumes that the explosion was sufficiently long ago so that the initial conditions do not impact the solution and (ii) that the explosion expands into a medium of negligible pressure (or temperature). For these assumptions, the solution describes a strong spherical shock wave whose position only depends on the injected energy

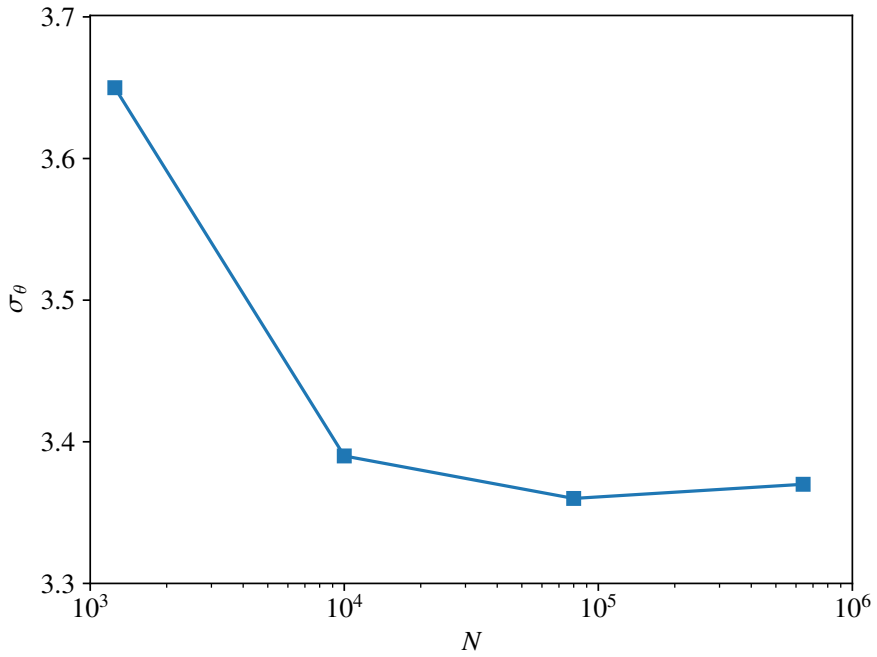

Figure A.1.: Convergence test of the shock-tube simulation for four different resolutions (1200, 10^4, 8×10^4 and 64×10^4 cells) in a $10 \times 1 \times 1$ simulation box for a magnetic obliquity of 45°. The plot shows the standard deviation σ_θ of the magnetic obliquity vs. the number of cells N used in the initial setup.

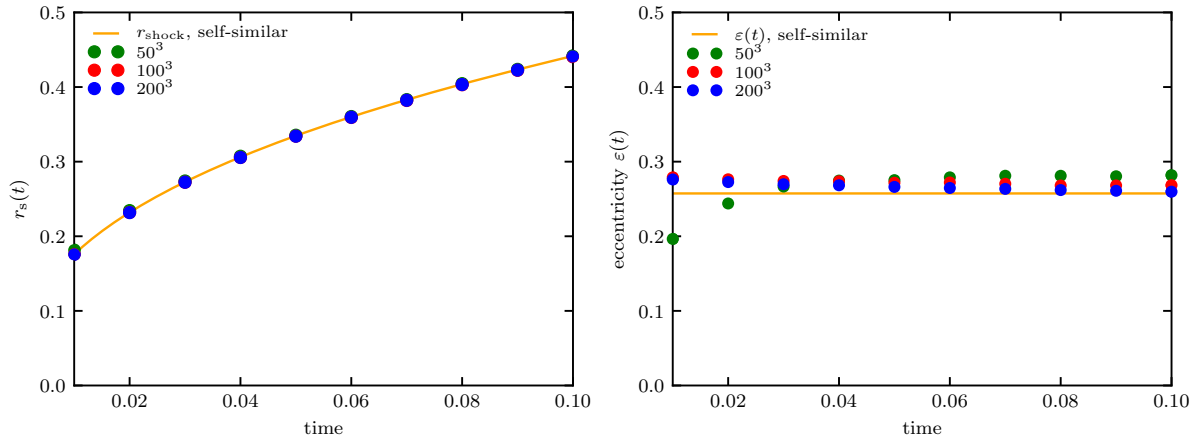

Figure A.2.: Convergence test for the Sedov-Taylor blast wave in the case of a homogeneous magnetic field and obliquity dependent CR acceleration with three different grid resolutions: $50^3, 100^3$ and 200^3. The left panel shows the time evolution of the average shock radius while the right panel shows the time evolution of the eccentricity of the oblate explosion. Except for early times ($t < 0.02$) the radius already converges for a simulation with 50^3 cells. In contrast, the eccentricity converges only at a resolution of 200^3 grid cells.

and the density of the ambient medium (Sedov, 1959; Taylor, 1950). These assumptions still hold when including a magnetic field that is flux-frozen into the gas. We follow the derivation by Landau & Lifshitz (1966) and only state the starting point and relevant definitions that are necessary to understand our final novel analytical expression of the self-similar parameter α in equation (3.13).

The velocity of the shock wave relative to the background gas at rest is given by (equation 3.13)

$$u_1 = \frac{\mathrm{d}r_\mathrm{s}(t)}{\mathrm{d}t} = \frac{2r_\mathrm{s}(t)}{5t} = \frac{2}{5}\left(\frac{E_1}{\alpha\rho_1 t^3}\right)^{1/5}. \tag{A.1}$$

Using the Rankine-Hugoniot expressions in the limit of strong shocks, the gas pressure P_2, mass density ρ_2 and velocity $v_2 = u_1 - u_2$ in the post-shock rest frame can be expressed in terms of the shock velocity u_1:

$$v_2 = \frac{2u_1}{\gamma+1}, \tag{A.2}$$

$$\rho_2 = \frac{\gamma+1}{\gamma-1}\rho_1, \tag{A.3}$$

$$P_2 = \frac{2\rho_1 u_1^2}{\gamma+1}. \tag{A.4}$$

To determine the gas flow in the region behind the shock, we introduce dimensionless variables V, G, Z for the gas velocity v, density ρ and the squared sound velocity c^2, respectively:

$$v = \frac{2r}{5t}V, \tag{A.5}$$

$$\rho = \rho_1 G, \tag{A.6}$$

$$c^2 = \frac{4r^2}{25t^2}Z. \tag{A.7}$$

These parameters are functions of the dimensionless variable

$$\xi = \frac{r}{r_\mathrm{s}(t)} = r\left(\frac{\alpha\rho_1}{E_1 t^2}\right)^{1/5}. \tag{A.8}$$

Using these dimensionless quantities the conservation of energy can be expressed in terms of Z and as an implicit function of ξ through $V(\xi)$ (Landau & Lifshitz, 1966):

$$Z = \frac{\gamma(\gamma-1)(1-V)V^2}{2(\gamma V - 1)}. \tag{A.9}$$

Following Landau & Lifshitz (1966), we arrive at the following set of equations:

$$\xi^5 = \left[\frac{1}{2}(\gamma+1)V\right]^{-2}\left\{\frac{\gamma+1}{7-\gamma}[5-(3\gamma-1)V]\right\}^{\nu_1} \times\left[\frac{\gamma+1}{\gamma-1}(\gamma V-1)\right]^{\nu_2}, \tag{A.10}$$

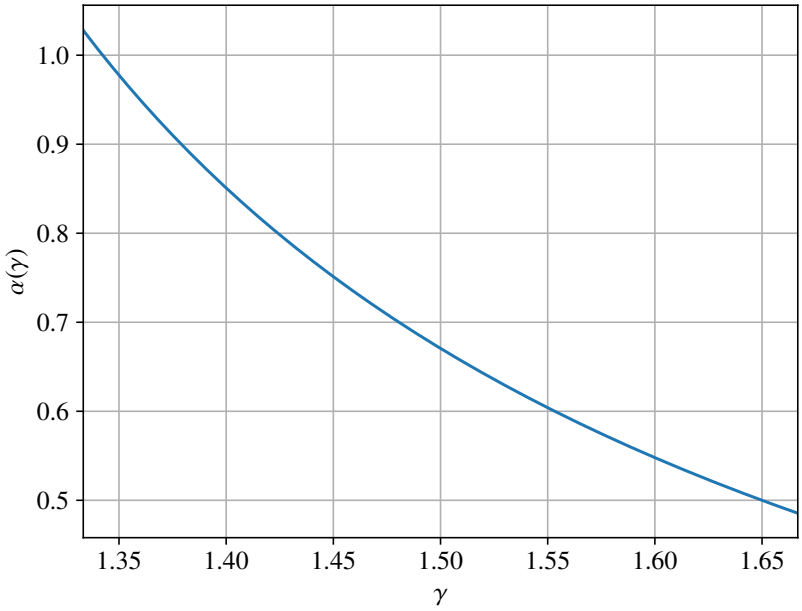

Figure A.3.: We show the self-similarity factor α of the Sedov-Taylor solution as a function of the ratio of specific heats γ.

$$G = \frac{\gamma+1}{\gamma-1}\left[\frac{\gamma+1}{\gamma-1}(\gamma V-1)\right]^{\nu_3}\left\{\frac{\gamma+1}{7-\gamma}[5-(3\gamma-1)V]\right\}^{\nu_4} \times\left[\frac{\gamma+1}{\gamma-1}(1-V)\right]^{\nu_5} \tag{A.11}$$

with

$$\nu_1 = -\frac{13\gamma^2-7\gamma+12}{(3\gamma-1)(2\gamma+1)}, \tag{A.12}$$

$$\nu_2 = \frac{5(\gamma-1)}{2\gamma+1}, \tag{A.13}$$

$$\nu_3 = \frac{3}{2\gamma+1}, \tag{A.14}$$

$$\nu_4 = -\frac{\nu_1}{2-\gamma}, \tag{A.15}$$

$$\nu_5 = -\frac{2}{2-\gamma}. \tag{A.16}$$

The variable α as a function of the independent variable ξ is determined by the condition

$$E_1 = \int_0^{r_s}\rho\left(\frac{1}{2}v^2+\frac{1}{\gamma-1}\frac{P}{\rho}\right)4\pi r^2\mathrm{d}r, \tag{A.17}$$

which states that the total energy of the gas is equal to the released energy of the original explosion. In terms of dimensionless quantities, this equation reads

$$\alpha = \frac{16}{25}\pi\int_0^1 G(\xi)\left[\frac{1}{2}V^2(\xi)+\frac{Z(\xi)}{\gamma(\gamma-1)}\right]\xi^4\mathrm{d}\xi = \alpha(\gamma). \tag{A.18}$$

As $\gamma = c_P/c_V$ (where c_P and c_V are the specific heats at constant volume and pressure, respectively) we have $1 < \gamma < 2$. In our simulations we adopt values of γ in the range $[4/3, 5/3]$, such that $\alpha(\gamma)$ can be approximated with high precision, slightly modifying the formula used by Mihalas & Mihalas (1984):

$$\alpha(\gamma) \approx \frac{16}{75}\left[\frac{\pi(3\gamma-1)}{(\gamma-1)(\gamma+1)^2} - \frac{3}{8}\right], \tag{A.19}$$

which is accurate to within 0.8% and is shown in Fig. A.3.

The dimensionless quantities defined via equations (A.5), (A.6) and (A.7) yield the implicit expressions for $v(r), \rho(r)$ and $P(r)$:

$$\begin{aligned} v(r) &= \frac{1}{2}(\gamma+1) r V(r), \\ \rho(r) &= G(r)\rho_1, \\ P(r) &= \frac{2\rho_1 u_1^2}{\gamma+1}\left[\frac{1}{2}(\gamma+1)V\right]^{-6/5}\left[\frac{\gamma+1}{\gamma-1}(1-V)\right]^{-\nu_5+1} \\ &\quad \times \left\{\frac{\gamma+1}{7-\gamma}[5-(3\gamma-1)V]\right\}^{-\frac{\nu_4+2\nu_1}{5}}. \end{aligned} \tag{A.20}$$

A.3. Ellipsoidal reference frame

The radial unit vector of a spherical coordinate system is not perpendicular to an oblate surface except for the poles at $z = \pm b$, which would complicate the relation to the magnetic obliquity for a homogeneous magnetic field aligned with the z axis. To simplify our computation of the magnetic obliquity on an oblate surface, we adopt the ellipsoid coordinate system. Here, the bisector of a tangent to point P intersects the z axis in Q, which varies according to the position of the point P on the oblate surface (see Fig. A.4). It assumes values from 0 (for a point on the semi-major axis) to $-\infty$ (for a point on the semi-minor axis).

A point P on the ellipse has the property that the sum of distances from the two focal points F_1 and F_2 to P is constant. A tangent to the ellipse in that point forms equal angles α with the two focal segments $\overline{F_1P}$ and $\overline{F_2P}$. Dropping the perpendicular to the tangent in P, by construction bisects the angle and intersects the z axis in Q. The angle between this bisector and the z axis defines the angle φ. Assuming a homogeneous magnetic field that is aligned with the z axis, implies that the pseudo-azimuthal angle coincides with the magnetic obliquity, $\varphi = \theta$.

The point P can be vertically projected onto a circumference in the point P_C, which forms an azimuthal angle ψ with respect to the semi-minor axis b. The angle φ is related to this angle via the following formula:

$$\tan\varphi = \frac{b}{a}\tan\psi. \tag{A.21}$$

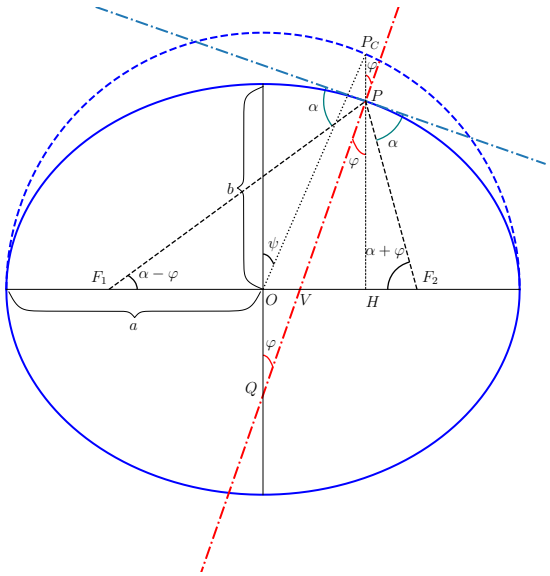

Figure A.4.: Elliptical section of an oblate that defines the ellipsoidal reference frame with the pseudo-azimuthal angle φ. The two focal points F_1 and F_2 determine a point P on the surface of the ellipse. The tangent to that point (blue dash-dotted line) forms two equal angles α with the lines to the focii $\overline{PF_1}$ and $\overline{PF_2}$. Thus, the perpendicular to the tangent in P (red dash-dotted line) intersects the z axis in point Q, which varies with the position of P and forms the desired angle φ.

A.4. Sedov-Taylor solution of a dipole field

As a last application, we study CR shock acceleration in the case of a magnetic dipole field with the dipole moment pointing in the positive x direction. We chose the dipole configuration because it is expected to be the dominant magnetic configuration emerging from a non-rotating star at large distances and because of its self-similarity. While the magnitude of the magnetic field strength decreases as r^{-3}, where r is distance from the source, the dipole field shows a constant magnetic obliquity at fixed latitude. This implies that the explosion encounters exactly the same replica of the magnetic field at different radii. We perform a 100^3-cell simulation with an extremely low $\zeta_0 = 0.02$ to reduce the effect of CR pressure on the explosion shape and apply a Plummer-type softening length for $r \to 0$ to avoid magnetic divergence at the origin. The magnetic field in the polar regions is oriented mostly parallel to the shock normal, which results in efficient CR acceleration as the blast wave sweeps across it. The resulting quadrupolar CR morphology is shown in Fig. A.5, resembling qualitative similarities to the homogeneous field case.

To analytically calculate the average efficiency we proceeded as follows. The normalised radial component of the magnetic dipole field is given by

$$\hat{\boldsymbol{b}} \cdot \hat{\boldsymbol{r}} = \frac{2\cos\vartheta}{\sqrt{1+3\cos^2\vartheta}}, \tag{A.22}$$

where $\hat{\boldsymbol{r}}$ denotes a radial unit vector and ϑ is the azimuthal angle. Thus, the

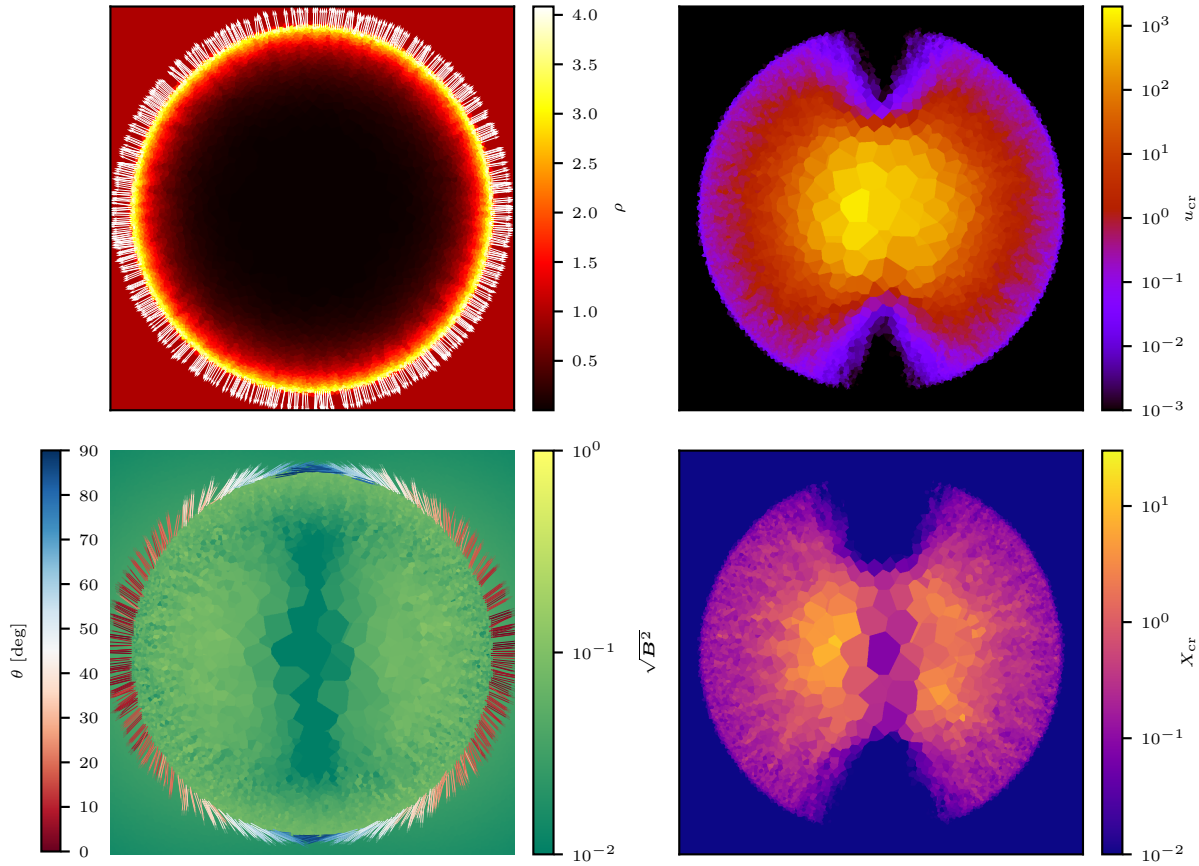

Figure A.5.: Sedov-Taylor blast wave with obliquity dependent CR acceleration expanding into a *d*ipole magnetic field that is centered at point of the explosion and initially oriented horizontally. Quantities are shown at $t = 0.1$ and are the same as in Fig. 3.5. Despite the different magnetic field morphology in comparison to the homogeneous case, the specific CR energy still exhibits a quadrupolar anisotropy, but with a broader region of CR production.

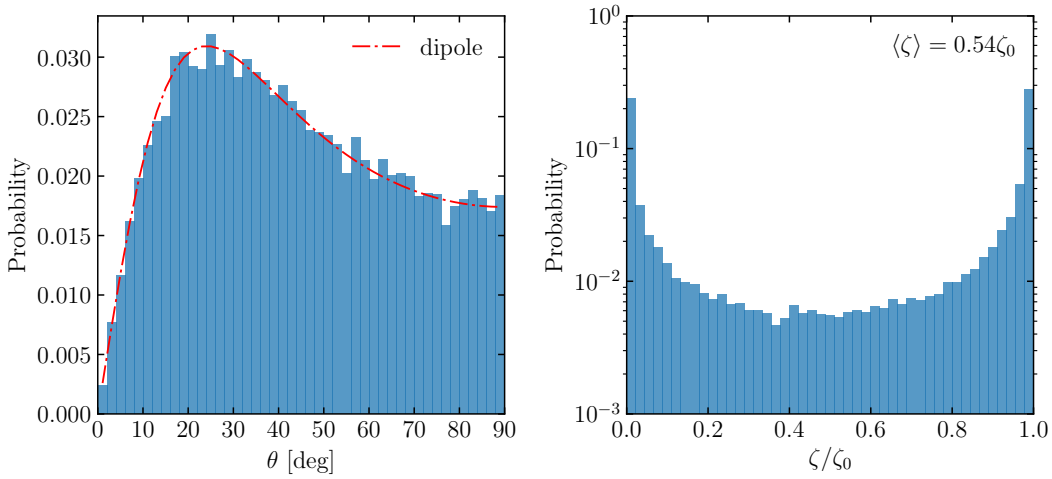

Figure A.6.: Probability distribution functions of the magnetic obliquity for the magnetic dipole case (left) and the resulting bimodal distribution for the acceleration efficiency (right). The theoretical distribution $f(\theta)$ of equation (A.27) (red dot-dashed line) compares nicely to our simulations.

magnetic obliquity reads as

$$\theta(\vartheta) = \arccos(\hat{\boldsymbol{b}} \cdot \hat{\boldsymbol{r}}) = \arccos\left(\frac{2\cos\vartheta}{\sqrt{1+3\cos^2\vartheta}}\right). \tag{A.23}$$

Capitalizing on the symmetry of both hemispheres, we calculate the average efficiency,

$$\langle\zeta\rangle = \int_0^{\pi/2} \zeta[\theta(\vartheta)] \sin\vartheta \, \mathrm{d}\vartheta = 0.55\zeta_0. \tag{A.24}$$

Note that the result is considerably larger in comparison to our previously discussed case of CR acceleration in a turbulent field.

In Fig. A.6 we show the obliquity distribution for a dipole field. To analytically predict this distribution, we invert equation (A.23) and obtain

$$\vartheta(\theta) = \arccos\left(\frac{\cos\theta}{\sqrt{4-3\cos^2\theta}}\right), \text{ with } \theta \in [0, \pi/2]. \tag{A.25}$$

The distribution of magnetic obliquity in the case of a dipole field is obtained through a change of variables:

$$\sin\vartheta \, \mathrm{d}\vartheta = \sin[\vartheta(\theta)] \left(\frac{\mathrm{d}\vartheta}{\mathrm{d}\theta}\right) \mathrm{d}\theta = f(\theta)\mathrm{d}\theta, \tag{A.26}$$

where

$$f(\theta) = \frac{4\sin\theta}{(4-3\cos\theta)^{3/2}}. \tag{A.27}$$

This analytical result compares favorably to the simulations (see left-hand panel of Fig. A.6). The simulated and theoretically expected average acceleration efficiencies agree within 2% (for our 100^3 cell simulation), demonstrating the accuracy of our numerical algorithms.

Bibliography

Abbott D. C., 1978, Astrophysical Journal, 225, 893

Abdo A. A., et al., 2010a, Astrophys. J. Suppl. Ser., 188, 405

Abdo A. A., et al., 2010b, Astrophysical Journal, 718, 348

Abdo A. A., et al., 2011, Astrophysical Journal, 734, 28

Acero F., Ballet J., Decourchelle A., 2007, Astron. Astrophys., 475, 883

Acero F., Lemoine-Goumard M., Renaud M., Ballet J., Hewitt J. W., Rousseau R., Tanaka T., 2015, Astron. Astrophys., 580, A74

Ackermann M. e. a., 2013, Science, 339, 807

Aharonian F. A., et al., 2004, Nature, 432, 75

Aharonian F., et al., 2005, Astron. Astrophys., 437, 135

Aharonian et al. F., 2006, Astron. Astrophys., 449, 223

Aharonian et al. F., 2007, Astrophysical Journal, 661, 236

Allen G. E., Chow K., DeLaney T., Filipović M. D., Houck J. C., Pannuti T. G., Stage M. D., 2015, Astrophysical Journal, 798, 82

Alsabti A. W., Murdin P., 2017, Supernovae and Supernova Remnants: The Big Picture in Low Resolution. p. 3, doi:10.1007/978-3-319-21846-5˙1

Amato E., Blasi P., 2006, Mon. Not. R. Astron. Soc., 371, 1251

Araya M., Frutos F., 2012, Mon. Not. R. Astron. Soc., 425, 2810

Archambault et al. S., 2017, Astrophysical Journal, 836, 23

Aschenbach B., Iyudin A. F., Schönfelder V., 1999, Astron. Astrophys., 350, 997

Atoyan A. M., Aharonian F. A., Tuffs R. J., Völk H. J., 2000, Astron. Astrophys., 355, 211

Axford W. I., Leer E., Skadron G., 1977, International Cosmic Ray Conference, 11, 132

Baade W., Zwicky F., 1934, Physical Review, 46, 76

Bamba A., Yamazaki R., Ueno M., Koyama K., 2003, Astrophysical Journal, 589, 827

Bamba A., Yamazaki R., Hiraga J. S., 2005, Astrophysical Journal, 632, 294

Bamba et al. A., 2008, Publications of the Astronomical Society of Japan, 60, S153

Bell A. R., 1978a, Mon. Not. R. Astron. Soc., 182, 147

Bell A. R., 1978b, Mon. Not. R. Astron. Soc., 182, 443

Bell A. R., 2004, Mon. Not. R. Astron. Soc., 353, 550

Bell A. R., 2005, Mon. Not. R. Astron. Soc., 358, 181

Bell A. R., 2015, Mon. Not. R. Astron. Soc., 447, 2224

Bell A. R., Schure K. M., Reville B., Giacinti G., 2013, Mon. Not. R. Astron. Soc., 431, 415

Berezhko E. G., Völk H. J., 2008, Astron. Astrophys., 492, 695

Berezhko E. G., Ksenofontov L. T., Völk H. J., 2003, Astron. Astrophys., 412, L11

Beshley V., Petruk O., 2012, Mon. Not. R. Astron. Soc., 419, 1421

Blandford R. D., Ostriker J. P., 1978, Astrophys. J. Lett., 221, L29

Blasi P., 2013, Astronomy and Astrophysics Review, 21, 70

Blasi P., 2014, Brazilian Journal of Physics, 44, 426

Blasi P., Gabici S., Vannoni G., 2005, Mon. Not. R. Astron. Soc., 361, 907

Blondin J. M., Wright E. B., Borkowski K. J., Reynolds S. P., 1998, Astrophysical Journal, 500, 342

Blumenthal G. R., Gould R. J., 1970, Reviews of Modern Physics, 42, 237

Bocchino F., Orlando S., Miceli M., Petruk O., 2011, Astron. Astrophys., 531, A129

Bohdan A., Niemiec J., Kobzar O., Pohl M., 2017, Astrophysical Journal, 847, 71

Bykov A. M., Ellison D. C., Renaud M., 2012, Space Sci. Rev., 166, 71

Candia J., Mollerach S., Roulet E., 2002, Journal of High Energy Physics, 2002, 032

Caprioli D., 2011, Journal of Cosmology and Astro-Particle Physics, 2011, 026

Caprioli D., 2012, Journal of Cosm. and Astropart. Phys., 2012, 038

Caprioli D., Spitkovsky A., 2014a, Astrophysical Journal, 783, 91

Caprioli D., Spitkovsky A., 2014b, Astrophysical Journal, 794, 46

Caprioli D., Amato E., Blasi P., 2010, Astroparticle Physics, 33, 307

Caprioli D., Pop A.-R., Spitkovsky A., 2015, Astrophys. J. Lett., 798, L28

Caprioli D., Zhang H., Spitkovsky A., 2018, Journal of Plasma Physics, 84, 715840301

Cardillo M., Amato E., Blasi P., 2016, Astron. Astrophys., 595, A58

Cassam-Chenaï G., Decourchelle A., Ballet J., Sauvageot J. L., Dubner G., Giacani E., 2004, Astron. Astrophys., 427, 199

Cassam-Chenaï G., Hughes J. P., Ballet J., Decourchelle A., 2007, Astrophysical Journal, 665, 315

Cassam-Chenaï G., Hughes J. P., Reynoso E. M., Badenes C., Moffett D., 2008, Astrophysical Journal, 680, 1180

Castro D., Slane P., Patnaude D. J., Ellison D. C., 2011, Astrophysical Journal, 734, 85

Celli S., Morlino G., Gabici S., Aharonian F. A., 2019, Mon. Not. R. Astron. Soc., 487, 3199

Chevalier R. A., 1974, Astrophysical Journal, 188, 501

Chevalier R. A., 1982, Astrophysical Journal, 258, 790

Chevalier R. A., 1983, Astrophysical Journal, 272, 765

Cioffi D. F., McKee C. F., Bertschinger E., 1988, Astrophysical Journal, 334, 252

Crocco L., 1937, Zeitschrift Angewandte Mathematik und Mechanik, 17, 1

Crowther P. A., 2007, ARA&A, 45, 177

Dubner G. M., Giacani E. B., Goss W. M., Green A. J., Nyman L. Å., 2002, Astron. Astrophys., 387, 1047

Duncan A. R., Green D. A., 2000, Astron. Astrophys., 364, 732

Dursi L. J., Pfrommer C., 2008, Astrophysical Journal, 677, 993

Dwarkadas V. V., 2005, Astrophysical Journal, 630, 892

Dyer K. K., Cornwell T. J., Maddalena R. J., 2009, The Astronomical Journal, 137, 2956

Ellison D. C., Vladimirov A., 2008, Astrophys. J. Lett., 673, L47

Elmegreen B. G., Scalo J., 2004, Annual Review of Astronomy and Astrophysics, 42, 211

Enßlin T. A., Pfrommer C., Springel V., Jubelgas M., 2007, Astron. Astrophys., 473, 41

Evoli C., 2018, The Cosmic-Ray Energy Spectrum, doi:10.5281/zenodo.2360277

Federici S., Pohl M., Telezhinsky I., Wilhelm A., Dwarkadas V. V., 2015, Astron. Astrophys., 577, A12

Fermi E., 1949, Physical Review, 75, 1169

Fermi E., 1950, Progress of Theoretical Physics, 5, 570

Fermi E., 1954, Astrophysical Journal, 119, 1

Fisk L. A., Gloeckler G., 2012, Astrophysical Journal, 744, 127

Fransson et al. C., 2015, Astrophys. J. Lett., 806, L19

Fukui Y., 2013, in Torres D. F., Reimer O., eds, Astrophysics and Space Science Proceedings Vol. 34, Cosmic Rays in Star-Forming Environments. p. 249

Fukui Y., et al., 2003, Publ. of Astron. Soc. of Japan, 55, L61

Fukui Y., et al., 2012, Astrophysical Journal, 746, 82

Fukui Y., et al., 2017, Astrophysical Journal, 850, 71

Gabici S., Aharonian F. A., 2014, Mon. Not. R. Astron. Soc., 445, L70

Gabici S., Aharonian F., 2016, in European Physical Journal Web of Conferences. p. 04001

Ghavamian P., Schwartz S. J., Mitchell J., Masters A., Laming J. M., 2013, Space Sci. Rev., 178, 633

Giacalone J., 2005, Astrophysical Journal, 624, 765

Giacalone J., Burgess D., Schwartz S. J., Ellison D. C., 1992, Geophys. Res. Lett., 19, 433

Ginzburg V. L., Syrovatsky S. I., 1961, Progress of Theoretical Physics Supplement, 20, 1

Giuliani A., et al., 2011, Astrophys. J. Lett., 742, L30

Goldreich P., Sridhar S., 1995, Astrophysical Journal, 438, 763

Gould R. J., 1972, Physica, 60, 145

Green D. A., 2014, Bulletin of the Astronomical Society of India, 42, 47

Greisen K., 1966, Phys. Rev. Lett., 16, 748

Gronke M., Oh S. P., 2018, Mon. Not. R. Astron. Soc., 480, L111

Guo X., Sironi L., Narayan R., 2014a, Astrophysical Journal, 794, 153

Guo X., Sironi L., Narayan R., 2014b, Astrophysical Journal, 797, 47

H.E.S.S. Collaboration 2010, Astron. Astrophys., 516, A62

H.E.S.S. Collaboration 2018a, Astron. Astrophys., 612, A6

H.E.S.S. Collaboration 2018b, Astron. Astrophys., 612, A7

HESS Collaboration et al., 2016, Nature, 531, 476

Hess V. F., 1912, Phys. Z., 13, 1084

Hillas A. M., 2005, Journal of Physics G Nuclear Physics, 31, R95

Hinton J. A., Hofmann W., 2009, Annual Review of Astronomy and Astrophysics, 47, 523

Hörandel J. R., 2004, Astroparticle Physics, 21, 241

Hwang U., Decourchelle A., Holt S. S., Petre R., 2002, Astrophysical Journal, 581, 1101

Inoue T., Yamazaki R., Inutsuka S.-i., Fukui Y., 2012, Astrophysical Journal, 744, 71

Iyudin et al. A., 1998, Nature, 396, 142

Ji S., Oh S. P., Ruszkowski M., Markevitch M., 2016, Mon. Not. R. Astron. Soc., 463, 3989

Jokipii J. R., 1987, Astrophysical Journal, 313, 842

Kamble et al. A., 2014, Astrophysical Journal, 797, 2

Kang H., Ryu D., 2013, Astrophysical Journal, 764, 95

Katsuda S., 2017, Supernova of 1006 (G327.6+14.6). p. 63, doi:10.1007/978-3-319-21846-5˙45

Katsuda S., Tsunemi H., Mori K., 2008, Astrophys. J. Lett., 678, L35

Katsuda S., Petre R., Long K. S., Reynolds S. P., Winkler P. F., Mori K., Tsunemi H., 2009, Astrophys. J. Lett., 692, L105

Katsuda S., Petre R., Mori K., Reynolds S. P., Long K. S., Winkler P. F., Tsunemi H., 2010, Astrophysical Journal, 723, 383

Kelner S. R., Aharonian F. A., Bugayov V. V., 2006, Phys. Rev. D, 74, 034018

Kirk J. G., Duffy P., Ball L., 1995, Astron. Astrophys., 293

Klein O., Nishina T., 1929, Zeitschrift fur Physik, 52, 853

Korolev V. V., Vasiliev E. O., Kovalenko I. G., Shchekinov Y. A., 2015, Astronomy Reports, 59, 690

Krymskii G. F., 1977, Akademiia Nauk SSSR Doklady, 234, 1306

Kulsrud R. M., 2005, Plasma physics for astrophysics

Kulsrud R. M., Cesarsky C. J., 1971, Astrophys. Lett., 8, 189

Kulsrud R., Pearce W. P., 1969, Astrophysical Journal, 156, 445

Lagage P. O., Cesarsky C. J., 1983, Astron. Astrophys., 125, 249

Landau L. D., Lifshitz E. M., 1966, Hydrodynamik

Landecker T. L., Routledge D., Reynolds S. P., Smegal R. J., Borkowski K. J., Seward F. D., 1999, Astrophysical Journal, 527, 866

Leahy D. A., Ranasinghe S., Gelowitz M., 2020, Astrophys. J. Suppl. Ser., 248, 16

Lee M. A., Völk H. J., 1973, Astrophys. and Space Science, 24, 31

Li J.-T., Decourchelle A., Miceli M., Vink J., Bocchino F., 2015, Mon. Not. R. Astron. Soc., 453, 3953

Lloyd S. P., 1982, IEEE Trans. Information Theory, 28, 129

Long K. S., Reynolds S. P., Raymond J. C., Winkler P. F., Dyer K. K., Petre R., 2003, Astrophysical Journal, 586, 1162

Malkov M. A., 1998, Phys. Rev. E, 58, 4911

Malkov M. A., Drury L. O., 2001, Reports on Progress in Physics, 64, 429

Mannheim K., Schlickeiser R., 1994, Astron. Astrophys., 286, 983

Marcowith A., et al., 2016, Reports on Progress in Physics, 79, 046901

Maxted N. I., et al., 2012, Mon. Not. R. Astron. Soc., 422, 2230

Maxted N. I., et al., 2018, Astrophysical Journal, 866, 76

Mazzali P. A., Röpke F. K., Benetti S., Hillebrandt W., 2007, Science, 315, 825

McCourt M., Oh S. P., O'Leary R., Madigan A.-M., 2018, Mon. Not. R. Astron. Soc., 473, 5407

McKee C. F., Ostriker J. P., 1977, Astrophysical Journal, 218, 148

Mihalas D., Mihalas B. W., 1984, Foundations of radiation hydrodynamics

Ming J., et al., 2019, Phys. Rev. D, 100, 024063

Minkowski R., 1941, Astronomical Society of the Pacific, 53, 224

Miyoshi T., Kusano K., 2005, J. Comput. Phys., 208, 315

Morlino G., 2017, High-Energy Cosmic Rays from Supernovae. Springer International Publishing, Cham, pp 1711–1736

Morlino G., Caprioli D., 2012, Astron. Astrophys., 538, A81

Morlino G., Amato E., Blasi P., Caprioli D., 2010, Mon. Not. R. Astron. Soc., 405, L21

Neronov A., 2017, Phys. Rev. Lett., 119

Obergaulinger M., Iyudin A. F., Müller E., Smoot G. F., 2014, Mon. Not. R. Astron. Soc., 437, 976

Ostriker J. P., McKee C. F., 1988, Reviews of Modern Physics, 60, 1

Pais M., Pfrommer C., Ehlert K., Pakmor R., 2018, Mon. Not. R. Astron. Soc., 478, 5278

Pais M., Pfrommer C., Ehlert K., Werhahn M., Winner G., 2020, Mon. Not. R. Astron. Soc., 496, 2448

Pakmor R., Springel V., 2013, Mon. Not. R. Astron. Soc., 432, 176

Pakmor R., Bauer A., Springel V., 2011, Mon. Not. R. Astron. Soc., 418, 1392

Pakmor R., Kromer M., Taubenberger S., Sim S. A., Röpke F. K., Hillebrandt W., 2012, Astrophys. J. Lett., 747, L10

Pakmor R., Springel V., Bauer A., Mocz P., Munoz D. J., Ohlmann S. T., Schaal K., Zhu C., 2016a, Mon. Not. R. Astron. Soc., 455, 1134

Pakmor R., Pfrommer C., Simpson C. M., Kannan R., Springel V., 2016b, Mon. Not. R. Astron. Soc., 462, 2603

Parizot E., Marcowith A., Ballet J., Gallant Y. A., 2006, Astron. Astrophys., 453, 387

Park J., Caprioli D., Spitkovsky A., 2015, Physical Review Letters, 114, 085003

Parker E. N., 1965, Journal of Plan. Sci., 13, 9

Petruk O., Beshley V., Bocchino F., Miceli M., Orlando S., 2011, Mon. Not. R. Astron. Soc., 413, 1643

Pfrommer C., Enßlin T. A., 2004, Astron. Astrophys., 413, 17

Pfrommer C., Jonathan Dursi L., 2010, Nature Physics, 6, 520

Pfrommer C., Jones T. W., 2011, Astrophysical Journal, 730, 22

Pfrommer C., Enßlin T. A., Springel V., 2008, Mon. Not. R. Astron. Soc., 385, 1211

Pfrommer C., Pakmor R., Schaal K., Simpson C. M., Springel V., 2017a, Mon. Not. R. Astron. Soc., 465, 4500

Pfrommer C., Pakmor R., Simpson C. M., Springel V., 2017b, Astrophys. J. Lett., 847, L13

Pohl M., 1996, Astron. Astrophys., 307, L57

Powell K. G., Roe P. L., Linde T. J., Gombosi T. I., De Zeeuw D. L., 1999, J. Comput. Phys., 154, 284

Reynolds S. P., 1996, Astrophysical Journal, 459, L13

Reynolds S. P., 2008, ARA&A, 46, 89

Reynolds S. P., 2017, Dynamical Evolution and Radiative Processes of Supernova Remnants. p. 1981, doi:10.1007/978-3-319-21846-5˙89

Reynoso E. M., Hughes J. P., Moffett D. A., 2013, Astronom. J., 145, 104

Rothenflug R., Ballet J., Dubner G., Giacani E., Decourchelle A., Ferrando P., 2004, Astron. Astrophys., 425, 121

Rowell G., Fukui Y., Burton M., Horachi H., Nicholas B., 2009, Tracing shocked/disrupted gas towards the TeV gamma-ray supernova remnant RXJ1713.7-3946, ATNF Proposal

Ruszkowski M., Yang H. Y. K., Reynolds C. S., 2017, Astrophysical Journal, 844, 13

Rybicki G. B., Lightman A. P., 1986, Radiative Processes in Astrophysics

Sano H., et al., 2015, Astrophysical Journal, 799, 175

Sarkar K. C., Nath B. B., Sharma P., 2015, Mon. Not. R. Astron. Soc., 453, 3827

Scalo J., Elmegreen B. G., 2004, Annual Review of Astronomy and Astrophysics, 42, 275

Schaal K., Springel V., 2015, Mon. Not. R. Astron. Soc., 446, 3992

Schlickeiser R., 2002, Cosmic Ray Astrophysics

Schneiter E. M., Velázquez P. F., Reynoso E. M., Esquivel A., De Colle F., 2015, Mon. Not. R. Astron. Soc., 449, 88

Schure K. M., Bell A. R., O'C Drury L., Bykov A. M., 2012, Space Sci. Rev., 173, 491

Sedov L. I., 1959, Similarity and Dimensional Methods in Mechanics

Skilling J., 1975, Mon. Not. R. Astron. Soc., 172, 557

Slane P., Hughes J. P., Edgar R. J., Plucinsky P. P., Miyata E., Tsunemi H., Aschenbach B., 2001, Astrophysical Journal, 548, 814

Soderberg A. M., Brunthaler A., Nakar E., Chevalier R. A., Bietenholz M. F., 2010, Astrophysical Journal, 725, 922

Sparre M., Pfrommer C., Vogelsberger M., 2019, Mon. Not. R. Astron. Soc., 482, 5401

Spitkovsky A., 2008a, Astrophys. J. Lett., 673, L39

Spitkovsky A., 2008b, Astrophys. J. Lett., 682, L5

Springel V., 2010, Mon. Not. R. Astron. Soc., 401, 791

Stage M. D., Allen G. E., Houck J. C., Davis J. E., 2006, Nature Physics, 2, 614

Stephenson F. R., Green D. A., 2002, Historical supernovae and their remnants, by F. Richard Stephenson and David A. Green. International series in astronomy and astrophysics, vol. 5. Oxford: Clarendon Press, 2002, ISBN 0198507666, 5

Takahashi T., et al., 2008, Publ. of Astron. Soc. of Japan, 60, S131

Tanabashi M. e. a., 2018, Phys. Rev. D, 98, 030001

Tanaka T., et al., 2008, Astrophysical Journal, 685, 988

Tanaka T., et al., 2011, Astrophys. J. Lett., 740, L51

Taylor G., 1950, Proceedings of the Royal Society of London Series A, 201, 159

Telezhinsky I., 2009, Astroparticle Physics, 31, 431

Thomas T., Pfrommer C., 2019, Mon. Not. R. Astron. Soc., 485, 2977

Toro E., 2009, Riemann Solvers and Numerical Methods for Fluid Dynamics: A Practical Introduction, doi:10.1007/b79761.

Truelove J. K., McKee C. F., 1999, Astrophys. J. Suppl. Ser., 120, 299

Tsuji N., Uchiyama Y., 2016, Publ. of Astron. Soc. of Japan, 68, 108

Uchiyama Y., Aharonian F. A., 2008, Astrophys. J. Lett., 677, L105

Uchiyama Y., Aharonian F. A., Takahashi T., 2003, Astron. Astrophys., 400, 567

Uchiyama Y., Aharonian F. A., Tanaka T., Takahashi T., Maeda Y., 2007, Nature, 449, 576

Vink J., 2012, A&ARev, 20, 49

Walch S., Naab T., 2015, Mon. Not. R. Astron. Soc., 451, 2757

Wang C.-Y., Chevalier R. A., 2001, Astrophysical Journal, 549, 1119

Wang C.-Y., Chevalier R. A., 2002, Astrophysical Journal, 574, 155

Wang Z. R., Qu Q. Y., Chen Y., 1997, Astron. Astrophys., 318, L59

Warren J. S., et al., 2005, Astrophysical Journal, 634, 376

Wentzel D. G., 1971, Astrophysical Journal, 163, 503

Wiener J., Zweibel E. G., Oh S. P., 2013, The Astrophysical Journal, 767, 87

Winkler P. F., Gupta G., Long K. S., 2003, Astrophysical Journal, 585, 324

Winner G., Pfrommer C., Girichidis P., Werhahn M., Pais M., 2020, arXiv e-prints, p. arXiv:2006.06683

Woosley S. E., Kasen D., Blinnikov S., Sorokina E., 2007, Astrophysical Journal, 662, 487

Xing Y., Wang Z., Zhang X., Chen Y., 2016, Astrophysical Journal, 823, 44

Yang R.-z., de Oña Wilhelmi E., Aharonian F., 2018a, Astron. Astrophys., 611, A77

Yang R.-z., Kafexhiu E., Aharonian F., 2018b, Astron. Astrophys., 615, A108

Zatsepin G. T., Kuzmin V. A., 1966, Soviet Journal of Experimental and Theoretical Physics Letters, 4, 78

Zhang D., Chevalier R. A., 2019, Mon. Not. R. Astron. Soc., 482, 1602

Zirakashvili V. N., Aharonian F. A., 2010, Astrophysical Journal, 708, 965

Zweibel E. G., 2013, Physics of Plasmas, 20, 055501

Zweibel E. G., 2017, Physics of Plasmas, 24, 055402

van Marle A. J., Meliani Z., Marcowith A., 2015, Astron. Astrophys., 584, A49